Valorization of industrial solid wastes as ingredients for construction materials

DESIGN, PERFORMANCE AND DURABILITY

Xuan Ling

Bouwstenen 400

Valorization of industrial solid wastes as ingredients for construction materials

Design, Performance and Durability

Xuan Ling

This research was partially carried out under project number T20014 and T22017 in the framework of the Research Program of the Materials innovation institute (M2i) (www.m2i.nl) supported by the Dutch government and was funded by Holland High Tech | TKI HSTM via the PPS allowance scheme for public-private partnerships.

CIP-DATA LIBRARY TECHNISCHE UNIVERSITEIT EINDHOVEN

Valorization of industrial solid wastes as ingredients for construction materials:

Design, Performance and Durability/ by Xuan Ling

A catalogue record is available from the Eindhoven University of Technology Library

ISBN: 978-90-386-6184-1

Bouwstenen

NUR 955

Cover design by Mengyan Guo, based on AI-generated images (via OpenAI and Midjourney)

Ph.D. thesis, Eindhoven University of Technology, the Netherlands

Valorization of industrial solid wastes as ingredients for construction materials

Design, Performance and Durability

PROEFSCHRIFT

ter verkrijging van de graad van doctor
aan de Technische Universiteit Eindhoven,
op gezag van de rector magnificus, prof. dr. S.K. Lenaerts,
voor een commissie aangewezen door het College voor Promoties,
in het openbaar te verdedigen op dinsdag 5 november 2024 om 16:00 uur

door

Xuan Ling

geboren te Lanxi, China

Dit proefschrift is goedgekeurd door de promotoren en de samenstelling van de promotiecommissie is als volgt:

Voorzitter:	prof. dr. ir. T.A.M. Salet
Promotor:	prof. dr. ir. H.J.H. Brouwers
Copromotor:	dr. Dipl.-Min. K. Schollbach
Promotiecommissieleden:	prof. dr. H. Justnes (Norwegian University of Science and Technology)
	prof. dr. L.M. Ottosen (Technical University of Denmark)
	prof. dr. M.C. Bignozzi (University of Bologna)
	prof. dr. W. Chen (Wuhan University of Technology)
	assoc. prof. dr. J. Yliniemi (University of Oulu)
	prof. dr. ir D.M.J. Smeulders

Het onderzoek of ontwerp dat in dit proefschrift wordt beschreven is uitgevoerd in overeenstemming met de TU/e Gedragscode Wetenschapsbeoefening.

Dedicated to my beloved parents

献给我亲爱的父母

Preface

I truly believe that every story comes to an end, but if that ending is not satisfactory, it means it is not the true ending. Please keep your patience and continue to work hard until the ending meets your expectations. As my doctoral journey is nearing its end, I cannot help but feel excited and grateful because I have persisted for over four years! This research was carried out under the funding of China Scholarship Council and supported by Eindhoven University of Technology. Meanwhile, this research was partially carried out under project number T20014 and T22017 in the framework of the Research Program of the Materials innovation institute (M2i) (www.m2i.nl) supported by the Dutch government and was funded by Holland High Tech | TKI HSTM via the PPS allowance scheme for public-private partnerships.

I would like to start with a word of thanks to my promotor Prof. H.J.H. Brouwers. Jos, this story began with our first meeting in Wuhan in 2017. At that time, you asked me about my dreams for the future. I have to admit, I was stumped. But you did not rush me. Instead, you gave me the time to find my words. Looking back, that simple question was probably the first big nudge you gave me on this journey. Later, you provided me with such a great opportunity to be a member of the Building Materials group. During my PhD study, you offered me all the necessary conditions for my investigation, as well as enough trust. Your suggestions and experiences always provided me with new insights to improve my work and life. I had lots of chances to learn from knowledgeable experts from many other fields, from which I improved and benefited a lot.

I would also like to express my warmest thanks to my co-promotor Dr. Katrin Schollbach. With your guidance, I have delved into multiple experimental procedures, all the while enhancing my theoretical understanding. Your Q-XRD courses were truly remarkable, leaving a lasting impression. Your expertise and suggestions have been invaluable, aiding me extensively in revising numerous manuscripts and offering profound insights. Throughout my PhD journey, you afforded me ample freedom and trust to pursue my research. Whenever I encountered challenges, your friendly encouragement and inspiration propelled me forward.

My great gratitude goes to my master's supervisor and committee member Prof. dr. Wei Chen, who guided me in the field of building materials at the very beginning in Wuhan. You taught me how to do research independently and provided invaluable guidance and support in my personal development.

I would like to extend my sincere appreciation to the other promotion committee members, Prof. dr. Harald Justnes (Norwegian University of Science and Technology), Prof. dr. Lisbeth M. Ottosen (Technical University of Denmark), Prof. dr. Maria Chiara Bignozzi (University of Bologna), Assoc. Prof. dr. Juho Yliniemi (University of Oulu), and Prof. dr. ir David M.J. Smeulders (Eindhoven University of Technology) for their precious time in reviewing my thesis and providing valuable comments and suggestions to improve the quality.

In the meantime, words of thanks also go to my project partners, in particular Mr. J.M.J Winter (ETM), Mr. Harry Beukema (ETM) and Dr. Jaap Steketee (TAUW) for a warm welcome and very pleasant cooperation. Also, I would like to thank Dr. Spiesz Przemek (Heidelberg

Materials), Mr. Kai Erik Ekstrøm (NOAH), Mr. Inge Johansson (NOAH) and Dr. Franz Bormann (M2i) for their technical support and professional discussions and suggestions.

Furthermore, the thesis cannot be finished without the efforts and help from my current and former colleagues. Being a member of the Building Materials group, an exceptional international team fills me with both pride and gratitude. Prof. Qingliang Yu, Prof. Sieger van der Laan, and Dr. Gauvin Florent, your dedication to academic research and hardworking nature, as well as the insightful conversations about various aspects of life, serve as constant sources of inspiration for me. I extend my heartfelt thanks to all the technicians, especially Ing. A.C.A Delsing and Mr. H.L.W Smulders, for their invaluable assistance and technical support throughout my research. Peipeng, Yangyueye, Shaohua, Gang and Yuxuan, your guidance and support during the initial stages of my study in Eindhoven are truly appreciated. Anna, Winnie, Kinga and Jawad, thank you for the delightful moments and shared meals. Karimi Hossein, your jokes brought joy to my days. Luyang, Fan, Yan, Yanjie & Yufei, Jinyang, Zixing, and Jia, our shared experiences have been unforgettable, and I treasure the memories we have created together. I also want to express my gratitude to the members of our Texas poker group (Daoru, Xinglong, Tao, Yanjie, Jinyang, Helong, Jiale, Quan, Yanshuo and Yilu) for the happiness, excitement, bluff, and heart-breaking time; to Jonathan Zepper for the wonderful learning experiences in Germany and also in several conferences; and to Naomi for the assistance with MIP samples analysis and for the fun you bring to every Sinterklaas Festival. Special thanks to the Sports Day team members for their efforts and great achievements; to Lili, Peng and Xiaoxiao for our memorable table tennis matches; and to Qilong, Qianhui, Rui, Yunjie & Pan, Israel, Yudan & Rishi, Yuming & Di, and Jiayu, our joyful reunions have been a source of immense enjoyment amid our research endeavors. Assoc Prof. Dr. Jun Hu, from Industrial Design, your Wednesday training sessions for healthy exercise habits are deeply appreciated.

My appreciation also goes to my dear colleagues, including but not limited to, Nataliya, Yan, Ricardo, Jia, Iris, Samantha, Beatrice, Ceren, Leila, Marina, Naomi, Jinyang, Yanshuo, Jiale, Samuel, Charles, Quan, Helong, Zhihan, Shashank, Alex, Yanjie, Zixing, Felix, Yilu, as well as our BPS Secretaries (Manon and Sonja). I take immense pleasure in working alongside each and every one of you, and I have been truly fascinated by the diverse cultures you bring. I wish you all the best in the future and hope our friendship will endure, no matter where life takes us.

Finally, and most importantly, I give my thanks from the bottom of my heart to my Mum (Aichun Jiang), and Dad (Xinhua Ling). Your unwavering support and encouragement in every choice and decision I have made mean the world to me. Your steadfast spiritual guidance has been my anchor through every challenging moment in my life. You are the best parents anyone could ask for. Also, I would like to thank my family, especially my uncle (Zhiyin Jiang), for their support and understanding throughout my formative years. Moreover, I would like to express my sincerest appreciation to my girlfriend (Mengyan Guo). Thank you for accompanying me throughout the past three years as I pursued this degree. We experienced both happiness and sadness during this time, but together, we made it. Let's cherish these memories and create many more together!

Xuan Ling

Eindhoven, July 2024

Summary

Valorization of industrial solid wastes as ingredients for construction materials: Design, Performance and Durability

As the volume of waste materials continues to increase across diverse sectors, the urgency of addressing solid waste disposal has grown significantly in recent years. This project facilitates the valorization of industrial waste by transforming it into sustainable construction materials. A diverse array of waste streams originating from sewage treatment, incineration processes, and the steel-making industry were considered. Due to the variability in physical and chemical characteristics of the wastes across different sources, this thesis proposes an investigation of various innovative systems including landfill sealing materials, alkali-activated materials, and steel slag-based cement-free materials.

The **first section** (**Chapter 2**, **Chapter 3**) of this thesis focuses on investigating the suitability of solid waste materials for landfill sealing materials purposes. Chapter 2 explores the utilization of various sludge types and industrial residues in formulating waterglass (Na_2SiO_4)-based landfill sealing materials. Low permeability sludge-based sealing materials have been developed, with limited heavy metal leaching concerns. Then, the carbonation behavior of sludge-based sealing materials is assessed in Chapter 3. The carbonation induces carbonates and monohydrocalcite formation, leading to impermeability deterioration. Waterglass is identified as beneficial in reducing degradation, which is attributed to the formation of silicate gel post-carbonation. The overall permeability after carbonation meets Dutch legislative requirements.

The **second section** (**Chapter 4** to **Chapter 7**) moves towards the recycling and recovery of solid wastes in alkali-activated materials (AAMs). In **Chapter 4**, Waste incineration filter dust (WIFD), a kind of air pollution control residue, characterized by a high concentration of portlandite and calcite, is developed as an activator in Na_2CO_3-activated granulated ground blast furnace slag (GGBFS). WIFD reacts with Na_2CO_3, improving alkalinity and accelerating the hydration of Na_2CO_3-activated GGBFS. However, the mechanical performance diminishes with increased WIFD content. **Chapter 5** investigates the effect of additional nano-silica (NS) and microsilica (SF) on this hybrid binder. NS and SF show various enhancements in mechanical performance, attributed to the different reaction products and the resulting microstructure, as well as the resistance to carbonation. **Chapter 6** proposes solidifying biomass bottom ash (BBA) in alkali-activated GGBFS and fly ash blended binders. Investigations into the influence of BBA content, fineness, silicate modulus of activators, and aluminum-anodizing waste on solidification performance are conducted, focusing on reaction mechanisms, phase assemblages, mechanical properties, and leaching behavior. The hybrid binder shows desirable mechanical performance and limited heavy metal leaching, enabling their use as potential construction materials. In **Chapter 7**, the focus shifts to the investigation of functional alkali-activated materials through the incorporation of TiO_2. The in-situ zeolite formation within metakaolin-based geopolymers notably enhances self-cleaning performance, enhancing mass transfer capacity through connective channels. The findings provide mechanistic insights into in-situ zeolite formation in metakaolin-based geopolymers and emphasize its promising potential for optimizing self-cleaning properties in cementitious materials.

The **third section** of the thesis (**Chapter 8**) delves into the potential application of Basic Oxygen Furnace (BOF) slag, a by-product of steel manufacturing, as a cement-free binder. Concurrently, stabilized gypsum is employed to enhance the performance of the BOF slag binder. Pentasodium diethylenetriamine pentaacetate (DTPA-5Na) activates the BOF slag successfully, through accelerated dissolution of brownmillerite by the chelating reaction. Additionally, flue gas desulphurization (FGD) gypsum promotes ettringite formation, thereby enhancing the mechanical performance. The novel BOF slag binder demonstrates significant advantages in terms of waste prevention, cement replacement, cost savings and reduced CO_2 emissions.

Contents

Preface **1**

Summary **3**

Contents **5**

Chapter 1 Introduction **11**

1.1 Background and Motivation **11**

1.1.1 Overview of investigated solid wastes 11

1.1.2 Sealing materials for landfill cover system 15

1.1.3 Alkali-activated materials 17

1.1.4 BOF slag-based binder 20

1.2 Scope and objectives **20**

1.3 Outline of the thesis **22**

Chapter 2 Low permeability sealing materials based on sewage, digestate and incineration industrial by-products in the final landfill cover system **25**

2.1 Introduction **26**

2.2 Materials and Experiments **27**

2.2.1 Raw materials 27

2.2.2 Sample preparation 27

2.2.3 Methodology 28

2.3 Results and Discussions **30**

2.3.1 Physical and chemical properties of raw materials 30

2.3.2 Compaction behavior of the fresh blends 33

2.3.3 Water permeability of the cured blends 34

2.3.4 Reaction products characterization 35

2.3.5 Environmental impact 40

2.3.6 Benefits and limits discussion 43

2.4 Conclusions **43**

Chapter 3 Carbonation of digested sewage sludge-based sealing material in a final landfill cover system: role of waterglass and additional industrial by-products **45**

3.1 Introduction **46**

3.2 Materials and Experiments **47**

3.2.1 Raw materials 47

3.2.2 Sample preparation 49

3.2.3 Methodology 50

3.3 Results **51**

3.3.1 Permeability 51
3.3.2 Phase changes 53
3.3.3 Physical changes 57
3.3.4 Environmental impact 60
3.4. Discussions 61
3.4.1 Carbonation mechanism of sealing materials 61
3.4.2 Limitations of the accelerated carbonation process 62
3.4.3 The effect of waterglass and various additives on the sealing materials 63
3.5. Conclusions 63
Chapter 4 Utilization of waste incineration filter dust in sodium carbonate-activated slag mortars 65
4.1 Introduction 66
4.2 Materials and Experiments 67
4.2.1 Raw materials 67
4.2.2 Sample preparation 69
4.2.3 Methodology 69
4.3 Results and Discussions 71
4.3.1 Flowability of NC-WIFD-GGBFS mortars 71
4.3.2 Reaction kinetics of NC-WIFD-GGBFS blends 72
4.3.3 Reaction products identification of NC-WIFD-GGBFS blends 74
4.3.4 Gel microstructure 79
4.3.5 Mechanical properties 82
4.3.6 Role of WIFD and Na_2CO_3 83
4.4 Conclusions 84
Chapter 5 The effect of nano-silica and silica fume on the sodium carbonate-activated slag system containing air pollution control residues 87
5.1 Introduction 88
5.2 Materials and Experiments 89
5.2.1 Raw materials 89
5.2.2 Mixture design and preparations 91
5.2.3. Methodology 91
5.3 Results 93
5.3.1 Flowability and compressive strength development 93
5.3.2 Reaction kinetics 94
5.3.3 Phase assemblage analysis 96
5.3.4 Gel pore characterization 99

5.3.5 Microstructure and gel composition 100
5.3.6 Carbonation depths and rate 102
5.4 Discussions 104
5.4.1 Preliminary study on CO_2 emissions and cost of the blended binder 104
5.4.2 Reaction mechanism of SF and NS 105
5.5 Conclusions 106
Chapter 6 Valorization of biomass bottom ash in alkali-activated GGBFS-fly ash: impact of biomass bottom ash characteristic, silicate modulus and aluminum-anodizing waste 109
6.1 Introduction 110
6.2 Materials and Experiments 111
6.2.1 Raw materials 111
6.2.2 Mixture design and specimen preparation 113
6.2.3 Methodology 114
6.3 Results 116
6.3.1 Reactivity of BBA, GBBA and AAW 116
6.3.2 Reaction kinetics of BBA-GGBFS-CFA blends 117
6.3.3 Phase assemblages 118
6.3.4 Microstructure 124
6.3.5 Leaching behavior 125
6.3.6 Mechanical properties 128
6.4 Discussions 129
6.4.1 The effect of BBA content 129
6.4.2 The effect of BBA fineness 130
6.4.3 The effect of silicate modulus 130
6.4.4 The effect of additional AAW 130
6.5 Conclusions 131
Chapter 7 Advancing self-cleaning performance in metakaolin-based geopolymers through in-situ zeolite formation and TiO_2 integration 133
7.1 Introduction 134
7.2 Materials and Experiments 135
7.2.1 Raw Materials 135
7.2.2 Specimen preparation 135
7.2.3 Methodology 136
7.3 Results 138
7.3.1 Phase assemblages analysis 138

7.3.2 Function group identification 142
7.3.3 Optical band gap energy and Urbach energy 144
7.3.4 Self-cleaning performance 146
7.3.5 Microstructure of geopolymers 148
7.4 Discussions 152
7.4.1 Enhanced mechanism of self-cleaning performance upon zeolite formation 153
7.4.2 Analysis of in-situ formation conditions of zeolites in geopolymers 154
7.5 Conclusions 156
Chapter 8 Pentasodium diethylenetriamine pentaacetate (DTPA-5Na) activated basic oxygen furnace slag 159
8.1 Introduction 160
8.2 Materials and methods 161
8.2.1 Raw materials 161
8.2.2 Specimen preparation 163
8.2.3 Methodology 164
8.3 Results of the clinker and waste gypsum cement 166
8.3.1 Setting time 166
8.3.2 Hydration kinetics 166
8.3.3 Mechanical performance 167
8.4 Results of the BOF slag-based binder materials 168
8.4.1 Hydration kinetics and its correlation with hydration products 168
8.4.2 Effects of DTPA-5Na and FGD gypsum on mechanical properties 171
8.4.3 Enhancement mechanism of DTPA-5Na and FGD gypsum 172
8.4.4 Environmental impact 179
8.4.5 BOF slag hydration model: theoretical water demand and chemical shrinkage 180
8.5 Discussions of BOF slag-based binder materials 184
8.5.1 Activation mechanism of DTPA-5Na 184
8.5.2 Effect of calcium and sulfate on the enhanced mechanism 186
8.6 Conclusions 188
Chapter 9 Conclusions and recommendations 191
9.1 Conclusions 191
9.1.1 Sludge-based sealing materials and their carbonation behavior 191
9.1.2 Recycling industrial solid waste in alkali-activated materials 192
9.1.3 Development of BOF slag-based cement-free binder 193
9.2 Recommendations 194

9.2.1 Sludge-based sealing materials and their carbonation behavior 194
9.2.2 Recycling industrial solid waste in AAMs 195
9.2.3 Development of BOF slag-based cement-free binder 196
Bibliography 197
Appendix A 223
Appendix B 224
Appendix C 226
Appendix D 230
Appendix E 232
List of abbreviations 234
List of publications 237
Curriculum vitae 239

Chapter 1 Introduction

1.1 Background and Motivation

In recent years, recycling and reusing waste materials have been pivotal concerns, especially amidst challenges posed by materials and energy scarcity. Waste is generated at all stages of the materials life cycle - from extraction or cultivation to production, consumption and disposal - emerging from diverse sources and compositions. In the EU, the generated waste from all economic activities and households was nearly 2,135 million tons in 2020 (latest data available) [1]. Notably, construction waste, alongside mining and quarrying waste, constitutes the major mineral waste categories, accounting for 37.5% and 23.4%, respectively (**Fig. 1.1**). On the other hand, waste arising from manufacturing, wastewater and households each contributes around 10% to the total waste output. The waste-to-resource approach can reduce the environmental and health impacts of the generated waste and improve resource efficiency. However, waste from various sources and processes possesses distinct properties, necessitating thorough characterization to determine their optimal applications. By comprehensively understanding the physical and chemical attributes of each waste type, suitable methods for recycling, disposal, or repurposing can be developed. This tailored approach ensures efficient waste management, minimizes environmental impact and maximizes resource recovery.

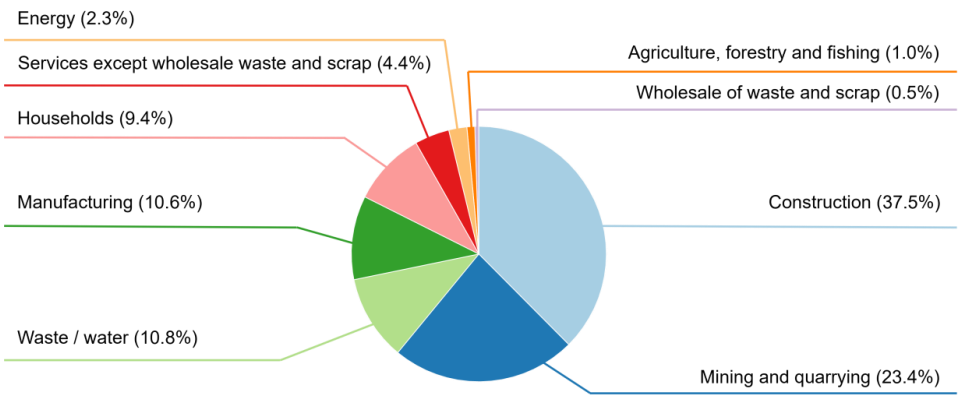

Fig. 1.1: Waste generation by economic activities and households, EU, 2020 (latest) (% share of total waste). Source: Eurostat (online data code: env_wasgen) [1].

1.1.1 Overview of investigated solid wastes

In this thesis, a diverse range of industrial solid wastes has been investigated, encompassing sewage sludge, digestate sludge, biomass bottom ash, aluminum-anodizing waste, waste incineration fly ash and filter dust, basic oxygen furnace slag and flue gas desulfurization gypsum. Their respective sources are summarized in **Table 1.1**.

Table 1.1: Overview of investigated solid waste.

Industrial solid waste	Sources
Sewage sludge	Sewage treatment plant
Digestate sludge	Municipal solid waste plant
Biomass bottom ash	Biomass power plant
Aluminum- anodizing waste	Anodizing plant
Waste incineration fly ash	Waste incineration plant
Waste incineration filter dust	Waste incineration plant
Basic oxygen furnace slag	Integrated steel plant
Flue gas desulfurization gypsum	Fossil-fuel plants

Sewage sludge is the residual solid waste remaining after sewage treatment, comprising organic and inorganic compounds separated from the liquid influent through various treatment processes such as primary and secondary treatment. Additional treatments like anaerobic digestion, aerobic digestion, dewatering and drying are commonly conducted to reduce the sludge volume and stabilize its composition [2]. A Thermal Pressure Hydrolysis (TPH) process has been developed to enhance biogas production and dewaterability [3,4]. The common Dutch sludge treatment chain is presented in **Fig. 1.2**.

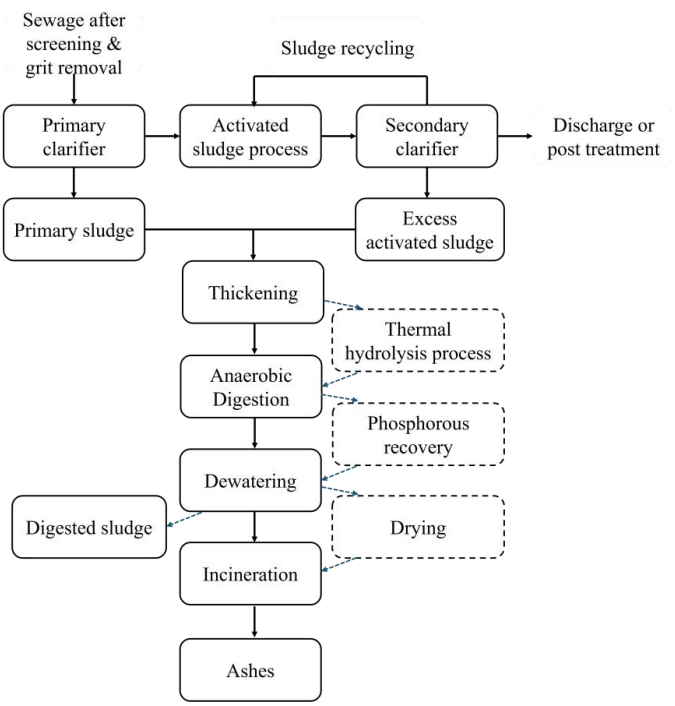

Fig. 1.2: Common Dutch sewage sludge treatment chain (Adapted from [5]). Dotted lines represent treatment steps that are less commonly applied.

Historically, sewage sludge was predominantly used as fertilizer in agricultural soils due to its rich nutrient content (N, P and K) [6]. However, stricter regulations (EU Sludge Directive

86/278/EC) have been implemented in EU countries to prevent the uptake of pathogens and heavy metals by crops [7], which results in a significant shift in sludge disposal practices. In the Netherlands, sewage sludge production (dry solid) exceeded 300,000 tons in 2020, with nearly 85% of it being incinerated [8]. While incineration significantly reduces volume and breaks down organic pollutants, it raises concerns about increased emissions of pollutants like nitrogen oxides and sulfur dioxide, as well as higher costs associated with ash disposal.

Digestate sludge is the material remaining after the anaerobic digestion of a biodegradable feedstock, such as sewage sludge, municipal wastes, agricultural wastes and industrial wastes [9]. Rich in nutrients like ammonia, phosphates, and micronutrient metals, its primary use is as a soil conditioner, provided it meets regulatory standards for toxic metals. If the heavy metal content is too high, further treatment or alternative disposal, such as landfilling, is necessary. For landfilling, the solids are usually thickened or dewatered to reduce the sludge volume and disposal costs. Additionally, processes like hydrothermal treatment can recover energy from the carbon content within the digestate, converting it to biochar [10].

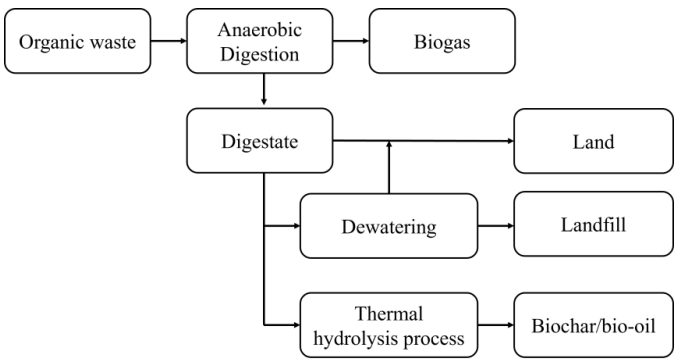

Fig. 1.3: Common digestate treatment chain.

Biomass bottom ash (BBA), together with biomass fly ash (BFA), are the by-products generated during the combustion of biomass materials. In recent years, the promotion of renewable energy resources in the EU has led to an increase in the contribution of biomass fuels to the gross final energy consumption. Biomass fuels, known for being cost-effective and producing lower emissions during combustion, undergo thermal treatment, resulting in a significant reduction in the volume and mass of biomass waste materials [11]. However, the surge in biomass usage has given rise to an elevated production of biomass ash (BA). According to Directive 2009/28/CE, approximately 15.5 million tons of BBA and BFA are generated annually in the EU-27. BBA is the coarse fraction settling under the grate of the combustion chamber or incinerator [12,13], accounting for 60-90 wt% of the total ash generated in a grate furnace [14]. Compared to coal fly ash and BFA, BBA typically contains lower levels of reactive SiO_2, Al_2O_3 and Fe_2O_3 [15]. Consequently, it is often directed to landfills.

Aluminum-anodizing waste (AAW) is a by-product generated during the aluminum anodizing process in the aluminum industry. It primarily consists of aluminum hydroxide with various polymorphisms, such as bayerite and boehmite. Due to the presence of heavy metals such as Cr and Ni, much of this waste is disposed of through sewage systems or landfills after undergoing prior treatment. In an effort to enhance the recycling of this aluminum-rich material, Correia et al. investigated its potential application as a coagulant in municipal wastewater treatment [16].

Furthermore, AAW has been identified for prospective utilization in diverse applications, including refractory materials [17,18], insulation panels [19], ceramic filters [20] and bricks [21].

Waste incineration fly ash (WIFA) is a by-product generated during the combustion of solid municipal waste. Waste incineration remains a widely used treatment method to handle increasing quantities of domestic and industrial waste, as it can reduce waste volume by up to 90%, recover energy, and destroy pathogens and toxic organic compounds. The incineration process produces various residues, including bottom ash and fly ash, whose physical and chemical properties vary depending on the type and source of the municipal solid waste. The disposal of WIFA poses significant environmental risks due to the toxic metals and the potential leaching of hazardous pollutants. To mitigate these environmental impacts, researchers have investigated the recovery of metals and other materials from fly ash, as well as its use as a filling material or in cement production [22,23].

Waste incineration filter dust (WIFD) is a type of air pollution control residue (APC) generated during the incineration of municipal solid wastes. This occurs by injecting a quick lime suspension into the hot flue gas, aimed at removing sulfur dioxide from the emissions in incineration plants. Generally, these kinds of residues are disposed of in landfilling or used in road base construction, which would be a waste of their highly reactive calcium content [24]. Separation processes, solidification/stabilization and thermal methods can be used to treat the APC residues [25]. However, these procedures take more time and result in extra costs. And while the WIFD is always rich in portlandite and calcite, its composition can vary widely, making the treatments more complicated. Shirley et. al proposed using a co-fired pulverized fuel ash to solidify the air pollution control residues [26].

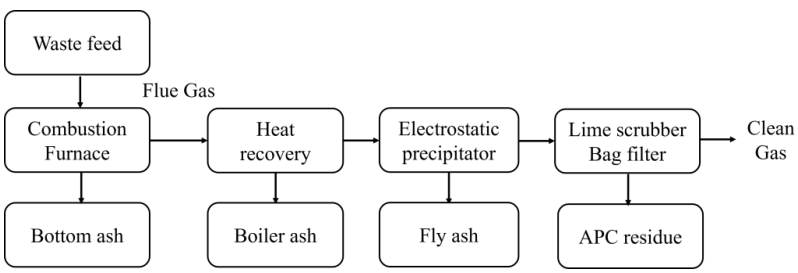

Fig. 1.4: Various wastes generated during the incineration of municipal solid waste (Adapted from [27]).

Basic oxygen furnace slag, a by-product of the steelmaking process, is generated in an amount of approximately 90-110 kg per ton of steel, resulting in an annual production of about 10.4 million tons in Europe [28,29]. Its mineral assemblage includes alite, belite, brownmillerite, lime, magnetite and wüestite, primarily composed of CaO (30-50 wt%), SiO_2 (10-20 wt%), Fe_2O_3 (20-40 wt%), Al_2O_3 (1-7 wt%), MgO (4-10 wt%), MnO (0-4 wt%), P_2O_5 (1-3 wt%), TiO_2 (0-2 wt%) [30,31]. In comparison to Ordinary Portland cement, BOF slag demonstrates lower reactive alite content (typically 0-5 wt%) and higher belite content (40-55 wt%) [32], limiting its potential as a binder constituent due to the low hydration capacity [33]. Currently, recycled BOF slag is primarily utilized in the construction industry as the aggregate in asphalt mixture [34,35]. Nevertheless, a significant portion of generated BOF slag is still either stacked or discarded, thereby occupying the land resources. Given the rapid depletion of natural resources

and the considerable volume of BOF slag available, it would be beneficial to recycle it as efficient binder material to mitigate its environmental impact [36].

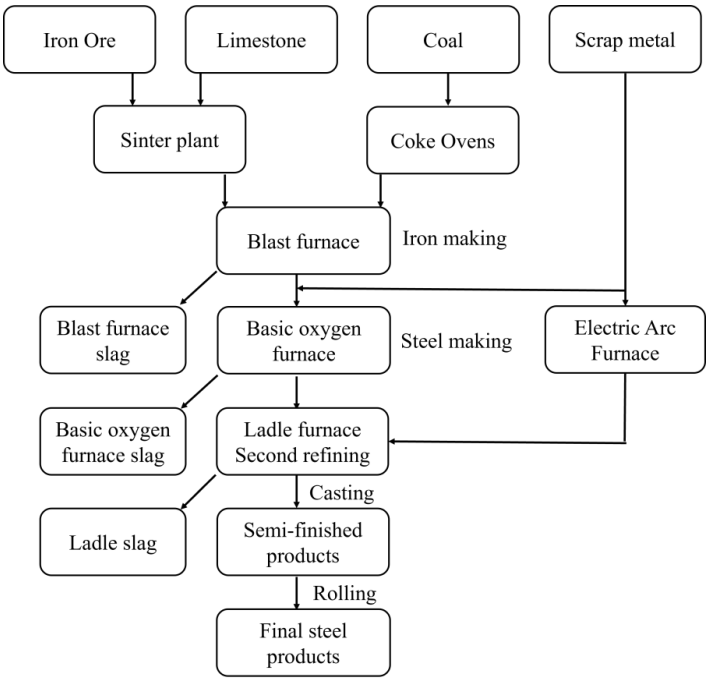

Fig. 1.5: Flowchart of the steel-making process (Adapted from [37]).

Flue gas desulfurization (FGD) gypsum is generated in substantial quantities as a by-product of the flue gas desulfurization processes utilized in combustion systems that burn sulfur-laden fuels, such as coal and residual oil. It primarily consists of calcium sulfate dihydrate ($CaSO_4 \cdot 2H_2O$), chemically identical to natural gypsum. Due to this equivalence to natural gypsum, FGD gypsum is a viable substitute for natural gypsum in numerous industrial applications. Besides its use in plaster, decorative elements, or screeds, a significant portion of gypsum is used in the production of drywalls, wallboards, and especially gypsum plasterboards. Furthermore, it can replace natural gypsum in the production of Portland cement and calcium sulphoaluminate cement, leveraging its similar properties and contributing to sustainable material management in the construction industry [38].

This thesis explores potential environmentally friendly and cost-effective approaches for the treatment and resource utilization of the aforementioned solid wastes. Detailed descriptions of the physicochemical properties of these wastes are presented in the respective chapters dedicated to their applications, which include sealing materials for landfill cover systems, alkali-activated materials, and BOF slag-based binder materials.

1.1.2 Sealing materials for landfill cover system

- **Design of Sludge-based sealing materials**

With the increasing anthropogenic activities and population growth, the total waste from all households generated in the European Union increased from 2.14 billion tons in 2008 to 2.33

billion tonnes in 2018 [39]. The treatments for those waste materials are recycling, energy recovery, backfilling, incineration, and landfill [40]. Great efforts are underway to increase recycling to address the demands of a circular and sustainable economy, reducing the amount of landfilled gradually. However, nearly two million tons of solid waste annually cannot be recycled or incinerated in the Netherlands. About 171 million tons of waste were disposed of in landfills in Europe in 2016. Landfilling plays a significant role in the waste management.

When a landfill reaches its capacity, a landfill cover must be placed over the site as a protective barrier. This cover serves to prevent the escape of landfill gas and minimize rainwater infiltration into the waste. It typically consists of multiple layers of materials, each carefully engineered to perform specific functions (**Fig. 1.6**). Currently, compacted clay (clay-contained) materials and high-density polyethylene (HDPE) geomembrane are often used as the sealing layer materials in landfill covers, owing to their low permeability and high unconfined compressive strength [41,42]. Natural Clay is a fine-grained natural soil material containing minerals such as kaolinite, montmorillonite and illite, which are hydrous aluminum phyllosilicates. These minerals give clay its notable plasticity and ability to harden when fired, making it widely used in construction (e.g. fabrication of bricks and roof tiles), ceramics (e.g. pottery and porcelain), agriculture (e.g. soil amendment), and liners for landfills. However, traditional compacted clay covers can shrink or swell under different humidity conditions, leading to cracks and deformations. Despite the abundant clay resources in the Netherlands, it is economically and environmentally beneficial to rationally reuse waste materials as alternatives to natural clay. Here we focused on developing sludge-based sealing materials with low permeability for landfill cover systems. This approach not only preserves valuable natural clay resources but also promotes sustainable waste management practices.

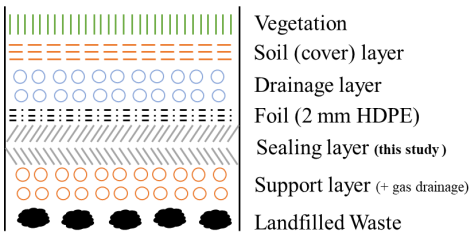

Fig. 1.6: Schematic of the layer structure in a final landfill cover system (modified from [43]).

- **Carbonation resistance of sludge-based sealing materials**

In efforts to conserve natural clay resources and promote waste recycling, sludge material has been proposed as an alternative to compacted clay for the preparation of a sealing layer in landfill cover systems. Under Dutch legislation, these residual-based sealing materials are expected to serve 50 years [43], necessitating a thorough examination of the factors influencing their durability.

It is crucial to mention that, besides infiltration issues, landfill gas emissions pose another significant challenge in landfill cover systems. The decomposition of landfilled waste materials results in the production of greenhouse gases (methane (CH_4) and carbon dioxide (CO_2), in equal volumetric ratios of 50%v/v) [44]. Implementing a gas collection system is often essential to mitigate these emissions. However, reported efficiency in landfill gas collection varies from 50 to 100% (with an average of 75%), contingent upon the cover type and extent of the

collection system [45,46]. Moreover, in older and abandoned landfills where installing a gas collection system is not economically or practically feasible, fugitive emissions from landfills become a predominant issue. During the gas escape process, exposure of sealing materials to greenhouse gases is unavoidable. It is noteworthy that calcium and magnesium ions are sensitive to carbonization, leading to the precipitation of carbonates. This process results in the decalcification of minerals, altering the pore volume within the matrix and the water permeability of the material. Therefore, a comprehensive investigation into the carbonation behavior of sealing materials is imperative to ensure their effective long-term performance.

1.1.3 Alkali-activated materials

Alkali-activated materials (AAMs), also known as geopolymers, have garnered extensive attention as a promising substitute for Portland cement-based materials. These materials are formulated by blending aluminosilicate precursors with alkaline activators. The commonly used aluminosilicate precursors are ground granulated blast furnace slag (GGBFS), coal fly ash (CFA) and metakaolin [47–52]. These materials can be activated by hydroxides (MOH), carbonates (M_2CO_3) and silicates (M_2SiO_3) (M represents the alkali ion, mostly K^+ and Na^+) [53–57]. This method circumvents the need for limestone calcination and the consequent fuel consumption inherent in Ordinary Portland cement production, resulting in a notable reduction in CO_2 emissions. Consequently, AAMs offer distinct advantages in terms of sustainability [58–60].

- **Sodium carbonate-activated materials**

The utilization of various activators within the reaction system shows a significant influence on the reaction kinetics, reaction products and mechanical performance of AAMs. Typically, MOH and M_2SiO_3 contribute to a fast reaction of AAMs; thereby potentially enhancing their performance at an early age. However, the intensive reaction may result in fast degradation of workability and heightened shrinkage [61,62], besides entailing substantial energy consumption in the production of hydroxides and silicates. Moreover, the high alkalinity of activators can pose safety risks during construction. To avoid these defects, research has explored sodium carbonate (Na_2CO_3) activated materials, characterized by lower alkalinity, yielding reaction products primarily comprising hydrotalcite, gaylussite and calcium silicate hydrate (C-S-H) gel [63]. These alternatives exhibit reduced shrinkage, costs, and safety risks compared to conventional AAMs activated by hydroxides and waterglass [64].

Nevertheless, the diminished alkalinity of Na_2CO_3 slows the dissolution of precursors, thus impeding early-stage strength development during hydration. To accelerate the reaction process of sodium carbonate-activated materials, various additives have been suggested, including calcined layered double hydroxides (LDHs), calcined dolomite, calcium carbide residue and $Ca(OH)_2$ [55,65–68]. These additives facilitate the removal of CO_3^{2-} ions by the formation of carbonates and generate OH^- ions within the aqueous phase to enhance the alkalinity. Meanwhile, the Ca^{2+} ions released from these additives contribute to the polymerization of C-(A)-S-H gel. In this study, we proposed using waste incineration filter dust (WIFD) in AAMs. WIFD is an air pollution control residue derived from municipal solid waste incineration (MSWI) and contains considerable amounts of portlandite and calcite.

- **Silica fume and nano-silica modified AAMs**

The utilization of WIFD accelerates the hydration of sodium carbonate-activated GGBFS materials; however, a high dosage of WIFD results in a significant reduction of the mechanical performance of sodium carbonate-activated slag. Similar degradation in mechanical properties has been documented while recycling other types of solid waste residues in AAMs [26,69–71], as summarized in **Table 1.2**. For instance, the inclusion of 40 wt% non-reactive bottom ash leads to a 50% reduction in the compressive strength of alkali-activated slag at 28d [72]. Compared with the traditional aluminosilicate precursors, solid waste materials have relatively lower pozzolanic reactivity. Consequently, the reduced gel formation adversely affects the mechanical properties of the resulting cementitious materials. Thus, a thorough understanding of the enhancement of mechanical properties in solid waste-combined binders is of vital importance for their application in construction materials, contributing to a more sustainable industry and improved solid waste management. The performance of AAMs depends on the properties of the precursors and alkaline activators, curing conditions, and the water-to-binder (w/b) ratio [73–77]. The influence of these parameters on reaction kinetics, mechanical properties and durability has been intensively investigated [78,79]. This study focuses on the impact of silica fume and nano-silica on the overall performance of WIFD and sodium carbonate-activated GGBFS.

Table 1.2: The compressive strength of alkali-activated materials with additional waste materials.

Waste materials	Compressive strength 28d (MPa)	Replacement level (wt%)	Strength Reduction (%)
Waste glass powder [80]	17	30	35
Bottom ash [72]	35	40	50
Air pollution control residues [26]	3	40	-
Waste rubber powder [81]	30	10	60
Steel slag [69]	75	10	18
Waste glass [70]	42	30	10
Desulphurization slag [82]	8	50	50
Incinerator fly ash [71]	25 (3d)	20	35
Porcelain ceramic waste [83]	16	10	33

- **Solidification of Biomass bottom ash (BBA) in AAMs**

The immobilization of heavy metals contaminated solid wastes using alkali-activated materials (AAMs) has garnered increasing research attention [84]. Various industrial by-products, such as electric arc furnace dust, red mud, and bottom ash from coal power plants, have been successfully utilized in AAMs, effectively immobilizing the contained heavy metals [85–87]. The main proposed mechanisms for immobilizing heavy metals in the AAMs system are as follows: a) Ion exchange of alkali metals during gel formation [88,89], e.g., divalent metal ions such as Zn^{2+} with a similar radius to Ca^{2+} can be exchanged in C-S-H gel. b) Covalent bonding of heavy metals to the aluminosilicate network [90], in which the negative charge of $[AlO_4]^-$ facilitates excellent immobilization of metal ions. c) Physical absorption by the gel products due to their high specific surface area [91]. d) Physical encapsulation in the AAMs matrix [92,93]. e) Precipitation in the form of hydroxides, carbonates and silicates [84]. It is crucial to

keep in mind that immobilization efficiency often results from a combination of these mechanisms within a given system.

BBA has been explored for civil engineering applications, serving as a filler in road embankments and substitutions for cement and aggregates in mortar/concrete formulations [12,94–96]. Previous studies have investigated the impact of substitution levels on the mechanical properties, shrinkage behavior and chloride penetration of the different cement/binders [94,96]. Despite containing highly leachable heavy metals (such as Pb, Cr, Zn, etc.), which pose environmental threats due to their long-term persistence, ecotoxicity, and bioaccumulation, the leaching behavior of BBA-modified blends has been infrequently addressed [97]. Hence, understanding the leaching of heavy metals from BBA and their solidification in AAMs is pivotal and beneficial for the valorization of BBA in civil engineering, advancing a more sustainable circular economy.

- **Design of AAMs with self-cleaning performance**

Prolonged exposure of cementitious materials to the environment leads to a diminished operational lifespan due to erosion caused by organic and inorganic contaminants [98,99]. This necessitates periodic maintenance, resulting in maintenance expenditures. Photocatalytic oxidation (PCO) technology has been widely studied in building materials to address the aforementioned problems, primarily through the integration of titanium dioxide (TiO_2) with ordinary Portland cement (OPC) [100–103]. When exposed to ultraviolet (UV) light, TiO_2-based photocatalysts can absorb photons with sufficient energy, facilitating the transfer of electrons from the valence band to the conduction band, thereby generating electron-hole (e^-/h^+) pairs [104]. Subsequently, these photogenerated electrons e^- and h^+ engage in reactions with oxygen (O_2) or water molecule (H_2O), producing highly reactive radicals (O_2^- and $OH\cdot$) that effectively initiate the degradation of surface-bound pollutants (e.g. volatile organic compounds and nitrogen oxides (NO_X) [100,104].

Numerous studies have been dedicated to enhancing the photocatalytic efficiency of TiO_2-modified cementitious materials, focusing on the properties of photocatalysts and cementitious constituents (surrounding media of TiO_2) [103,105–109]. Some researchers have explored some interactions between photocatalysts and cementitious materials, particularly the roles of hydration and carbonation processes [110–112]. The major hydration products in OPC systems are C-S-H gel and portlandite, while the use of reactive pozzolans can transform $Ca(OH)_2$ to additional C-S-H gel. Liu et al. observed that substituting 25 wt% of microsilica in OPC-based materials results in a low Ca/Si ratio C-S-H gel with a more porous structure, enhancing self-cleaning performance [112]. However, the authors also pointed out that the increased formation of C-S-H gel during the hydration process exacerbates the "sheltering" effect on TiO_2 photocatalysts, leading to deteriorated self-cleaning performance at a longer curing age [113]. Moreover, the abundant OH^- generated during the hydration of OPC retards the photocatalytic oxidation process (oxidization of H_2O_2 to $OH\cdot$) due to the chemical equilibrium, wherein OH^- is generated as a reaction product [112]. These observations collectively suggest that OPC-based matrixes may not be the ideal substrates for photocatalytic self-cleaning applications. Therefore, this study investigates the self-cleaning AAMs, aiming to address the challenge of performance deterioration by facilitating the in-situ formation of zeolite A. The findings suggest a novel approach; incorporating aluminosilicate solid waste to control the in-situ formation of zeolite, thereby extending the lifespan of these functionalized building materials.

The in-situ formation of zeolites was achieved by adjusting the silica/aluminum ratio of the starting materials. Specifically, this study utilized metakaolin and sodium silicate/hydroxide solutions. Using high-purity raw materials allowed precise control over the composition of the final hardened materials, minimizing the influence of other components on photocatalytic efficiency. The study demonstrated that in-situ zeolite formation significantly enhanced photocatalytic performance. It should be clarified that while metakaolin is not typical of industrial solid waste, the experiments suggest that adjusting the silica/aluminum ratio in the reaction system can effectively control in-situ zeolite formation. These findings provide a new perspective for recycling aluminum-silica-containing industrial solids. Future research will explore the use of these kinds of industrial solid wastes, such as aluminum-anodizing waste, to promote their application in functional alkali-activated materials.

1.1.4 BOF slag-based binder

Global climate change and resource depletion highlight the need for low-carbon, resource-efficient and circular economy approaches to achieve sustainable development [114,115]. The cement industry accounts for approximately 8% of global anthropogenic CO_2 emissions [116], primarily due to the high-temperature processes in clinker production, which requires significant fuel energy, and the decomposition of limestone into CaO and CO_2 [115,117]. While green energy can replace the substantial fuel input, CO_2 emissions from limestone decomposition cannot be mitigated by improving energy efficiency [118]. Therefore, developing alternative low-carbon binders, such as AAMs, is urgently needed to reduce CO_2 emissions [29]. In this chapter, we focused on recycling BOF slag as the binder material.

The primary challenge to effectively utilizing BOF slag as a cementitious material lies in its low hydraulic activity during the early stages of hydration [119]. Due to the significant presence of belite within BOF slag, current research endeavors are predominantly directed towards enhancing belite hydration through mechanical grinding and the application of chemical activators such as alkali hydroxides, salts (e.g., $CaCl_2$, Na_2CO_3, Na_2SiO_3), and boron-bearing dopants [120–124]. Nevertheless, these accelerators have been shown to have little effect on the hydration of BOF slag. One potential reason is the simultaneous precipitation of calcium silicate hydrate (C-S-H) and calcite on the belite surface, impeding further hydration owing to the absence of transportable cations between the solid surface and the solution [125]. Additionally, if BOF slag is used as a supplementary cementitious material in ordinary Portland cement (OPC) [126], the recommended replacement percentage is very low, typically up to 5% by volume, to ensure satisfactory performance [126]. Consequently, Ahmed et al. proposed employing BOF slag in belite calcium sulphoaluminate cement, revealing a 30%-50% volume replacement with desirable 90 d and 180 d compressive strength attributed to the later-stage hydration of BOF slag [127]. Nonetheless, BOF slag does not contribute to the early hydration process, and the performance of the resulting cementitious materials at earlier ages (7d and 28d) is notably reduced by the quantity of BOF slag employed. Therefore, this study focused on developing suitable activators for BOF slag-based binders to optimize their use as promising construction materials.

1.2 Scope and objectives

Recently, there has been significant attention directed towards the recycling of industrial waste in the realm of construction materials. This interest stems from the imperative to achieve

circularity objectives and conserve resources. This dissertation endeavors to contribute to this discourse by enhancing the integrated recycling and recovery processes of industrial solid waste within construction materials. This pursuit is realized through the utilization of waste materials in three distinct systems. Firstly, the study proposes the design of novel alternative sealing materials tailored for employment within landfill cover systems. Secondly, it centers on the advancement of eco-friendly technologies (alkali-activated materials), to facilitate the valorization of waste materials. Finally, the research explores the development and implementation of BOF slag-based binders. These objectives are addressed in the following topics.

Sludge-based sealing materials and carbonation resistance

- The innovative sealing material primarily comprises sludge, sand (as aggregate), other incineration solid waste (as additives), and waterglass. The effect of sludge and additives characteristics on the reaction products, microstructural properties, and permeability behavior of the sealing materials is investigated. An assessment of potential environmental impact is conducted, particularly focusing on the leaching of heavy metals.
- Since there is significant potential for CO_2 emissions resulting from the decomposition of organic matter within landfills, the dissertation evaluates the impact of CO_2 exposure on the efficacy and permeability of the sealing materials. This assessment is accomplished through an accelerated carbonation process, wherein the degradation mechanism is revealed from both physical and chemical perspectives.

Development of low CO_2 footprint AAMs and functionalization

- The limited early-age strength development of sodium carbonate-activated GGBFS restricts its high-end application. To address this issue, this study proposes the integration of waste incineration filter dust (WIFD), an air pollution control residue. The investigation assesses the impact of WIFD on the hydration kinetics, resulting reaction products, microstructural characteristics, and mechanical properties of sodium carbonate-activated GGBFS. However, it is noted that the mechanical performance of the sodium carbonate-activated GGBFS is diminished with a high incorporation of WIFD. To enhance the performance of the hybrid binder, the study explores the addition of silica fume and nano-silica, evaluating their effect on the overall performance of the resulting binder and its resistance to carbonation.
- The recycling of industrial solid waste is often limited by the presence of high-leachable heavy metals. This study explores the potential of AAMs in the solidification of biomass bottom ash (BBA). Investigations into the effects of BBA content, fineness, silicate modulus of activators, and the inclusion of aluminum-anodizing waste (AAW) on solidification performance are conducted. The study emphasizes analysis of reaction mechanisms, phase assemblages, mechanical properties, and leaching behavior to comprehensively evaluate the efficacy of AAMs in this application.
- The self-cleaning performance of cementitious materials is often diminished during the hydration process, as the resultant hydration products tend to shield the photocatalysts, hindering the photocatalytic reaction. This study advocates for the advancement of

AAMs endowed with self-cleaning capabilities, which could be enhanced through the in-situ formation of zeolite. The effect of in-situ formation of porous minerals on the microstructural properties, optical properties and self-cleaning performance is evaluated.

BOF slag-based cementitious binder modified with FGD gypsum

- Currently, the utilization of BOF slag within the cement and concrete industry is limited by its insufficient reactivity during the early stages of hydration. This study introduces a novel approach centered on the chemical activation of BOF slag using pentasodium diethylenetriamine pentaacetate (DTPA-5Na). The chelating effect of DTPA-5Na accelerates the dissolution of minerals in BOF slag. Additionally, the study investigates the addition of sulfate to regulate the hydration speed, specifically using flue gas desulfurization (FGD) gypsum. The influence of FGD gypsum was compared to that of sodium sulfate. Overall, the effects of DTPA-5Na and FGD gypsum on the hydration kinetics, resulting reaction products, and microstructural attributes of BOF slag binders have been investigated. The potential environmental hazards of the formulated BOF slag binder are evaluated through a one-batch leaching test to assess its feasibility for industrial application.

1.3 Outline of the thesis

The research framework is shown in **Fig. 1.3**. The contents of the chapters are briefly introduced in the following paragraphs.

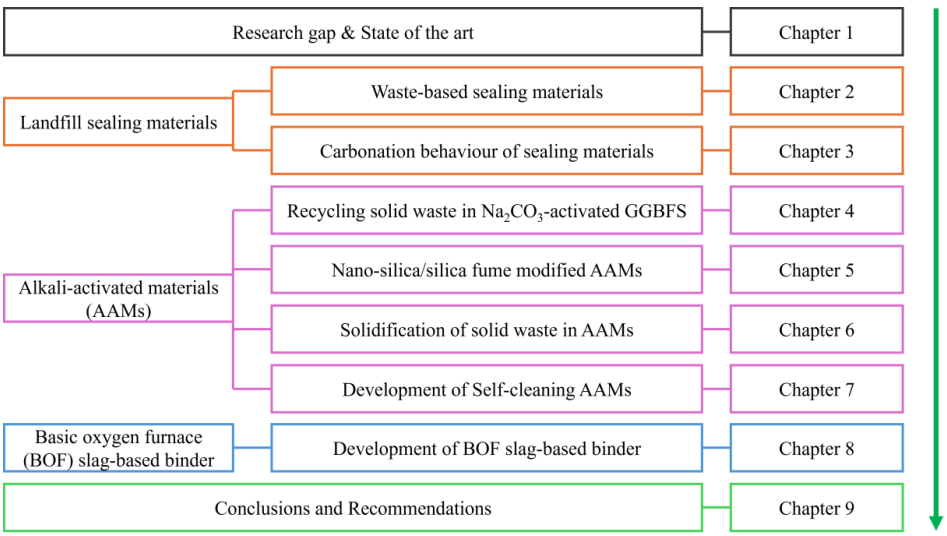

Fig. 1.3 Outline of the thesis.

Chapter 2 investigates sewage sludge-based sealing materials. The characteristic of various treated and sourced sludge materials was evaluated, along with several types of solid waste from incineration and aluminum industries applied as the additives. The entirely waste-based sealing materials were prepared and systematically studied, focusing on the permeability and

interaction between sludge materials and additives. The reaction products and microstructure of the prepared sealing materials were analyzed by X-ray diffraction (XRD), thermogravimetry (TG), N_2 adsorption analysis, and scanning electron microscopy (SEM). The potential environmental impact of the sealing materials was estimated by the one-batch leaching test.

In **Chapter 3**, an accelerated carbonation of the sludge-based sealing materials was carried out, aiming at understanding the effect of released CO_2 from landfills on the permeability of the sealing materials. Meanwhile, the study explored the influence of waterglass dosage and properties of additional solid waste on carbonation behavior. This investigation delved into phase changes, microstructure alterations, and the leaching of heavy metals.

Chapter 4 investigates the feasibility of repurposing industrial solid waste in sodium carbonate-activated GGBFS materials. The applied solid waste, named waste incineration filter dust (WIFD), originates from the air pollution control process in an incineration plant, characterized by a high content of portlandite and calcite. The interaction between WIFD and sodium carbonate-activated GGBFS was investigated regarding hydration kinetics, reaction products, and mechanical performance.

Chapter 5 delves into exploring the effect of nano-silica and silica fume on WIFD-modified sodium carbonate-activated GGBFS materials. Nano-silica was synthesized by dissolving olivine in sulfuric acid in a laboratory setting, while silica fume is a commercially available product. Their effect on the hydration kinetics, phase composition, microstructure, and mechanical performance was systematically revealed. Additionally, the carbonation behavior of the formulated materials was analyzed, alongside an assessment of their carbon footprint.

Chapter 6 investigates the solidification of industrial solid waste in alkali-activated materials, focusing on biomass bottom ash (BBA) generated during biomass incineration. Due to high levels of leachable heavy metals, the solidification of these heavy metals within alkali-activated materials was explored, considering factors such as BBA content, BBA fineness, the silicate modulus of the activator, and the potential co-disposal with aluminum anodizing waste. Additionally, the study analyses the reaction kinetics, phase assemblages, and mechanical properties of the resulting materials to evaluate their suitability as potential construction materials.

Chapter 7 explores the advancing self-cleaning performance of alkali-activated metakaolin through in-situ zeolite formation and TiO_2 integration. Considering that the deterioration of self-cleaning properties of cementitious materials upon hydration is mainly attributable to the sheltering effect of hydration products, the design centered on forming in-situ zeolites with a porous structure to enhance self-cleaning performance. This was achieved by adjusting the initial reactive Si/Al ratio within the raw materials and alkali activators. The phase composition, optical properties and microstructure of the resulting materials were analyzed. A mechanism elucidating the improved self-cleaning performance was proposed to give insight into the role of the porous structure in the photocatalytic process.

In **Chapter 8**, basic oxygen furnace (BOF) slag, a by-product of steel manufacturing, was utilized to produce a cement-free binder. BOF slag predominantly comprises belite, wüestite, magnetite and brownmillerite. However, the low reactivity of these minerals at early ages limits

their applicability in construction materials. To address this, an activation method involving pentasodium diethylenetriamine pentaacetate (DTPA-5Na) was proposed, aimed at accelerating the dissolution of brownmillerite through a chelating reaction. The hydration kinetics and mechanical performance of the resulting materials were investigated. An activation mechanism of DTPA-5Na was proposed, alongside a hydration model for BOF slag. Additionally, flue gas desulphurization (FGD) gypsum was employed to enhance the performance of the DTPA-5Na-activated BOF slag binder.

Chapter 9 summarizes the conclusions of this research and provides recommendations for future study.

Chapter 2 Low permeability sealing materials based on sewage, digestate and incineration industrial by-products in the final landfill cover system

This chapter explores repurposing municipal solid waste from the sewage, digestate, and incineration industries as landfill-sealing materials, aligning with circular economy principles. The main materials include digested sewage sludge (DSS), pretreated digested sewage sludge (PDSS), and digestate sludge (DS), with biomass bottom ash (BBA) and aluminum anodizing waste (AAW) introduced as additives, complemented by 1.5 wt% waterglass (Na_2SiO_4) to enhance the sealing performance. The research evaluates the characteristics of the various treated and sourced sludges and additives, assessing their influence on water permeability, reaction products and environmental consequences. Results demonstrate the achievement of low permeability in the sludge-based sealing materials, with optimal performance observed in the specimens prepared with DSS and AAW (k value = 3.78×10^{-12} m/s). Thermal pressure hydrolysis pre-treatment in sewage plants reduces the organic content in PDSS, resulting in a slight increase in permeability. DS-based specimens exhibit higher permeability due to their relatively lower organic content in DS. Gypsum is the primary reaction product attributed to leachable sulfate in BBA and AAW. Waterglass addition in BBA-modified specimens promotes silica gel formation, while AAW effectively reduces matrix permeability as an externally added gel-like substance. Additionally, heavy metals (As, Pb and Cr) derived from the by-products are effectively immobilized in the sealing materials owning to the coagulation effect of organic matter in the sludge and sulfates in the products. Overall, this novel approach to landfill sealing materials exhibits promising applications in the Netherlands, offering cost savings and reduced environmental impact by recycling industrial by-products.

This chapter is partially published elsewhere:

X. Ling, W. Chen, K. Schollbach, H.J.H. Brouwers, Low permeability sealing materials based on sewage, digestate and incineration industrial by-products in the final landfill cover system, Construction and Building Materials, 412, 134889, 2024.

2.1 Introduction

Utilizing sewage sludge to formulate a sealing barrier for landfill covers is an effective and ecological recycling strategy that aligns with the objectives of the European Green Deal to promote circularity in resource management and recovery [128]. Li et al. employed fly ash, lime and ferric chloride to dehydrate sludge, and the dewatered sludge was fabricated into a landfill covering material with a permeability coefficient from 10^{-10} to 10^{-7} $m \cdot s^{-1}$ [129]. Oh and Shin prepared the solidified/stabilized dye sludge char with lime, ladle slag and hydroxyapatite and revealed the applicability as a landfill cover material through hydraulic conductivity and micro-structural analysis [130]. Rosli et al. proposed recycling sewage sludge and red gypsum as potential materials for temporary landfill covers. They found an optimum compressive strength of 524 kPa was achieved when the ratio of sewage sludge to red gypsum was 1:1 [131]. Kim et al. used converter slag and lime to solidify digested sewage sludge, and the solidified sludge exhibited desirable geotechnical properties as landfill cover [132]. Liu et al. used industrial calcium-containing waste, including slag, desulfurized gypsum and fly ash, to modify the municipal dewatered sludge, and the hydraulic conductivity of the modified sludge was characterized after six wet-dry cycles to ensure its long-term stability during the local rainy season [133]. The studies mentioned above have explored the modifications of sewage sludge into landfill cover material using various additives. The results showed that sewage sludge exhibited promising impermeability, and the formation of calcium silicate hydrate (C-S-H: $CaO \cdot SiO_2 \cdot nH_2O$) played an important role in the binding and stabilization of the sludge [130–133]. However, most research has focused on various modifications of sewage sludge, disregarding the impact of sludge properties on sealing performance. Given the increasing need to recycle sludge from diverse industrial processes and wastewater treatment systems, it is crucial to investigate the application of different sludge qualities. Notably, the physicochemical properties of sewage sludge are influenced by the treatment process and the effluent source, which is further influenced by regional technological developments and management practices associated with the sludge. In the Netherlands, the main types of sewage sludge generated include normally digested sewage sludge (DSS), digested sewage sludge pretreated (PDSS) with a Thermal Pressure Hydrolysis (TPH) process to enhance biogas production and dewaterability [3,4], and digestate sludge (DS) derived from the organic municipal waste. This research aims to contribute to the energy-efficient disposal of various sludges while providing fundamental theoretical support for regulating their applications.

In sealing materials, achieving low permeability is crucial as it effectively restricts the flow of liquids or gases through the materials. Current strategies for enhanced sealing performance primarily focus on optimizing the physical compaction of the matrix and utilizing chemical reaction products to fill the voids [134]. Wiśniewska and Stępniewski proposed using quick lime and waterglass to effectively reduce the permeability of waste rock from coal mining [135]. The C-S-H gel forms in the void space, reducing porosity and binding the grains. However, to minimize the reliance on lime as an additive and explore more sustainable alternatives, the present study adopts a lime-containing industrial by-product, namely biomass bottom ash, derived from the biomass grate furnace. This approach minimizes environmental impact while still achieving the desired sealing performance.

While there has been extensive research on the in-situ generation of C-S-H gel in sludge-based sealing materials, the impact of externally added gel (amorphous) materials is often overlooked

due to the associated increase in cost. However, a viable alternative approach is to explore the utilization of industrial solid waste materials that possess similar properties, thereby alleviating cost concerns. One such material is Aluminum anodizing waste (AAW), a by-product generated during aluminum anodizing. AAW predominantly comprises various $Al(OH)_3$ polymorphs, with approximately 80 wt% of its structure being amorphous [136]. It is noteworthy that EU countries produce an estimated annual quantity of 100,000 metric tons of AAW [137]. In this study, we proposed the application of AAW in sludge-based sealing materials, aiming to harness its unique characteristics, such as its amorphous structure and ultra-fine particle size.

To the best of our knowledge, few studies have explored the impact of BBA and AAW in preparing sludge-based sealing materials. Therefore, this chapter aims to establish an effective system for recycling and reusing the above industrial waste by focusing on the sealing performance of various sludge-based materials, the influence of BBA on gel formation, and the feasibility of utilizing AAW as an external gel to enhance sealing performance. Industrial by-products from local plants in the Netherlands are characterized and used to develop environmentally friendly sealing materials that could be used in a final landfill cover system. Comprehensive laboratory-scale analyses are conducted to assess geotechnical properties, reaction processes, microstructure, water permeability and leaching behavior. The findings in this research contribute to sustainable waste management and resource utilization.

2.2 Materials and Experiments

2.2.1 Raw materials

The present work assesses the feasibility of using three types of sludge as sealing materials for landfill covers. The sludge types include Digested sewage sludge (DSS) and Pretreated digested sewage sludge (PDSS) obtained from Waste Water Treatment Plants (WWTPs) (Deventer, Netherlands), where the activated sludge with biological chemical phosphate and nitrogen removal process is applied for the digestion. The PDSS undergoes a Thermal pressure hydrolysis (TPH) process (8 bar, 150 ~ 160 °C) prior to digestion. The third type of sludge, Digestate sludge (DS), originates from the Municipal Solid Waste Plant (MSWP) (Omrin. Netherlands).

Biomass bottom ash (BBA) and Al-anodizing waste (AAW) were utilized as additives in the mixture. The BBA was sourced from a local grate furnace, in which waste wood was incinerated for biomass fuel and the fly ash was removed in a cyclone. The AAW was obtained from a local WWTP that collects wastewater from the aluminum anodizing process in the alumina industry. The waterglass powder with a composition of 20.1 wt% Na_2O and 62.7 wt% SiO_2 was employed, which has been reported to enhance reactive [SiO_2] content for gel formation and reduce permeability [138]. Additionally, a mixture of 30 wt% blasting grit and 70 wt% normal sand was used as aggregate, both of which are considered inert, and their characterization tests are not included in this study.

2.2.2 Sample preparation

According to the Dutch legislation for the solid waste used in the soil layer, the proportion of the residue-based sealing layer is regulated to 46 wt% sludge, 9 wt% ash/filter, and 45 wt% sand fractions. The group labeled DSS-B denotes specimens prepared with DSS and BBA, while DSS-A represents specimens prepared with DSS and AAW. Additionally, all mixes are

supplemented with 1.5 wt% waterglass, based on previous literature recommendations for its use in sealing materials within the range of 1-5 wt% [139]. The samples were externally prepared by Ingenieurbüro Kügler in Essen, Germany.

Based on the results of the optimal moisture content tests for each mixture (see details in **Section 2.3.2**), the grain and sludge materials were dried accordingly to ensure that each mix reached the optimum moisture content before molding. Subsequently, they were well dispersed in a laboratory mixer. BBA/AAW and waterglass were gradually added while stirring to ensure uniform homogenization. Next, all the materials were cast into a cylinder mold (D = 95 mm, H = 50 mm) and compacted according to DIN 18127. The compacted blends (**Fig. 2.1**) were sealed in plastic bags for 70 d of curing at an ambient temperature.

2.2.3 Methodology

The flowchart of the process is presented in **Fig. 2.1**.

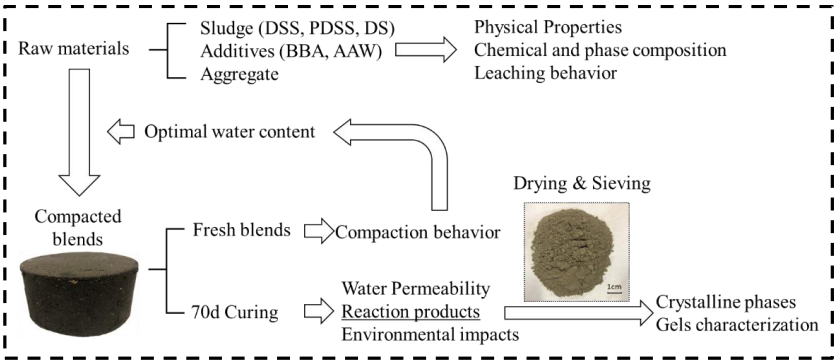

Fig. 2.1: Flowchart of the process for studying the sludge-based sealing materials.

- **Characterization of raw materials**

Raw materials were dried at 105 °C until a stable mass to determine their moisture content. A high-temperature furnace measured the weight loss between 105 and 1000 °C. The specific density of the dried materials was tested by using a He-pycnometer (Accupyc II 1340 Micromeritics).

The particle size distribution of the raw materials was measured using a laser light scattering technique in isopropanol (Malvern Mastersizer 2000). To prevent agglomeration of sludge and AAW after drying, the test was conducted using wet raw materials, and 10 minutes of ultrasonic dispersion was performed beforehand. Due to relatively large particles in the BBA, sieve towers with 0.125, 0.25, 0.5, 1.0, 2.0, and 4.0 mm were employed to determine the particle size distribution.

The chemical composition of raw materials was determined using X-ray fluorescence spectrometry (XRF) (PANalytical Epsilon 3). The borate fusion method was employed for the preparation of fused beads. The phase composition of raw materials was characterized by X-ray diffraction (XRD), Thermogravimetry (TG), and Fourier transform infrared spectroscopy (FT-IR). The XRD test was conducted by using a Bruker D4 phaser, with a step size of 0.02° and a 2θ range from 10° to 60° (Co-Kα, 40 kV, 30 mA). The TG test was carried out using a STA 449 F1 instrument for all materials at a heating rate of 10 K/min under the N_2 atmosphere.

FT-IR spectroscopy was conducted by using a Varian 3100 instrument to identify the bonding in the mineral phases with the wavenumber range of 4000 – 400 cm^{-1}.

The leaching behavior of the raw materials was investigated following the one-batch leaching test (EN 12347-2). Raw materials smaller than 4 mm were mixed with distilled water in polyethylene bottles at a liquid-to-solid (L/S) ratio of 10. The bottles were then sealed and placed horizontally on a linear reciprocating shaking device (Stuart SSL2) for 24 h, with a constant shaking rate of 250 rpm and an amplitude of 20 mm. Afterward, the solids were filtered out, and the pH of the leachate was measured. The leachate was subsequently analyzed using ion chromatography (Dionex 1100) equipped with an ion-exchange column AS9-HS and inductively coupled plasma optical emission spectroscopy (ICP-OES Spectral Blue).

- **Characterization of the blends**

The optimal water content of each mixture was determined according to the DIN 18127:2012-09 standard. The sludge materials were pre-dried at 40 °C for varying durations to adjust the water content of the initial material. Subsequently, all the raw materials were mixed and compacted. The cylindrical mold was filled with 3 kg of mixed samples, and each sample was prepared with three layers, each layer receiving 25 blows.

Permeability tests were conducted externally by Ingenieurbüro Kügler in Essen, Germany, following DIN18130 Part 1. The cylinder specimens, which had undergone 70 d of curing, were used for the permeability tests. These specimens were placed in a pressure cell with side pressure. The test duration was set at 75 d to ensure the stability of the permeability test results.

Phase assemblage characterization was conducted to identify the potential reaction products in all mixes. After 70 d of curing, the cylinder specimens were gently crushed and dried in a vacuum oven at 60 ºC until constant weight. The dry samples were then sieved through a 63 µm sieve to remove the coarse aggregate and concentrate the reaction products for better analysis (**Fig. 2.1**). The fraction (< 63 µm) is a uniform grey powder. XRD, TG and FT-IR analysis of the finer fraction (< 63 µm) from each mixture was conducted as earlier mentioned. N_2 sorption analysis of the finer fraction (< 63 µm) was performed by using Micrometrics. The gel pore size distribution was calculated from the adsorption branch by the Barrett - Joyner - Hallenda method [140].

The micromorphology of the finer fraction (< 63 µm) was observed using a Scanning Electron Microscope (SEM) and the chemical compositions of reaction products were analyzed with an EDX (15KV) detector (Phenom Pro). The finer fraction (< 63 µm) was dried at 40 °C for 24 hours and then coated with Au using a Quorum 150TS plus sputter coater.

The pore solution of each cylinder specimen after 70 d of curing was collected through pore solution expression, in which mechanical pressure was used to force the pore solution from the material. The pH of each pore solution was measured by a pH meter three times.

One-batch leaching tests were conducted on all specimens to evaluate heavy metal leaching. The testing and analysis procedures are detailed in **Section 2.3.1**.

2.3 Results and Discussions

2.3.1 Physical and chemical properties of raw materials

The chemical compositions, moisture content and loss on ignition (LOI) of raw materials are shown in **Table 2.1**. The sludge has a high moisture content and contains relatively high levels of iron sourced from wastewater and the iron-based coagulants used during sewage treatment in the plants. The particle size distribution of all raw materials is shown in **Fig. 2.2**. DSS and PDSS exhibit a similar particle size distribution with a d50 of approximately 20 µm, indicating little influence on the particle size due to the TPH process. DS shows a larger particle size of around 30 µm, attributed to the lower soil content in the organic waste. BBA has an average particle size of 90 µm, while AAW has the smallest average particle size of around 11 µm.

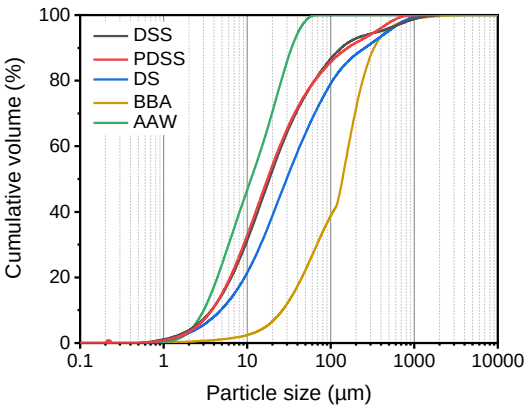

Fig. 2.2: Particle size distribution of each raw material.

Table 2.1: Chemical compositions of raw materials determined by XRF (wt%).

Elements	DSS	PDSS	DS	BBA	AAW
Na_2O	0.1	0.1	0.1	0.2	4.2
MgO	0.9	0.5	1.1	1.6	-
Al_2O_3	0.7	1.3	2.4	2.5	55.2
SiO_2	2.6	2.0	11.2	20.8	0.8
P_2O_5	4.5	6.6	1.7	1.4	0.2
SO_3	1.9	2.3	2.9	5.8	11.8
K_2O	0.5	0.4	1.6	4.8	-
CaO	4.9	6.7	15.9	34.5	1.0
TiO_2	0.4	0.4	0.7	8.5	-
MnO	0.2	/	0.1	0.7	-
Fe_2O_3	18.1	16.4	13.8	7.2	0.6
ZnO	0.5	0.6	0.2	1.7	-
Cl	0.1	0.2	0.6	1.6	-
Others	0.4	0.5	0.2	1.6	2.4
Total LOI	64.2	62.0	47.5	7.1	23.8
Density (g/cm^3)	1.69	1.64	1.78	2.87	2.54

Moisture content and LOI are given in wt% (weight percentage). The high LOI in sludge is due to its high content of organic matter as well as some calcite.

The mineral composition of each raw material is characterized in **Fig. 2.3**. In the sludges, the presence of quartz (SiO_2 PDF# 83-2465) and calcite ($CaCO_3$ PDF#72-1937) is observed, along with other minerals such as vivianite ($Fe_3(PO_4)_2 \cdot (H_2O)_8$ PDF#75-1186) in DSS and chabazite-Na ($Na_{15.2}Al_{15.2}Si_{32.8}O_{96}$ PDF#83-1295) in PDSS. The broad diffused peaks between 20 and 30 (° 2θ) indicate a high organic content in the sludge. BBA consists of anhydrite ($CaSO_4$ PDF#72-0916), lime (CaO PDF# 77-2010), calcite and quartz. AAW primarily contains boehmite (AlO(OH) PDF#49-0133), thenardite (Na_2SO_4 PDF#05-0631) and bayerite ($Al(OH)_3$ PDF#01-0287). The broad peaks of boehmite in AAW confirm its low crystallinity.

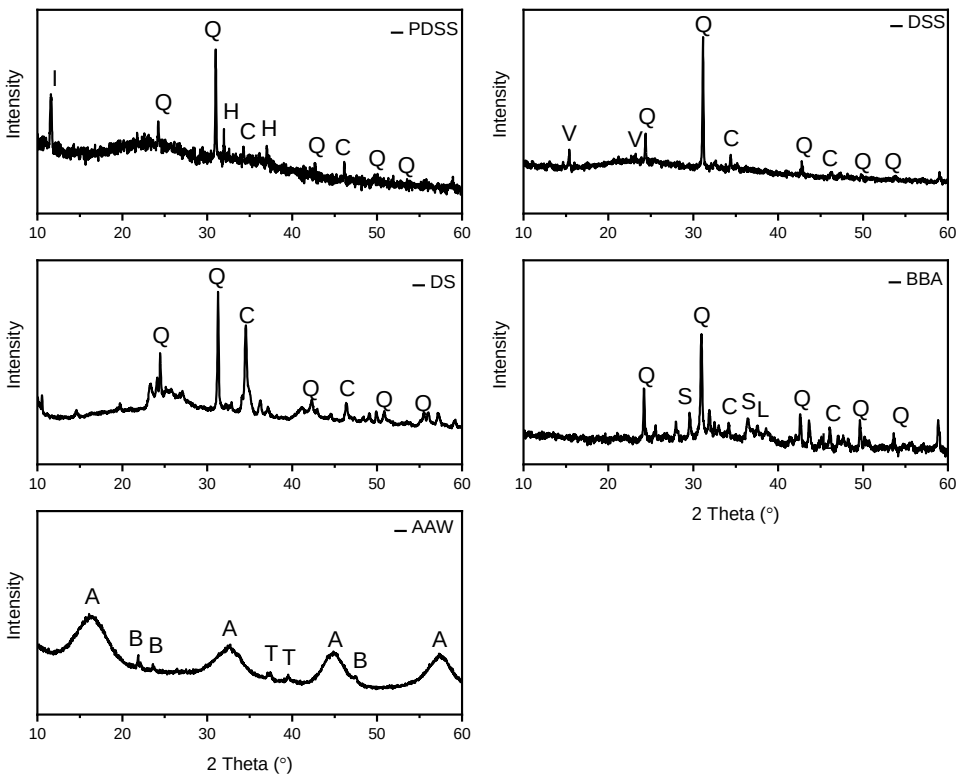

Fig. 2.3: XRD patterns of the raw materials. (A - boehmite: AlO(OH), B - bayerite: $Al(OH)_3$, C - calcite: $CaCO_3$, H - sodium chloride: NaCl, I - chabazite: $Na_{15.2}Al_{15.2}Si_{32.8}O_{96}$, L - lime: CaO, Q - quartz: SiO_2, S - anhydrite: $CaSO_4$, T - thenardite: Na_2SO_4, V - vivianite: $Fe_3(PO_4)_2 \cdot 8H_2O$).

To further validate the findings from the XRD analysis, the FT-IR spectrum of each raw material is obtained and presented in **Fig. 2.4**. In the sludges, broad bands centered around 3245 cm^{-1} and 1630 cm^{-1} correspond to the stretching and bending vibrations of H-OH bonds [141]. The adsorption peaks at 2918 cm^{-1} and 2851 cm^{-1} can be attributed to the symmetric and asymmetric stretching bands of CH_2 [142], confirming the presence of organic content in the sludge materials. The adsorption peaks around 1416 cm^{-1} and 872 cm^{-1} represent the vibration of ν_3 [CO_3^{2-}] and ν_2 [CO_3^{2-}] in calcite, respectively [143]. The strong band around 1013 cm^{-1} may be due to the C-O stretching vibration from cellulose [142,144], but it is worth noting that the stretching vibration of the Si-O-Si bond in quartz or other silicates also absorbs this region [145]. In BBA, in addition to the adsorptions as mentioned above, the adsorption bands at around 1096 cm^{-1} and 648 cm^{-1} are attributed to the vibration of ν_3 [SO_4^{2-}] and ν_4 [SO_4^{2-}] from

anhydrite [146]. Furthermore, strong adsorption around 3646 cm^{-1} is assigned to the vibration of hydroxyl groups, confirming the presence of lime in BBA [147]. AAW exhibits prominent adsorptions around 474 cm^{-1}, attributed to the [AlO_6] vibrations in boehmite [148].

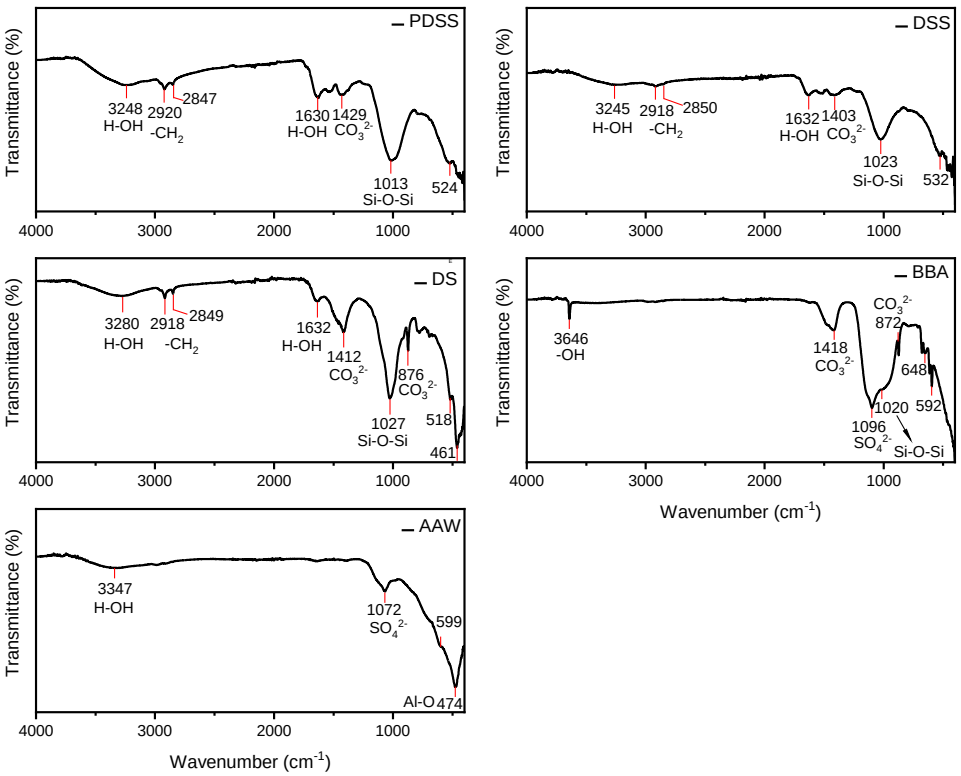

Fig. 2.4: FT-IR spectra of the raw materials.

Thermal analysis is performed to assess the volatile components in the raw materials, and the results are presented in **Fig. 2.5**. In the case of the sludges, the primary mass loss occurs between 250 °C and 500 °C, which is attributed to the decomposition of the organic compounds such as hemicellulose, cellulose, and the lignin present in the sludge [149]. Comparing DSS to PDSS, the pre-treatment of TPH leads to a slight decrease in organic content as high thermal pre-treatment may promote the transformation of organic content in PDSS from the particulate to the soluble fraction [150], whilst a significant reduction of organic compounds is observed in DS. The mass loss observed around 750 °C is associated with the decarbonation of calcite [151], which is also found in BBA. Regarding AAW, the initial mass loss occurs at around 105 °C, indicating moisture removal [152]. The subsequent mass loss between 250 °C and 400 °C is attributed to the dihydroxylation of interlayer OH in boehmite and bayerite [153].

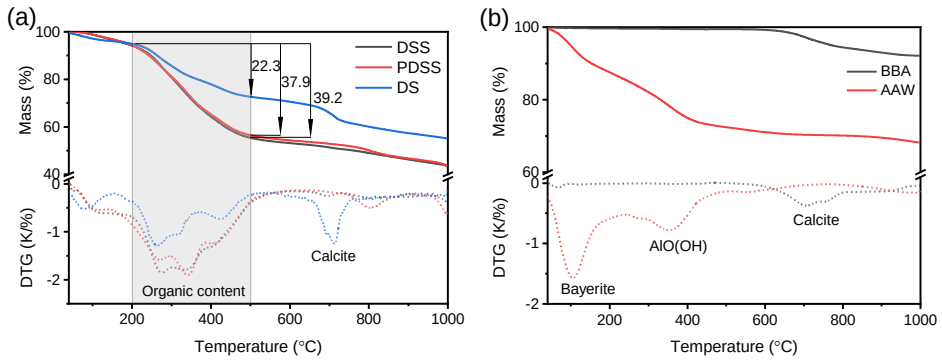

Fig. 2.5: TG and DTG curves of the raw materials (a: sludges, b: additives).

2.3.2 Compaction behavior of the fresh blends

Compaction tests are conducted on each fresh blend to ensure the sealing materials achieve minimal void spaces after proper compaction, reducing the potential for leachate migration. The dry density vs. moisture content curves are presented in **Fig. 2.6**. The maximum dry density ($\gamma_{d\ max}$) of the fresh DS-B, PDSS-B, and DSS-B blends is 1.12 g/cm^3, 1.07 g/cm^3 and 0.95 g/cm^3, respectively. The corresponding optimum water content is 41.5 wt%, 44.4 wt%, and 56.4 wt%. The higher optimal water content in the DSS-B group indicates increased plasticity of the matrix prepared with DSS. This higher plasticity of the DSS-based matrix may be partially attributed to the higher organic content, as inferred by the TG results in **Fig. 2.5**, which can act as binding agents that enhance water retention [154]. On the other hand, using AAW in the sealing materials achieves a higher dry density than BBA. This enhancement can be associated with the finer particle size of AAW, which promotes better dispersion within the matrix.

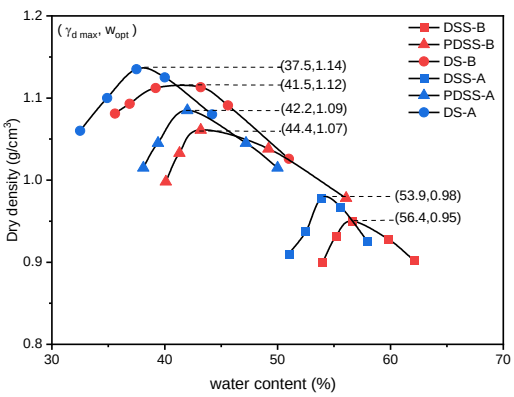

Fig. 2.6: Compaction curves for each mix (γ_{dmax} - Maximum dry density, w_{opt} - Optimal water content).

Compacted blends were then prepared according to the optimal water content for each group of mixtures to ensure efficient compaction and achieve the lowest possible permeability. The following measurements are conducted with the compacted blends after 70 d of curing. The actual moisture content in the specimens after curing is listed in **Table 2.2**: The actual moisture content in specimens after 70 d of curing.. Interestingly, the actual moisture content is lower than the optimal water because some water may evaporate during the mixing process and curing

period. Besides, free water could be bounded into the newly formed minerals and gels during curing. Therefore, in addition to the geotechnical properties, reaction products also influence the microstructure of the sealing materials, as elaborated in more detail later.

Table 2.2: The actual moisture content in specimens after 70 d of curing.

Group ID	DSS-B	DSS-A	PDSS-B	PDSS-A	DS-B	DS-A
Actual moisture%	36.4 (± 1.5)	41.8 (± 0.8)	34.1 (± 1.2)	36.8 (± 2.0)	30.6 (± 1.1)	34.9 (± 0.7)

2.3.3 Water permeability of the cured blends

Fig. 2.7 presents the permeability results of the cured samples, along with the limitation value indicated by the red line. The long-term permeability requirement for a mineral sealing layer composed of landfill residues in the Netherlands is less than 20 mm/year, considering a layer thickness of 60 cm [155]. This legal requirement corresponds to a maximum k-value of 6.34×10^{-10} m/s for the sealing materials we designed. Overall, the k-values of the DSS and PDSS-based specimens satisfactorily meet the legislative requirements, while the DS-based specimens exhibit permeability slightly above the critical value. Therefore, the prepared DSS and PDSS-based sealing materials show promise for landfill applications in terms of impermeability. It is noteworthy that the lowest achieved permeability, approximately 3.78×10^{-12} m/s in DSS-A, falls below the majority of reported permeability values for sludge-modified sealing materials, which typically ranged from 1.0×10^{-4} - 1.2×10^{-11} m/s [156–158].

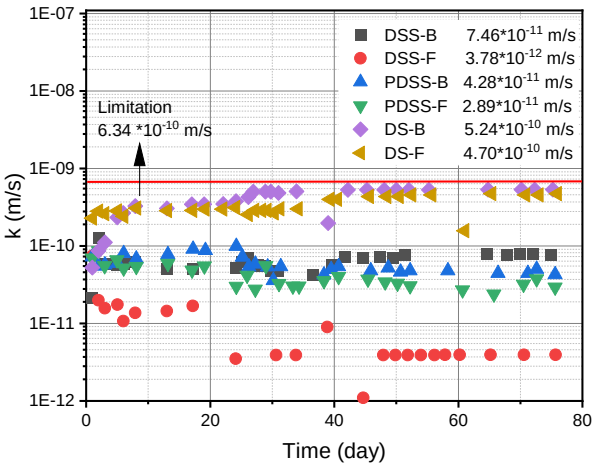

Fig. 2.7: The permeability test of the sludge-based landfill cover samples within 70 d. The red line represents the permeability requirement in the Netherlands.

Regarding the effect of different sludge types, the permeability results are in agreement with the compaction curves presented in **Fig. 2.6**. With higher plasticity, the DSS-based blends effectively reduce the void spaces within the matrix after the compaction. Furthermore, the AAW-modified specimens exhibit lower permeability compared to the BBA-modified specimens. This improvement could be attributed to the finer particle size of AAW, which refines the pore size distribution of the matrix more effectively than BBA, confirming the positive effect of AAW as external gel products on permeability. Their potential contribution

of the reaction products to the sealing materials will be further elucidated in the subsequent sections.

2.3.4 Reaction products characterization

- **Crystalline phases**

The analysis of the reaction product composition focuses on the finer fraction below 63 µm of each sample, as it is expected to contain the highest amount of reaction products, while the larger fractions largely consist of inert aggregate. **Fig. 2.8(a)** shows the XRD patterns of the sample prepared with different sludges and additives. Similar curves are observed, indicating that the different sludge and additive types have no significant influence on the formation of crystalline phases. The main crystalline phases identified include anhydrite ($CaSO_4$: PDF#: 72-0916), calcite ($CaCO_3$:PDF#: 72-1937), gypsum ($CaSO_4•2H_2O$: PDF#: 33-0311), sodium chloride (NaCl: PDF#: 70-2509) and quartz (SiO_2: PDF#: 83-2465). Additionally, some other minerals, such as Vivianite ($Fe_3(PO_4)_2·(H_2O)_8$: PDF#: 75-1186) and Chabazite-Na ($Na_{15.2}Al_{15.2}Si_{32.8}O_{96}$: PDF#: 83-1295), originate from the raw materials DSS and PDSS, respectively.

Meanwhile, the formation of the gypsum in the mixture is confirmed through the FT-IR spectrums in **Fig. 2.8(b)**. The band adsorptions at around 3536 cm^{-1}, 3392 cm^{-1} and 1675 cm^{-1} are assigned to the stretching vibration peaks of the hydroxyl group, while the peaks at 1614 cm^{-1} and 1118 cm^{-1} are attributed to the stretching vibration of S-O and S=O, respectively [159]. The peaks at 667 cm^{-1} and 599 cm^{-1} represent the stretching and bending vibration of sulfate [160]. The C-O stretching and bending vibrations around 1425 cm^{-1} and 865 cm^{-1} are identified due to the presence of the calcite. A slight difference in the adsorption peak of 1022 cm^{-1} is observed among all FT-IR spectrums. It is noteworthy that both C-O stretching vibration from the cellulose structure (organic content in sludge) and Si(Al-O) vibrations from silicates/aluminates (e.g. quartz, silica gel, calcium silicate hydrate gel) can contribute to this band [161,162]. Further details about the formation of gels are illustrated later.

TGA tests were performed on all samples to evaluate the formed gypsum amount, and the results are presented in **Fig. 2.9(a-c)**. The TG curves show two major mass losses around 110 - 180 °C and 600 - 800 °C, which could be attributed to the dehydration of gypsum and the decarbonation of the calcite [151,163]. Each mass loss is then calculated based on the tangential method [164], and the results are labeled in the figures. Interestingly, the AAW-modified specimens show a higher formation of gypsum than the BBA-modified specimens. This could be explained by the presence of thenardite in AAW, which contributes to a higher sulfate leaching than anhydrite in BBA (see details in **Section 2.3.5**). Besides, a slight mass loss peak around 85-105 °C is observed in the DTG curves of all specimens, which is associated with the dehydration of the gel products. The AAW-modified specimens exhibit a higher mass loss than the BBA-modified specimens for this peak, which could be accounted for by the bound water in AAW, as depicted in **Fig. 2.5**.

In conclusion, gypsum and gel products are the main new phases detected in the established sealing materials. As indicated by the TG-DTG curves in BBA-modified and AAW-modified specimens, the gypsum content is related to the leachable sulfate content in each mix, and the low bound water content indicates the relatively low formation of gel content. Meanwhile, the

transformation of free water into bound water explains the described reduction in moisture content of the matrix presented in **Table 2.2**.

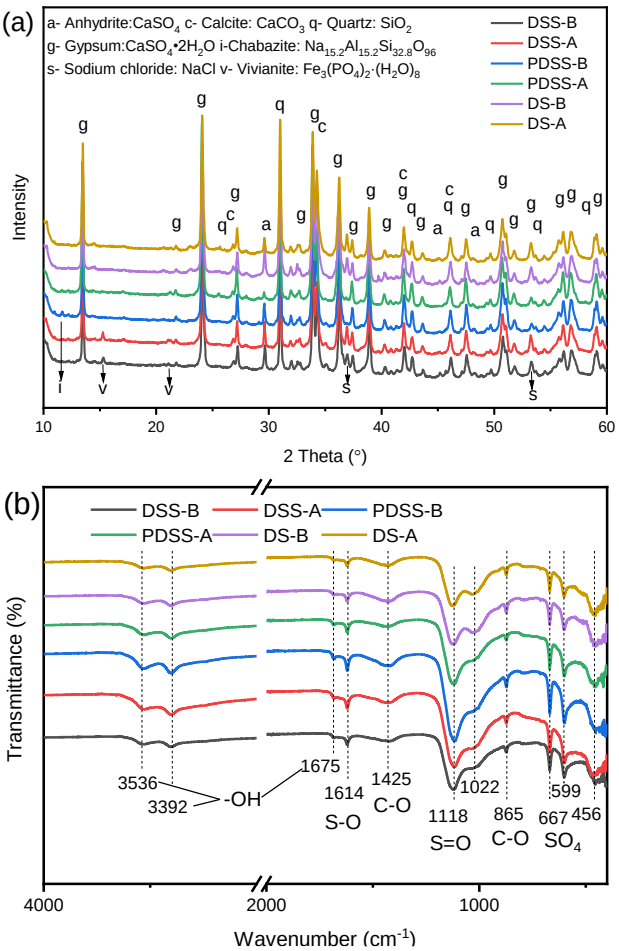

Fig. 2.8: (a) XRD patterns, (b) FT-IR spectra of the finer fraction (below 63 µm) from each mix.

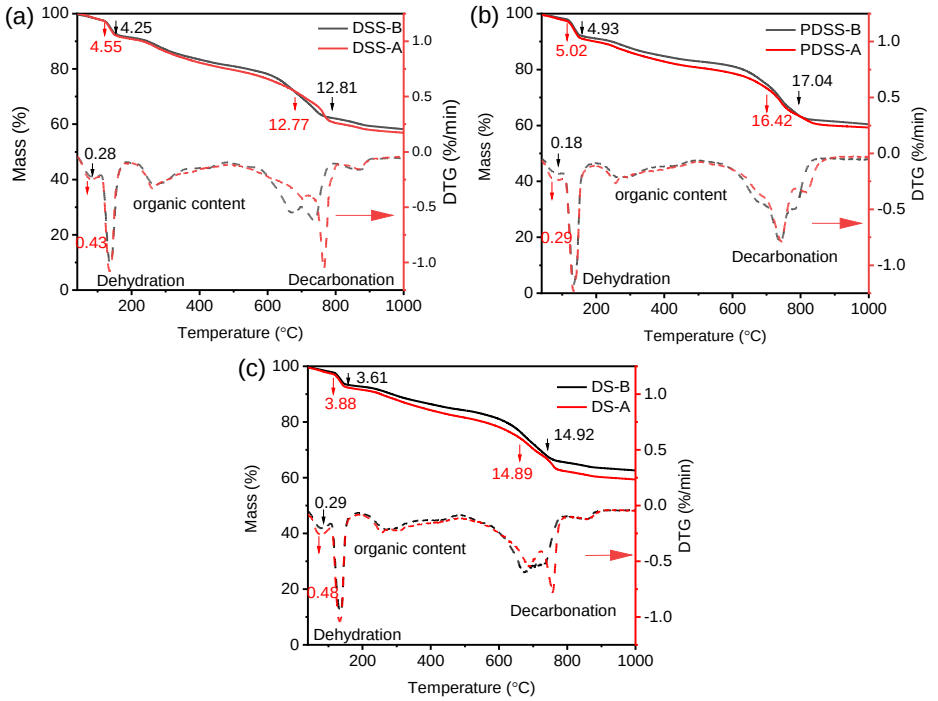

Fig. 2.9: TG-DTG curves of the finer fraction (below 63 µm) from each mix.

- **Amorphous phases**

N_2 adsorption of the finer fraction (below 63µm) from each mix, alongside the raw BBA and AAW, was performed to examine the formation of gel products further, as presented in **Fig. 2.10**. In terms of pore size, gel pores (less than 10 nm) and capillary pores (10 ~ 100 nm) are the two main classes of pores [165]. For the raw materials, two maxima around 3 nm and 7 nm are observed in the raw AAW, whereas no gel pores are observed in the raw BBA. The main component of AAW is colloidal boehmite with very low crystallinity (see **Fig. 2.3**). It has been reported that the porosity of colloidal boehmite is ultimately correlated with its crystallite size [152]. Hence, colloidal boehmite is likely present in two different particle sizes in the raw materials AAW.

Regarding the cured blends, the AAW-modified specimens exhibit a higher total pore volume than the BBA-modified specimens, likely due to the presence of higher gel pores in raw AAW. Nevertheless, one of the maxima at around 3 nm disappears in the AAW-modified specimens, indicating the potential reaction of colloidal boehmite or the crystallization of colloidal boehmite over time. On the other hand, the BBA-modified specimens show relatively lower gel pore volumes, consistent with the TG results, suggesting the lower formation of gel products. It is important to note that while gel pores increase the total porosity of the matrix, they do not increase the permeability [165]. Instead, an abundance of gel pores in the matrix indicates higher gel contents that can fill the larger porosity and reduce permeability [166]. Therefore, the lower permeability of AAW-modified specimens could be attributed to the increased gels sourced from AAW, while BBA-modified specimens exhibit less gel formation.

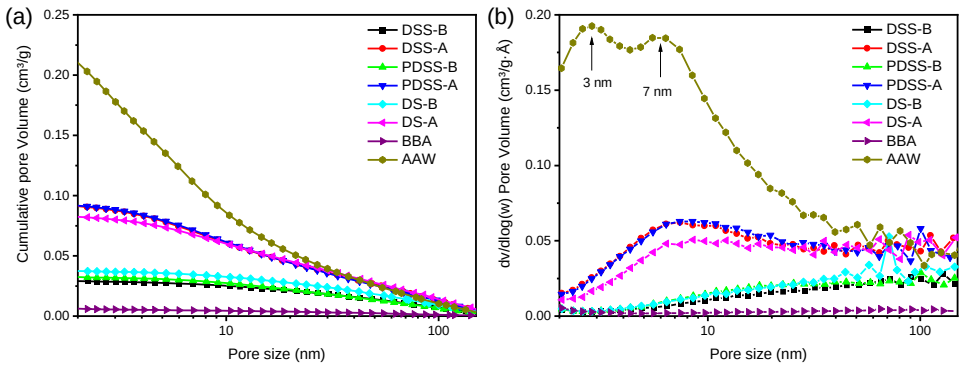

Fig. 2.10: N_2 adsorption behavior of the finer fraction (below 63 μm) from each group and raw materials BBA and AAW: (a) - Cumulative pore volume, (b) - Pore size distribution.

The effects of BBA and AAW on the gel composition of the specimens were further investigated. The finer fraction (below 63 μm) from DSS-B and DSS-A was subjected to SEM analysis with backscattered electron imaging, and the elemental composition was studied using EDX mapping. **Fig. 2.11** displays the observed particles, including organic fibers, gypsum, and quartz. Analyzing the mapping results of DSS-B specimens in **Fig. 2.11(a)**, it is evident that the distribution of Ca element is primarily influenced by the presence of gypsum. Interestingly, despite the expected formation of C-S-H gel resulting from the reaction between lime (from BBA) and waterglass [167], there is no observed correlation between elemental Ca and Si in the mapping results. This lack of correlation may be attributed to interference from the composition of gypsum and quartz or suggest that the resulting C-S-H gel has decomposed due to the low alkalinity of the environment. **Table 2.3** presents the pH value of the pore solution obtained by compressing the cured specimens, indicating that the C-S-H gel is not stable in such an environment, as the pH value is close to neutrality [168]. This instability is likely due to the low dosage of lime-containing BBA used, which might not have provided sufficient alkalinity to stabilize the C-S-H gel. The reduced gel pore volume in the BBA-modified specimens further supports this observation. It should be noted that over time, the C-S-H gel may undergo decomposition through carbonation, leading to increased permeability of the matrix [169]. Based on the hydrolysis properties of waterglass in a neutral environment, the main product of the reaction appears to be silica gel, which exhibits resistance to carbonation [170]. Consequently, it can be inferred that silica gel serves as the primary gel product in BBA-modified specimens and offers advantages in terms of stability.

Table 2.3: pH measurement of the pore solutions of all cured specimens.

Group	DSS-B	DSS-A	PDSS-B	PDSS-A	DS-B	DS-A
pH	8.2 ± 0.2	8.2 ± 0.1	8.2 ± 0.2	7.8 ± 0.3	8.3 ± 0.1	8.2 ± 0.1

Note: After 70 d of curing, the pore solution of each specimen is obtained by compression. pH of the pore solution is then measured using a pH meter.

According to N_2 adsorption behavior, the gel pores observed in AAW-modified specimens are related to colloidal boehmite in AAW. Consequently, three particles with high Al content in the mapping results in **Fig. 2.11(b)** were selected for further spot analysis. Ten spots were tested

for each particle, detecting elements including Na, Si, Mg, Ca and S. The average mass proportion of these elements is calculated and presented in **Table 2.4**. When compared with the XRF bulk compositions of the raw AAW, the three particles exhibit a decrease in Al_2O_3 content. The SO_3 content in these particles also varies due to the high mobility and leaching of sulfate (Na_2SO_4) from AAW. However, a portion of the leached sulfate is partially redeposited as the precipitation of anhydrite/gypsum, as confirmed by the increased CaO content within the three particles. Overall, the relatively low CaO, Na_2O and MgO contents indicate the absence of C/N-(A)-S-H gel or magnesium silicate hydrate (M-S-H) gel formation. The relatively high SiO_2 content likely originates from the dissolved waterglass, also evidencing the formation of silica gel. In conclusion, the main gel products in the AAW-modified specimens are the original colloidal boehmite and the formed silica gel, and the nature of the bonding between them remains unclear.

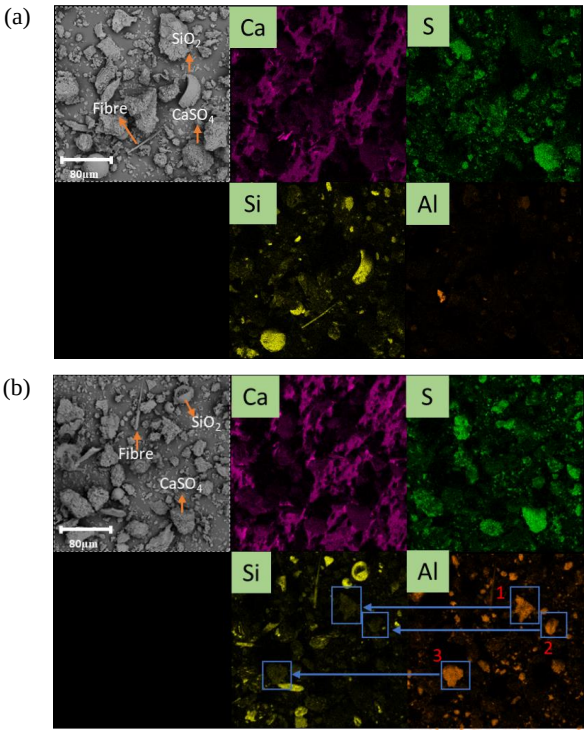

Fig. 2.11: EDS mapping of (a): DSS-B and (b): DSS-A, including BSE image. (Three particles rich in Al element are marked 1, 2, and 3, further analyzed with EDX spot analysis).

Table 2.4: The element composition of three Al-rich particles from the DSS-A sample in **Fig. 2.11** and the raw material AAW from XRF analysis.

Mass proportion%	Particle 1	Particle 2	Particle 3	AAW
Al_2O_3	61.0 ± 2.9	66.9 ± 2.3	66.9 ± 1.4	75.6
SiO_2	19.2 ± 1.6	17.1 ± 1.4	17.1 ± 2.3	1.1
Na_2O	5.7 ± 2.0	4.0 ± 0.9	4.1 ± 0.6	5.8
SO_3	7.6 ± 1.7	5.9 ± 1.7	5.0 ± 0.5	16.2
CaO	3.8 ± 1.0	3.7 ± 1.9	2.8 ± 0.4	1.4
MgO	2.6 ± 0.2	2.5 ± 0.2	4.1 ± 1.2	-

Note: "-" means no Mg element in raw AAW. Ten spots for each particle are collected, and the average values are calculated.

2.3.5 Environmental impact

In principle, landfills are designed with leachate collection systems to minimize the impact of the landfills on the environment and surrounding communities. In a practical application in the Netherlands, a 2 mm HDPE layer will be installed on the top of the sealing layer. The purpose of this HDPE layer is to prevent rainwater infiltration (**Fig. 1.6**) and to separate the vegetation layer from the sealing layer. This also allows for the utilization of industrial by-products as sealing material. In this work, the leaching behavior of both the raw materials and the prepared sealing materials was tested to mitigate its environmental impact in the event of unanticipated damage to the HDPE layer during installation or after prolonged use.

- **Leaching behavior of raw materials**

The chemical compositions of the leachates obtained from the raw materials, in comparison with the respective limit values for disposal in landfills, are presented in **Table 2.5**. The leachable elements in the sludge materials include the heavy metals As, Ni, Pb, Zn, Cu, Mo and Fe, as well as the alkali metals Na, K, Ca and Mg. The BBA exhibits high leaching levels of sulfate and Ca due to the anhydrite and lime. Heavy metals such as Pb, Zn and Cr are also observed in the leachate of BBA. As for the AAW, the leachate comprises the sulfate and Na due to the Na_2SO_4. Overall, the leaching level of As in the DSS, Pb and Cr in the BBA, and sulfate in the AAW exceed landfill disposal limits for non-hazardous materials. Consequently, further leaching tests of the cured specimens focus on the above heavy metal ions and sulfate anions.

Table 2.5: The leaching of all materials obtained via a one-batch leaching test in comparison with disposal limits for non-hazardous materials (mg/kg dry materials, UDL for under detection limits).

Raw material	DSS	PDSS	DS	BBA	AAW	Disposal Limits
Chloride	830	660	860	4590	3490	15000
Sulphate	2120	2730	380	19270	**69910**	20000
As	**2.65**	1.55	0.51	UDL	0.04	2
Ni	3.85	3	0.58	UDL	UDL	10
Pb	4.25	3.3	UDL	**304.4**	0.12	10
Zn	1.75	1.45	0.40	28.95	0.01	50
Ba	0.15	0.15	0.07	1.76	0.05	100
Cr	0.2	0.1	0.05	**25.39**	0.79	1
Cu	1.2	1.65	UDL	0.16	0.05	10
Mo	1.7	2.5	0.19	3.28	0.17	50
Sb	0.2	0.25	UDL	UDL	0.04	10
B	3.1	5	2.38	2.85	45250	-
Fe	38.4	52.2	2.19	UDL	UDL	-
Mg	486.8	196.1	114	0.03	13.28	-
Mn	0.7	0.35	0.12	UDL	0.04	-
Sr	1.95	1.45	1.62	40.46	0.73	-
Nitrate	7.9	18	UDL	UDL	UDL	-
Phosphate	100	100	UDL	UDL	UDL	-
NH_4^+	1550	980	1900	UDL	UDL	-
Na^+	960	830	720	2480	41280	-
K^+	540	310	540	6070	24	-
Ca^{2+}	460	390	330	6120	133	-
Al^{3+}	5	8.1	0.20	0.08	0.46	-
pH	8.14	8.07	8.31	12.93	8.39	-

- **Leaching of the cured blends**

Fig. 2.12 presents a summary of the leachable content of sulfate, As, Cr and Pb from the cured specimens, determined through one-batch leaching analyses. The immobilization rate of each element is expressed by:

$$\gamma = \sum M_C \times m_i \times L_i \quad \textbf{(2.1)}$$

$$\alpha = (1 - \frac{M_C \times L_C}{\gamma}) \times 100\% \quad \textbf{(2.2)}$$

Where γ represents the theoretical maximum leachable content in each cured specimen (mg), M_C is the mass of the cured specimen (kg), m_i is the mass proportion of component i (i.e., sludge or additives) (%), L_i denotes the leachable elements in component i (mg/kg), L_C refers to the leachable elements in the cured specimen (mg/kg), α represents the immobilization rate of the element in the cured specimens (%).

It is essential to note that the one-batch leaching test employs a L/S ratio of 10, with crushed solid particles below 4 mm in size. This approach enables the measurement of potentially

leachable ions and eliminates the need for simulating the process of a compacted seal being flushed through rainwater to obtain the filtrate. Overall, all cured blends exhibit desirable leaching levels for sulfate (< 20000 mg/kg), As (<2 mg/kg), Cr (<1 mg/kg) and Pb (< 10 mg/kg), indicating the absence of heavy metal pollution concerns in the prepared sealing materials. The relatively higher sulfate leaching in all blends is primarily attributed to the solubility of gypsum (~2 g/L, 25 °C), as confirmed by the XRD patterns shown in **Fig. 2.9**. It also explains the observed regressive sulfate immobilization rates in the cured specimens.

The leaching of As, mainly originating from the sludge DSS and PDSS, is observed in the DSS-based and PDSS-based specimens. Incorporating AAW, in comparison to BBA, reduces the leached As content. This enhanced immobilization rate of As is likely attributed to higher leached sulfate from AAW. As ferrous sulfate and aluminum sulfate are commonly used coagulation agents to remove As [171], a similar effect may be achieved because of the sufficient iron and sulfate content in the sealing materials. In the case of Cr leaching, it is only observed in the BBA-modified specimens, as Cr primarily originates from the raw BBA. According to the study on Cr leaching behavior in soil by Weng et al. [172], the lower leaching content of Cr in DSS-based specimens is associated with the higher organic content in the DSS (**Fig. 2.9**). Pb leaching is mainly from DSS and BBA, resulting in the highest Pb leaching from DSS-B. However, most cured specimens show a desirable immobilization rate of Pb. Leachable Pb is often stabilized as the silicate species, as reported by [173]. Thus, the 1.5 wt% waterglass is sufficient for the precipitation of $PbSiO_3$. Notably, some previous studies have reported the effect of organic content on absorbing the Pb [174,175]. In summary, the high immobilization of heavy metal ensures no soil pollution occurs in the landfill cover system.

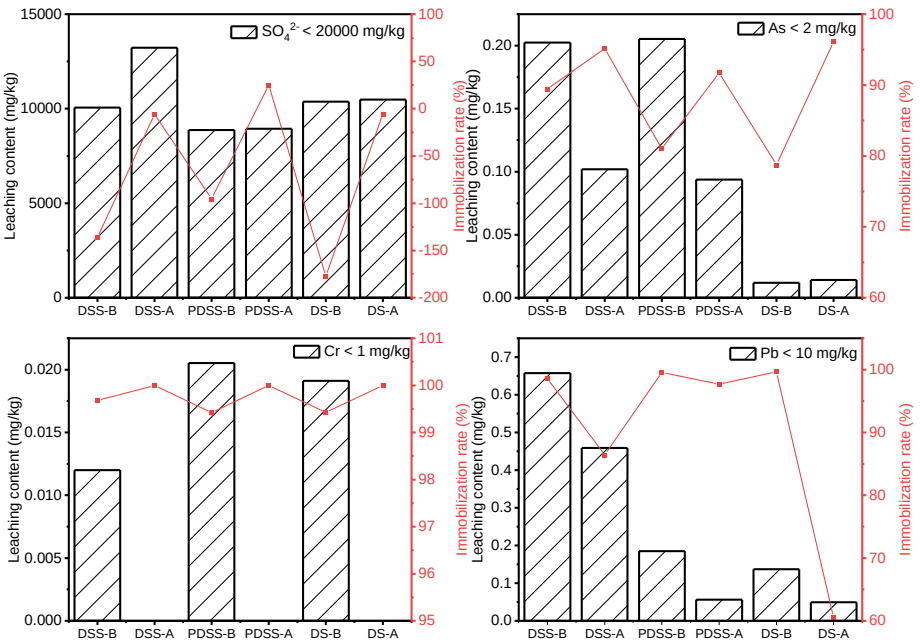

Fig. 2.12: Leaching content of the sulfate, As, Cr, and Pb from the cured specimens (mg/kg dried materials).

2.3.6 Benefits and limits discussion

The installation of a landfill cover system is crucial for landfill closure. As depicted in **Fig. 2.13**, the Netherlands has a significant number of operational landfills [176]. When these landfills approach full capacity in the future, a substantial amount of sealing material will be required for their closure. By utilizing sludge from WWTPs, raw material costs can be reduced, and the ecological impact of clay excavation can be eliminated. This approach also enables the sustainable recycling of industrial by-products, making it a more environmentally friendly alternative to using excavated clay. In the Netherlands, the annual production of DSS, PDSS and DS from WWTPs and MSWPs is 1400, 20, and 50 metric tons, respectively. These solid waste resources offer a sufficient and economical supply of sealing materials for landfill closure without compromising the primary objective of effective waste containment.

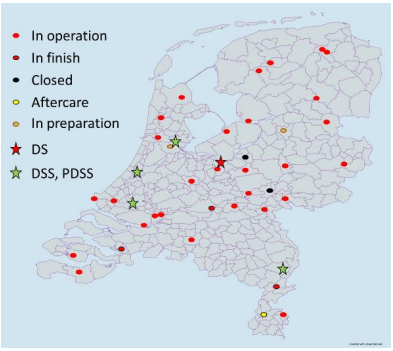

Fig. 2.13: Overview of landfills and WWTPs in the Netherlands (The map is created with mapchart.net).

The toxicity of industrial solid waste is often criticized for its high-leached heavy metals, leading to high waste management costs. However, applying BBA in sludge-based sealing materials can effectively utilize the organic content in the sludge to adsorb Pb and Cr from BBA. On the other hand, the highly leached sulfate in AAW and BBA is stabilized as the gypsum in the sealing materials, filling voids and further improving the impermeability along with the original amorphous boehmite and the formed silica gel. Moreover, the high sulfate concentration facilitates the adsorption of As from the sludge [171]. The heavy metals are effectively stabilized in the sealing material. This approach offers new insights into the solidification of heavy metals-containing solid waste within the sealing materials. It is important to note that HDPE separates the sealing layer from the vegetation layers above, thereby preventing the heavy metal contamination of the upper soil. Meanwhile, it also indicates the application limitations of this sealing material, i.e. the corresponding protective HDPE is required.

2.4 Conclusions

This chapter aims to co-product low-permeable sealing materials for final landfill cover systems by utilizing industrial solid waste. Various industrial products, including DSS, PDSS, DS, BBA and AAW from WWTPs and MSWPs, have been selected and characterized for this purpose. The study explores the effect of different types of sludge on sealing performance and investigates the influence of various additives on gel formation within the blends. Furthermore,

the potential environmental impact of the prepared sealing materials is revealed through their leaching behavior. Based on the obtained results, the following conclusions can be drawn.

- The sealing materials derived from industrial by-products have achieved low permeability, with DSS-A showing the optimal permeability, boasting a k-value of 3.78×10^{-12} m/s. Despite a slight degradation in permeability caused by the pre-treatment of TPH, PDSS-based specimens still comply with Dutch requirements for soil capping, highlighting its potential as a sustainable end-of-life solution. However, the permeability of DS-based specimens slightly exceeds the requirements due to the relatively lower organic content in DS.

- The primary reaction product in the sealing materials is gypsum, which is attributed to the high leachable sulfate from the BBA and AAW. Considering the low pH of the pore solution in the BBA-modified specimens, the addition of waterglass is expected to result in the formation of silica gel rather than the C-S-H gel. On the other hand, AAW proves to be an effective external gel, providing the desired permeability for AAW-modified specimens. The colloidal boehmite in AAW remains stable and behaves similarly to the gel products, effectively filling the voids and reducing the porosity.

- The heavy metals from the industrial by-products are well immobilized in the sealing materials. The reduction of As leaching from DSS is attributed to the coagulation of sulfates. The leachable Cr from BBA is adsorbed in the organic content in the sludge, whereas Pb is stabilized as the $PbSiO_3$. There are no heavy metal pollution concerns in the sludge-based sealing materials.

Chapter 3 Carbonation of digested sewage sludge-based sealing material in a final landfill cover system: role of waterglass and additional industrial by-products

Landfills are significant sources of greenhouse gases, particularly methane (CH_4) and carbon dioxide (CO_2), generated during the decomposition of waste materials. However, the interactive effects of CO_2 and the used landfill sealing materials are rarely studied but can significantly impact the long-term durability of landfill cover systems. This chapter investigated the impact of carbonation on landfill sealing materials derived from digested sewage sludge, waterglass, sand aggregate, and various additives, including waste incineration fly ash, biomass bottom ash, and aluminum anodizing waste. An accelerated carbonation process was employed to simulate the diffusion of CO_2 within the sealing materials. The effect of waterglass and different additives on carbonation resistance and overall performance of the sealing materials was studied through the assessment of permeability, chemical and physical changes, and environmental implications through post-carbonation leaching tests. Results reveal that the prepared sewage sludge-based landfill sealing materials meet permeability standards set by Dutch regulations. However, carbonation leads to the formation of carbonates and monohydrocalcite, slightly altering pore volumes and increasing permeability. While these changes remain within acceptable limits, it is crucial to consider the increased leaching behavior following carbonation and the extent of leaching is correlated with the nature of the additives utilized. Additionally, using a higher dosage of waterglass can mitigate the deterioration of impermeability, potentially attributed to the residual silicate gel that occupies the pores even after carbonation. The findings enhance understanding of the carbonation behavior of sludge-based landfill sealing materials, offering insights into the selection of appropriate industrial by-products for high-end applications.

This chapter is partially from the following article:

X. Ling, Y.X. Chen, K. Schollbach, H.J.H. Brouwers, Carbonation of digested sewage sludge-based sealing materials in a final landfill cover system: role of waterglass and additional industrial by-products (in preparation).

3.1 Introduction

In the previous chapter, we developed sludge-based sealing materials using by-products from sewage, digestate and incineration industries, focusing on their effect on permeability, mineralogical composition and environmental impacts of the investigated sludge materials [177]. From the literature study, some other solid wastes, including lime, crushed concrete, and incineration ash, have been utilized as additives to improve mechanical properties through the formation of cementitious products binding the particles [178–181]. Rosli et al. proposed the formation of calcium silicate hydrate gels in landfill-sealing materials prepared with sewage sludge and red gypsum [131]. Li et al. revealed that the main hydrated products are calcium silicate hydrate and ettringite in a dewatered sludge-fly ash-lime system through microstructure analyses [129]. However, it must be noted that significant landfill gas emissions, predominantly methane (CH_4) and carbon dioxide (CO_2) in equal volumetric ratios (50%v/v) [44], can permeate the landfill cover system despite the installation of a gas collection system aimed at minimizing these emissions [45,46]. Since implementing a gas collection system is often economically or practically unfeasible in older and abandoned landfills, fugitive emissions from landfills have emerged as a significant concern. While conventional clay-based sealing materials may not raise durability concerns post-CO_2 diffusion, as there is limited carbonate-forming potential, alternative landfill sealing materials containing higher levels of calcium from waste materials warrant attention. The presence of calcium-containing minerals, as well as the formed calcium silicate hydrates and ettringite, in these materials poses a considerable risk to their stability, as these minerals are prone to carbonation [54,70], leading to the formation of calcite and subsequent changes in phase volumes and porosity within the matrix [182]. Specifically, the capillary porosity, particularly in the range of ~100 -2000 nm in diameter, increases, as well as the water diffusion rate of the matrix [183]. Unfortunately, to the best of the authors' knowledge, few studies have revealed the effect of CO_2 on the permeability and microstructure of sludge-based sealing materials. This limitation may impede the application and effective durability assessment of sealing materials composed of industrial wastes such as sewage sludge.

In this chapter, the challenge of enhancing the carbonation resistance of sludge-based sealing materials is addressed by proposing two strategies. 1) Enhancing the impermeability of sludge-based material matrix to slow down the penetration of CO_2. Building on the findings of Gartung et al. [184], which suggest that the addition of waterglass, polymers, or other suitable chemicals can reduce the permeability of mineral sealing materials, the effect of waterglass on carbonation resistance was investigated. It is noteworthy that the sodium ions introduced by waterglass act as soluble metal cations and do not contribute to the precipitation of carbonate. However, considering that waterglass may react with CaO to form C-S-H gels, which can be carbonated and increase porosity, various waterglass content was used to investigate this aspect. 2) Controlling the calcium oxide content in the waste materials used. To evaluate the impact of calcium oxide content on carbonation behavior, three distinct industrial wastes were employed as additives: waste incineration fly ash (WIFA), biomass bottom ash (BBA) and aluminum-anodizing waste. The first two, from the incineration industry, contain close to 30 wt% CaO, while the latter, from the aluminum anodizing industry, is nearly free of CaO. Prior research has shown that the combined use of lime and waterglass can improve the compatibility and water permeability of waste rock from coal mining [135], as the pore volume of the barrier system is reduced by formed precipitations due to the chemical reaction. However, the

carbonation behavior of these newly proposed sludge-based sealing materials has not been thoroughly investigated, and the interaction between waterglass and these additives remains not fully understood.

Based on the above considerations, this work aims to advance the understanding of the carbonation behavior of the sludge-sealing materials. An accelerated carbonation process was employed to simulate the diffusion of CO_2 within the sealing materials. The potential effect of waterglass and various additives on the permeability, reaction products, and volume stability were characterized through multiple analyses, including X-ray diffraction (XRD), Thermogravimetry test (TG), Fourier-Transform Infrared (FT-IR), nitrogen adsorption. Additionally, the potential environmental impact of the sealing materials post-carbonation is evaluated based on their leaching behavior. The findings provide the basis for the selection of waterglass and industrial by-products in the application of sludge-based sealing materials.

3.2 Materials and Experiments

3.2.1 Raw materials

Digested sewage sludge (DSS), sourced from a local Wastewater Treatment Plant in Deventer, The Netherlands, served as the matrix materials. Three distinct industrial by-products with varying characteristics were incorporated as additives in the formulation of sludge-based sealing materials. Biomass bottom ash (BBA) was from a grate furnace, where wooden waste materials underwent incineration. Waste incineration fly ash (WIFA) obtained from a Dutch Municipal Solid Waste Plant, with the fly ash separated using electrostatic precipitators and aluminum anodizing waste (AAW), represented aluminum-containing residues generated during the aluminum anodizing process in the alumina industry. Waterglass (WG) (20.1 wt% Na_2O and 62.7 wt% SiO_2, PQ France) was introduced in the preparation of sealing materials to reduce overall permeability [139]. Furthermore, a blend comprising 30 wt% blasting grit and 70 wt% normal sand was utilized as aggregate.

The chemical composition of the raw materials was analyzed using X-ray fluorescence (XRF) on a PANalytical Epsilon 3 instrument. The borate fusion method was used to prepare fuse beads. The results are presented in **Table 3.1**. The mineral composition of raw materials was determined through X-ray diffraction (Bruker D4 phaser), as shown in **Fig. 3.1**. DSS comprises quartz (PDF# 83-2465), calcite (PDF#72-1937), and baricite (PDF#72-1937). WIFA and BBA contain anhydrite (PDF#72-0916), formed during the incineration for sulfur dioxide control. WIFA exhibits high halite and potassium chloride peaks, which are attributed to the disposal of K- and Na-contained waste materials during incineration. AAW contains low-crystalline boehmite (PDF#49-0133), bayerite (PDF#01-0287), and thenardite (PDF#05-0631). The particle size distribution of raw materials was determined using a laser light scattering technique (Mastersizer 2000, Malvern). Raw materials were dispersed in isopropanol with a 10 min ultrasonic dispersion to prevent agglomeration, and the results are depicted in **Fig. 3.2**. The average particle size (d50) for DSS, WIFA, BBA, and AAW are approximately 18 μm, 57 μm, 138 μm, and 11 μm, respectively.

Table 3.1: Chemical composition and physical properties of raw materials.

Elements	DSS	WIFA	BBA	AAW	WG
Na_2O	0.1	4.7	-	4.2	20.1
MgO	0.9	0.9	1.6	-	-
Al_2O_3	0.7	2.6	2.5	55.2	-
SiO_2	2.6	6.8	20.8	0.8	62.7
P_2O_5	4.5	0.5	1.4	0.2	-
SO_3	1.9	8.9	5.8	11.8	-
K_2O	0.5	8.9	4.8	-	-
CaO	4.9 [2.4]	28.9 [6.3]	34.5 [7.1]	1.0 [0]	-
TiO_2	0.4	2.3	8.5	-	-
Fe_2O_3	18.1	3.1	7.2	0.6	-
ZnO	0.5	3.8	1.7	-	-
Cl	0.1	17.6	1.6	-	-
Others	0.6	2.1	2.3	2.4	-
LOI	64.2	8.8	7.3	23.8	17.2
Specific gravity (cm^3/g)	1.69	2.74	2.87	2.54	2.42
Moisture (%)	66.6	1.0	0.6	76.0	-

[ ] represents CaO content from the calcite within the raw materials based on their TG results (see **Appendix Fig. A.1**). M_{CaO} % = (Mass loss between 550 °C and 800 °C) × 56/44 × 100%.

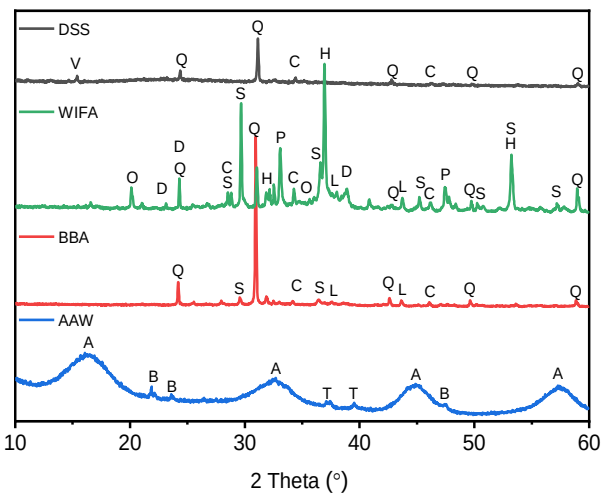

Fig. 3.1: XRD patterns of the raw materials. (A- boehmite: AlO(OH), B-bayerite: $Al(OH)_3$, C-calcite: $CaCO_3$, D- andradite: $Ca_3Fe_2(SiO_4)_3$, H-halite: NaCl, L-lime: CaO, V-vivianite: $Fe_3(PO_4)_2•8H_2O$, O-Bassanite: $CaSO_4•0.5H_2O$, P- potassium chloride: KCl, Q- quartz: SiO_2, S-anhydrite: $CaSO_4$, T-thenardite: Na_2SO_4).

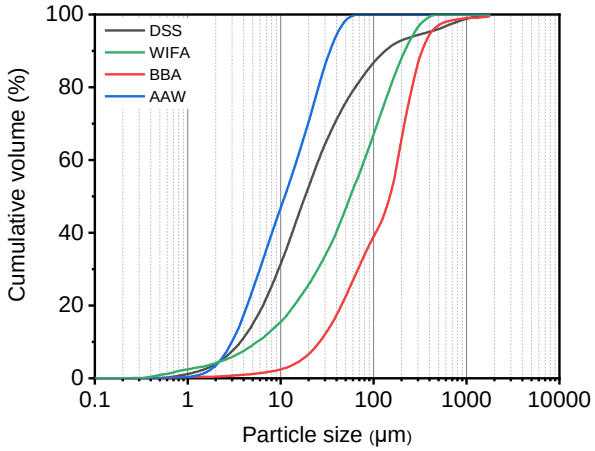

Fig. 3.2: Particle size distribution of each raw material.

3.2.2 Sample preparation

As detailed in **Table 3.2**, the formulated mixtures consist of a 45 wt% sand fraction, 46 wt% DSS, and 9 wt% additives. Additional 1.5 wt% and 2.0 wt% WG were incorporated based on previous literature recommendations for its application in sealing materials, falling within the range of 1 - 5 wt% [139]. The preparation process involved mixing DSS and the grain fraction in a laboratory mixer until well dispersed. Subsequently, the additives and WG were gradually added during stirring. The resulting blends were cast into a cylinder mold (D = 95 mm, H = 50mm) and compacted following DIN 18127 with a compaction degree of 95%. The samples were externally prepared by Ingenieurbüro Kügler in Essen, Germany. Then, the prepared specimens were sealed in plastic bags and stored in a chamber at 20 °C and 90% relative humidity for a curing period of 70 d. For the carbonated samples, the specimens were transferred to a carbonation chamber with a 65% relative humidity, 25 ± 0.1°C for one month. For the uncarbonated samples, the specimens were maintained in the previous chamber under the same curing conditions for one month.

Table 3.2: Formulations of the designed samples (wt%).

Group ID	Grain Fraction	DSS	WIFA	BBA	AAW	Additional WG (%)
DW1.5	45	46	9	0	0	1.5
DB1.5		46	0	9	0	
DA1.5		46	0	0	9	
DW2.0		46	9	0	0	2.0
DB2.0		46	0	9	0	
DA2.0		46	0	0	9	

DSS: digested sewage sludge, WIFA: waste incineration fly ash, BBA: biomass bottom ash, AAW: aluminum anodizing waste, and WG: waterglass.

3.2.3 Methodology

The flowchart of the investigation process is presented in **Fig. 3.3**.

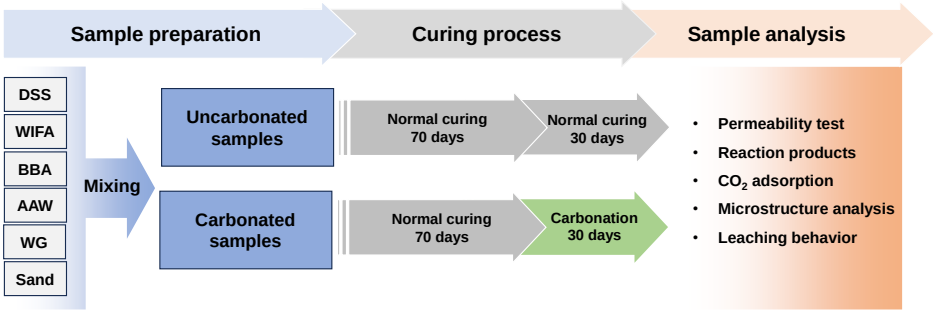

Fig. 3.3: Investigating the impact of carbonation on sludge-based sealing materials flowchart.

- **Carbonation**

The specimens were moved into a carbonation chamber (Memmert ICH260C). A circular airflow with 3% CO_2 gas by volume was applied continuously during the test. The relative humidity was set to 65%. Since few related parameters could be referenced from studies on the carbonation of landfill cover systems, the mentioned value was set according to the reported optimal value in the carbonation test for concrete and cement [185,186].

- **Permeability test**

Permeability tests for both uncarbonated and carbonated samples were performed in accordance with DIN18130 and DIN EN ISO 17892. Cylindrical specimens were placed in pressure cells with side pressure, and permeability values were recorded every three days. The test was externally conducted by Ingenieurbüro Kügler in Essen, Germany.

- **Phase characterization**

Following both the normal curing and carbonation curing, the phase assemblages of the prepared specimens were characterized through X-ray diffraction (XRD), Thermogravimetry (TG), and Fourier transform infrared spectroscopy (FT-IR). The specimens were slightly crushed and dried in a vacuum oven at 60 °C to remove the free water. The characterization was then performed on the powder samples (< 63 µm), obtained through sieving the dried samples to remove coarse aggregates and concentrate the carbonated products. The XRD analysis was carried out by a Bruker D4 phaser, with a step size of 0.02° and a 2θ range from 10° to 60° (Co-Kα, 40 kV, 30 mA). The TG test was conducted by a STA 449 F1 instrument at a heating rate of 10 K/min under a N_2 atmosphere. For FT-IR analysis, a Varian 3100 instrument was employed to identify bonding in the mineral phases within the wavenumber range of 4000 – 400 cm^{-1}.

- **Microstructure analysis**

N_2 sorption analysis of both uncarbonated and carbonated samples was conducted using Micrometrics Tristar II plus. The pore size distribution was determined at 77K from the adsorption branch employing the Barrett – Joyner – Hallenda (BJH) method [140]. The samples were pretreated by nitrogen gas flow with a heating rate of 10 K/min and heated at 60 ºC for 24h to remove moisture and impurities.

- **Leaching behavior**

The leaching behavior of both uncarbonated and carbonated samples was analyzed using the one-batch leaching test (EN 12347-2). The cylindrical samples were crushed into small pieces (< 4 mm) and mixed with deionized water in polyethylene bottles. These bottles were then sealed and placed horizontally on a linear reciprocating shaking device (Stuart SSL2) for 24 h shaking. The pH value of the leachate was initially measured using a pH meter and then acidified with HNO_3. The concentration of chloride (Cl^-) and sulfates (SO_4^{2-}) in leachates were analyzed by ion chromatography (Dionex 1100) equipped with an ion-exchange column AS9-HS. All other elements were quantified with inductively coupled plasma optical emission spectroscopy (ICP-OES Spectral Blue).

3.3 Results

3.3.1 Permeability

- **Effect of different additives and waterglass dosage on the permeability**

The permeability of the specimens is evaluated using the k-value. **Fig. 3.4(a)** shows the evolution of the k-values in the initial 75 d for each uncarbonated specimen with 1.5 and 2.0 wt% waterglass. After the first 20 d, the permeability value stabilizes, and the average value post this period is considered as its permeability value. Dutch legislation prescribes overall permeability limits of 6.34×10^{-10} m/s for the residue-based sealing layer materials [155]. The k-values of the investigated samples consistently fall below this threshold, ranging from 4.04×10^{-12} m/s to 6.48×10^{-10} m/s. This suggests the feasibility of using WIFA, BBA, and AAW in the preparation of landfill sealing materials concerning permeability. AAW-modified samples stand out with the lowest permeability. The reasons for this distinctive characteristic have been discussed in Chapter 2 [177], attributed to the finer particle size of AAW and the improved formation of gypsum that improves the packing system.

Furthermore, it is noteworthy that the waterglass dosage exerts varying effects on the permeability of the samples. Specifically, the permeability of DB2.0 samples decreases with higher waterglass content. A plausible explanation for the observed decrease in permeability in DB2.0 is that the additional waterglass may fill void spaces, thereby improving the overall packing system. Moreover, waterglass may contribute to the formation of other precipitates (gel products) that effectively reduce the porosity of the matrix, further contributing to the observed decrease in permeability. On the other hand, the permeability for DW2.0 and DA2.0 increases with more waterglass. One potential reason could be the dissolution of minerals within WIFA and AAW when mixing with waterglass, as the waterglass provides a localized strong alkaline environment. Specifically, boehmite in AAW could be dissolved as [136,187]:

$$AlOOH + OH^- + H_2O \rightarrow Al(OH)_4^- \quad \textbf{(3.1)}$$

This dissolution process may introduce pathways for fluid flow, consequently leading to higher permeability in AAW-modified samples.

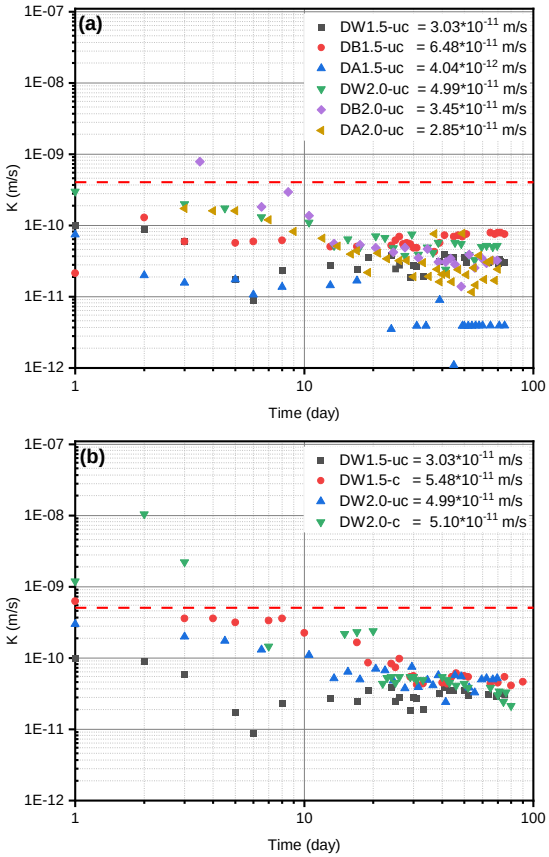

Fig. 3.4. The permeability test of the prepared samples within 75 d. (a): with different waterglass content and additives, (b): with (-c) or without (-uc) carbonation process for DW samples. Mixture details can be found in **Table 3.2**. The red line represents the maximum allowable k-value for landfill sealing materials according to Dutch legislation.

- **Effect of carbonation on the permeability**

The relatively lower CaO content in AAW makes it less vulnerable to the impacts of CO_2. Consequently, among the two remaining additives with relatively higher CaO content, WIFA was selected to assess its performance following carbonation. The effect of carbonation on the permeability of DW1.5 and DW2.0 is presented in **Fig. 3.4(b)**. The k-value of DW1.5 experiences a substantial increase from 3.03×10^{-11} m/s to 5.48×10^{-11} m/s, indicating the formation of a higher pore volume post-carbonation. Upon the incorporation of 2 wt% waterglass, the permeability of DW2.0 remains largely unchanged, maintaining values between 4.99×10^{-11} m/s and 5.10×10^{-11} m/s. This suggests that the higher waterglass dosage reduces the degradation of the permeability caused by carbonation. One possible explanation is that waterglass facilitates the precipitation of silica gel, which remains unaffected by carbonation. Hence, the higher amount of precipitated silica gel from waterglass effectively obstructs the connective pores [36], thereby mitigating the adverse impact of carbonation. Fortunately, both DW1.5-c and DW2.0-c meet the requisite standards even after undergoing carbonation.

Subsequent sections delve into the detailed mechanisms of permeability degradation in the specimens, exploring both micro-scale and macro-scale perspectives influenced by the carbonation process.

3.3.2 Phase changes

- **X-ray diffraction analysis (XRD)**

To reveal the potential chemical reaction during the normal curing and carbonation process, the phase compositions of the samples were characterized by XRD. **Fig. 3.5(a)** presents the XRD patterns of all samples containing 1.5 wt% waterglass. The uncarbonated samples, after the same curing ages at normal humidity, exhibit similar peaks, indicating a consistent phase composition, including gypsum ($CaSO_4$•$2H_2O$ PDF#: 33-0311), anhydrite ($CaSO_4$, PDF#: 72-0916), calcite ($CaCO_3$ PDF#: 72-1937), vivianite ($Fe_3(PO_4)_2$•$(H_2O)_8$ PDF#: 75-1186), sodium chloride (NaCl PDF#: 70-2509) and quartz (SiO_2 PDF#: 89-8935). The formation of gypsum within the sealing materials is associated with the soluble sulfate and calcium content from raw materials (see **Appendix Table A.1**). It should be noted that the presence of anhydrite could be attributed to the transformation of the gypsum during the drying process of the XRD sample preparation. The primary distinction among the uncarbonated samples modified with BBA, WIFA, or AAW lies in the varied intensity of gypsum, attributed to the distinct sulfate content in the raw additives (as depicted in **Table 3.1**). For the carbonated samples, no significant changes are observed in DB1.5-c and DA1.5-c compared to DB1.5-uc and DA1.5-uc in terms of phase composition. However, visible alterations occur in DW1.5-c, where monohydrocalcite ($CaCO_3$•H_2O PDF#: 84-0049) emerges. The formation of monohydrocalcite entails the consumption of calcite, accompanied by the absorption of a portion of free water from the matrix, which becomes chemically bound within the monohydrocalcite structure. Nonetheless, the amount of this bound water is assumed to be minimal, given the low intensity of monohydrocalcite peaks.

Upon the incorporation of 2 wt% waterglass, the XRD patterns for all samples, both with and without carbonation, are depicted in **Fig. 3.5(b)**. The higher dosage of waterglass has no discernible influence on the phase composition of the mixture. Meanwhile, the formation of monohydrocalcite is evident in the DW2.0-c as well.

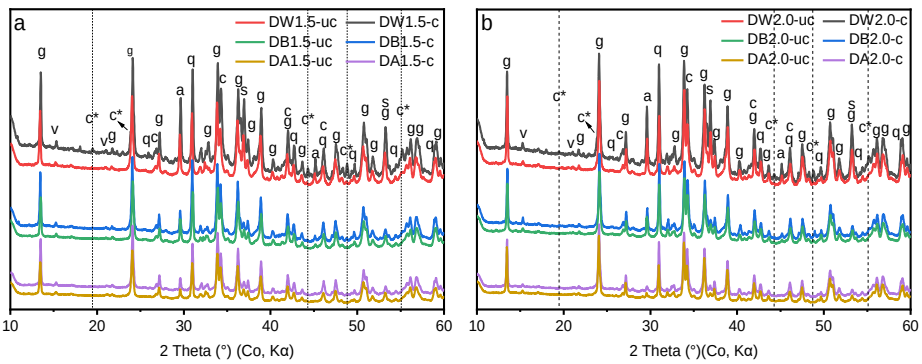

Fig. 3.5: XRD patterns of the powder samples in each group with (-c) or without (-uc) carbonation. (a-Anhydrite: $CaSO_4$, c- Calcite: $CaCO_3$, c*- Monohydrocalcite: $CaCO_3$•(H_2O), g- Gypsum: $CaSO_4$•$2H_2O$, q- Quartz: SiO_2, s- Sodium chloride: NaCl, v- Vivianite: $Fe_3(PO_4)_2$•$(H_2O)_8$).

- **Thermogravimetric analysis (TGA)**

To quantify the amount of formed gypsum, monohydrocalcite and calcite, both uncarbonated and carbonated samples were subjected to Thermogravimetric analysis. **Fig. 3.6** illustrates the TG and DTG curves of all prepared samples. For the uncarbonated samples, major mass losses are observed at approximately 135 ºC, 265 ºC, and 750 ºC. These are attributed to the dehydration of gypsum [163], the decomposition of organic content originating from the sewage sludge [188] (see TG and DTG results of raw DSS in **Appendix Fig. A.1**), and the decarbonation of calcite [151], respectively. Similar mass losses can be observed in the carbonated samples. Interestingly, there is minimal variation in the curves representing organic content from the sludge, indicating its stability during the carbonation process. However, some differences are highlighted in the mass loss due to the dehydration of gypsum and the decarbonation of calcite. Hence, their specific mass loss was calculated using the tangential method [164], with the results summarized in **Table 3.3**.

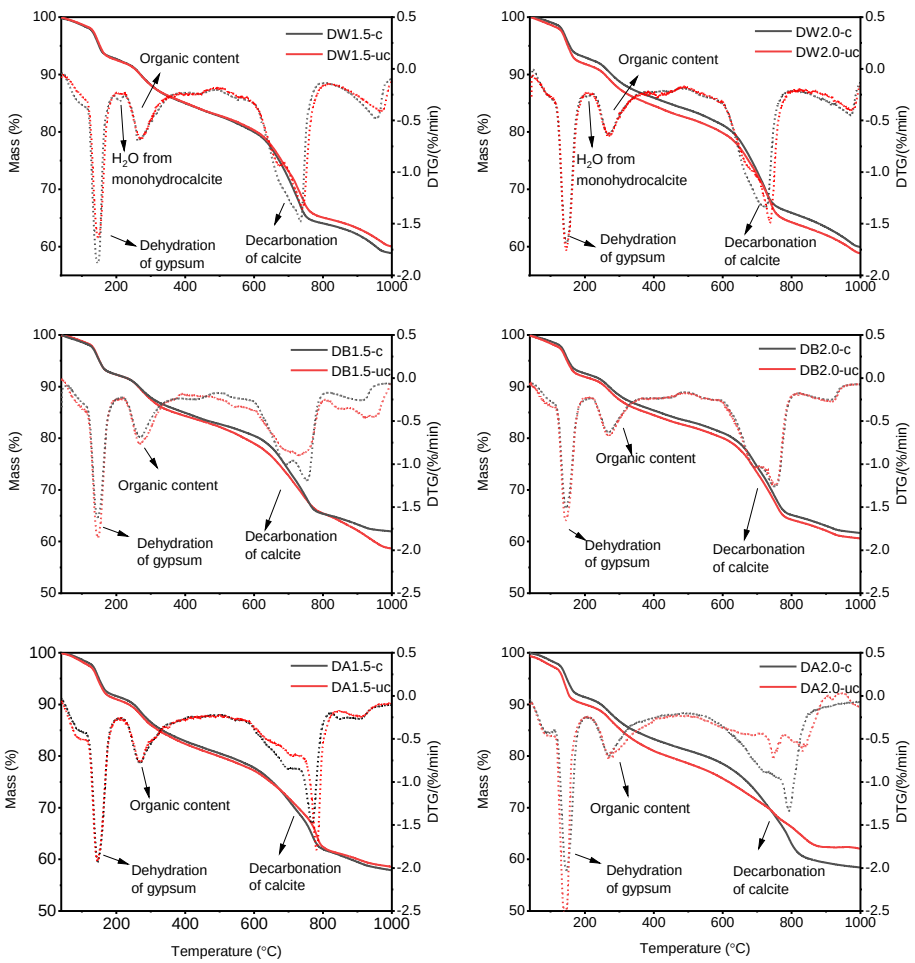

Fig. 3.6:TG-DTG curves of each sample with (-c) or without (-uc) carbonation. (a): DW1.5, (b): DW2.0, (c): DB1.5, (d): DB2.0, (e): DA1.5, (f): DA2.0. Mixture details can be found in **Table 3.2**.

The analysis of bound water content reveals variations in gypsum formation depending on the additives used, particularly with higher sulfate content in AAW resulting in increased gypsum formation in DA1.5 and DA2.0. However, comparing bound water in uncarbonated and carbonated samples shows only slight differences, suggesting a slight decrease in gypsum production. This decrease may be attributed to the consumption of calcium ions during the carbonation curing process. To visualize the potential effect on pore volume induced by this phase transition, theoretical chemical deformation was calculated based on literature data [189–194], resulting in a chemical deformation of 0.082 ml/g_{gypsum}, as summarized in **Table 3.4**. Considering the minor changes observed in bound water, possibly influenced by sample variability, and the effectiveness of normal curing phases in facilitating significant gypsum formation [177], it can be inferred that the carbonation process has minimal impact on pore volume due to gypsum production variations. Meanwhile, confirmation of monohydrocalcite formation in DW1.5-c and DW2.0-c was achieved through the detection of a tiny peak around 200 ºC [195]. The chemical deformation resulting from monohydrocalcite formation was calculated to be -0.062 ml/$g_{calcite}$. This further supports that the formation of monohydrocalcite has limited influences on the porosity of the matrix.

Additionally, different groups of samples exhibit varying degrees of calcite increase post-carbonation. Despite the anticipation that higher CaO content in the raw materials would lead to greater CO_2 adsorption, DW1.5-c and DW2.0-c absorb the lowest CO_2 content. One potential explanation for this contrast is the reactivity of calcium in the samples, which heavily influences their susceptibility to carbonation. The majority of calcium in WIFA exists in forms such as calcite, gypsum, bassanite and andradite, which are less prone to carbonation. However, it is also crucial to consider errors in the TG testing process, including issues with representative sampling and potential carbonation during sample preparation. These factors could contribute to discrepancies in the observed CO_2 adsorption. Interestingly, DA1.5-c and DA2.0-c show a relatively high increase in CO_2 adsorption. The reasons behind this phenomenon remain unclear. Li et al. [196] have revealed that hierarchical porous AlOOH hollow microspheres can improve CO_2 capture. A similar function may be associated with the amorphous AlOOH present in the AAW. Overall, the CO_2 adsorption capacity of the sealing materials is relatively low, especially in DW groups, accounting for the low degradation of impermeability post-carbonation.

Table 3.3: Mass loss calculation at different temperature ranges based on the TG results (wt%).

Group	Bound water Temperature range (110 - 200°C)		Decarbonation of carbonates Temperature range (600 - 800°C)	
	Without Carbonation (-uc)	With Carbonation (-c)	Without Carbonation (-uc)	With Carbonation (-c)
DW1.5	5.7	5.3 (0.8) *	15.2	15.8
DB1.5	5.9	5.8	13.5	15.1
DA1.5	7.0	6.8	14.8	15.8
DW2.0	6.1	6.1 (0.7) *	15.6	15.3
DB2.0	6.0	5.8	15.8	16.0
DA2.0	7.0	6.6	13.3	15.5

* represents the mass loss due to the dehydration of monohydrocalcite from DW1.5-c and DW2.0-c.

Table 3.4: Calculation of chemical deformation due to the formation of calcite and monohydrocalcite.

Reactants/Reaction products	Moles	Mass (g)	Molar volume (ml/mol)	Volume (ml)
$CaSO_4 \cdot 2H_2O$	1	172.17	74.3 [189]	74.3
OH^-	2	17.01	-4.3 [190]	-8.6
SO_4^{2-}	1	96.06	13.9 [191]	13.9
Ca^{2+}	1	40.08	26.20 [197]	26.20
Volume changes due to gypsum formation			1.8 ml	
$CaCO_3$	1	100.09	36.9 [192]	36.9
OH^-	2	17.01	-4.3 [190]	-8.6
Ca^{2+}	1	40.08	26.20 [197]	26.20
H_2O	3	18.02	18.0 [190]	54.0
Volume changes due to calcite formation			15.9 ml	
Chemical deformation			0.082 ml/g gypsum	
$CaCO_3$	1	100.09	36.9 [192]	36.9
H_2O	1	18.2	18.0 [190]	18.0
$CaCO_3 \cdot H_2O$	1	118.10	48.7 [193]	48.7
Volume changes due to monohydrocalcite			-6.2 ml	
Chemical deformation			-0.062 ml/g calcite	

- **Fourier transform infrared spectroscopy (FT-IR)**

Fig. 3.7 presents the FT-IR spectra of the investigated samples, both with and without carbonation. The observed broad bands around 3528 - 3405 cm^{-1} and 1684 - 1614 cm^{-1} are ascribed to the stretching and bending vibrations of the H–OH bond in gypsum, respectively [198]. The peaks around 1112 cm^{-1}, 667 cm^{-1}, and 596 cm^{-1} are assigned to the stretching and bending modes of sulfate in gypsum or anhydrite [199]. The absorption peaks at 1411 cm^{-1} and 871 cm^{-1} originate from the vibration of v_3 [CO_3^{2-}] and v_2 [CO_3^{2-}] from the calcite and monohydrocalcite, respectively. The increased intensity of these two adsorptions after the carbonation process also confirms the heightened carbonate formation.

Additionally, a notable difference observed after the carbonation process is the adsorption peak around 1026 cm^{-1}, attributed to the Si-O-Si vibrations originating from the waterglass. Hua et al. [200] have proposed the reaction of waterglass in the presence of gypsum, as shown by

$$CaSO_4 + Na_2O \cdot nSiO_2 \rightarrow CaO \cdot nSiO_2 + Na_2SO_4 \quad \textbf{(3.2)}$$

However, the formed $CaO \cdot nSiO_2$ is sensitive to the carbonation process and will undergo further decomposition with the formation of calcite and silicate gel [201]. Similar adsorption shifts to higher wavenumbers due to the carbonation have also been reported in the study of the carbonated alkali-activated slag system [202]. In conclusion, the additional waterglass participates in the formation of silicate gel in the final carbonated samples. This implies that a higher dosage of waterglass results in a greater formation of silicate gel, which may account for the lower permeability obtained after carbonation due to the filler effect of silicate gel within the matrix.

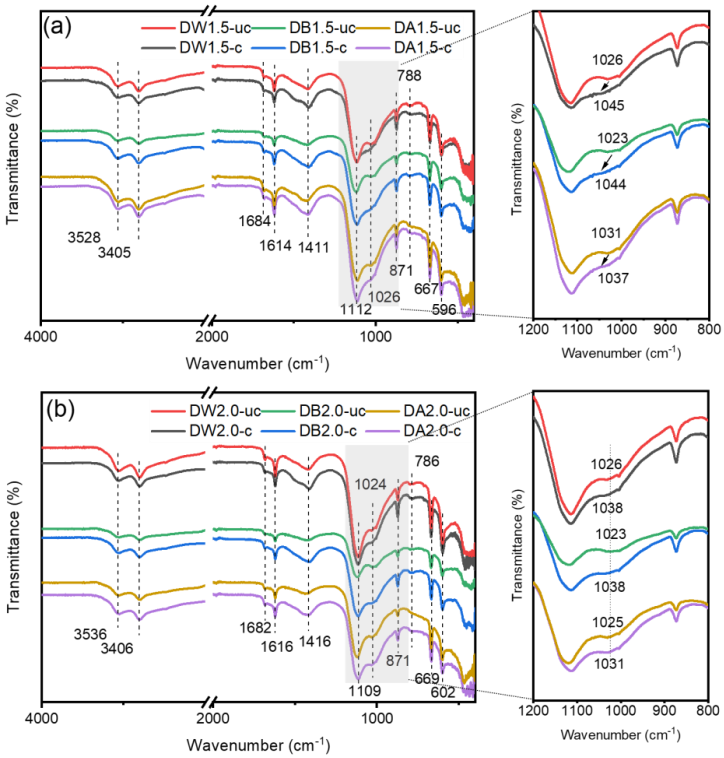

Fig. 3.7: FT-IR spectra of each sample with (-c) or without (-uc) carbonation.

3.3.3 Physical changes

- **Microstructure**

The permeability of sealing materials is notably influenced by their microstructure, with pores creating pathways for fluid flow. To assess the impact of the carbonation process on the microstructure, N_2 adsorption analysis was conducted on both the samples and raw additive materials. Following the International Union of Pure and Applied Chemistry classification, pores are categorized as micropores (< 2 nm), mesopores (2 – 50 nm) and macropores (> 50 nm) based on their pore size [203]. The application of the BJH method in N_2 adsorption analysis is recommended for determining mesopores [204]. Within the mesopores range, two primary classes are identified: gel pores (2 - 10 nm) and capillary pores (10~50 nm) [165]. The pore size distribution for each sample was calculated, and the results are illustrated in **Fig. 3.8**.

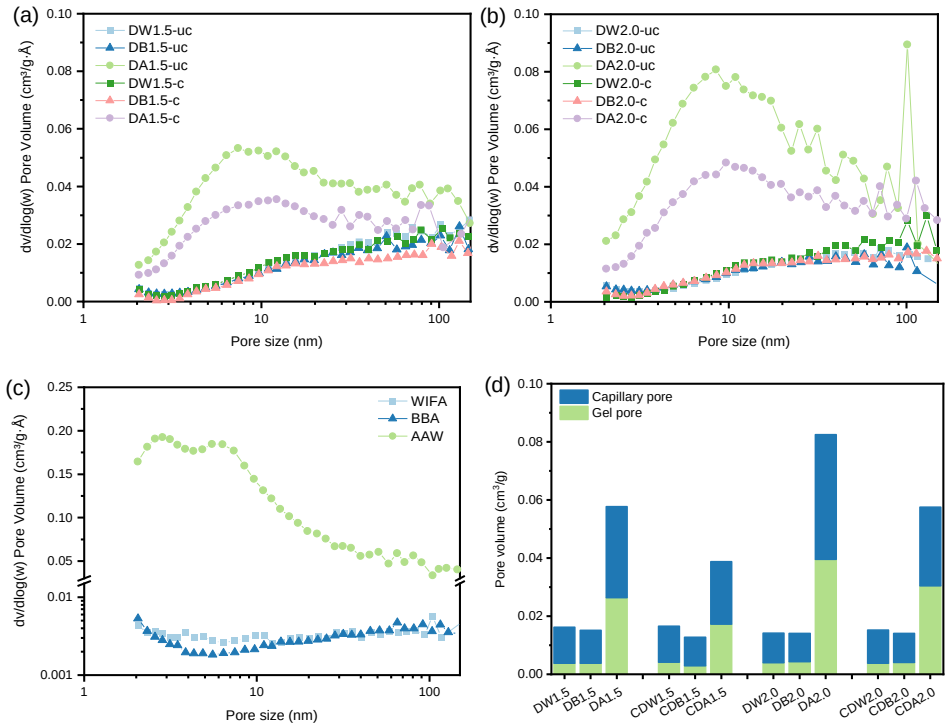

Fig. 3.8: Pore size distribution of each sample from BJH adsorption: (a) samples with 1.5 wt% waterglass, (b) samples with 2.0 wt% waterglass, (c) raw WIFA, BBA and AAW, (d) cumulative pore volume of capillary pore and gel pore. Mixture details can be found in **Table 3.2**.

The pore size distribution in the samples with normal curing is predominantly influenced by the additives employed. Specifically, the AAW-modified samples demonstrate high volumes of gel and capillary pores. This tendency is linked to the presence of low crystalline boehmite, as confirmed by XRD presented in **Fig. 3.1**. The higher gel content in AAW contributes to the lower permeability observed in AAW-modified samples, as illustrated in **Fig. 3.4**. In contrast, other additives contribute minimally to the volume of gel and capillary pores. Upon applying a higher dosage of waterglass, both pores and capillary pores in AAW-modified samples increase, with limited impact on other samples. This phenomenon is attributed to the dissolution of boehmite within AAW in an alkaline environment. Additionally, this observation elucidates the rationale behind the increased permeability of AAW-modified samples with higher waterglass dosage.

In the carbonated samples, a notable reduction in gel pores and capillary pores is observed in AAW-modified samples (DA1.5-c and DA2.0-c) after carbonation, whereas minimal changes are noted in other samples. The decrease in pore volume may stem from the “pore blocking” effect resulting from the formation of carbonates [205]. Additionally, a higher dosage of water induces an increase in gel pore volume due to the formation of silicate gel.

- **Macro-scale change**

After the carbonation process, a significant mass loss was observed in all specimens. This can be attributed primarily to the evaporation of free water during the carbonation. Moreover, based on the XRD and TG analysis, the absorbed CO_2 during the carbonation curing plays a crucial role in forming carbonates and the formation of monohydrocalcite also contributes to the bonding of free water in the matrix. To illustrate the complexities of these mass changes, a schematic representation is presented in **Fig. 3.9(a)**.

Subsequently, the calculation of CO_2 adsorption and newly bonded water in each mixture was carried out in accordance with the formulations presented by

$$M_t = M_{uc} - M_c \quad \textbf{(3.3)}$$

$$M_w = M_{uc} \times w_{uc} - M_c \times w_c \quad \textbf{(3.4)}$$

$$\varepsilon_{(CO_2 + \text{bound water})} = (M_w - M_t)/M_{uc} \quad \textbf{(3.5)}$$

where ε is the total CO_2 and bound water adsorption for each mixture, w_{uc} and w_c denote the moisture content from the uncarbonated and carbonated samples, respectively. Similarly, M_{uc} and M_c correspond to the total mass of the uncarbonated and carbonated samples, while M_w is the mass of the evaporated free water and M_t is the total mass change.

The results in **Fig. 3.9(b)** indicate that the overall mass change in the specimens is primarily associated with the chosen additives. Specifically, samples from the DW group exhibit a higher mass change in the overall adsorption of CO_2 and bound water. This outcome is ascribed to the augmented formation of monohydrocalcite within the DW group, as evidenced by the TG and DTG results in **Fig. 3.6**, resulting in higher bound water content. The application of a higher dosage of waterglass slightly amplifies each mass change, likely attributed to the presence of free water within the waterglass and its reaction with minerals, resulting in the formation of hydrates.

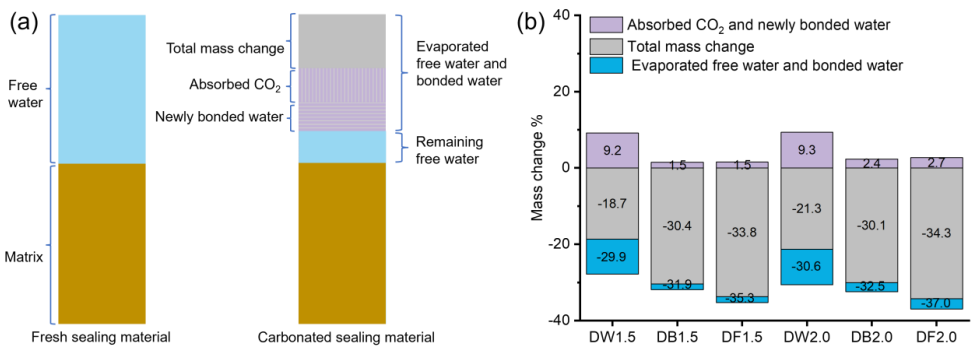

Fig. 3.9: (a) schematic of mass changes within the matrix (b) calculation of the mass change in each carbonated sample. (The negative value means the mass loss of the matrix).

3.3.4 Environmental impact

In addition to permeability, the leaching behavior of sealing materials represents a crucial consideration, particularly in mitigating soil pollution risks. Despite the common implementation of leachate collection systems in contemporary landfill infrastructure, the propensity for leaching in sealing materials subsequent to carbonation warrants thorough investigation [158]. In this study, we present the design and evaluation of sludge-based landfill sealing materials, with a particular focus on elucidating the leaching behavior of both uncarbonated and carbonated samples. Through systematic analysis, we aim to assess the potential environmental implications associated with these materials comprehensively.

Table 3.5 presents the leaching results obtained from both uncarbonated and carbonated samples. The leaching behavior of the formulated sealing materials is notably influenced by the carbonation process. Specifically, the leaching of various elements increases in the carbonated specimens, including chloride, cadmium, copper, nickel, lead, antimony, zinc, sodium, potassium, iron, and magnesium, aligning with findings from previous studies highlighting augmented leaching quantities of these elements in carbonated samples [206–208]. Of significance is the contrasting leaching behavior observed for certain elements, particularly sulfate and calcium, which show decreased leaching. The potential reason for the reduced sulfate leaching is the reaction with Ba^{2+}, leading to the precipitation of $BaSO_4$, while for Ca, it is the chemical binding within calcite or carbonates [209].

Table 3.5: Leaching results of uncarbonated and carbonated specimens (mmol/kg of dry raw material).

Elements	DW1.5		DB1.5		DA1.5		DW2.0		DB2.0		DA2.0		Limit*
	uc	c	uc	c	uc	c	uc	c	uc	c	uc	c	
Cl^-	420.1	**508.2**	164.6	210.9	150.8	216.8	**767.5**	**507.7**	174.5	219.7	125.8	106.2	422.5
SO_4^{2-}	86.86	79.45	75.17	76.96	103.1	85.91	151.5	98.95	99.80	89.46	147.9	128.5	208.3
As	0.009	0.006	0.007	0.009	0.004	0.007	0.011	0.008	0.010	0.012	0.006	0.009	0.027
Ba	0.002	0.002	0.001	0.001	0.001	0.001	0.002	0.002	0.001	0.001	0.001	0.001	0.728
Cd	0.002	0.007	-	-	-	-	0.002	0.004	-	-	-	-	0.009
Cr	-	0.001	-	0.001	-	-	-	-	-	0.001	-	-	0.192
Cu	0.077	0.152	0.007	0.110	0.003	0.029	0.050	0.230	0.027	0.079	-	0.013	0.787
Mo	0.026	0.016	0.016	0.017	0.010	0.014	0.030	0.024	0.014	0.018	0.005	0.010	0.104
Ni	0.005	0.007	0.005	0.009	0.004	0.008	0.006	0.011	0.005	0.009	0.008	0.012	0.170
Pb	0.011	0.013	0.015	0.017	0.009	0.020	0.012	0.021	0.012	0.022	0.020	0.023	0.048
Sb	**0.009**	**0.012**	0.003	0.004	0.004	0.005	**0.012**	**0.015**	0.005	0.005	0.002	0.002	0.006
Zn	0.015	0.038	0.011	0.019	0.007	0.017	0.020	0.044	0.008	0.025	0.002	0.012	0.765
Na	351.8	392.1	164.8	221.7	182.3	262.6	624.1	430.1	199.7	252.0	231.1	235.8	
K	113.7	121.5	43.61	53.60	31.08	43.69	180.8	116.6	45.37	54.17	24.16	22.69	
Ca	29.99	20.20	20.04	15.17	20.05	14.67	52.61	20.82	24.06	15.54	24.21	12.23	
B	0.441	0.390	0.445	0.385	0.412	0.457	0.546	0.447	0.445	0.382	0.545	0.417	
Fe	0.004	0.006	0.004	0.012	0.002	0.006	0.005	0.008	0.004	0.016	0.003	0.011	
Li	0.691	0.668	0.616	0.438	0.593	0.511	0.904	0.649	0.861	0.424	0.866	0.469	
Mg	21.11	24.50	13.58	15.93	12.62	16.52	22.73	27.19	16.77	17.21	11.45	12.06	
Sr	0.082	0.081	0.051	0.043	0.056	0.044	0.088	0.076	0.059	0.045	0.061	0.039	
pH	8.20	8.07	8.16	8.05	8.22	8.07	8.26	8.21	8.19	8.05	8.36	7.99	

uc = Uncarbonated sample, c = Carbonated sample. * - The Council Decision 2003/33/EC limits [210]. Underlined values are above the limits.

Compared with the permissible emission limits regulated by the European Council Decision 2003/33/EC [210], only the leaching of chloride and antimony levels in the DW group exceed the prescribed limits. The high leaching of these elements originates from the raw WIFA component (see **Appendix Table A.1**). Since chloride and antimony are leachable from the WIFA, a pre-treatment such as a washing process may be necessary and recommended before their use in the formulation of sealing materials. However, further efforts are needed to handle the resulting leachate from an environmental safety perspective. Overall, the potential for heavy metal pollution resulting from leaching after carbonation of the designed landfill sealing materials appears to be limited. The formulated DB and DA groups emerge as viable alternatives for preparing landfill sealing materials.

3.4. Discussions

3.4.1 Carbonation mechanism of sealing materials

In this study, an accelerated carbonation process has been utilized to investigate the impact of CO_2 released from decomposed organic waste in landfills on the permeability of sealing materials. Then, the degradation mechanism of impermeability is elucidated from both the chemical and physical perspectives. Despite the low permeability of the formulated sealing materials, the diffusion of CO_2 within the matrix is inevitable and leads to the formation of calcite and monohydrocalcite. Nishiyama et al. have demonstrated that the formation of monohydrocalcite typically necessitates its surroundings to be saturated with magnesium carbonate to prevent its dehydration to anhydrous calcium carbonate [211]. A similar equilibrium between monohydrocalcite and magnesium carbonate is also observed in some saline lakes [211]. Consistently, the formation of monohydrocalcite is more pronounced in the WIFA-modified samples, attributed to high leachable magnesium content from WIFA (see **Appendix Table A.1**), resulting in sufficient formation of magnesium carbonates. This is supported by the prominent peak of magnesium carbonates in XRD patterns observed in Carbonated DW samples, as depicted in **Fig. 3.10**.

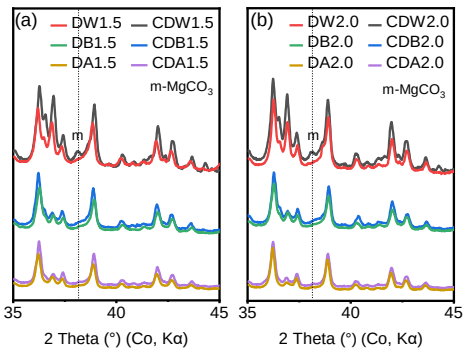

Fig. 3.10: The XRD pattern of all samples with 2 Theta range of 35° to 45° (m: $MgCO_3$ – PDF# 086-2346).

In terms of the long-term permeability of the sealing materials, one of the crucial factors is the volume stability of the matrix. When the carbonate formation results in volume expansion, the subsequent formation of monohydrocalcite leads to volume shrinkage. Therefore, leveraging both of these behaviors to offset volume changes appears to be a rational approach, ultimately

contributing to the stability of the matrix volume. Increasing the magnesium content of additives can promote monohydrocalcite production, potentially enhancing the volume stability of the sealing materials post-carbonation.

3.4.2 Limitations of the accelerated carbonation process

Due to the limited availability of relevant studies examining the potential impact of released CO_2 on the permeability of sealing materials, we have to choose an accelerated carbonation process commonly used in cement systems [212,213]. However, it is imperative to point out the differences between accelerated carbonation and the natural carbonation process within this context. The principal distinguishing factors are outlined in **Fig. 3.11**, encompassing gas types and concentrations, temperature, infiltration paths and free water evaporation. In the natural carbonation process, the simultaneous generation of CO_2 and CH_4 occurs during the biodegradation of organic waste materials. This biodegradation process leads to an escalation in greenhouse gas concentrations. Furthermore, the resultant exothermic chemical reactions frequently induce an elevated temperature within conventional landfill environments [214]. Studies have indicated temperature escalations from ambient levels to 38 ~ 54 ℃ after years of closure [215]. Additionally, because of the stratified configuration of the landfill cover system, gas migration predominantly occurs upward solely from the bottom surface during the natural carbonation process, differing from its diffusion pattern emanating from the perimeter towards the center in the accelerated carbonation process. Lastly, evaporation of sealing materials is inevitable within the carbonation chamber, whereas the sealing layer exhibits limited evaporation of free water as an internal layer in a compacted cover system. However, the influence of these differences on carbonation outcomes primarily resides in the rate at which carbonation penetrates, with fewer impacts on the composition and structure of the carbonation post-application. Free water evaporated from the surface will be replenished during the permeability test, rendering the observed permeability degradation in the experimental findings reliable. Overall, the decreased impermeability of the sealing materials (see **Fig. 3.4**) still complies with the requirements outlined in Dutch legislation concerning residues-based sealing materials used for landfill cover systems [155]. It should be noted that for an effective assessment of the long-term service viability of sealing materials, constructing an improved carbonation model that aligns with the actual carbonation process would be recommended, facilitating a more precise evaluation.

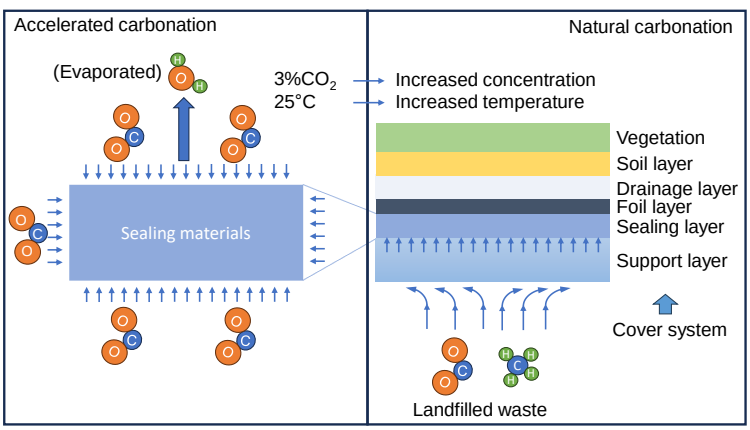

Fig. 3.11: Comparison of accelerated carbonation process and natural carbonation process.

3.4.3 The effect of waterglass and various additives on the sealing materials

Previous studies have highlighted the beneficial impact of waterglass in reducing the permeability of sealing materials [139]. However, these studies did not incorporate a wide range of additives, neglecting the potential interaction between waterglass and the diverse raw materials used in formulating sealing materials. The alkalinity inherent in waterglass can facilitate the dissolution of minerals, consequently diminishing the solid phase and leading to a decrease in the dry density of the compacted materials. Additionally, waterglass exhibits lower carbonation sensitivity, resulting in silica gel formation. The amorphous silicate gel possesses the capability to occupy voids within the matrix, which may elucidate the reason that higher dosages of waterglass tend to exhibit lower impermeability degradation after carbonation.

To enhance the recycling of industrial wastes from diverse sources, the study utilized a variety of waste materials to prepare sealing materials for performance evaluation. Notably, particle size and chemical composition are the key factors influencing the permeability. Particle size closely affects the compacted structure, as evidenced by the lowest permeability observed in the case of AAW. Meanwhile, chemical composition plays a crucial role in interactions with other components like waterglass and sewage sludge, leading to variations in gypsum formation levels. Moreover, the leaching behavior of these industrial wastes directly impacts the leaching behavior of final products.

3.5. Conclusions

The primary objective of this chapter is to assess the effects of carbonation on landfill sealing materials derived from various industrial by-products such as digested sewage sludge (DSS), waste incineration fly ash (WIFA), biomass bottom ash (BBA) and aluminum anodizing waste (AAW). The compacted layer materials were prepared as alternative landfill sealing materials and subjected to an accelerated carbonation process. The permeability, chemical and physical changes, and leaching behavior were analyzed in detail. Based on the results obtained, the following conclusions can be drawn:

- The landfill sealing materials, formulated with solid waste derived from Dutch industrial processes such as digested sewage sludge, waste incineration fly ash, biomass incineration fly ash, and aluminum anodizing waste, exhibit advantageous permeability properties conducive to their utilization as residual-based sealing layers in the final landfill cover system.

- Following the diffusion of CO_2, the permeability of sewage sludge-based sealing materials undergoes augmentation, concomitant with the formation of carbonates and monohydrocalcite. The formation of monohydrocalcite is likely influenced by the leachable magnesium content present in the raw materials. The observed degradation in permeability is likely ascribed to volume alterations induced by mineral carbonation processes. The organic content from the sludge is stable during the carbonation process, as evidenced by the minimal variation in TG curves.

- A higher dosage of waterglass mitigates the deterioration in permeability resulting from carbonation, a phenomenon attributable to the continued presence of silicate gel, which actively participates in filling the void spaces.

- Utilizing smaller particle sizes of industrial by-products in the fabrication of sealing materials is recommended due to its contribution to reduced permeability. Nevertheless, it is imperative to consider the leaching behavior of raw materials, as it influences the release of toxic elements. The impact of carbonation on the leachability of toxic elements is intricately linked to the nature of the raw materials employed. Hence, pre-treatment becomes essential when applying waste containing high levels of leachable toxic elements to mitigate potential environmental risks.

Chapter 4 Utilization of waste incineration filter dust in sodium carbonate-activated slag mortars

This chapter utilizes Waste Incineration Filter Dust (WIFD) as a green ingredient in a sodium carbonate-activated ground granulated blast furnace slag (GGBFS) system. WIFD is produced with a high portlandite and calcite content in municipal solid waste incineration (MSWI) plants. The reaction kinetics and reaction products of the system are analyzed through isothermal calorimetry, X-Ray diffraction (XRD), thermogravimetric analysis (TG-DTG), FT-IR, SEM/EDX, N_2 adsorption tests. The flowability and compressive strength of WIFD mixed samples are evaluated. The results show that the WIFD and Na_2CO_3 have a synergistic effect on the activation of GGBFS. The portlandite from WIFD could replace the pure $Ca(OH)_2$ and react with Na_2CO_3 to improve the alkalinity. The incorporation of WIFD accelerates the Na_2CO_3-activated GGBFS with the main products, including C-(A)-S-H gel, hydrotalcite and hemicarboaluminate. Besides, the calcite from WIFD is beneficial to form the hemicarboaluminate and decrease the porosity of the matrix. Though the mechanical performance of samples is reduced with more WIFD, it is still high enough for a potential application in construction with lower strength requirements. The results also confirm that GGBFS could be activated by WIFD and the addition of sodium carbonate helps the strength development and increases reaction speed. The work shows the potential of WIFD applying as a green building material.

This chapter is partially published elsewhere:

X. Ling, K. Schollbach, G. Liu, H.J.H. Brouwers, The utilization of waste incineration filter dust (WIFD) in sodium carbonate activated slag mortars, Construction and Building Materials, 313, 125494, 2021.

4.1 Introduction

In recent years, Alkali-activated materials have been widely investigated for their environmental, economic, and performance benefits, making them a promising alternative to traditional construction materials. The commonly used activators are sodium and potassium hydroxides and silicates. Despite these activators ensuring the high reactivity of the precursors and desirable mechanical properties, their high alkalinity raises concerns regarding handling safety issues and significant chemical shrinkage of the hardened binder. Therefore, some milder alkali activators have been investigated such as sodium carbonate (Na_2CO_3) and calcium hydroxide.

However, the activation of GGBFS by Na_2CO_3 is slow due to the lower initial pH compared to NaOH. Several works verified the slow reaction process of Na_2CO_3-activated GGBFS and unsatisfied early strength development during the early reaction period [55,63]. Hence, an accelerated setting time and improved early strength development are essential for Na_2CO_3-activated AAMs. Several approaches have been proposed to enhance the performance of Na_2CO_3-activated AAMs. For example, additives such as $Mg(OH)_2$ and MgO play the role of filler to decrease the porosity of the binder [216] [217]. Calcined layered double hydroxides [55], calcined dolomite [65], limestone powder [218] and $Ca(OH)_2$ [67,68] have been added in the Na_2CO_3-activated AAMs to accelerate the consumption of CO_3^{2-} ions and improve the initial pH value of the pore solution [219], consequently, early-age performance can be improved. Notably, the chemical method shows more effectiveness and efficiency in the early strength development of the binder. Compared to other calcined additives, $Ca(OH)_2$ and limestone draw more attention due to their low costs and wide distributions. However, the production of $Ca(OH)_2$ releases large amounts of CO_2 into the atmosphere due to the calcination of raw materials [220]. Therefore, the demand for proposing green and economic alternates as new additives in sodium carbonate-activated materials to enhance early age reaction is required.

The calcium hydroxide and calcite may play the role of accelerator for enhancing the reaction process of Na_2CO_3-activated GGBFS based on the above research review. Therefore, it is possible and convenient to apply WIFD in Na_2CO_3-activated GGBFS as a green and low-cost additive. Nearly 5 kt/yr of WIFD were produced per year for air pollution control in the incineration plants in the Netherlands. Because of the relatively low production of WIFD compared with the alkali-activated slag binders, all WIFD could be recycled while using the optimal content of 5 wt%. The reuse of the WIFD in the AAMs has advantages both in cost and energy savings, CO_2 emission and waste management.

In this chapter, the early reaction of Na_2CO_3 and portlandite from WIFD was designed to improve the alkalinity of the pore solution, which is beneficial for early strength development. The influences of Na_2CO_3 and WIFD on alkali-activated GGBFS were investigated. The couple effects of Na_2CO_3 and WIFD on the reaction products, reaction kinetics and mechanical properties of this cement-free binder were investigated. The X-ray diffraction (XRD), thermo-gravity (TG), Fourier transform infrared spectroscopy (FT-IR) and the Scanning Electron Microscope (SEM) with EDX analysis were conducted. The related results can provide a new application of WIFD in sodium carbonate-activated materials.

4.2 Materials and Experiments

4.2.1 Raw materials

Ground granulated blast furnace slag (GGBFS) used in this study was provided by Heidelberg Materials Benelux, Netherlands. The waste incineration filter dust (WIFD) in **Fig. 4.1(a)** was provided by Euro Trust Management, Netherlands. The chemical compositions of raw materials were measured using X-ray fluorescence (PANalytical Epsilon 3) and are shown in **Table 4.1**. Sulphur and calcium are the main elements in WIFD. The mineral compositions in **Fig. 4.1(b)** show that the main crystalline phases of WIFD are calcite (PDF#47-1743), portlandite (PDF#44-1481) bassanite (PDF#24-1068) and dolomite (PDF#73-2409). The portlandite and calcite amounts are 36.38 wt% and 37.43 wt%, respectively, calculated from TG results in **Fig. 4.2**, which accounts for the high LOI of WIFD. The particle size distributions of GGBFS and WIFD are shown in **Fig. 4.3**. The average particle size of GGBFS and WIFD is around 13 µm. The chemical composition of the leachates obtained from WIFD via one batch leaching test is presented in **Table 4.2**. The high Ca^{2+} and SO_4^{2-} concentrations are coherent with the XRF results. Na_2CO_3 (powder, analytical grade, supplied by Sigma-Aldrich) was used to prepare the activator.

Table 4.1: Chemical compositions of raw materials.

Chemical Composition	WIFD	GGBFS
Na_2O	0.15	-
MgO	0.73	9.02
Al_2O_3	0.20	13.09
SiO_2	0.59	31.24
SO_3	6.51	5.15
K_2O	0.21	0.29
CaO	53.97	38.56
TiO_2	0.02	1.30
Fe_2O_3	0.07	0.67
Cl	0.62	0.04
LOI%	36.24	0.64
Surface area (m^2/g)	25.1	1.00
Specific density (g/cm^3)	2.32	2.93

*LOI = loss on ignition at 1000 C for 2 h.

Table 4.2: Leaching behavior of WIFD obtained via a one-batch leaching test (mg/kg).

Elements	K	Ca	Na	Mg	Ba	Sr	Zn	NO_3^-	SO_4^{2-}	Cl^-	pH
WIFD	1360	17510	2280	0.21	3.5	70.29	1.14	310	13430	5910	12.98

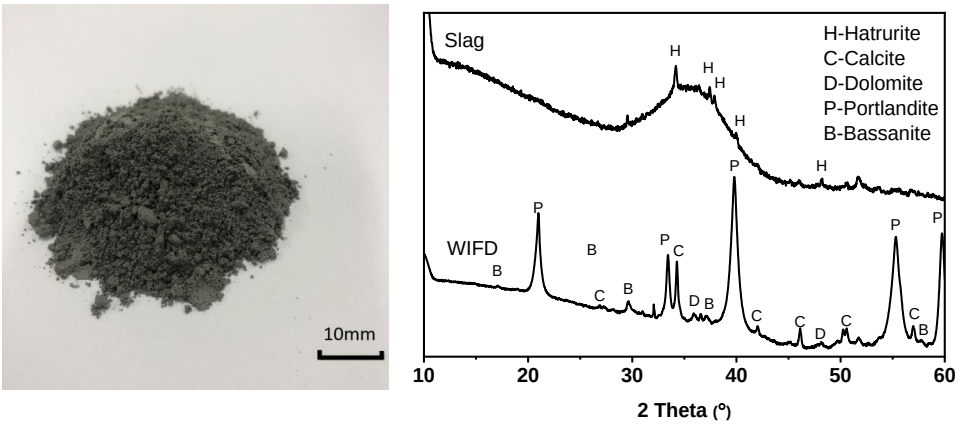

(a) (b)

Fig. 4.1: Raw material and XRD pattern of Waste incineration filter dust (WIFD) and GGBFS.

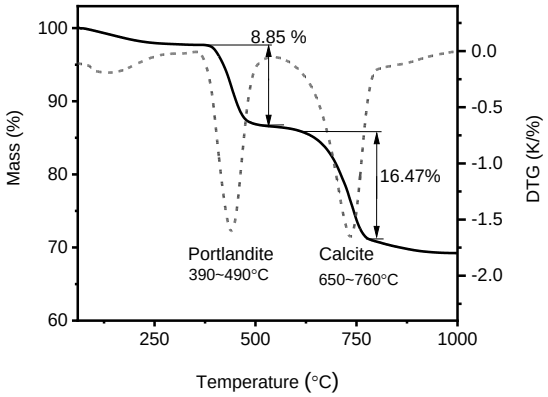

Fig. 4.2: TG and DTG curves of Waste incineration filter dust.

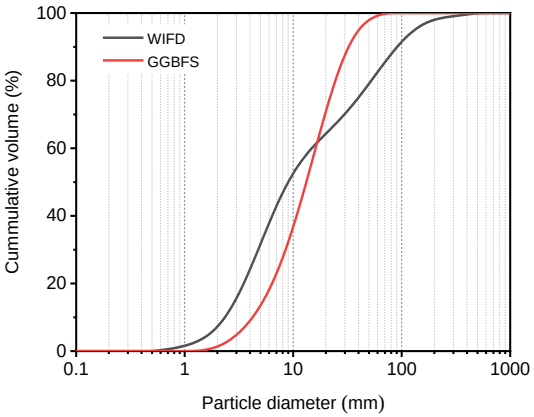

Fig. 4.3: Particle size distribution of each raw material.

4.2.2 Sample preparation

Two sets of paste and mortar samples were prepared according to the mix proportions in **Table 4.3**. To reveal the influences of WIFD on the performance of sodium carbonate-activated GGBFS, In the first set the amount of Na_2CO_3 was 8 wt% (equivalent sodium oxide (Na_2O) content of 4.6 wt% by weight of binder), while the amount of WIFD was from 0 wt%, 5 wt%, 10 wt%, 15 wt% to 20 wt%. To reveal the effects of Na_2CO_3 concentration on GGBFS-WIFD binder systems, the second set was prepared as follows, the amount of WIFD was kept constant (10 wt%) and the amount of Na_2CO_3 was varied (2.3 wt%, 4.6 wt% and 6.9 wt% of total mass of WIFD and GGBFS). The water/binder ratio by mass was 0.5 for the paste and 0.6 for the mortar to meet the water demand of the fine aggregates. The sand-to-binder ratio was 3.0 for mortar samples.

All the samples were mixed in a laboratory mixer. The binder and sand were well dispersed and then the water was added at a low speed for 30 s. Then stop the mixer for 30 s to stir the bottom specimens. After another 120 s mixing at a medium speed, the samples were poured into 40×40×160 mm^3 styrofoam molds and vibrated for 1 min. After 1 d curing, the specimens were demolded and sealed with plastic films, then stored under laboratory conditions with 50% RH and 20 °C.

Table 4.3: Mix proportions of paste and mortar specimens.

Sample	Na_2CO_3 wt% / (Na_2O wt%)	Waste/g	Slag/g	Sand/g	w/b
N8W0	8 (4.6)	0	100	0 (paste)	0.5 (paste)
N8W5	8(4.6)	5	95		
N8W10	8(4.6)	10	90		
N8W15	8(4.6)	15	85		
N8W20	8(4.6)	20	80	300 (mortar)	0.6 (mortar)
N0W10	0(0)	10	90		
N4W10	4(2.3)	10	90		
N12W10	12(6.9)	10	90		

4.2.3 Methodology

- **Isothermal calorimeter**

The reaction kinetics were determined by an isothermal calorimeter (TAM Air, Thermometric) at 20°C. The raw material was first mixed in a bottle according to the paste mixture. Then the water was added, and the content was mixed with a vortex mixer. The mixed paste was injected into a sealed glass ampoule and loaded into the calorimeter for 6 d. The heat release and heat flow results were normalized by the mass (g) of the binder.

- **Leaching test**

To assess the leaching potential of the WIFD, a one-batch leaching test was employed according to NEN-EN12457-4. WIFD powder and distilled water were mixed in a polyethylene bottle with a solid-to-liquid mass ratio of 1/10. The bottle was placed horizontally on a liner reciprocating shaking device (Stuart SSL_2) at a rate of 250rpm for 24 h. Then the leachate

samples were filtered with a 0.2 um PTFE filter and acidified with ultrapure nitric acid. The leaching analysis was conducted with ion chromatography (IC) and inductively coupled plasma optical emission spectroscopy (ICP-OES).

- **Phase assemblage analysis**

The phase composition of paste samples was characterized by X-ray diffraction (XRD), thermal gravity (TG) and Fourier transform infrared spectroscopy (FT−IR). The paste samples were broken into small pieces by an iron hammer and immersed into isopropanol to stop the hydration process for 24 h. Then the samples were dried at 60 °C for 24 h and grounded in an agate mortar until passing the 75 μm sieve for further analysis.

The dried powder samples were measured by a Bruker D4 phaser instrument with a step size of 0.02° and a 2θ range from 10° to 90° (Co-K_{α}, 40 kV, 30 mA).

The thermo-gravimetric (TG) test was conducted using a STA 449 F1 instrument under N_2 atmosphere at a heating rate of 10 K/min up to 1000 °C. Differential thermo-gravity (DTG) results are calculated from thermo-gravity (TG). The quantification of calcite and $Ca(OH)_2$ content was calculated by using the mass loss during different decomposition temperature ranges in TG, for example, 600°C to 850 °C for calcite [151], and 390°C to 500°C for $Ca(OH)_2$ [221].

Fourier-transform infrared (FT-IR) spectroscopy was conducted by using the Varian 3100 instrument to identify the bonding in the mineral phases and the amorphous contents in samples with the wavenumber range of 4000–400 cm^{-1}.

- **Fresh behavior and mechanical test of mortars**

The flowability of the fresh mortars was determined using the mini spread flow table test according to EN 1015-3:2007.

The mechanical properties of the mortar are studied according to EN 196-1:2016. The samples covered by the plastic film with a size of 40×40×160 mm^3 curing at ambient temperature were tested at a loading rate of 2400 N/s for compressive strength after 7 d, 28 d and 91 d. Compressive strength tests were conducted on 6 specimens for each mixture.

- **Microstructure analysis of reaction products**

The microstructure of paste samples after 28 d of curing was observed by using a Scanning Electron Microscope with EDX (15KV) detector (Phenom Pro). The crushed samples were immersed in isopropanol to stop the reaction process and dried at 40 °C for 24 hours. Afterward, the samples were embedded in resin and polished with grinding papers. The polished surface was then coated with Au by using Quorum 150TS plus sputter coater.

The Nitrogen adsorption analysis of dried samples was conducted by using TriStar II 3020, Micrometrics. The powder samples (< 400 um) were dried at 105°C until the mass was constant before the test. The gel pore size distribution was calculated from the adsorption branch by the Barrett - Joyner - Hallenda method [140].

4.3 Results and Discussions

4.3.1 Flowability of NC-WIFD-GGBFS mortars

The flowability of the fresh mortars is shown in **Fig. 4.4**. The N8W0 shows a satisfied flowability of 250 mm. After the WIFD gradually replaced the GGBFS, the workability of mortar decreased significantly. The high surface area of WIFD compared to GGBFS induces a high water demand for blends. On the other hand, the increase of Na_2CO_3 in the activator also reduced the workability of mixtures containing 10 wt% of WIFD. It can be seen in **Fig. 4.5**, that the sample without Na_2CO_3 shows a flowability of 180 mm, and it gradually decreased to 130 mm when Na_2CO_3 increased to 12 wt%. The increased Na_2CO_3 dissolved in the solution would accelerate the calcium consumption in the pore solution and promote the formation of carbonates. The increased precipitation of carbonates inhibits the flow of mortars. The above results indicate that the addition of Na_2CO_3 and WIFD reduces workability due to the fast precipitation reaction between Na_2CO_3 and the high surface area of WIFD. It is worth noting that the heat released during the initial precipitation and the accompanying heat from mineral dissolution, which occur before the system stabilizes in the calorimeter test, cannot be effectively detected.

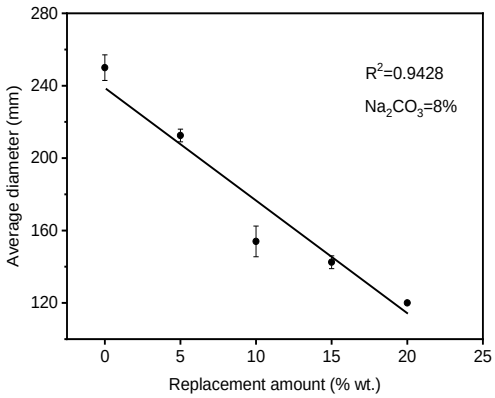

Fig. 4.4: Spread flow diameter of 8 wt% Na_2CO_3 activated GGBFS mortars containing WIFD.

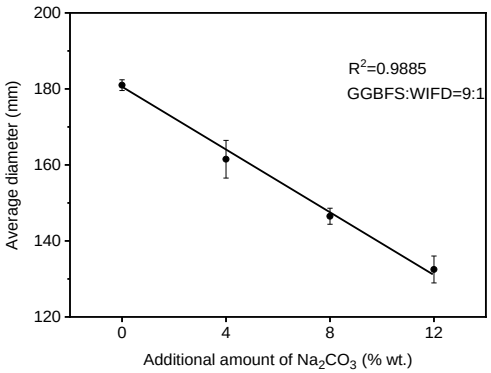

Fig. 4.5: Spread flow diameter of the GGBFS-WIFD mortars activated by different amounts of Na_2CO_3.

4.3.2 Reaction kinetics of NC-WIFD-GGBFS blends

To investigate the effects of WIFD and Na_2CO_3 on the reaction process of various mixtures, the calorimeter test was conducted, and the results are shown in **Fig. 4.6**. As can be seen, the increased WIFD in mixtures accelerates the reaction process, reducing the duration of the induction period. In N8W0, two exotherm peaks occur at around 4 h and 60 h after the initial peak caused by particle wetting and dissolution. The first small exotherm peak could be attributed to the formation of gaylussite ($Na_2Ca(CO_3)_2$•$5H_2O$) and calcite, which are general reaction products in sodium carbonate-activated GGBFS system [222]. The second main exotherm is assigned for the formation of C-(A)-S -H type gel as the main reaction products in the sodium carbonate-activated GGBFS system [222]. It takes nearly 2 d for sodium carbonate-activated slag to reach the heat flow peak, which is consistent with some previous results that show even longer retardation when only Na_2CO_3 was used in the activator [223,224].

However, the heat flow curves become quite different and only one exotherm peak could be found after incorporating WIFD. The time to reach the main exotherm peaks was reduced to 9.79 h and 2.31 h when incorporating 5 wt% and 10 wt% WIFD, respectively. Then the reaction process shows no more significant improvement after the amount of WIFD is higher than 10 wt%; for example, N8W15 takes 1.65 h and N8W20 takes 1.56 h to reach the main exotherm peak. The main reason is the amount of Ca^{2+} provided by the dissolving portlandite in WIFD is higher than the amount of Na_2CO_3 and the system becomes oversaturated. Nevertheless, the cumulative heat of each mixture increases with higher amounts of WIFD in the reaction as summarized in **Table 4.4**. Therefore, WIFD acts as an extra activator to accelerate the reaction process and shows the potential to be effectively applied in the Na_2CO_3-activated GGBFS.

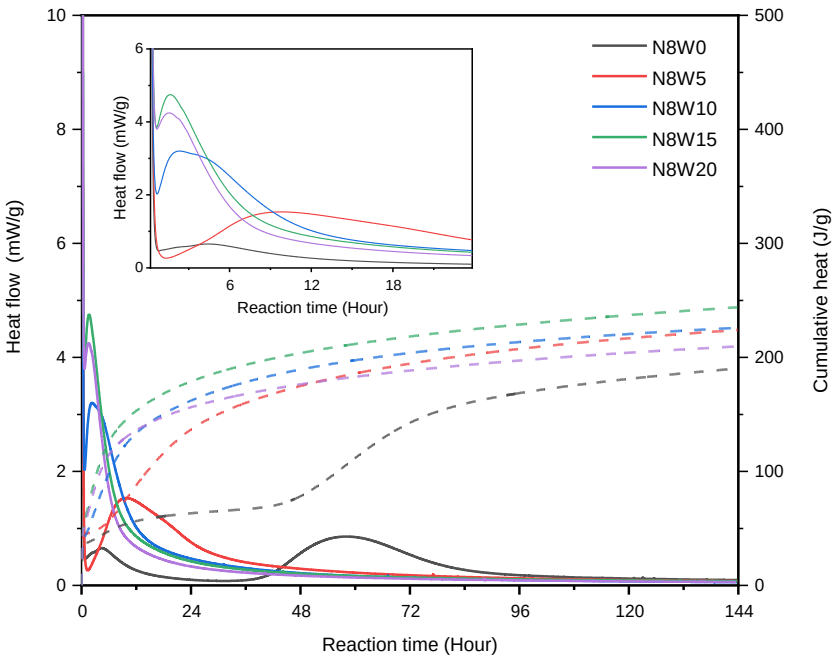

Fig. 4.6: Heat release of the Na_2CO_3 activated GGBFS with different WIFD replacements from 0 wt% to 20 wt%.

The effect of Na_2CO_3 content on the reaction process of GGBFS-WIFD blends is shown in **Fig. 4.7**. N0W10 also shows a prolonged induction period, which is similar to the sample N8W0. It shows two exotherm stages at around 24 h and 51 h, respectively. The first exotherm as seen arrow can be induced by the formation of ettringite due to the existence of SO_3 and aluminate in raw materials. Then the main exotherm around 51 h is attributed to the formation of C-(A)-S-H gel and hemicarboaluminate as seen in **Fig. 4.9(b)**. This indicates that only WIFD also can effectively activate GGBFS, which plays the role of activator. However, the pH it generates in N0W10 is lower because the OH^- provided by portlandite is limited, leading to a slower reaction process at early ages, which is consistent with the reported work about calcium hydroxide-activated GGBFS [225].

In contrast to N0W10, incorporating Na_2CO_3 (N4W10, N8W10 and N12W10) results in only one exotherm followed by a small shoulder. The main peak is attributed to the formation of C-(A)-S-H gel and the small shoulder is probably a result of the other reaction products including hemicarboaluminate and hydrotalcite. The additional Na_2CO_3 accelerated the reaction through the fast reaction with portlandite, and then the formation of sodium hydroxide; consequently, the reduction of time to reach the maximum hydration peak can be observed in Table 4. Meanwhile, the 144h cumulative heat increases from 149.16 J/g in N4W10 to 244.89 J/g in N12W10. It could be explained that more GGFBS can be activated when more Na_2CO_3 content is applied. However, the 144h cumulative heat of N4W10 is lower than that of N0W10 (154.36 J/g) which could be explained by additional heat generated by the ettringite formation. The additional Na_2CO_3 in N4W10 probably induces the formation of calcium carbonates rather than the ettringite. To conclude, a synergistic effect between Na_2CO_3 and WIFD can be spotted during the activation of GGBFS. The presence of WIFD effectively overcomes the retardation effects of Na_2CO_3-activated GGBFS.

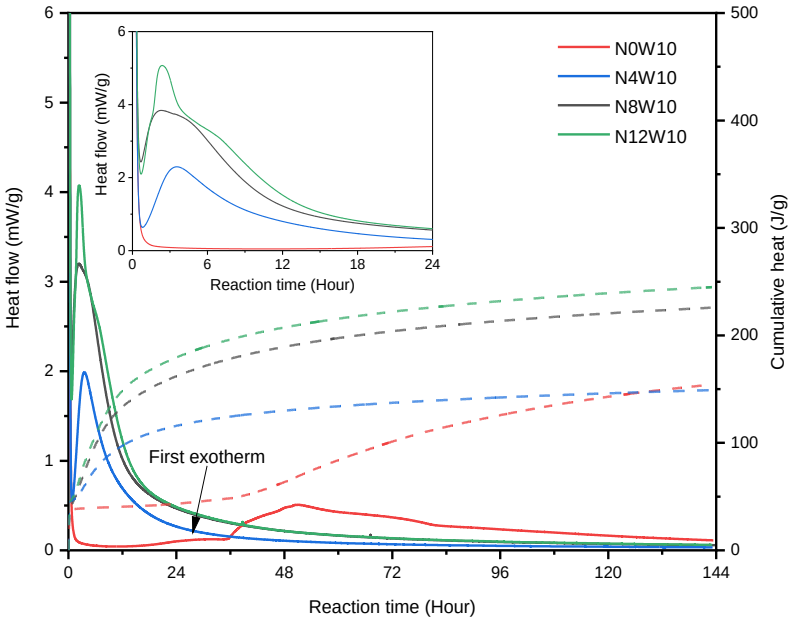

Fig. 4.7: Heat release of the 90 wt% GGBFS and 10 wt% WIFD blended binder with the additional amount of Na_2CO_3 from 0 wt% to 12 wt%.

Table 4.4: Summary of cumulative heat of samples at 144 h.

Group	Time (h) (to reach the heat flow peak)	Cumulative heat at 144 h (J/g slag)
N8W0	58.06	190.40
N8W5	9.79	224.05
N8W10	2.31	225.96
N8W15	1.65	243.93
N8W20	1.56	209.55
N0W10	51.15	154.36
N4W10	3.53	149.16
N8W10	2.31	225.96
N12W10	2.38	244.89

4.3.3 Reaction products identification of NC-WIFD-GGBFS blends

- **XRD analysis**

The X-ray diffraction patterns of Na_2CO_3-activated GGBFS samples with different WIFD replacement ratios after 28 d of curing are shown in **Fig. 4.8(a)**. The main crystalline phases in samples are hydrotalcite ($Mg_6Al_2CO_3(OH)_{16}\cdot 4H_2O$) (PDF#89-0460), calcite (PDF#72-1937), dolomite (PDF#75-1759), hemicarboaluminate (PDF# 41-0221) and dolomite (PDF#75-1759), along with the portlandite ($Ca(OH)_2$) and calcite (PDF#72-1937) from the WIFD. Only the reference (N8W0) contains gaylussite ($Na_2Ca(CO_3)_2\bullet 5H_2O$) (PDF#74-1235), which is not observed in samples N8W5-N8W20, indicating that the increased WIFD may inhibit the formation of gaylussite. After 28 d of curing, the increased intensity of hemicarboaluminate, hydrotalcite, calcite, and dolomite in each sample indicates that the increasing WIFD content promotes the formation of carbonates in the reaction system. Notably, C-(A)-S-H gel, which is known to be produced as the main reaction product in the alkali-activated GGBFS with low crystallinity, is difficult to distinguish in XRD patterns [226]. Additionally, the main specific peak overlaps with that of calcite around 34.2º(2θ).

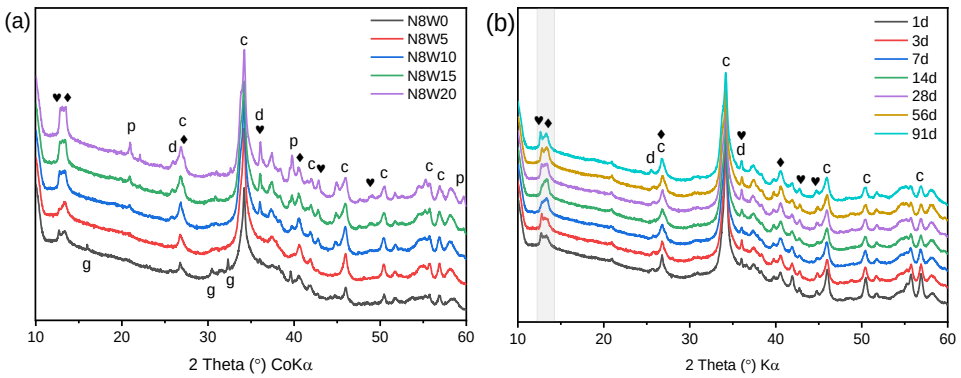

Fig. 4.8: (a) XRD patterns of samples with different replacement of WIFD after 28 d curing, (b) XRD patterns of sample N8W10 at different curing ages (c-Calcite, d-Dolomite p-Portlandite, ♥-Hemicarboaluminate, ♦ - Hydrotalcite, g- Gaylussite).

Fig. 4.8(b) shows the reaction product of N8W10 at different ages. The main phase composition in N8W10 shows little difference after a 1 d reaction, as the main reaction has taken place after 24h from the calorimetric test results shown in **Fig. 4.6**. The main reaction products are the same as mentioned above. However, the intensity of the specific peaks of hemicarboaluminate and hydrotalcite shows a variation at a late age.

The effects of Na_2CO_3 content on reaction products of mixtures containing 90 wt% GGBFS and 10 wt% WIFD after 28 d of curing are shown in **Fig. 4.9(a)**. The main reaction products are calcite, dolomite, ettringite, hydrotalcite and hemicarboaluminate in the sample of blended GGBFS and WIFD without Na_2CO_3 (N0W10), which confirms the activation effect of WIFD on the GGBFS. After the Na_2CO_3 was applied in the activator, the peaks of ettringite were not observed in mixtures(N4W10-N12W10).

Fig. 4.9(b) shows the XRD patterns of sample N0W10 at different curing ages. The peaks of ettringite and calcite are identified after 1 d of reaction, which may contribute to the first exotherm in N0W10 at around 24 h in the calorimetric test results in **Fig. 4.7**. Then hemicarboaluminate and dolomite were observed in the sample after 3 d reaction in the XRD patterns, which may also contribute to the main exotherm in N0W10 around 51 h in **Fig. 4.7**. Then the peak intensity of hydrotalcite gradually increases from 7 d to 91 d, which confirms the ongoing reaction process. The peak of Ikaite (PDF#75-1733) is not particularly sure due to its low intensity and the overlap with other minerals.

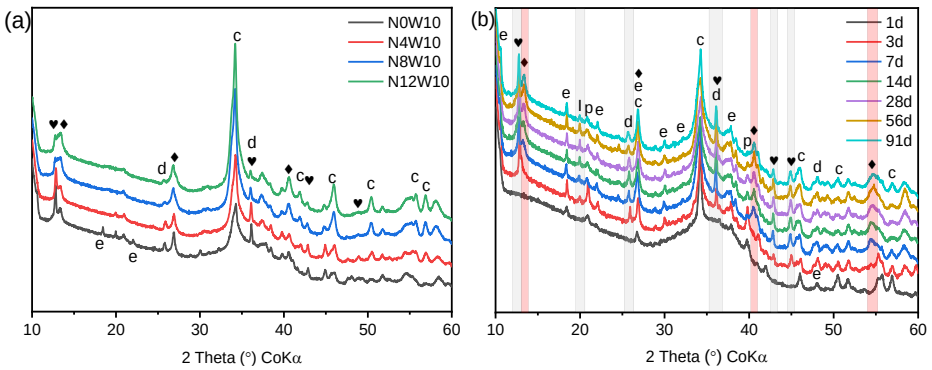

Fig. 4.9: (a) XRD patterns of samples with additional Na_2CO_3 after 28 d curing, (b) XRD patterns of sample N0W10 at different curing ages (c-Calcite, d-Dolomite, ♥- Hemicarboaluminate, ♦ - Hydrotalcite, e-Ettringite, I- Ikaite). (Peaks marked grey and red first appear after 3 d, 7 d respectively).

- **FT-IR analysis**

The phase assemblage of reaction products after 28 d curing was characterized by FT-IR and the results are shown in **Fig. 4.10**. The content of WIFD shows no significant influence on the FT-IR results of reaction products as shown in **Fig. 4.10(a)**. The broad bands centered around 3405 cm^{-1} and 1649 cm^{-1} present the stretching and bending mode of the H–OH bond in the samples. These resonances may be caused by the bound water or interlayer water from gaylussite or C-(A)-S-H gels [227]. The absorption peaks at 1414 cm^{-1} and 874 cm^{-1} originate from the vibration of v_3 [CO_3^{2-}] and v_2 [CO_3^{2-}] respectively, which is coherent with the formation of calcite, hydrotalcite and hemicarboaluminate during the reaction. The sharp peaks at around 973 cm^{-1}, 817 cm^{-1} and 664 cm^{-1} in the spectrum represent the Si-O asymmetric

stretching vibration and Si-O-Si bending vibration in the C-(A)-S-H gel [228,229]. Besides, both the increased Na_2CO_3 and WIFD content result in a sharper peak at around 817 cm^{-1}, indicating the formation of C-(A)-S-H gel [228]. The band centered around 1130 cm^{-1}, which is assigned to the v_3 [SO_4^{2-}], is getting more intense in **Fig. 4.10(a)** due to the increased WIFD content providing more sulfate ions. The gradually disappearing band centered at around 892 cm^{-1} is due to the presence of TO_4 (T is Si or Al) from the original slag [63,230], which was decreased after more slag was reacted. The results of 90 wt% GGBFS and 10 wt% WIFD blended samples activated by different amounts of Na_2CO_3 are shown in **Fig. 4.10(b)** and exhibit similar resonances. Notably, Si-O stretching in C-(A)-S-H gel is shifted from 960 cm^{-1} to 936 cm^{-1}, indicating the decreased polymerization of C-(A)-S-H gel due to the lower proportion of GGBFS in the mixture.

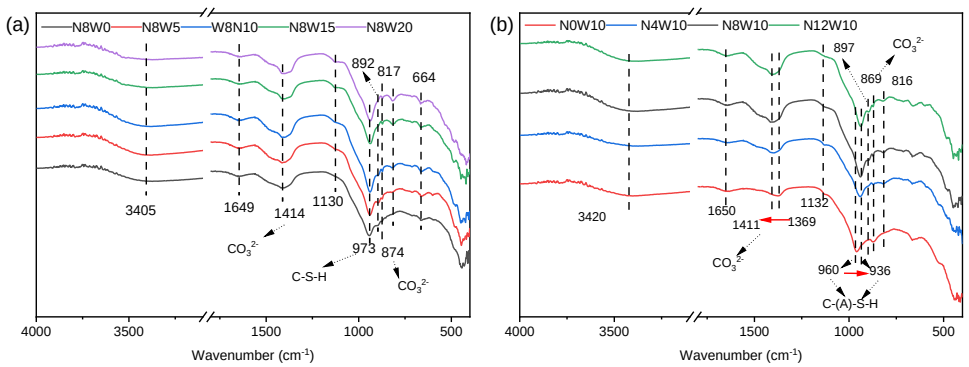

Fig. 4.10: FT-IR spectrum of mixtures after 28 d: (a) with different amounts of WIFD and (b) with different amounts of Na_2CO_3.

- **TG-DTG analysis**

Fig. 4.11 shows the TG-DTG results of Na_2CO_3-activated GGBFS samples with different WIFD replacements after 3 d. The first peak of DTG curves between 40 ºC and 240 ºC is associated with the dehydration of C-(A)-S-H gel, hemicarboaluminate and hydrotalcite. Notably, a distinct peak around 120 ºC is assigned to the dehydration of gaylussite [63], which is coherent with the observation with XRD results (**Fig. 4.8(a)**), where the N8W0 is the only sample containing gaylussite. The small shoulders at around 200ºC are caused by the loss of the bound water from hydration products like hydrotalcite and hemicarboaluminate [231]. The portlandite from WIFD, visible in the XRD results, is supposed to decompose at around 430 ºC. However, it's pretty difficult to identify the mass loss of portlandite due to the decarbonation of hydrotalcite that also occurs at 400 ~ 650 ºC [232]. Besides, the portlandite would be consumed over time by the reaction with Na_2CO_3. The weight loss of around 700 ºC is induced by the decarbonation of calcite originating from the raw material WIFD, as seen in the TG results in **Fig. 4.2**. The weight loss of around 800 ºC is related to the decarbonation of carbonates which are newly formed or from the thermal decomposition of hydrotalcite or hemicarboaluminate during the TG test [233].

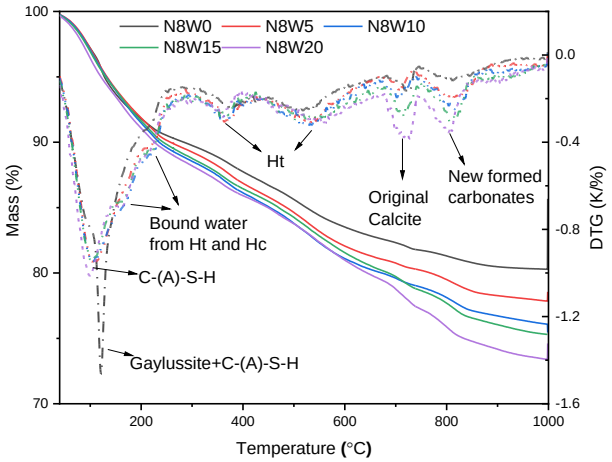

Fig. 4.11: TG-DTG curves of reaction products with different WIFD replacements after 3 d (Ht-Hydrotalcite, Hc-Hemicarboaluminate).

Table 4.5 summarizes the mass loss of the different phases at different temperature ranges. To evaluate the amount of the formation of C-(A)-S-H gel, the mass loss between 40 ºC and 150 ºC is treated as bound water from the gel. Here the bound water from gaylussite which is only found in N8W0 is also included. Therefore, the calculated bound water in N8W0 would be higher than the theoretical value. As can be seen, the increased amount of bound water from 3 d to 91d confirms the reaction process and the formation of hydration products. Theoretically, incorporating WIFD would decrease the bound water due to the reduced proportion of GGBFS in the mixture. However, the amount of bound water in N8W5-N8W20 is almost similar, indicating a higher reaction degree of GGBFS with more WIFD. Besides, the formation of hydrotalcite (400 ~ 650 ºC) and hemicarboaluminate (as newly formed in **Table 4.5**) increases when more WIFD is incorporated. Then the mass loss between 650 ºC and 760 ºC is caused by the decarbonation of calcite from the WIFD, which is marked as original calcite in the WIFD (**Fig. 4.2**). Using the TG data from pure WIFD, it is possible to calculate the theoretical quantity of calcite from WIFD for each mixture. The amount of original calcite after hydration is lower than the theoretical amount due to the formation of hemicarboaluminate and hydrotalcite. To conclude, though the incorporation of WIFD decreases the proportion of GGBFS, it promotes the reaction degree of GGBFS and the formation of hydrotalcite and hemicarboaluminate.

Table 4.5: Weight loss (wt%) of each phase with the temperature range.

Group	Dehydration of Bound water 40~150 ºC			Decarbonation of Hydrotalcite 400~650 ºC			Decarbonation of Carbonates 650~760 ºC			Calcite from WIFD	Newly formed carbonates 760~850 ºC		
	3d	28d	91d	3d	28d	91d	3d	28d	91d		3d	28d	91d
N8W0	6.1	8.4	17.4	0.6	0.6	0.4	0.3	0.2	0.1	0	0.5	0.1	0.1
N8W5	5.7	8.4	16.8	1.2	1.4	1.1	0.2	0.2	0.2	0.5	1.0	1.1	0.2
N8W10	5.8	7.9	15.1	1.3	1.6	1.3	0.3	0.3	0.3	1.0	0.9	1.4	0.7
N8W15	5.7	7.7	16.4	1.7	1.5	1.1	0.5	0.6	0.3	1.6	1.2	1.3	1.2
N8W20	6.2	7.1	15.2	1.5	1.4	0.9	0.9	1.1	0.4	2.1	1.1	1.0	1.4

Note: TG-DTG curves of 28d and 91d samples are presented in **Appendix Fig. B.1**.

Fig. 4.12 shows the TG-DTG results of mixtures with different amounts of Na_2CO_3 at the curing ages of 3 d. The dehydration of the ettringite in mixture N0W10 is not visible because it overlaps with the dehydration of the C-(A)-S-H gel. The shoulder around 155 ºC is due to the dehydration of hydrotalcite. The mass loss around 450 ºC is only visible in N0W10 and is attributed to the portlandite from WIFD, which confirms the low reaction speed of mixture N0W10 at 3 d. The other mass loss is the decarbonation of carbonates as mentioned above.

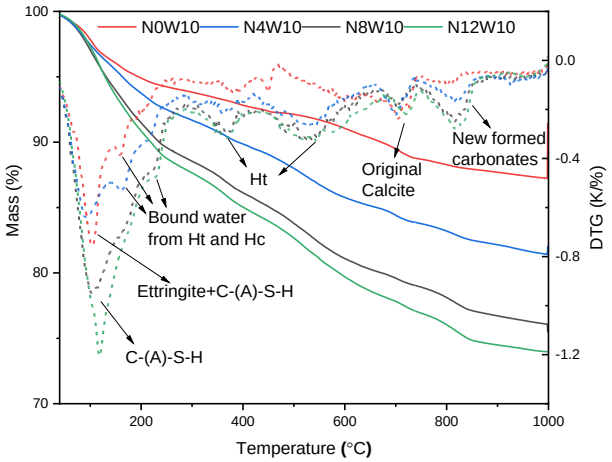

Fig. 4.12: TG-DTG curves of reaction products with different amounts of additional Na_2CO_3 after 3 d (Ht-Hydrotalcite, Hc-Hemicarboaluminate).

Table 4.6 summarizes the mass loss of different phases at different temperature ranges. As can be seen, the bound water at 3d in N0W10 and N4W10 is relatively lower than that in N8W10 and N12W10, which is coherent with low reactivity at an early age in the calorimetric test. However, it shows a higher amount of bound water at 91 d in N0W10 than in N4W10 due to the formation of ettringite. With more Na_2CO_3 incorporated, the formation of hydrotalcite and hemicarboaluminate is increased, while the amount of calcite from the WIFD decreases in the samples. In general, Na_2CO_3 also plays a significant role in activating 90 wt% GGBFS and 10 wt% WIFD blends, which improve the alkali concentration by the reaction with portlandite in WIFD. Besides, Na_2CO_3 promotes the consumption of calcite from WIFD to form the hemicarboaluminate and hydrotalcite [63].

Table 4.6: Weight loss of each phase with the temperature range (by percentage).

	Dehydration of Bound water 40~150 ºC			Decarbonation of Hydrotalcite 400~650 ºC			Decarbonation of Carbonates 650~760 ºC			Calcite from WIFD	Newly formed carbonates 760~850 ºC		
	3d	28d	91d	3d	28d	91d	3d	28d	91d		3d	28d	91d
N0W10	3.6	5.3	17.2	0.7	0.9	0.1	0.7	0.4	0.2	1.1	0.2	0.5	0.6
N4W10	4.1	5.0	6.0	1.4	1.2	1.1	0.5	0.6	0.3	1.1	0.7	0.2	0.9
N8W10	5.8	7.9	15.0	1.3	1.6	1.3	0.3	0.3	0.3	1.0	0.9	1.4	0.7
N12W10	6.0	8.0	16.9	1.4	1.9	0.7	0.2	0.2	0.2	1.0	1.0	1.5	1.8

Note: TG-DTG curves of 28d and 91d samples are presented in **Appendix Fig. B.2**.

4.3.4 Gel microstructure

The morphology of the mixtures with different replacement levels of WIFD at 28 d and element compositions of reaction products are studied using SEM & EDX (**Fig. 4.13**). Notably, unreacted slag particles still exist in the inner matrix as seen in polished samples. The flaky structures could be hydrotalcite [234]. Further details about the reaction products were determined through EDX spot measurements to determine the element composition on the polished surface. The results are summarized in **Fig. 4.14**. According to a study on a model for the C-A-S-H gel, the Ca/Si ratio is between 0.86 to 1.21 and the Al/Si ratio is between 0.22 to 0.42 in alkali-activated GGBFS [235]. The initial Ca/Si and Al/Si ratio in GGBFS, according to the chemical composition in Table 1 was calculated to be around 0.96 and 0.36, which is similar to those ratios in the C-A-S-H gel. However, there is no Na content in GGBFS, which helps distinguish it from the reaction products, as seen in **Fig. 4.14**. Besides, the formation of hydrotalcite and calcite or dolomite according to the XRD results may lead to higher Al/Si and Ca/Si ratios, respectively, as indicated by the direction of arrows for the red spots in **Fig. 4.14**. The formation of ettringite in N0W10 also leads to a higher Al/Si and Ca/Si ratio. Some spots around the unreacted GGBFS still contain sodium which indicates the potential formation of N-A-S-H gel.

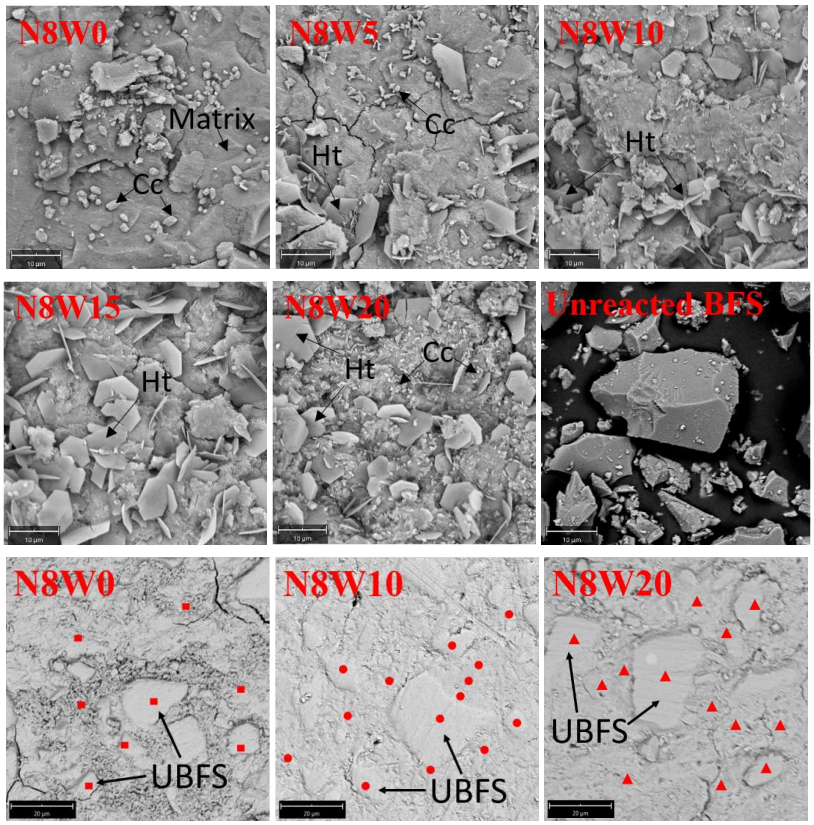

Fig. 4.13: SEM images of 28d samples. Ht-Hydrotalcite, Cc-Calcite, UBFS-Unreacted GGBFS. The red points in the polished samples (N8W0, N8W10 and N8W20) mark the measurement spots in **Fig. 4.14**.

The morphology of the 90 wt% GGBFS and 10 wt% WIFD blended mixtures activated by Na_2CO_3 at 28 d are investigated by using SEM (**Fig. 4.15**). As can be seen, the needle-like structures nearly cover the surface of the matrix in the sample N0W10, indicating the formation of ettringite as found in XRD patterns in **Fig. 4.9(b)**. Besides, the higher Ca/Al ratio in ettringite leads to a higher Al/Si ratio and Ca/Si ratio, as seen in **Fig. 4.14**. The silhouette of unreacted slag grain can still be found in both N0W10 and N4W10. The porous structure on the surface in N4W10 indicates the number of reaction products is not enough to fill the pores due to the low reaction degree of GGBFS. The small calcite grains and the flaky hydrotalcite are found in each mixture. The formed particle size of flaky hydrotalcite grows up gradually with increased Na_2CO_3 from N4W10 to N12W10.

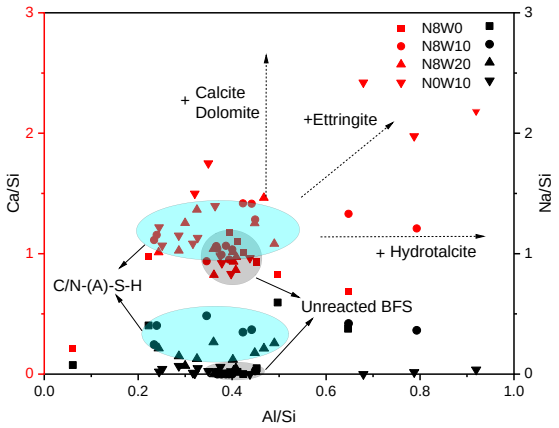

Fig. 4.14: Plot of EDX spot map atomic ratios comparing Ca/Si and Na/Si to Al/Si in the matrix (black spots for the Ca/Si and red spots for the Na/Si).

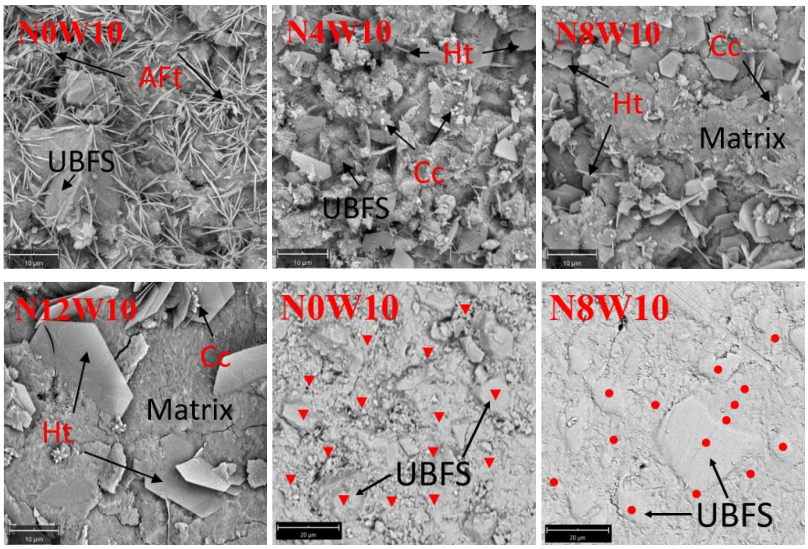

Fig. 4.15: SEM images of 28d samples. Aft-Ettringite, Ht-Hydrotalcite, Cc-Calcite, UBFS-Unreacted GGBFS. The red points in the polished samples (N0W10 and N8W10) mark the measurement spots shown in **Fig. 4.14**.

Fig. 4.16(a) shows the cumulative pore volume of paste samples with different proportions of WIFD after 28 d of curing. It can be seen that the incorporation of WIFD significantly influences the total pore volume of the Na_2CO_3-activated GGBFS. At low replacement levels of from 5 wt% to 10 wt%, the total gel porosity of the samples is decreased due to the filling effect of hemicarboaluminate and hydrotalcite formed in the reaction. However, samples of high replacement ratios around 15 ~20 wt% show the opposite trends. This could be explained by two reasons. At first, the reduced amount of GGBFS in the binder leads to a reduction of hydration products (e.g. C-(A)-S-H) which forms in the pore structure. Secondly, as the water to binder (GGBFS and WIFD) ratio is kept the same, higher amounts of WIFD in the reaction system led to a reduction in flowability as in **Fig. 4.4** because of the high water demand of WIFD. Then, the low flowability results in high gel porosity.

The pore size distribution of the paste between 2 and 200 nm is presented in **Fig. 4.16(b)**. Generally, the gel pores (less than 10 nm) and capillary pores (10~100 nm) are the two main classes of pores [165]. As can be seen, the reference group shows a smaller critical size of the pores indicating a less porous structure filling with more reaction products. Then with the increased WIFD in the mixtures, the porosity of gel pores was increased due to the promoted reaction process by the WIFD. However, it also increases the volume of capillary pores, which was induced by the degradation of flowability due to the incorporation of WIFD. Besides, the formation of hydrotalcite and hemicarboaluminate is increased even though only 5 wt% WIFD was applied as shown in **Table 4.5**, which is significant for the reducing gel porosity. However, a further increase of the WIFD content shows no effect on the critical pore size.

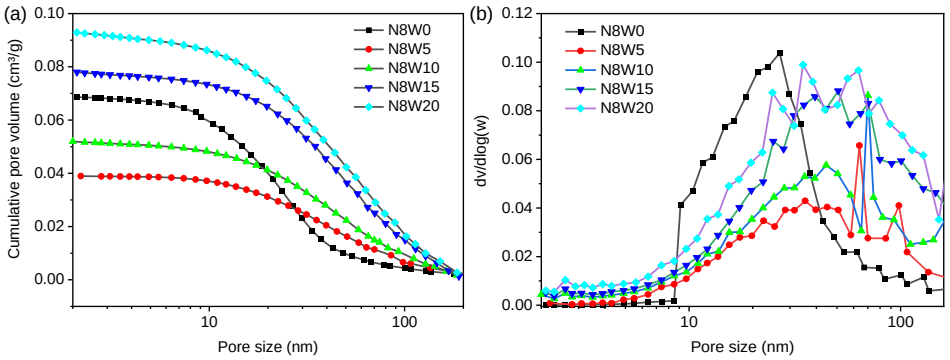

Fig. 4.16: Samples with different replacements of WIFD from BJH adsorption: a - Cumulative pore volume, b - Pore size distribution.

Fig. 4.17(a) shows the cumulative pore volume of 90 wt% GGBFS and 10 wt% WIFD blended paste with different amounts of Na_2CO_3 after 28 d of curing. The cumulative pore volume of the slag pastes decreases from 0.1276 cm^3/g to 0.0236 cm^3/g with the increase of Na_2CO_3 content. The pore structure is filled with the reaction products such as the hydrotalcite, hemicarboaluminate and C/N-(A)-S-H gel to form a more compact structure according to SEM results (**Fig. 4.15**). The pore size distribution of the paste between 2 and 200 nm is presented in **Fig. 4.17(b)**. The increase of the Na_2CO_3 content would improve the porous structure of the matrix and the critical pore size decreases from 90 nm to 40 nm. However, the dosage of Na_2CO_3 makes the differences in the formation quantity of products which would be helpful to reduce the porosity of the matrix and form a denser structure.

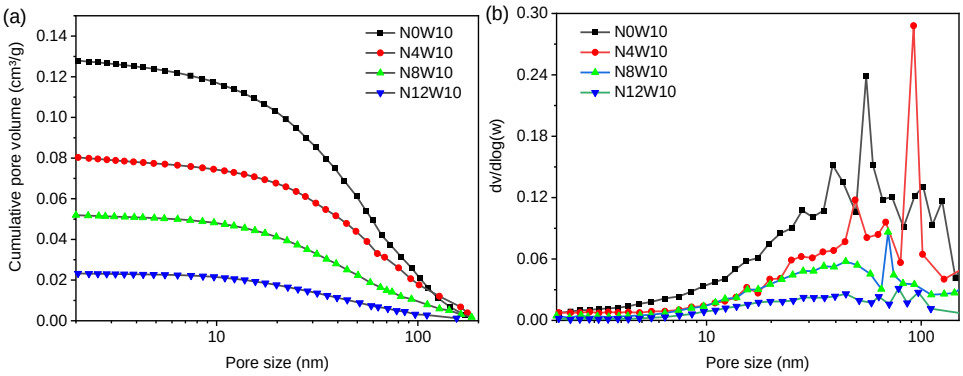

Fig. 4.17: Samples with different amounts of Na_2CO_3 from BJH adsorption: a - Cumulative pore volume, b - Pore size distribution.

4.3.5 Mechanical properties

The compressive strength of Na_2CO_3 activated mixture with different amounts of WIFD after 7 d, 28 d and 91 d curing are shown in **Fig. 4.18**. Understandably, the more slag replaced by WIFD leads to a reduction of the compressive strength. The formation of C/N-(A)-S-H gel as the main contribution to the mechanical properties of samples, is limited by the GGBFS content rather than WIFD. As shown in **Table 4.5**, though the bound water/ GGBFS of each mixture is comparable, the total bound water content decreases with the reduced GGBFS. The reduced compressive strength is also coherent with cumulative pore volume in **Fig. 4.17(a)** because WIFD increases higher pore volume. The reduction of flowability caused by the WIFD addition may also lead to higher pore defects. However, the mechanical performance of samples is still high enough for a potential application in construction with lower strength requirements.

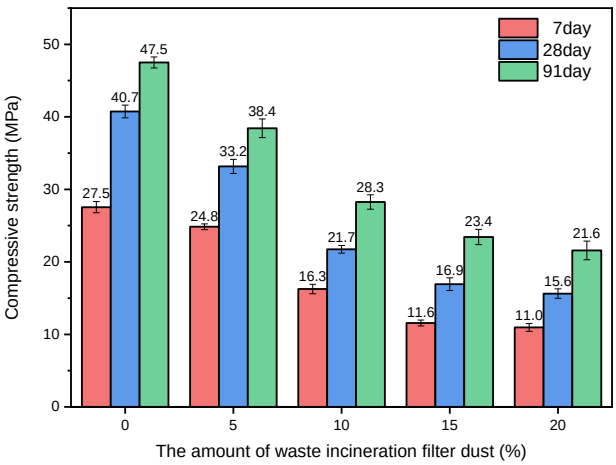

Fig. 4.18: Effect of WIFD content and curing age on the compressive strength of materials.

The compressive strength of 90 wt% GGBFS and 10 wt% WIFD blend binder with various Na_2CO_3 at the curing ages of 7 d, 28 d and 91 d are shown in **Fig. 4.19**. The mixture without Na_2CO_3 (N0W8) still presents a compressive strength. Besides, the N0W10 shows better mechanical properties than that of the N4W10, which is possible to be induced by the formation

of ettringite in N0W10, reducing the porosity of the samples. When the additional amount of Na_2CO_3 is up to 8 wt%, the compressive strength is increased significantly due to the higher reaction degree of GGBFS. When the additional amount of Na_2CO_3 is 12 wt%, the compressive strength shows no further increase due to the limited proportion of GGBFS in the mixture.

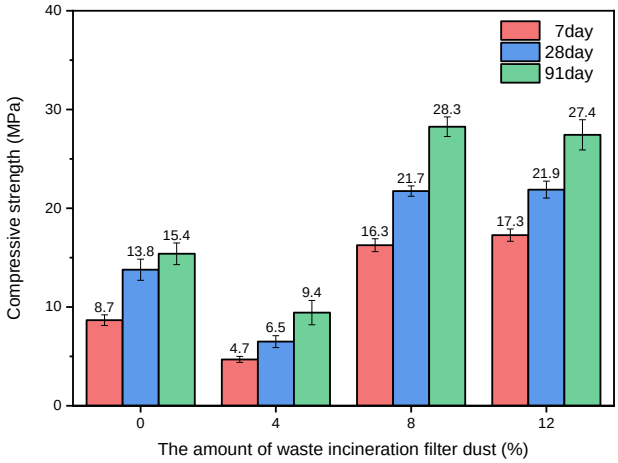

Fig. 4.19: Effect of Na_2CO_3 and curing age on the compressive strength of mortars.

4.3.6 Role of WIFD and Na_2CO_3

Previously, Akturk and Kizilkanat [236] investigated the effect of $Ca(OH)_2$ on Na_2CO_3-activated blast furnace slag and reported that the use of lime would decrease the concentration of CO_3^{2-} in the pore solution. Meanwhile, the fresh state behavior of Na_2CO_3-activated slag paste was well investigated, determining setting time, pH of pore solution and rheological properties [236]. Some similar results are achieved in this work when the WIFD is used as a green $Ca(OH)_2$ source in the Na_2CO_3-activated GGBFS. However, the performance of Na_2CO_3-activated slag with WIFD at the longer curing ages was studied in this work, including the reaction assemblage, the mechanical properties and the gel microstructure. As shown in **Fig. 4.20**, WIFD is composed of portlandite and calcite, portlandite provides the OH^- through the reaction with sodium carbonate; part of calcite would be consumed to form the hydrotalcite and hemicarboaluminate. Further details about the effects of WIFD on the Na_2CO_3-activated activated GGBFS were divided into chemical and physical aspects.

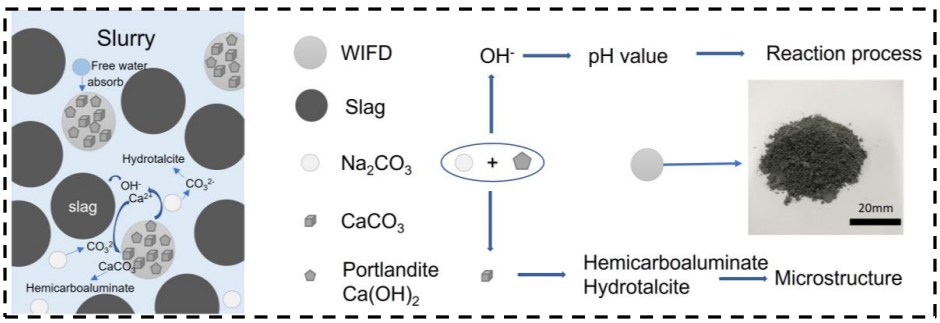

Fig. 4.20: Schematics of the reaction mechanism in the NC-WIFD-GGBFS blends.

- **Chemical effect**

The addition of WIFD effectively affects the reaction process of Na_2CO_3-activated GGBFS systems. Even 5 wt% WIFD in the reaction system could reduce the time to reach the heat flow peak from 2 d to 9 hours. At first, the Ca concentration (from portlandite and calcite) can be increased during an initial period, and the increased Ca/Si ratio would influence the structure of the formed gels. Secondly, portlandite in WIFD provides a higher initial pH than Na_2CO_3, as the initial pH value is a significant factor in the hydration rate [237,238]. The reaction between portlandite and Na_2CO_3 promotes the further increase of pH [55,224]. Finally, the formation of hemicarboaluminate benefits from the calcite originating from WIFD.

Besides, it's proved that the GGBFS could be activated by the WIFD alone (N0W10), with the main reaction products such as ettringite, hydrotalcite and C/N-(A)-S-H gel, which corresponds to the previous results reported by Mobasher and Bernal [239]. However, the formation of hemicarboaluminate was identified in this work due to the initial calcite from the WIFD, which did not exist in a previous study on the hydrated lime-activated GGBFS [219]. In addition, the effect of limestone powder in Na_2CO_3-activated GGBFS was revealed by Yuan et al. [218], and the formation of hemicarboaluminate was not observed either in the Na_2CO_3-activated GGBFS system without portlandite. Therefore, the portlandite and calcite from WIFD show a significant role in the formation of hemicarboaluminate. When Na_2CO_3 and WIFD were used together as in sample N8W10, the ettringite did not form, indicating that Al^{3+} was consumed for the formation of hydrotalcite ($Mg_6Al_2CO_3(OH)_{16}\cdot 4H_2O$) promoted by the Na_2CO_3. In general, WIFD and Na_2CO_3 have synergy in the reaction process by improving pH value and both can affect the types of reaction products.

- **Physical effect**

As we found in the flowability test of mortar samples, the incorporation of WIFD results in a reduction of flowability, which probably causes high porosity and reduces compressive strength. However, low WIFD (N8W5 and N8W10) could decrease the cumulate pore volume, indicating that the reaction products promoted by WIFD show a filling effect in the pore. Therefore, the low replacement of WIFD (5 wt% ~ 10wt%) with additional proper superplasticizers would be beneficial to improve the fresh workability and gel porosity of the matrix.

4.4 Conclusions

This chapter aims to utilize waste incineration filter dust (WIFD) in Na_2CO_3-activated slag. The workability, reaction kinetics, and reaction products of GGBFS activated by WIFD and Na_2CO_3 are characterized by isothermal calorimetry, XRD, TG-DTG, FT-IR and SEM. Furthermore, the influence of WIFD content, Na_2CO_3 dosages and curing ages on the workability and mechanical properties was investigated. The following conclusions can be drawn according to the obtained results.

- The incorporation of WIFD reduces the workability of the mortar due to its high water demand. The mixture with low WIFD content ($\leq$ 10 wt%) is recommended.

- When Na_2CO_3 or WIFD activates GGBFS alone, it shows a prolonged reaction process with nearly 2 d to reach the heat flow peak. Na_2CO_3 and WIFD have a synergistic effect on the activation of GGBFS. The initial alkalinity of the pore solution is raised by the

reaction between Na_2CO_3 and WIFD, which leads to the acceleration of the reaction process. For example, the time to reach the heat flow peak is reduced from 58 h to 10 h by 5 wt% WIFD.

- The main reaction products in the NC-WIFD-GGBFS blends are hemicarboaluminate, hydrotalcite and C-(A)-S-H gels. WIFD and Na_2CO_3 significantly promote the formation of hemicarboaluminate and hydrotalcite. The formation of ettringite is only observed in the WIFD-GGBFS blends, indicating that additional Na_2CO_3 consumes aluminum ions to form the hydrotalcite preferentially.

- In the NC-WIFD-GGBFS blends, the replacement level of WIFD and the dosage of Na_2CO_3 are crucial for the microstructure of the matrix. Though the incorporation of WIFD improves the gel content and gel porosity, it also leads to a reduction of workability and induces more capillary pores. On the contrary, Na_2CO_3 is beneficial to form a denser structure with lower gel porosity.

- WIFD and Na_2CO_3 show different effects on the mechanical properties of the NC-WIFD-GGBFS blends. More WIFD reduces the compressive strength due to the lowered proportion of GGBFS. Na_2CO_3 improves the compressive strength of the mortar by the accelerated reaction process and products.

- The work shows an alternative approach to green building materials prepared with blast furnace slag and Waste incineration filter dust (WIFD). The use of WIFD in the system can help save energy, reduce CO_2 emissions and provide an application for WIFD. Further studies will focus on improving the utilization of waste incineration filter dust (WIFD) in the AAMs with higher mechanical properties.

Chapter 5 The effect of nano-silica and silica fume on the sodium carbonate-activated slag system containing air pollution control residues

This chapter discusses the role of silica fume (SF) and nano-silica (NS) derived from olivine within a sodium carbonate-activated GGBFS system incorporating air pollution control (APC) residues. The dosage of silica additives and APC residues ranges from 0 - 6 wt% and 0 - 15 wt%, respectively. The mechanical properties, reaction kinetics, phase composition, microstructure and carbonation resistance of the blended binder were investigated. Results indicated that SF slightly improved the early compressive strength with the formation of C-(A)-S-H gel (Ca/Si = 1.47, Al/Si = 0.23), hemicarboaluminate and hydrotalcite; reactive NS retarded the activation of GGBFS and inhibited the formation of hemicarboaluminate and hydrotalcite, while promoting the formation of C-A-S-H gel (Ca/Si = 1.01, Al/Si =0.23), resulting in an impressive 80.3% enhancement in compressive strength. Notably, NS-modified samples exhibited decreased carbonation resistance due to increased porosity and C-(A)-S-H gels that are vulnerable to carbonation. Conversely, 2 wt% SF addition decreased the diffusion rate of CO_2, and APC residues improved the carbonation resistance by facilitating the formation of C-(A)-S-H gel with a higher Ca/Si ratio. This study provided an alternative management practice for APC residues with favorable early strength development and offered new insights into using silica additives to enhance waste-combined alkali-activated materials.

This chapter is partially published elsewhere:

X. Ling, K. Schollbach, Y. X. Chen, H.J.H. Brouwers, The effect of nano-silica and silica fume on the sodium carbonate-activated slag system containing air pollution control residues, Waste Management, 322, 129105, 2021.

5.1 Introduction

It has been acknowledged nanomaterials, including $CaCO_3$ [240], Al_2O_3 [241], and TiO_2 [111], SiO_2 [242,243], can enhance the mechanical properties of binders. The enhancement is attributed to their nano-filling effect, which optimizes particle arrangement and reduces voids. Additionally, nanomaterials serve as nucleation sites, promoting the formation of gel products in alkali-activated materials. Notably, nano-silica (NS) and silica fume (SF) are favored due to their pozzolanic reactivity and ability to form more C-(A)-S-H gels [244]. NS induces the formation of C-(A)-S-H gel with higher density through accelerated polymerization of silicate chains [245], thereby expectedly refining pore structures and improving the mechanical properties of the modified binders [243]. Comparative studies on the effect of SF and NS on the performance of both Ordinary Portland cement (OPC) and AAMs have been conducted [242,246]. However, it is important to note that the alkali-activated reaction system differs from that of OPC, particularly in terms of alkali involvement. While portlandite forms during cement hydration, alkali activators are consumed to dissolve aluminosilicate precursors in AAMs. The competition between silica additives and aluminosilicate precursors for OH^- ions emerges as a significant factor influencing the performance of AAMs. Despite extensive investigation into the influence of SF and NS on AAMs [246], most research has primarily focused on sodium hydroxide, potassium hydroxide, and sodium silicate-activated AAMs. There is a scarcity of reports on the performance of sodium carbonate-activated slag modified with silica additives, particularly in the context of WIFD, thus hindering the broader application of cost-effective and environmentally friendly sodium carbonate-activated materials.

Notably, aside from silica additives, the incorporation of portlandite from the utilized WIFD significantly impacts the formation of C-(A)-S-H gel. This influence arises due to their structural characteristic, particularly concerning the interlayer distance, which is correlated with the initial Ca/Si ratio of the raw precursors. [247]. Specifically, the basal spacing decreases from 14.17 Å to 11.74 Å when the Ca/Si ratio in C-(A)-S-H gel increases from 0.8 to 1.1 and remains quite constant when the Ca/Si is beyond 1.1 [248]. However, there is limited available information regarding the relationship between the Ca/Si ratio, silica additives and the gel composition in the sodium carbonate-activated slag systems. Hence, the role of the initial Ca/Si ratio on the blended binder was addressed as well for the effective utilization of WIFD.

Furthermore, the carbonation resistance of AAMs is considered an important aspect of their durability. The diffusion of CO_2 in AAMs reduces the pH in the pore solution [249]. Since sufficient protection of steel rebar requires a pH between 12 and 14, the carbonation resistance dictates the corrosion resistance and service duration of the reinforcing steel [249]. Previous research on the carbonation of AAMs focused on alkali-silicate or hydroxide as the activator [183,250]. In contrast, few studies have reported the carbonation resistance of the reaction systems using sodium carbonate as the activator. Given that the early strength development of sodium carbonate-activated slag materials can be accelerated by WIFD, the present work comprehensively characterizes and offers new insights into the carbonation behavior with varying silica additives and WIFD dosages.

Therefore, SF and NS were utilized to improve the performance of alkali-activated slag with WIFD. The primary objective of this study is to investigate the effect of silica additives and the initial Ca/Si ratio of the binder on the valorization of WIFD in the sodium carbonate-activated slag. The mechanical properties, reaction kinetics, microstructure, and composition of the

reaction products are intensively studied with multiple characterization techniques. Moreover, the present work advances the current understanding of the degradation mechanisms of sodium carbonate-activated slag binders prepared with various silica additives exposed to a CO_2 environment.

5.2 Materials and Experiments

5.2.1 Raw materials

The ground granulated blast furnace slag (GGBFS) sourced from Heidelberg Materials Benelux, Netherlands, and waste incineration filter dust (WIFD) obtained from Euro Trust Management (Netherlands) were used as the primary materials for producing the sodium carbonate-activated slag. The raw WIFD was derived from a Dutch MSWI plant, generated through the injection of a suspension of quick lime into the hot flue gas. It primarily consists of calcite and portlandite (**Fig. 5.1**). No additional treatment was conducted before its combination with GGBFS. Sodium carbonate (powder, analytical grade) was supplied by Sigma-Aldrich. Silica fume (SF) (Elkem 920ED) and nano-silica (NS) were used as the silica source. Nano-silica (Euro support, Netherlands) was produced by dissolving olivine in 3M sulfuric acid [251]. The unreacted olivine and inert minerals are removed from the final suspension by sedimentation. Subsequently, the silica can be cleaned from the resulting mixture by washing and filtering. After the filtration, a cake with around 20 wt% solid content of nano-silica is obtained.

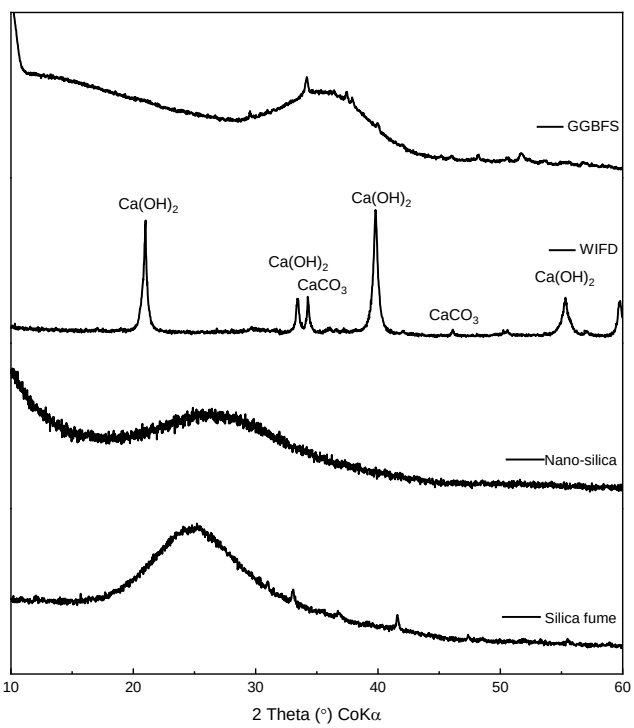

Fig. 5.1: XRD patterns of the used raw materials: ground granulated blast furnace slag (GGBFS), waste incineration filter dust (WIFD), nano-silica and silica fume.

The raw GGBFS, WIFD, SF and NS were characterized with X-ray fluorescence (XRF, PANalytical Epsilon 3) spectroscopy and X-ray diffraction (XRD, Bruker D4 PHASER) in **Table 5.1** and **Fig. 5.1.** The main oxides composition of WIFD are CaO and SO_3, and the main mineral phases are 36.38 wt% portlandite and 37.43 wt% calcite [252]. The main oxides in GGBFS are CaO, SiO_2, Al_2O_3, SO_3 and MgO, and it is almost completely amorphous, as observed from the broad hump between 30° to 40° (2θ) in **Fig. 5.1**. SF and NS show similar chemical compositions with high SiO_2 content. A similar hump exists in the XRD pattern attributed to the amorphous phase. The particle size distribution of WIFD and GGBFS was measured with a laser granulometry instrument (Master sizer 2000), and the median particle size (d50) of WIFD and GGBFS is 8.94 μm and 13.36 μm, respectively. The SF and NS particle size were tested with a Transmission electron microscope (TEM) in **Fig. 5.2**. The surface area was characterized through the N_2 adsorption test using a Brunauer-Emmett-Teller (BET) method.

Table 5.1: Chemical and physical properties of used powders in the investigated AAMs.

The substituent (wt%)	WIFD	GGBFS	SF	NS
CaO	53.97	38.56	0.89	0.04
SiO_2	0.59	30.94	91.04	92.4
Al_2O_3	0.20	13.09	-	-
Fe_2O_3	0.70	0.67	2.02	0.03
K_2O	0.21	0.29	1.13	-
Na_2O	0.15	-	0.62	-
SO_3	6.51	5.15	1.25	-
MgO	0.70	9.02	0.68	0.04
TiO_2	0.02	1.30	-	-
ZnO	0.11	-	-	-
SrO	0.04	-	-	-
MnO	0.02	0.40	0.07	-
Cl	0.60	0.01	-	-
LOI	36.18	0.64	2.17	7.46
d50 μm	8.94	13.36	-	-
Specific density (g/cm^3)	2.32	2.90	2.32	2.60
BET surface area (m^2/g)	25.1	1.0	18.4	274.6

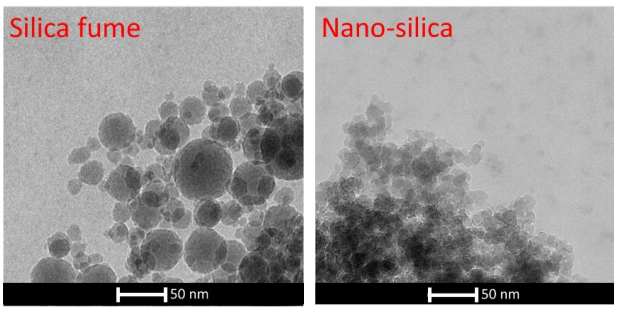

Fig. 5.2:TEM images of the (a) Silica fume and (b) Nano-silica.

5.2.2 Mixture design and preparations

The group Ref consisted of 10 wt% WIFD and 90 wt% GGBFS mixed with sodium carbonate with an equivalent Na_2O concentration of 3.5 wt%. Considering that optimal mechanical strength can be achieved by 4 wt% SF in sodium carbonate-activated materials according to [253], the effect of SF and NS on the performance of the blended binder was investigated by adding 2%, 4 wt% and 6 wt% of the total binder, respectively. In addition, the influence of the initial Ca/Si ratio in the raw material was investigated with a constant silica content of 4 wt%, as shown in **Table 5.2**. The Ca/Si ratio was varied as 0.93, 0.99, and 1.05 to clarify the effect of basal spacing changes of the C-(A)-S-H gels on the performance of the binder, whereas the Al/Si ratio was controlled by adjusting the proportion of WIFD and GGBFS in the reaction system.

Table 5.2: Mix proportions of paste and mortar specimens (wt%).

	WIFD	GGBFS	SF	NS	w/b	Ca/Si	Al/Si
Ref	10	90	0	0		1.12	0.36
S2R1.05	9.8	88.2	2	0		1.05	0.34
S4R1.05	14.0	82.0	4	0		1.05	0.32
S4R0.99	9.6	86.4	4	0	Paste	0.99	0.32
S4R0.93	5.2	90.8	4	0	= 0.5	0.93	0.32
S6R0.93	9.4	84.6	6	0		0.93	0.30
N2R1.05	9.8	88.2	0	2	Mortar	1.05	0.34
N4R1.05	14.0	82.0	0	4	= 0.6	1.05	0.32
N4R0.99	9.6	86.4	0	4		0.99	0.32
N4R0.93	5.2	90.8	0	4		0.93	0.32
N6R0.93	9.4	84.6	0	6		0.93	0.30

Note: Superplasticizer 4 wt%, Na_2CO_3 6 wt% (3.5 wt% Na_2O).

Both paste and mortar samples were prepared according to the mixture formulations. For example, the S4R1.05 and N4R1.05 represent the 4 wt% replacement of SF or NS with an overall Ca/Si ratio of 1.05. The water-to-binder ratio by mass is 0.5 for the paste and 0.6 for the mortar to meet the water demand of the fine aggregates. The standard sand-to-binder ratio was 3.0 for the mortar samples. All the raw materials except the silica additives were added to a laboratory mixer and mixed for 30 s to achieve homogeneity. Then, the silica additives were added gradually during the stirring to achieve better dispersion. The standard sand was added afterward, followed by another 30 s mixing. Then water was added at a low speed for 30 s. After 30 s rest, the mix was stirred for another 120 s at medium speed. Samples were cast into 40×40×160 mm^3 molds, covered with plastic films for 24 h before demolding and sealed with plastic films. Curing was conducted under a laboratory condition at 20 ± 0.5 °C and 50 ± 5% relative humidity.

5.2.3. Methodology

- **Flowability, pH value and mechanical performance of mortar**

The flowability of the fresh mortar was determined using the mini spread flow table test in accordance with EN 1015-3:2007. A standard conical ring (Hägermann cone 70 mm diam. × 100 mm diam. × 60 mm ht) was filled with fresh mortar. Two perpendicular diameters were

measured after 15 impacts and their average value was considered the slump flow of each mixture.

For the initial pH value test, two paste samples were prepared for each recipe. After mixing and stirring, the pH detector (Voltcraft pH-100ATC) was immediately inserted into the fresh paste. Record the value when the readings stabilize and calculate the average as the pH value.

After 7 d, 28 d and 180 d, the compressive strength of the mixture was tested according to EN 196-1:2005. Six samples were tested with a loading rate of 2400 N/s for each mortar and the average value was considered the compressive strength of each mixture.

- **Isothermal calorimeter**

The reaction kinetics of all mixtures were analyzed by an isothermal calorimeter (TAM Air, Thermometric) at 25°C. Paste samples were prepared and injected into a sealed glass ampoule for 7 d calorimetric tests. Heat flow and total heat release were normalized by the total mass of the solid. The initial peak occurring within the first few minutes due to the dissolution of raw precursors was excluded from the analysis. The results of all mixtures were recorded starting 30 min after sample mixing.

- **Phase assemblage analysis**

The phase composition of paste samples was identified by X-ray diffraction (XRD), thermo-gravimetric (TG) and Fourier transform infrared spectroscopy (FT-IR). After 28 d of curing, the paste samples were grounded manually in an agate mortar until powders could pass through the 75 μm sieve and immersed in isopropanol for 24 h to stop the reaction. The samples were vacuum dried at 45 °C and then measured by a Bruker D4 phaser instrument with a step size of 0.02° and a 2θ range from 10° to 60° (Co-Kα, 40 kV, 30 mA). The results were analyzed by using Highscore plus (PANalytical). The thermo-gravimetric (TG) and derivative thermogravimetry (DTG) analysis of all samples were conducted by STA 449 F1. The dried pieces were placed in an Al_2O_3 crucible and heated from 40 °C to 1000 °C at a heating rate of 10 K/min with N_2 as carrier gas. Fourier-transform infrared (FT-IR) spectroscopy was performed in a Varian 3100 instrument with a wavenumber range of 4000 to 400 cm^{-1}. The samples were tested with a resolution of 1 cm^{-1} and 30 scan accumulations.

- **Microstructure analysis**

The analysis was carried out employing a scanning electron microscope (SEM) with an energy-dispersive X-ray diffraction (EDX) (15KV) detector (Phenom Pro). The morphology images were collected with the backscattered electron (BSE). The microstructure of NS and SF were observed by JEOL JEM-1400 Plus transmission electron microscopy. The images were captured by a charge-coupled device camera. After 28 d of curing, the paste samples were selected for the microstructure analysis. The samples were ground into small pieces and immersed in isopropanol for 24 h. Afterward, the samples were vacuum-dried at 40 °C for 3 h and embedded in epoxy resin. Then the solidified samples were polished with grinding papers (120, 600, 1200, 2500, 4000 grit) and coated with Au using a Quorum 150TS plus sputter coater. The nitrogen sorption analysis was conducted using a TriStar II 3020 instrument (Micrometrics). The powder samples were dried in a vacuum oven at 60 °C before the test. The gel pore size distribution was calculated by the Barrett-Joyner-Hallenda (BJH) method from the adsorption branch [254]. Brunauer–Emmett–Teller (BET) surface area of each sample was characterized.

- **Carbonation resistance**

After 28 d of curing, the samples were moved into a carbonation chamber. The relative humidity was set to 65% according to the reported optimal value for carbonation [185]. The temperature was set at 25°C, and a circular airflow with 3% CO_2 gas by volume was applied in the chamber continuously during the test. These parameters are widely used in carbonation resistance evaluation [186].

5.3 Results

5.3.1 Flowability and compressive strength development

Fig. 5.3(a) shows the flowability of the fresh mortar with different silica sources. The silica additives reduce the workability of all samples due to their smaller particle size. Notably, NS, with a higher specific surface area than silica fume, leads to a more pronounced reduction in the spreading flow. The flowability of the fresh mortar with different WIFD content is shown in **Fig. 5.3(b)**, where SF or NS substitutes 4 wt% of the total binder. It is important to highlight that the flowability of the SF and NS modified mortar also decreases with increasing WIFD content owing to the higher water demand of WIFD [21]. The dissolution of portlandite in WIFD consumes free water. Moreover, the higher surface area of WIFD results in higher water adsorption, thereby reducing the workability of the blends.

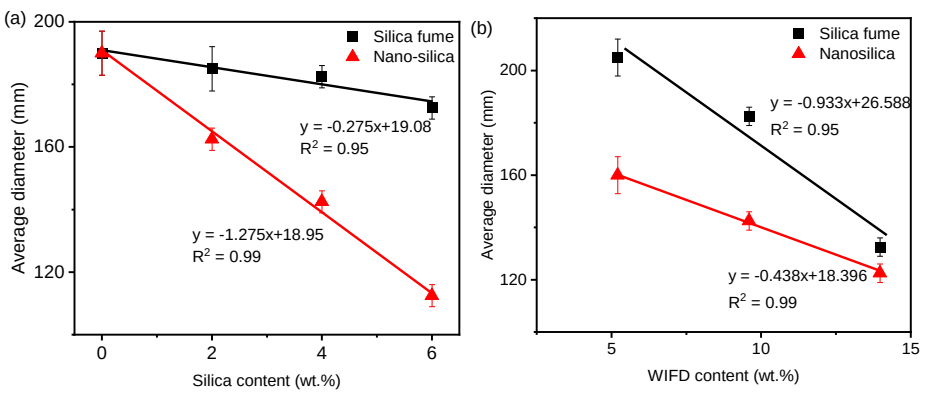

Fig. 5.3: Spread flow diameter of the mixture with different (a) silica content and (b) WIFD content.

Fig. 5.4 presents the compressive strength of the specimens with varying silica content. All the silica-modified samples demonstrate similar or higher compressive strength compared to the reference mortar at 7 d and 28 d. Specifically, the SF-modified samples exhibit a slight increase in compressive strength, whereas NS significantly promotes compressive strength at different ages, despite the reduction in spread flow. For instance, the sample with 4 wt% NS (N4R0.99) improves the compressive strength by 80.3% compared to the reference at 28 d. A similar trend was also observed elsewhere [255,256], suggesting a better enhancement of compressive strength by NS compared to SF. Furthermore, although Cheah et al. [253] reported that the mortar with 4 wt% of SF exhibited the highest mechanical strength at 90 d, the optimal 7 d and 28 d compressive strength was achieved with 6 wt% SF (S6R0.93) in this study. However, the S6R0.93 sample exhibits lower 180 d compressive strength than other SF-modified samples, indicating a lower contribution of SF as fillers at a later stage. Conversely, mortars prepared

with NS can compensate for lower workability through improved paste-aggregate interfacial transition zone densification, leading to improved mechanical properties at 180 d due to the promoted formation of C-(A)-S-H gels (detailed discussion is provided in **Section 5.3.3**).

Fig. 5.4 presents the compressive strength of the specimens with 4 wt% SF or NS. These specimens have different initial Ca/Si ratios from 0.93 to 1.05, adjusted by the WIFD content. The compressive strength of both SF and NS-modified samples follows a similar trend, where a higher WIFD content induces a higher Ca/Si ratio, subsequently resulting in reduced mechanical strength. This trend can be attributed to the fact that WIFD is a less reactive pozzolanic material compared to GGBFS, and the decreased workability of the binder leads to a more porous matrix structure. However, noteworthy differences emerge between the NS-modified and the SF-modified samples. The NS-modified samples show higher compressive strength than those containing silica fume at an equivalent Ca/Si ratio, indicating that NS exhibits greater reactivity than SF and contributes to the activation process together with WIFD and GGBFS.

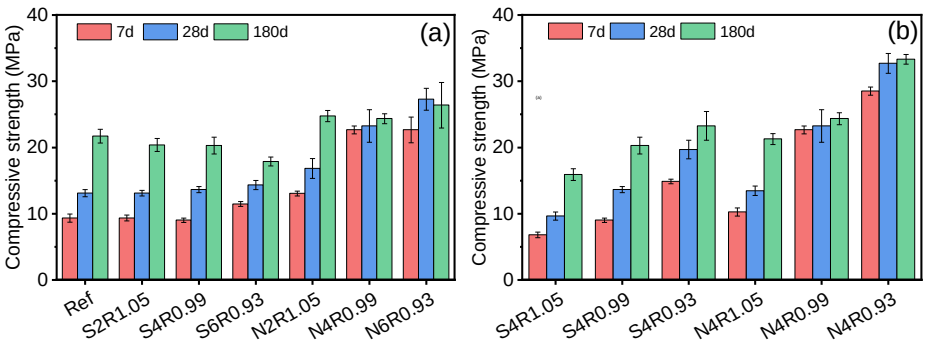

Fig. 5.4: 7 d, 28 d and 180 d compressive strength of the mixture with different (a) silica content (0 – 6 wt%) and (b) initial Ca/Si ratio (1.05, 0.99 and 0.93).

In total, the 28 d compressive strength of all samples ranged from 10.1 to 33.5 MPa. It is crucial to highlight that the compressive strengths of most current formulations are lower than that of OPC. Consequently, attaining further improvements in strength is essential to demonstrate its potential as a cement substitute. Potential strategies for enhancing strength involve optimizing sodium carbonate dosage and adjusting the water-binder ratio. However, these efforts are beyond the scope of the current research objectives and will be continued in future investigations.

5.3.2 Reaction kinetics

Fig. 5.5(a) and **Fig. 5.5(b)** show the effect of the SF and NS dosage on the reaction process of the blended binder within 7 d. The dosage of SF has a negligible influence on the reaction process, as observed in the heat flow curves. It takes nearly 2 h for all SF-modified groups to reach the peaks of heat flow, indicative of the formation of reaction products [55,257]. Furthermore, only a slight decrease in cumulative heat of the binder is observed with increasing SF content, e.g., 150.1 J/g in the group Ref while it is 131.7 J/g in the 6 wt% SF-modified paste (S6R0.93). This reduction is attributed to the overall decrease in GGBFS content resulting from the incorporation of SF.

The NS-modified binders show different heat flow curves in **Fig. 5.5(b)**. The dosage of NS results in a delayed reaction process, as evidenced by the exothermic peak occurring at different times: 1.1 h for N2R1.05, 24.5 h for N4R0.99, and 40.8 h for N6R0.93. Its intensity decreases with higher NS content, in line with findings from a previous study [134], which is attributed to an increased activator modulus [258]. The incorporation of NS increases the silicate content of the mortar, thereby correspondingly decreasing the pH value [259]. This change in pH impacts the silicate equilibrium, affecting the alkalinity of the reaction solution. Hence, the dissolution of the silicates from GGBFS is delayed, extending the reaction time of the binder. However, the extra NS in the binder promotes higher cumulative heat. The increased reactive silicate content provided by NS contributes to the polymerization reaction, releasing more reaction heat. In general, the silicate source determines the effect on the reaction process based on the reaction degree of the added silicate. When the paste is modified with SF, no further chemical interaction occurs. SF acts as a physical filler during the reaction, whereas NS contributes more soluble silicate resulting in a lower pH (See **Appendix Fig. C.1**) and a reduced reactivity of GGBFS during the initial stages. Nevertheless, the portlandite in WIFD can be more extensively combined with NS and a higher content of polymerized C-(A)-S-H can be formed.

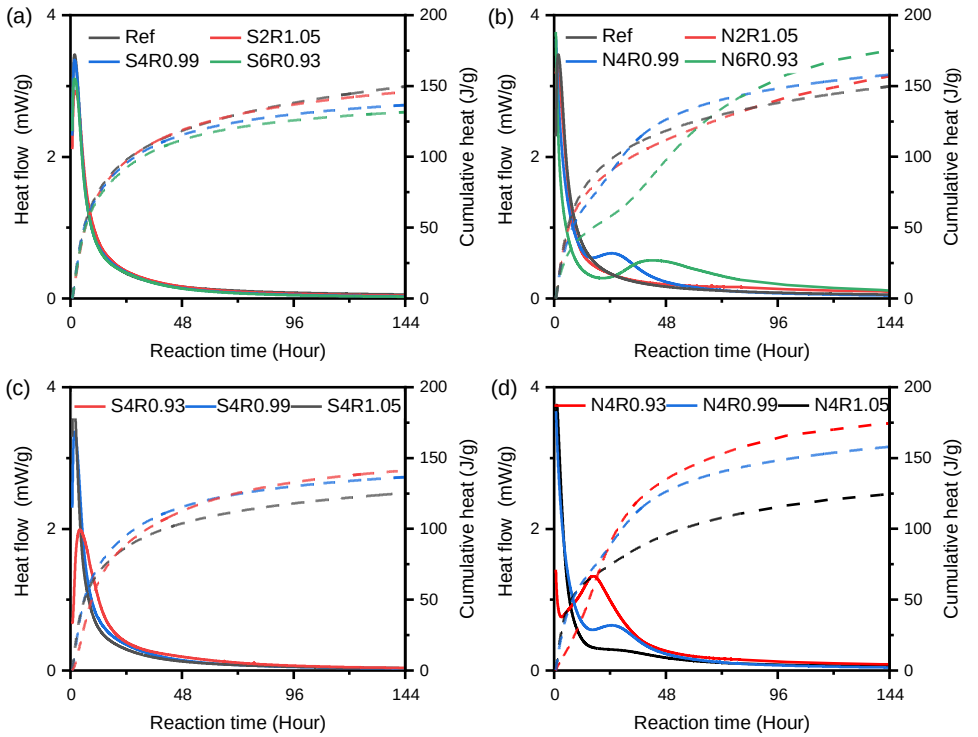

Fig. 5.5: Heat release of the binder with different silica source replacement from 2 wt% to 6 wt% (a: SF, b: NS); heat release of the binder with 4 wt% silica replacement at different Ca/Si mole ratios (c: SF, d: NS).

Fig. 5.5(c) and **Fig. 5.5(d)** illustrate the heat evolution rates and cumulative heat of the mixtures with different initial Ca/Si ratios. When the Ca/Si ratio increases in pastes modified with varying sources of silicate, the cumulative heat decreases due to the lower proportion of GGBFS

in the mixture, associated with the pozzolanic reaction. In the SF-modified paste, the peak of heat evolution appears after 3.8 h with a Ca/Si ratio of 0.93. As the Ca/Si ratio increases to 1.05, this peak shifts to 1.5 h with higher intensity. The duration of the main hydration reaction decreases with more incorporated WIFD due to the reduction of the overall content of GGBFS and increased portlandite content. Conversely, in the NS-modified paste, NS significantly promotes the formation of gels, providing nucleation sites for subsequent hydration products during the reaction [260]. In summary, the present work confirms the adverse effect of solid waste addition on the reaction process. The decrease in cumulative heat developed upon the WIFD supplement is also consistent with the reduction in compressive strength.

5.3.3 Phase assemblage analysis

Fig. 5.6(a) shows the XRD patterns of the 28 d paste samples prepared with different dosages of SF and NS. In the group Ref, the major crystalline phases identified were calcite (PDF#72-1937), hydrotalcite (PDF#89-0460), $Ca(OH)_2$ (PDF#87-0673), and hemicarboaluminate (PDF#41-0221), in agreement with previous studies on the sodium carbonate-activated slag [55,227]. The broad hump around 32-38º indicates the presence of poorly crystallized C-(A)-S-H gel [68,261], though not distinctly marked in the XRD pattern due to overlap with calcite. This gel plays a significant role in strength development for alkali-activated materials. Notably, a portion of $Ca(OH)_2$ and calcite may originate from the raw WIFD. Xuan et al. [252] revealed that the calcite in WIFD contributes to the formation of hemicarboaluminate. Similar findings were observed in the study of a limestone-modified slag paste [261,262]. The incorporation of SF (S2R1.05, S4R0.99, S6R0.93) slightly affects the intensity of hemicarboaluminate, hydrotalcite and $Ca(OH)_2$, attributed to different relative contents of raw material in each mixture. The decreased intensity of $Ca(OH)_2$ in both the SF and NS-modified paste could be attributed to the pozzolanic reaction. On the other hand, when preparing paste with NS (N2R1.05, N4R0.99, N6R0.93), the peaks of hemicarboaluminate are absent. This absence can be attributed to NS consuming more Ca^{2+} ions for the formation of C-(A)-S-H gels, resulting in an insufficient Ca^{2+} ions content. Additionally, more Al^{3+} ions are incorporated into the additional C-(A)-S-H gels that form. Nonetheless, identifying an increase in C-(A)-S-H gels content solely through XRD patterns proves challenging. Therefore, the corresponding conclusion will be further validated later in the analysis of TG-DTG results. The effect of initial Ca/Si ratios on the reaction products is illustrated in **Fig. 5.6(b)**. In the SF-modified paste, the formation of hemicarboaluminate is significantly affected by the Ca/Si ratio. When the Ca/Si is higher than 0.93, the pore solution attains a sufficient Ca^{2+} concentration to facilitate the hemicarboaluminate formation, evident from the increased peak intensities. Conversely, lower peaks of hemicarboaluminate are observed in all NS-modified pastes, as NS consumes higher amounts of Ca^{2+} and Al^{3+} ions in the pore solution to form the C-(A)-S-H gel.

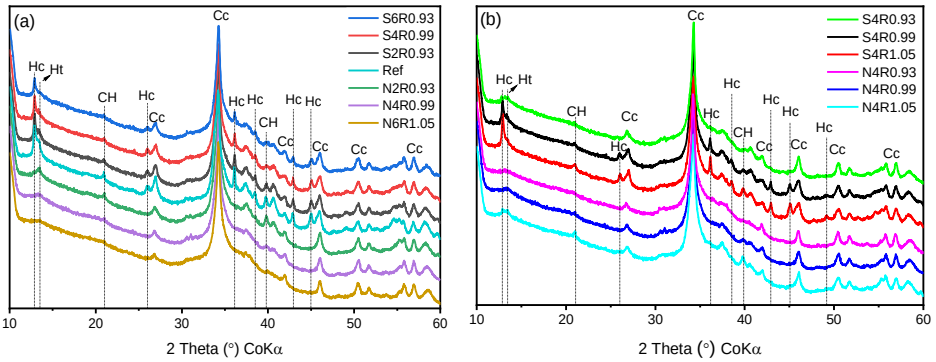

Fig. 5.6: XRD patterns of the 28 d paste samples prepared with (a) different dosages of silica additives, (b) 4 wt% silica replacement at different Ca/Si mole ratios (Hc-Hemicarboaluminate, Ht-Hydrotalcite, CH-$Ca(OH)_2$, Cc-Calcite).

Fig. 5.7(a) shows the infrared spectra of the 28 d samples prepared with different dosages of SF and NS. The addition of SF and NS mainly affects the position of the band around 950 cm^{-1}, assigned to the asymmetric stretching mode of the Si-O-T (T=tetrahedral Si or Al) bonds in the C-(A)-S-H gel [47,228,261]. This band shifts toward a higher frequency with increasing SF or NS in the mixture, indicating enhanced polymerization of the silicate chains [263]. The broad bands around 3405 cm^{-1} and 1638 cm^{-1} correspond to the stretching and bending vibration of the H-O-H bond, respectively. These resonances are from the bound water or interlayer water in the C-(A)-S-H gel, hydrotalcite and hemicarboaluminate [227,263]. The increased intensities of these bonds in SF-modified pastes are mainly attributed to hemicarboaluminate, absent in NS-modified samples as indicated in the earlier XRD results. The adsorption peaks at 1416 cm^{-1} and 873 cm^{-1} represent the vibration of v_3 [CO_3^{2-}] and v_2 [CO_3^{2-}] [228], respectively, which may originate from the calcite, hydrotalcite and hemicarboaluminate. **Fig. 5.7(b)** shows the FT-IR spectra of the 28 d paste samples with 4 wt% NS or SF. Decreasing the WIFD content and lowering the initial Ca/Si ratio from 1.05 to 0.93 leads to a shift of the main peak around 946 cm^{-1} to higher wavenumber both in NS-modified and SF-modified samples. This shift indicates progressive polymerization of the silicate chains, highlighting the influence of dissolved Ca^{2+} ions from WIFD on the formation of C-(A)-S-H gel. The degree of polymerization of the gels correlates with the proportion of the WIFD in the mixture.

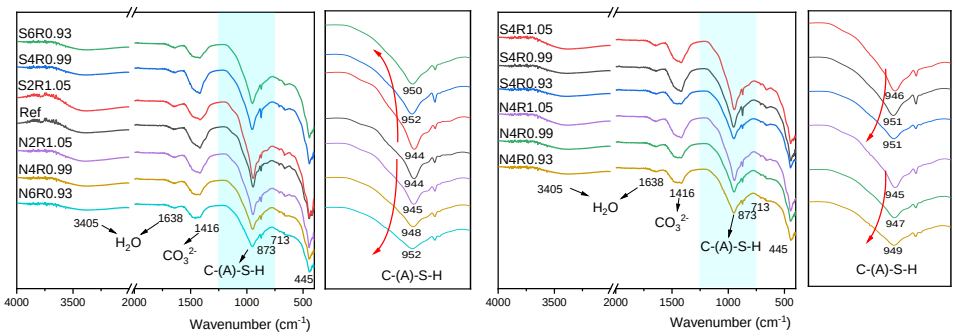

Fig. 5.7: FT-IR spectra of the 28 d paste samples prepared with (a) different dosages of silica additives, (b) 4 wt% silica replacement at different Ca/Si mole ratios.

The thermal analysis of the 28 d paste samples modified with different dosages of SF or NS is presented in **Fig. 5.8(a)** and **Fig. 5.8(b)**. All the samples were dried at 45 °C before the TG test, rendering the residual free water in the paste negligible. In the group Ref, a remarkable mass loss occurs around 140 °C, attributed to the dehydration of several reaction products, including the C-(A)-S-H gel [217], hemicarboaluminate [264,265], and hydrotalcite [266,267]. Upon modifying the paste with SF, the mass loss caused by the dehydration of these minerals decreases, indicating a lower content of reaction products due to different proportions of initial materials. On the other hand, the DTG curves of all NS-modified samples show notably smaller peaks for the dehydration of these minerals than the group Ref. This is because the addition of NS inhibits the formation of hemicarboaluminate according to the XRD analysis. Consequently, the primary mass loss in NS-modified paste is attributed to the dehydration of C-(A)-S-H. It is noteworthy that an augmented mass loss is observed with an increase in NS content, implying greater incorporation of free water into the gel products during the hydration process. Simultaneously, the peak associated with $Ca(OH)_2$ decomposition confirms that NS promotes the consumption of WIFD and the consequent formation of additional C-(A)-S-H gel, consistent with the increased cumulative heat and enhanced compressive strength.

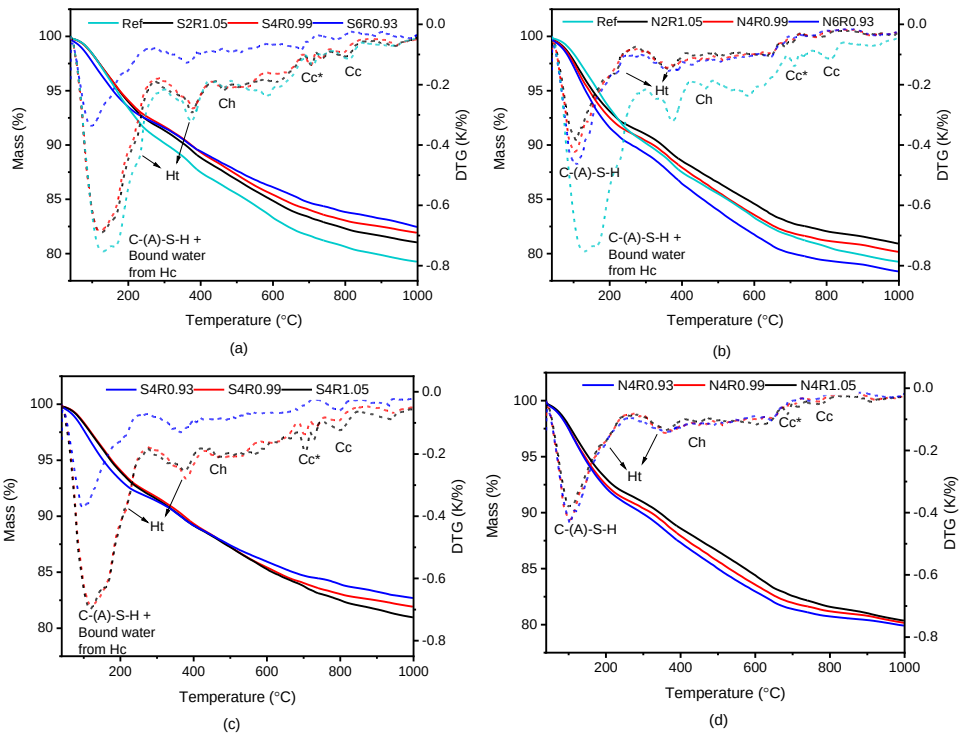

Fig. 5.8: TG and DTG curves of the 28d paste samples with different dosages of silica additives and 4 wt% silica additives at different Ca/Si molar ratios (a and c: SF; b and d: NS).

Fig. 5.8(c) and **Fig. 5.8(d)** present the TG and DTG curves of the 28d paste modified with 4 wt% SF or NS. The mass loss due to the dehydration of bound water around 140°C is influenced by the initial Ca/Si ratio. A higher Ca/Si ratio induces the formation of hemicarboaluminate in SF-modified samples, which contain a higher amount of bound water. When the Ca/Si ratio is above 0.99, the DTG curves of S4R0.99 and S4R1.05 are similar, indicating the presence of

sufficient Ca^{2+} ions in the solution. However, the initial Ca/Si ratio shows a different effect on the reaction products in the NS-modified paste. This difference can be attributed to the heightened concentration of reactive silicate content introduced by NS, which subsequently results in the consumption of Ca^{2+} ions during the formation of C-(A)-S-H gels. Therefore, an increased Ca/Si ratio contributes to the development of a less polymerized structure, accompanied by a reduction in the amount of bound water.

5.3.4 Gel pore characterization

The pore size distribution (2 - 110 nm) and specific surface area of the samples are shown in **Fig. 5.9**. The addition of SF or NS influences the formation of C-(A)-S-H gel, which constitutes a porous gel with a high specific surface area. Generally, the voids within the cementitious system are classified as interlayer space (< 0.5 nm), gel pores (0.5 - 10 nm), capillary pores (10 nm - 50 μm) and air voids (> 50 μm) [268]. The gel pores and capillary pores exhibit sensitivity to the different silica sources (**Fig. 5.9(a)**). The use of SF leads to a negligible difference in the gel pores, while reducing the volume of capillary pores and increasing the surface area from 11.0 to 12.1 m^2/g. This illustrates the relatively lower pozzolanic reactivity and filler effect of SF. In contrast, when NS is utilized in paste preparation, the volume of the larger capillary pores (> 50 nm) decreases and the volume of the smaller capillary pores (10 - 50 nm) increases, accompanied by a higher surface area of 15.6 m^2/g. This is because the larger capillary pores are filled with the newly formed gel products and transformed into smaller pores. Similar results were reported for a NS-modified cement paste [269], where the creation of a more porous bulk structure due to the blocking of ions diffusion from the unreacted cement particles by the gel products was observed. However, the strength and permeability characteristics of the blended binders are determined by the capillary pores larger than 50 nm [270]. Therefore, in comparison to SF, the greater reduction in the volume of the larger capillary pores achieved by NS contributes to a better 28 d compressive strength.

Since the different initial Ca/Si ratios result in different hydration products, the pore size distribution in the SF and NS-modified samples is clarified in **Fig. 5.9(b)** and **(c)**, respectively. The higher Ca/Si ratio induced by WIFD addition in both reaction systems leads to an increased volume of capillary pores, aligning with the reduced compressive strength detectable in **Fig. 5.4**. When the Ca/Si ratio increases from 0.99 to 1.05, the BET surface area for both S4R1.05 and N4R1.05 increases, suggesting that more $Ca(OH)_2$ from WIFD is beneficial for the pozzolanic reaction of SiO_2 and enhances the formation of C-(A)-S-H gel. However, it is insufficient to compensate for the reduction of the overall hydrated phase caused by replacing GGBFS with WIFD [260]. When the Ca/Si ratio is lowered by the decreased WIFD content, this leads to a reduction in the volume of the smaller capillary pores in S4R0.93 and gel pores in N4R0.93. Hence, the inclusion of silica additives significantly influences the pore structure of the blends.

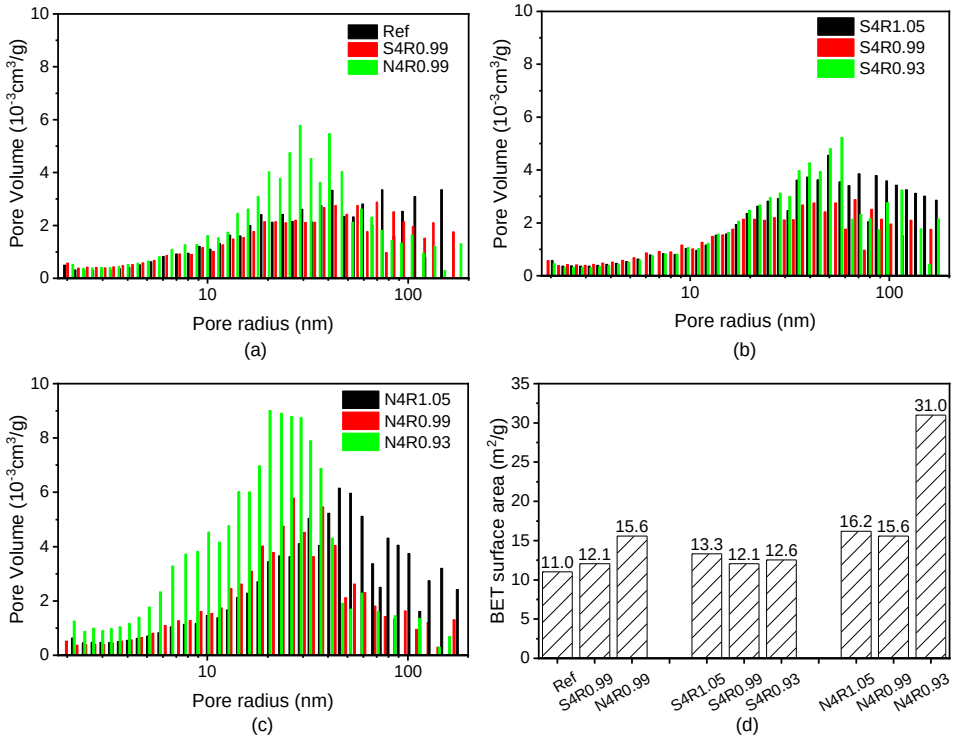

Fig. 5.9: (a-c) BJH pore size distributions and (d) BET surface area of 28 d samples.

5.3.5 Microstructure and gel composition

SF and NS-modified pastes show differences in the formation of hemicarboaluminate and polymerization degree of the gels, subsequently influencing the composition and structure of the C-(A)-S-H gel. Hence, the Ca/Si and Al/Si ratios of the gel products are quantitatively evaluated through BSE-EDX analysis. **Appendix Fig. C.2** shows a typical BSE image from group Ref after 28 d curing. Within the image, unreacted slag grains and their surrounding reaction rims can be clearly distinguished, along with large pores and calcite. The regions characterized by darker greyscale values correspond to the reacted slag fines [216].

To verify the composition of the reaction products, 100 EDX analysis spots (excluding the unreacted slag, calcite and pores) were randomly collected for each sample. The compositional analysis of the samples prepared both with and without SF and NS is shown in **Fig. 5.10**.

Regardless of the silica additives, a distinct correlation between the Mg/Si and Al/Si ratios is evident in **Fig. 5.10(a),** confirming the presence of a hydrotalcite-type phase with an approximate Mg/Al molar ratio of 1.9. Similar Mg/Al ratios for hydrotalcite have been revealed in previous studies [216,271]. However, some spots in Ref and S4R0.99 show notably lower Mg/Al ratios, attributable to the inclusion of hemicarboaluminate ($C_4Ac_{0.5}H_{12}$) within the bulk matrix. Furthermore, an Al/Si ratio of approximately 0.23 is observed when Mg/Si=0, suggesting an approximated Al/Si ratio within the C-(A)-S-H gels, in agreement with the Al/Si ratio depicted in **Fig. 5.10(b)**. This demonstrates a consistent Al(IV) substitution ratio for Si in

C-(A)-S-H gel regardless of the silica additives [272]. Likewise, the presence of $C_4Ac_{0.5}H_{12}$ in Ref and S4R0.99 leads to a higher Al/Mg ratio in some spots.

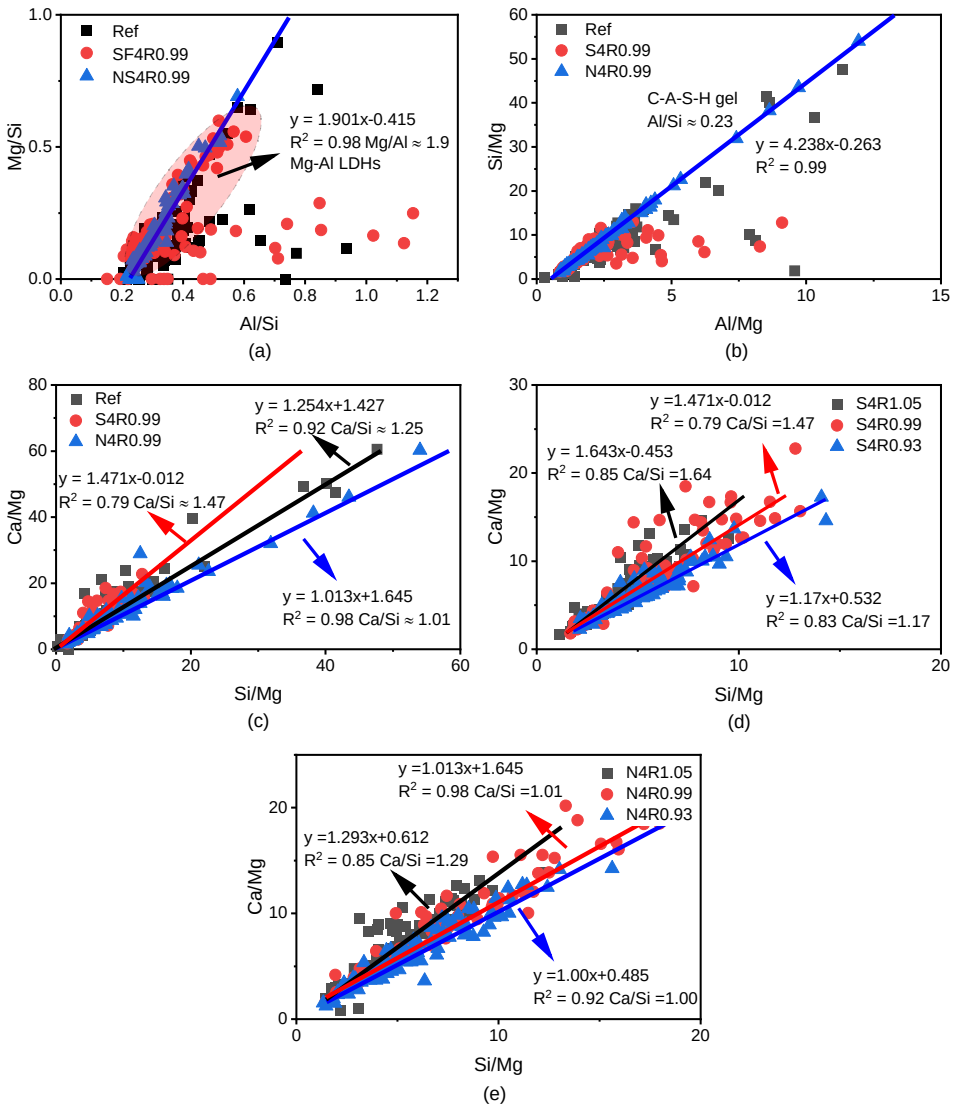

Fig. 5.10: Compositional plots of the different spots measured (100 spots) in the 28 d samples with molar ratios of (a) Mg/Si and Al/Si; (b) Si/Mg and Al/Mg; (c-e) Ca/Mg and Si/Mg (The trend lines are fit to the measured spots, and the slope of each line is calculated which represents the Mg/Al ratio in (a), Al/Si ratio in (b), and Ca/Si ratio in (c-e)).

Fig. 5.10(c) shows the Ca/Si ratio within the C-(A)-S-H gels under the influence of SF and NS modifications. Despite the presence of $C_4Ac_{0.5}H_{12}$ in the Ref, resulting in a higher Ca concentration, the Ca/Si ratio in the C-(A)-S-H gel remains approximately 1.25. The relatively low Ca/Si ratio in alkali-activated slag indicates the presence of a C-S-H (I) gel structure [273]. Contrary to expectations for a pozzolanic reaction, the SF-modified samples, as illustrated by

the red curve in **Fig. 5.10(c)**, do not exhibit a significant reduction in the Ca/Si ratio, implying the low reactivity of SF. On the other hand, the addition of NS reduces the Ca/Si ratio within the C-(A)-S-H gels to 1.01. This reduction affirms an enhanced polymerization degree of the C-(A)-S-H gel with longer silicate chains, attributed to improved Q^2 content by NS [274], which is coherent with the findings from the FT-IR results in **Fig. 5.7(b)**.

The actual Ca/Si ratio of the formed C-(A)-S-H gel within each mixture, with different dosages of WIFD incorporated into the SF-modified and NS-modified samples, are presented in **Fig. 5.10(d)** and **Fig. 5.10(e)**, respectively. The actual Ca/Si ratio is higher than the initial Ca/Si ratio provided in **Table 5.2**, e.g., the Ca/Si ratio is 1.64, 1.47 and 1.17 in SF-modified mixtures. This phenomenon could be attributed to the unreacted GGBFS and the release of more reactive Ca^{2+} from WIFD. Moreover, the addition of NS leads to the development of a C-(A)-S-H gel with a lower actual Ca/Si ratio compared to the samples modified with SF, indicating that NS promotes the hydration process of WIFD within the matrix.

5.3.6 Carbonation depths and rate

The carbonation front is indicated by phenolphthalein for each mixture, as shown in **Fig. 5.11**. The diffusion of CO_2 in alkali-activated materials lowers the pH value of the pore solution [54,273] and decalcifies calcium-bearing phases such as the C-(A)-S-H gels [54,186,275]. The magenta in the center represents the uncarbonated parts. Increased carbonation occurs in the mortar prepared with NS (N4R0.99>S4R0.99>Ref) after 8 d accelerated carbonation. Upon incorporation of varying dosages of WIFD to adjust the initial Ca/Si ratio, distinct carbonation depths are observed in the SF-modified and NS-modified samples, as illustrated in S4R1.05-0.93 and N4R1.05-0.93. Notably, while the uncarbonated area increases with a lower Ca/Si ratio in SF-modified samples, it initially decreases in NS-modified samples with a reduction in the Ca/Si ratio but increases when the Ca/Si ratio is further lowered.

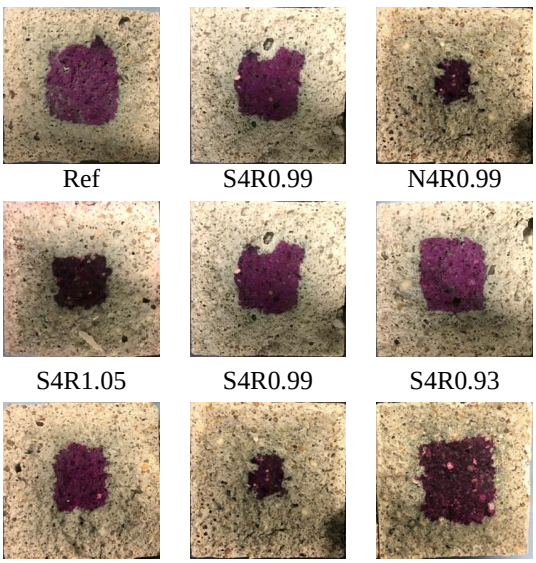

Fig. 5.11: Illustration of the carbonation front indicated by phenolphthalein for the mortar samples after 8 d of accelerated carbonation.

To assess the carbonation rate of various samples, the evolution of carbonation depth in the mortar samples is presented in **Appendix Fig. C.3**. The linear correlation between carbonation depth and the square root of exposure time confirms the diffusion-controlled process. Linear fitting is performed for each mixture, excluding the full carbonation point (20 mm), and the slope of each fitted line is considered as the carbonation rate in **Table 5.3**. The resistance to carbonation shows variation between the two silica additives. In comparison to the group Ref, the addition of 2 wt% SF (S2R1.05) can reduce the carbonation rate. However, a further increase in SF content leads to an accelerated diffusion of CO_2. Conversely, among the NS-modified samples, higher NS content improves carbonation resistance (N2R1.05, N4R0.99, N6R0.93). As the incorporation of silica additives can enhance the mechanical properties of the blends, an improvement in carbonation resistance was expected, particularly for mixtures modified with NS. However, NS-modified samples exhibit a faster carbonation rate compared to group Ref. Several potential reasons contribute to this phenomenon: a) the lower workability of NS-modified samples introduces more air voids in the matrix; b) while NS promotes the gel formation, the matrix retains less portlandite, allowing diffused CO_2 to react directly with the gels instead of carbonating portlandite first; c) C-(A)-S-H gels formed in NS-modified samples show a lower Ca/Si ratio, resulting in decreased CO_2 binding capacities; d) the higher BET surface area of gel products in NS-modified samples facilitates CO_2 diffusion; e) more free water remaining in the NS-modified sample induces higher internal relative humidity and accelerates the penetration of CO_2 [276], whereas more free water in Ref samples is bounded into the formation of hemicarboaluminate, hydrotalcite and C-(A)-S-H gel. With further hydration processes, the consumption of free water also contributes to the formation of voids.

On the other hand, the different initial Ca/Si ratio of raw material induces various carbonation responses in the mortars. In the SF-modified samples, as the proportion of WIFD increases from S4R0.93 to S4R1.05 in the mixture, the carbonation rate decreases, indicating that WIFD retards the carbonation process. A similar trend is observed in N4R1.05 when compared with N4R0.99. Notably, N4R0.93 shows the best carbonation resistance among all NS-modified mixtures, attributed to the increased gel products that fill the voids, reduce the pore size of the matrix, and consequently slow down the diffusion of CO_2.

In conclusion, the carbonation behavior of the blended binder was studied by varying the content of NS, SF, and WIFD. Among the groups studied, S2R1.05 and N4R0.93 demonstrate better carbonation resistance compared to the group Ref. Considering the aim of optimizing WIFD waste utilization, formulations such as S2R1.05 are recommended for blend preparation.

Table 5.3: The carbonation rate of each mixture by linear fitting analysis of **Appendix Fig. C.3** (Note: the full carbonation points are excluded during the fitting, the slope is then considered as the carbonation rate, and the fitting results are presented in **Appendix Fig. C.3**).

Group ID	Ref	S2R 1.05	S4R 1.05	S4R 0.99	S4R 0.93	S6R 0.93	N2R 1.05	N4R 1.05	N4R 0.99	N4R 0.93	N6R 0.93
Carbonat -ion rate ($mm/d^{1/2}$)	5.212	4.938	5.639	5.686	5.807	5.666	7.439	5.745	7.390	4.915	5.456
R-Square	0.998	0.999	0.995	0.999	0.993	0.998	0.991	0.993	0.999	0.998	0.968

5.4 Discussions

5.4.1 Preliminary study on CO_2 emissions and cost of the blended binder

The development of AAMs is primarily motivated by the need to reduce the adverse environmental impacts of cement production and usage, particularly in terms of CO_2 emission reduction [277]. Hence, the embodied CO_2 of the mixes developed in this work was preliminary estimated and compared with other types of binder systems [134,278,279], along with a cost analysis of raw materials. CO_2 emissions (kg CO_2/ton) and overall cost (€/ton) of the mix were calculated by multiplying the mass of each ingredient (in 1 m^3) by its CO_2 coefficient and price, respectively. The CO_2 emission and price indicators of each ingredient were obtained from the literature [59,134,280–286], as presented in **Appendix Table C.1**.

The CO_2 emission and the cost of S4R0.99 and N4R0.99 from the current study and other types of concrete are presented in **Fig. 5.12**. It confirms the highest CO_2 emission in OPC concrete, mainly attributed to the usage of CEM I. Reduction of CO_2 emissions is achieved in different AAM-based concrete. Notably, activators may significantly contribute to CO_2 emissions in sodium silicate or sodium hydroxide-activated materials [280], as evidenced in **Fig. 5.12**. Lower CO_2 emissions are achieved by using sodium carbonate as an activator in S4R0.99 and N4R0.99. Additionally, sodium carbonate is cheaper than sodium silicate or sodium hydroxide-based activators, reducing the cost of the S/N4R0.99.

Generally, the use of NS will significantly increase energy consumption and cost in the production of AAMs. When compared with SF-modified samples, a higher CO_2 footprint is confirmed in NS-modified samples. Notably, the NS used in this study was derived from olivine. Previous research conducted by our group has revealed its CO_2 footprint and cost through laboratory and bench-scale testing [134,286]. When compared to the conventional production of NS using waterglass, the cost of raw materials can be reduced from 2084 €/tone to 941€/tone, and the CO_2 emission can be lowered from 8800kg/tone to 461 kg/tone [286,287]. Overall, the contribution of NS to CO_2 emission is relatively lower than that of other ingredients in the concrete. Therefore, improving the integration of WIFD in the sodium carbonate-activated GGBFS with NS or SF is acceptable with lower costs and a reduced carbon footprint.

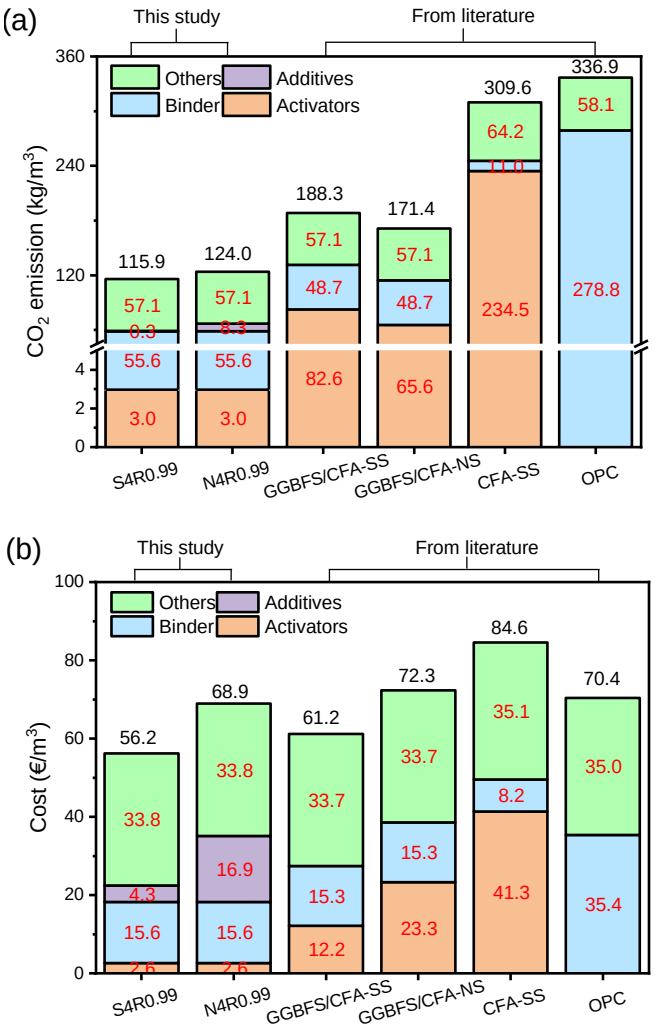

Fig. 5.12: The (a) CO_2 emissions and (b) cost analysis of S4R0.99 and N4R0.99 in this study and other types of binder systems. Note:1) GGBFS/CFA-SS [134]: the blended binder of GGBFS and class F fly ash (CFA) with the activator of commercial sodium silicate (SS), GGBFS/CFA-NS [134]: the blended biner of GGBFS and CFA with the activator prepared with sodium hydroxide and nano-silica, CFA-SS [278]: CFA with the activator formulated with sodium silicate and sodium hydroxide SH), OPC [279]: the CEM I 42.5N. 2) Binder materials include GGBFS, CFA and cement. Activators include sodium carbonate, sodium hydroxide and sodium silicate. Additives include silica fume and nano-silica. Others include water, fine aggregate and coarse aggregate).

5.4.2 Reaction mechanism of SF and NS

The present work reveals various effects of SF and NS on the reaction process and overall performance of the blends. The schematic diagram of the proposed mechanism is presented in **Fig. 5.13**. The pozzolanic reaction of silica additives can be considered a major factor that improves the gel production and, thereby, the mechanical properties of the blends [269]. However, a significant promotion of gel formation is evident exclusively in blends containing

NS, which explains the remarkable enhancement of the mechanical properties of the blends in this case. The formed C-(A)-S-H gel shows a lower Ca/Si ratio and higher polymerization, indicating a longer aluminosilicate tetrahedra chain and enhanced gel density [288]. Notably, the improved compressive strength of the NS-modified blends does not guarantee a better carbonation resistance of the matrix. SF slightly contributes to the mechanical properties of the blends as fillers, and the resulting C-(A)-S-H gel has a higher Ca/Si ratio. Sevelsted and Skibsted have documented a decline in carbonation rate with an elevated Ca/Si ratio of C-S-H gel [289]. A similar improvement in carbonation resistance is achieved within the group with 2 wt% SF addition. To sum up, SF and NS contribute to the mechanical properties from different physicochemical mechanisms, making it feasible to optimise the performance of WIFD-sodium carbonate-activated materials to align with specific construction demands. However, further advancements in mechanical attributes are imperative for these materials serve a viable cement alternative, given that the compressive strength of most modified samples remains below the 32.5 MPa at 28 d.

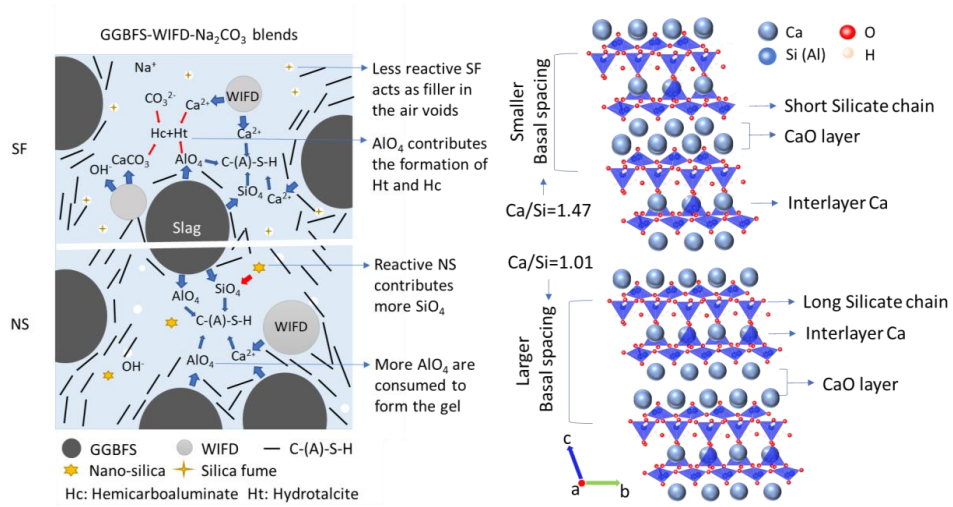

Fig. 5.13: Schematics of the role of nano-silica and silica fume on the activation process of the GGBFS-WIFD-Na_2CO_3 system.

5.5 Conclusions

The effect of silica fume (SF) and nano-silica (NS) on the workability, mechanical properties, reaction kinetics, phase and gel composition, microstructure and carbonation resistance of the novel WIFD-combined binder is intensively investigated in the present work, along with the evaluated CO_2 footprint and cost analysis. The following conclusions can be drawn based on the obtained results:

- SF increases the compressive strength of the blended mortar slightly at early ages due to the filler effect but decreases at longer ages due to a lower amount of hydration products, whereas NS enhanced the compressive strength at all ages due to better pozzolanic reactivity and improved formation of C-(A)-S-H gels that refine the pore structure.

- NS promotes the consumption of WIFD in the matrix and enhances the cumulative heat released due to the improved gel formation in the blends. However, it retards the reaction process, as a result of the reduced pH value of the pore solution due to the pozzolanic reaction.

- The main reaction products of the WIFD-sodium carbonate-activated binders are C-(A)-S-H gel, hemicarboaluminate ($C_4Ac_{0.5}H_{12}$), hydrotalcite (Mg-Al LDHs) and calcite. The addition of NS inhibits the formation of $C_4Ac_{0.5}H_{12}$ and Mg-Al LDHs by the consumption of Ca^{2+} and Al^{3+} in gel formation.

- 4 wt% NS leads to a relatively lower Ca/Si ratio of 1.01 in C-(A)-S-H gels and induces a higher polymerization degree of silicate chains, whereas no significant influence of SF in gel composition with a relatively higher Ca/Si ratio of 1.47. The substitution of Al in silica chains is approximately 0.23 regardless of the silica additives.

- Though NS enhances the mechanical properties of the blends, it also induces a lower carbonation resistance of the matrix. Instead, using 2 wt% SF and WIFD is beneficial to improve the carbonation resistance, which can be optimized as the S2R1.05.

- The designed WIFD-sodium carbonate-activated slag concrete offers advantages in terms of reducing CO_2 emissions and the cost of raw materials when compared to the OPC system and sodium silicate/hydroxide-activated system. In addition, the work provides an alternative management practice for air pollution control residues.

- The findings presented in this chapter are confined to the examination of the compressive strength, reaction process and products, microstructure and carbonation behavior of the GGBFS-WIFD-Na_2CO_3 system. While the compressive strength requires further enhancements, other aspects such as shrinkage behavior and durability require comprehensive elucidation and analysis before considering the implementation of this process on a bench or industrial scale.

Chapter 6 Valorization of biomass bottom ash in alkali-activated GGBFS-fly ash: impact of biomass bottom ash characteristic, silicate modulus and aluminum-anodizing waste

Growing production of green energy from biomass has led to a surge in biomass bottom ash (BBA) generation, often relegated to landfills due to high leachable heavy metal content. This chapter proposed solidifying BBA in alkali-activated granulated ground blast furnace slag (GGBFS) and class F fly ash (CFA) blended binders. Investigations into the influence of BBA content, fineness, silicate modulus of activators, and aluminum-anodizing waste (AAW) on solidification performance were conducted, focusing on reaction mechanisms, phase assemblages, mechanical properties and leaching behavior. Results indicate relatively low reactivity of BBA and high leachable chloride (Cl^-), sulfate (SO_4^{2-}), chromium (Cr), molybdenum (Mo), lead (Pb) and zinc (Zn) contents from BBA. Increased BBA substitution leads to strength deterioration, while ground biomass bottom ash (GBBA) improves mechanical performance slightly. This improvement is attributed to the increased reactive aluminosilicate content and an enhanced packing system resulting from finer particles. However, GBBA induces an increased heavy metals leaching. Higher silicate modulus activators enhance mechanical properties and reduce the leaching of Mo and Cl^-, while lower silicate modulus activator accelerates the reaction process, promoting the formation of hydrotalcite-like phases and reducing the leaching of Cr and SO_4^{2-}. Incorporating 0.5 wt% aluminum anodizing waste improves the immobilization efficiency of toxic ions, but further increases in dosage lead to higher leaching due to weakened mechanical performance. Overall, hybrid binders with 10 wt% G/BBA exhibit desirable mechanical properties, along with sufficient immobilization of leachable heavy metals, enabling their use as potential construction materials.

This chapter is partially published elsewhere:

X. Ling, W. Chen, K. Schollbach, H.J.H. Brouwers, Valorization of biomass bottom ash in alkali-activated GGBFS-fly ash: impact of biomass bottom ash characteristic, silicate modulus and aluminum-anodizing waste, Construction and Building Materials, 428, 136408, 2024.

6.1 Introduction

In recent years, Alkali-activated materials (AAMs) have been widely investigated due to their lower carbon footprint and promising mechanical performance. The performance of AAMs is governed by various factors, including the composition of solid precursors [290], curing temperature [291], types and modulus of activators [292], as well as additives such as calcined dolomite and layered double hydroxides [55,293]. Xu demonstrated the effect of activator modulus and GGBFS-CFA ratio on the reaction kinetics, hydrated gel structures and compressive strength of the blends, highlighting the advantages in mechanical properties with optimal parameters [290].

Besides, AAMs offer a combination of high alkalinity, dense microstructure and chemical stability, making them highly effective for immobilizing heavy metals from industrial solid waste. However, the leaching behavior of AAMs, particularly when solid waste is used to produce them, is significantly shaped by micro-scale matrix properties. The solidification of BBA in such blends is expected to introduce variations in chemical composition and related properties. A thorough understanding of the reaction process of BBA-GGBFS-CFA blends is crucial for optimizing the properties of the hybrid binders. Moreover, ingredient characteristics influence the mechanical performance of the blends. Komljenović et al. revealed that the compressive strength of alkali-activated fly ash is enhanced with the finer fly ash content [294]. Nevertheless, limited attention has been paid to the BBA fineness, despite its significant impact on the dissolution process, particle packing in the matrix, and the leaching capacity of heavy metals. Therefore, in this chapter, the role of BBA fineness is explored to optimize the strength and leachability trade-off in the BBA-GGBFS-CFA blends.

Aluminum-anodizing waste (AAW) is a by-product of the aluminum anodizing process, primarily composed of aluminum hydroxide polymorphs like bayerite and boehmite. This waste often contains heavy metals such as Cr and Ni, leading to its disposal through sewage systems or landfills. To enhance the recycling of this aluminum-rich material, Souza et al. elucidated that AAW exhibits promise as a shrinkage-compensating admixture when combined with Portland cement, attributed to the promoted formation of ettringite [295]. Additionally, AAW has been suggested as a viable component in the manufacturing process of calcium sulphoaluminate cement via the hydrothermal calcination method [296,297]. However, to the best of our knowledge, few studies investigate the application of AAW in AAMs, despite the fact that aluminosilicates are the reaction precursors of AAMs. This chapter also aimed to utilize the high aluminum content in AAW to effectively modify the resulting reaction products. Based on the feature that the negative charge of tetrahedral $[AlO_4]^-$ in the gel chains enhances the immobilization of metal ions as previously mentioned, the possibility of synergistic treatment of AAW and BBA in AAMs has been explored in this chapter to improve the solidification efficiency of heavy metals and to achieve the concept of multiple waste reuse.

Based on the above considerations, the primary objective of this chapter is to solidify BBA in AAMs to render it as a construction material, thereby leveraging the advantages of AAMs instead of resorting to landfilling. Given the complexity of the AAMs matrix, the interaction between AAMs and BBA, as well as the resulting immobilization efficiency, are expected to vary. The chapter investigates the influence of BBA content, fineness, silicate modulus (Ms) of activators, and AAW on the solidification process, focusing on the reaction mechanism, phase

assemblages, mechanical properties and leaching behavior. The findings contribute to establishing a theoretical foundation, feasibility assessment, and principles of the selection of raw materials and additives for the solidification of BBA.

6.2 Materials and Experiments

6.2.1 Raw materials

Granulated ground blast furnace slag (GGBFS), Class F fly ash (CFA), Biomass bottom ash (BBA) and Aluminum anodizing waste (AAW) were used as the raw materials in this chapter. GGBFS was provided by Heidelberg Materials Benelux, Netherlands. CFA was purchased from Vliegasunie, Netherlands. BBA and AAW were provided by Eurotrust Management, Netherlands. The BBA was originally collected from a local bio-power plant that utilized a grate furnace and a steam boiler for energy production. The plant burned B-wood, classified by the Ministry of Infrastructure and the Environment, Netherlands, which includes painted and glued wood, as well as wood-wool composite boards [298]. Notably, the received BBA contained some charcoal fragments (5 wt%) as shown in **Fig. 6.1(a)**, which had larger particle sizes exist in the received BBA. To prevent any adverse effects of the charcoal fragments on the mechanical properties of the blends [299], the received BBA was initially sieved for homogeneity, reducing it to below 1 mm as depicted in **Fig. 6.1(b)**. To reveal the influence of BBA fineness on the blends, the BBA was then ground for 5 min at 250 rpm in a ball mill, resulting in the production of ground BBA powder as shown in **Fig. 6.1(c),** hereinafter referred to as GBBA. AAW was collected from a local wastewater treatment plant where aluminum was removed from the sewage using electrodialysis technology. The received AAW was dried at 60 °C to remove the free water and subsequently ground for 1 min at 250 rpm for further characterization and application.

(a) (b) (c)

Fig. 6.1: Morphology of raw BBA with different particle sizes (a: charcoal fragments >1 mm, b: BBA < 1 mm, c: ground biomass bottom ash (GBBA)).

The particle size distribution of raw materials was determined using a laser light scattering technique (Mastersizer 2000, Malvern), and the results are presented in **Fig. 6.2**. The average particle size (d50) of GGBFS, CFA, BBA, GBBA and AAW is found to be 13.3 µm, 14.0 µm, 125.5 µm, 30.0 µm and 5.8 µm respectively. The particle size of BBA is larger compared to that of CFA and GGBFS, while GBBA exhibits a similar particle size. It should be noted that longer grinding times and higher speeds would result in finer particles. However, this would also lead to increased costs and time requirements in the pre-treatment process. Therefore, the effect of both milled and un-milled BBA on its solidification performance is considered in the

present work. The chemical composition of raw materials was determined by X-ray fluorescence spectrometry (XRF) (PANalytical Epsilon 3). The borate fusion method was used for the preparation of fused beads. The chemical composition of the raw materials is given in **Table 6.1** in the form of oxides, along with the specific density and the Blaine specific surface area (as per European standard EN 196–6). For the preparation of the activating solution with various Ms (1.0, 1.4, 1.8), commercial sodium silicate solution procured from Labshop (Mass ratio: 26.9% SiO_2, 8.0% Na_2O, 65.1% H_2O) and sodium hydroxide pellets (97%, Sigma-Aldrich) were used in combination with distilled water.

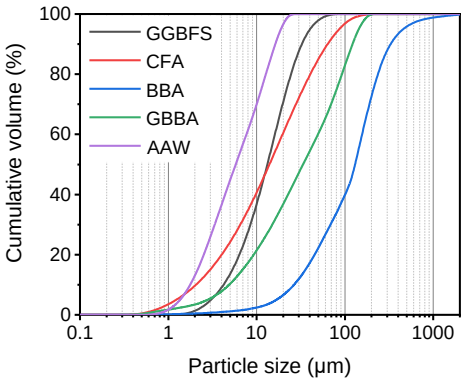

Fig. 6.2: The particle size distribution of raw materials.

Table 6.1: Chemical and physical properties of raw materials.

The substituent (%)	GGBFS	CFA	BBA	GBBA	AAW
CaO	38.6	6.1	17.3	17.1	1.0
SiO_2	31.2	54.6	48.9	49.6	0.8
Al_2O_3	13.1	21.6	6.2	7.5	55.2
Fe_2O_3	0.7	9.0	3.0	2.6	0.6
K_2O	0.3	2.9	1.9	2.1	-
P_2O_5	-	-	1.3	1.2	0.2
Na_2O	-	-	-	-	4.2
SO_3	5.2	0.4	2.9	2.6	11.8
MgO	9.0	1.2	2.9	2.5	-
TiO_2	1.3	-	3.6	3.2	-
Cr_2O_3	-	-	0.1	0.1	-
ZnO	-	-	0.5	0.5	-
PbO	-	-	0.1	0.1	-
Others	-	2.1	3.9	3.6	2.4
LOI	0.6	2.1	7.4	7.3	23.8
Specific density (g/cm^3)	2.90	2.14	2.87	2.89	2.54
Blaine specific surface area (m^2/kg)	460	325	165	295	490

6.2.2 Mixture design and specimen preparation

The reference blend (70 wt% GGBFS and 30 wt% CFA) was activated using sodium silicate solution (Ms = 1.4, Na_2O = 5.6 wt%). Different proportions of CFA were replaced with 33.3, 66.6 and 100 wt% BBA, corresponding to 10, 20 and 30 wt% of the total binder, respectively. The water-to-binder (w/b) ratio was maintained at 0.4 for the pastes based on the previous study on the alkali-activated slag and fly ash blends [300]. A higher w/b ratio of 0.45 was employed for the mortars to accommodate the water demand of the fine aggregates [301]. Notably, free water from the original sodium silicate solution was included in the calculation of the w/b ratio. Activator solutions with Ms of 1.0,1.4 and 1.8 were used to assess the influence of active [SiO_2] contents on the performance of the blended systems. The activating solution was naturally cooled to ambient temperature for 24 h before mixing. Furthermore, the role of BBA fineness was studied using 10 wt% and 20 wt% GBBA. The effect of additional AAW content (0.5 wt% to 2.5 wt%) was investigated in the groups with 10 wt% GBBA. Detailed information on mix proportions and flowability can be found in **Table 6.2**. Compared with the spherical shape of CFA particles, the angular shape of BBA and AAW particles results in a larger surface area and higher water demand. Therefore, increasing the dose of BBA and AAW decreases their flowability.

Paste and mortar samples were prepared for micro-scale and mechanical properties analyses. The paste samples were mixed using a laboratory mixer. The binder materials were first mixed for 1 min to reach a homogeneous state, followed by the addition of an activating solution. After stirring the bottom specimens for 30 s, then further mixed for another 120 s at a medium speed. The fresh paste was then cast into plastic molds of 40 × 40 × 160 mm^3 and vibrated for 1 min. A plastic film was applied to the top surface for 24 h curing. Finally, all specimens were demolded and cured at 20 ± 1°C with a relative humidity of 95% until the testing age. For the mortar samples, the corresponding standard sand was added during the stirring and the sand/binder ratio was set as 3 according to EN 196-1: 2016.

Table 6.2: The proportion of each material and flowability in the designed mixtures (wt%) (Na_2O wt% = 5.6).

ID	GGBFS	CFA	BBA	GBBA	AAW	Ms	w/b	Sand	Flowability (mm)	Setting time (min)
R0-1.4	70	30	0	-	-	1.4	Paste = 0.4 Mortar = 0.45	300	261	36/82
R10-1.4		20	10	-	-	1.4			223	32/76
R20-1.4		10	20	-	-	1.4			191	28/72
R30-1.4		0	30	-	-	1.4			157	26/70
R10-1.0		20	10	-	-	1.0			215	28/70
R10-1.8		20	10	-	-	1.8			228	36/82
R20-1.0		10	20	-	-	1.4			175	24/66
R20-1.8		10	20	-	-	1.8			198	32/78
G10-1.4		20	-	10	-	1.4			249	30/76
G20-1.4		10	-	20	-	1.4			224	28/70
G10A0.5		20	-	10	0.5	1.4			219	32/80
G10A1.5		20	-	10	1.5	1.4			189	38/86
G10A2.5		20	-	10	2.5	1.4			150	40/96

Note: G10-1.4 is also used as G10A0 in the comparison of additional AAW, and Ms is silicate modulus, initial/final setting time.

6.2.3 Methodology

- **Reactivity analysis of raw materials**

The reactivity of BBA, GBBA and AAW was evaluated by subjecting them to a high alkali concentration solution. Previous studies have established that an 8 M NaOH solution is adequate for activating fly ash and metakaolin [302,303]. Luo et al. utilized an 8M NaOH solution to investigate the reactivity of the ladle slag, a by-product of the steelmaking process [304]. Accordingly, an 8M NaOH solution was employed, with a liquid-to-solid (L/S) ratio of 50 to ensure a sufficient reaction. 20 g dry materials and alkaline solution were mixed in the sealed polyethylene bottles and placed horizontally on a linear reciprocating shaking device (Stuart SSL2) at a constant rate of 250 rpm with an amplitude of 20 mm for 24 h. Then the residual was collected by filtering with 0.45 μm paper and washed with deionized water. After 24 h vacuum drying at 60 °C, the residual mass was recorded, and its chemical and phase composition were characterized with XRF and XRD test. The calculation of reactive elements is normalized with the dry materials, as expressed by:

$$R_X = X_d - X_r \times \left(\frac{M_d}{M_r}\right) \quad \textbf{(6.1)}$$

Where the R_x is the reactive content of element x (%), X_d is the content of element x in the dry raw material (%), X_r is the content of element x in the residual (%), M_d is the mass of dry raw material used in the reactivity test (g), M_r is the mass of dry residual (g). Additionally, a similar treatment was performed on GBBA in distilled water to reveal its dissolution behavior.

- **Isothermal calorimeter**

The reaction kinetics of the blends were determined by an isothermal calorimeter (TAM Air, Thermometric). The raw materials were initially mixed according to the paste mixture. Then the activating solution was added for around 1 min vibration using an electrical vibrator. The mixed paste was injected into a sealed ampoule and loaded into the calorimeter. The heat release and heat flow results were normalized by the mass of the solid binder. The measurement was conducted for the first 160 h at a temperature of 20 ± 0.2 °C.

- **Workability and compressive strength**

The mini spread flow table test was conducted to determine the flowability of the fresh mortars according to EN 1015-3:2007. The fresh mortar was introduced into a truncated conical mold (60 mm in height, 100 mm in diameter at the bottom, and 70 mm in diameter at the top). After raising the mold vertically, the mortar was spread onto the disc by jolting the flow table 15 times. The diameter of the mortar in two perpendicular directions was then measured. The compressive strength of the mortar after 7 d, 28 d curing was measured according to EN 196-1:2016. A loading rate of 2400 N/s was applied to six specimens for each mixture. The obtained average value was recorded as the compressive strength value.

- **Leaching test of raw materials and hydrated samples**

The one-batch leaching test was performed with raw materials and 28 d paste samples (EN 12457-1:2002). The paste samples were crushed and milled into powders (0.125 ~ 1 mm), then mixed with distilled water in a polyethylene bottle with a liquid-to-solid (L/S) ratio of 10. Afterward, a similar shaking process was conducted with the sealed bottle on the Stuart SSL2 for washing at a constant rate of 250 rpm for 24 h. The solids were then filtered out, and the pH

of the leachate was measured. The element analysis was then carried out with inductively coupled plasma optical emission spectroscopy (ICP-OES Spectral Blue) and ion chromatograph (IC, Dionex 1100). The calculation of the leachable elements from each raw material and hydrated samples could be expressed by:

$$C_R = \frac{Ci \times Vi}{M_{raw}} \quad \textbf{(6.2)}$$

$$C_M = \frac{Ci \times Vi}{M_{mix}} \quad \textbf{(6.3)}$$

Where C_R and C_M are the leached amount of an element (mg/kg) from the raw materials and mixes, respectively, C_i is the concentration of an element (i) in the leachate (mg/L), V_i is the volume of the leachate (L), M_{raw} and M_{mix} is the mass of raw materials and mixes (kg), respectively. Then the solidification efficiency of an element in each mix was calculated by:

$$Ccl = \sum W_R \times C_R \quad \textbf{(6.4)}$$

$$E\% = 100 - \frac{C_M}{Ccl} \times 100\% \quad \textbf{(6.5)}$$

Where Ccl is the cumulative leachable capacity of an element (mg/kg) in each mix, W_R is the mass proportion of each ingredient in the mix (%), and E is the immobilization efficiency of the element in each mix (%).

- **Phase assemblage analysis of raw materials and hydrated samples**

The phase composition of the blended paste samples was analyzed by X-ray diffraction (XRD), Thermogravimetry (TG), and Fourier transform infrared spectroscopy (FT-IR). XRD characterization as performed on raw materials, the residual BBA after the reactivity test, and the hydrated assemblages. The test was carried out with a step size of 0.02° and a 2θ range from 10° to 60° (40 kV, 30 mA) by using a Bruker D4 phaser equipped with a Co X-ray tube. The PDF numbers of the identified phases are provided in **Appendix Table D.1**. The TG test was performed on the hydrated samples by a STA 449 F1 instrument test at a heating rate of 10 K/min up to 1000 °C under the N_2 atmosphere. The Fourier-transform infrared (FT-IR) spectrum of samples was conducted using a Varian 3100 instrument to identify the bonding in the mineral phases. All samples were scanned 15 times at a resolution of 1 cm^{-1} with a wavenumber range of 4000–400 cm^{-1}. To facilitate the identification of distinct bands and differentiate between wavenumbers, the second derivative of the measured transmittance (%) over the wavelength (cm^{-1}), denoted as d^2T/dW^2, was employed [141,305].

- **Mercury intrusion porosimetry (MIP) analysis of hydrated samples**

MIP analysis was performed to characterize the pore structure of the blends by using a mercury porosimeter (AutoPore IV 9500, Micromeritics). The hardened 28d pastes were crushed into around 4 mm granular pieces and then immersed in isopropanol to terminate the hydration. The pieces were vacuum-dried at 40 °C for 24 h before the test.

6.3 Results

6.3.1 Reactivity of BBA, GBBA and AAW

The reactive content within BBA, GBBA and AAW was assessed under conditions of high alkalinity solution, wherein minerals might undergo dissolution, and new reaction products could precipitate. Therefore, the mineralogical composition of raw materials was characterized both before and after the reaction. The results for GBBA are presented in **Fig. 6.3**, while **Appendix Fig. D.1** illustrates the corresponding findings for BBA. The raw BBA and GBBA primarily consist of quartz (SiO_2), anhydrite ($CaSO_4$), microcline ($K_2O{\cdot}Al_2O_3{\cdot}6SiO_2$), rutile ($TiO_2$), calcite ($CaCO_3$), lime (CaO) and smaller proportion of other minerals such as gehlenite ($2CaO{\cdot}Al_2O_3{\cdot}SiO_2$) and calcium titanium oxide ($CaTiO_3$). Significantly, certain minerals like anhydrite have shown susceptibility to dissolution, a fact supported by the XRD pattern analysis of the residues in distilled water (refer to **Appendix Fig. D.2**). These observations are further corroborated by the changes observed in the chemical composition, as demonstrated in **Appendix Table D.2**, wherein notable reductions in CaO and SO_3 levels are evident subsequent to the dissolution process in distilled water.

After 24 h of reaction with 8M NaOH solution, 17.6 g of residues remained for BBA and 17.2 g of residues for GBBA. The dissolution of anhydrite and lime was also observed during this process, as evidenced by the disappearance of associated peaks in the XRD patterns. Significantly, a higher mass loss in GBBA indicates an enhanced reactive content due to the milling process, as corroborated by the elevated reactive content of Ca, Al and Si as presented in **Table 6. 3**. Furthermore, traces of hydrotalcite-like phases ($Mg_6Al_2CO_3(OH)_{16}4H_2O$) are discernible around 13° (2θ, Co Kα) in both GBBA and BBA residues. In summary, BBA inherently possesses a certain amount of reactive content, contributing to the formation of hydrotalcite-like phases. The milling process of BBA further amplifies the reactive content within GBBA.

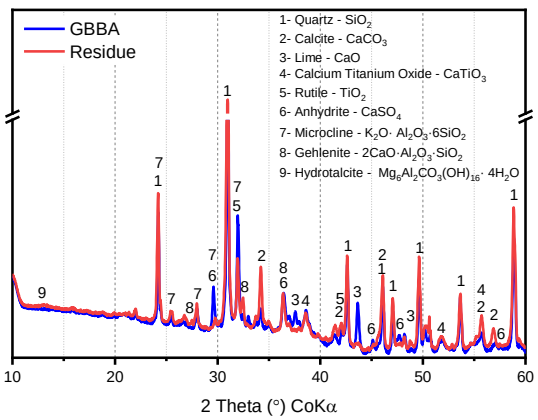

Fig. 6.3: XRD pattern of the raw GBBA and the residue GBBA after 24 h reactive test in 8 M NaOH solution. (Legend: 1- Quartz, 2- Calcite, 3- Lime, 4- Calcium titanium oxide, 5- Rutile, 6- Anhydrite, 7- Microcline, 8- Gehlenite, 9- Hydrotalcite).

In the case of AAW, no residues were detected after the reaction in the high-alkali solution. Given that the raw AAW comprises low-crystallinity boehmite (AlOOH), bayerite ($Al(OH)_3$), and thenardite (Na_2SO_4) (see detailed XRD pattern in **Section 6.3.3**), the reaction process is elucidated by [136,187]:

$$AlOOH + OH^- + H_2O \rightarrow Al(OH)_4^- \quad \textbf{(6.7)}$$

$$Al(OH)_3 + OH^- \rightarrow Al(OH)_4^- \quad \textbf{(6.8)}$$

The high reactivity of $[AlO_4]$ in AAW designates it as the aluminum source for the formation of aluminum-containing phases, including hydrotalcite-like compounds and C-A-S-H gels.

Table 6. 3: The chemical composition of the BBA/GBBA and residue BBA/GBBA after 24 h reactive test in 8 M NaOH solution.

Oxide (wt%)	MgO	Al_2O_3	SiO_2	P_2O_5	SO_3	K_2O	CaO	TiO_2	Fe_2O_3	Others	Mass (g)
BBA	2.9	6.2	48.9	1.3	2.9	1.9	17.3	3.6	3.0	4.6	20.0
Residue	2.7	5.5	47.1	1.1	0.1	1.3	14.4	3.3	3.0	4.0	17.6
Change	0.2	0.7	1.8	0.2	2.8	0.6	2.9	0.3	0.0	0.6	
GBBA	2.5	7.5	49.6	1.2	2.6	2.1	17.1	3.2	2.6	4.3	20.0
Residue	2.1	6.1	46.5	1.0	0.0	1.4	14.6	2.8	2.4	3.7	17.2
Change	0.3	1.4	3.1	0.2	2.6	0.8	3.5	0.4	0.2	0.6	

Note: all the chemical composition of the residue BBA/GBBA is normalized with the unreacted BBA/GBBA.

6.3.2 Reaction kinetics of BBA-GGBFS-CFA blends

Fig. 6.4 illustrates the hydration kinetics of all blends within the initial 160 h. The heat flow, normalized by the dry solid of the blended binder (with 10, 20 and 30 wt% BBA and the Ms = 1.4 of activator solution), is presented in **Fig. 6.4(a)**. The reaction process of alkali-activated materials generally includes four stages: dissolution, induction, acceleration and stable period [291,306]. The initial heat release from the dissolution of solid precursors is not depicted in the present results [307]. After that, a higher replacement level of BBA diminishes the intensity of heat flow peaks, indicating reduced heat release compared to R0-1.4. However, 10 wt% BBA exhibits the highest normalized cumulative heat within 168 h, suggesting its positive impact on reactivity. Considering that CFA has a relatively low influence on the reaction at an early age [301], substituting it with BBA does not lead to a significant reduction in heat release. Instead, the dissolution of minerals (lime and anhydrite) in BBA particles enhances the reactive $[Ca^{2+}]$ content, promoting the formation of C-(A)-S-H gel at an early age.

In **Fig. 6.4(b)**, when alkali solutions with various Ms are applied to blends containing 10 wt% and 20 wt% BBA, a higher Ms of the activator extends the induction stage and reduces the intensity of the primary heat flow peak. The increase in the SiO_2/Na_2O ratio in the activator leads to a drop in the alkalinity [308], thereby slowing down the dissolution of the solid precursors. A similar trend is observed in samples with 20 wt% BBA, where a lower Ms of the activator accelerates the reaction process.

In **Fig. 6.4(c),** the substitution of BBA with GBBA slightly promotes the reaction due to the finer particles, which facilitate the dissolution of lime and anhydrite, resulting in an increased release of reactive [Ca^{2+}] and accelerated hydration. Moreover, GBBA contains higher reactive Al_2O_3 and SiO_2 content compared to BBA, as outlined in **Section 6.3.1**, contributing to the gel formation and further augmenting the cumulative heat. Conversely, the presence of additional AAW in **Fig. 6.4(d)** retards the reaction process by consuming alkaline ions and reducing the alkalinity of the reaction environment.

Overall, the replacement of CFA by BBA does not significantly impact the reaction behavior, suggesting the feasibility of using BBA in blends from the perspective of the reaction process. Meanwhile, the reaction process can be regulated by adjusting the Ms of the activator and AAW content, with the finer BBA particles slightly enhancing the reaction.

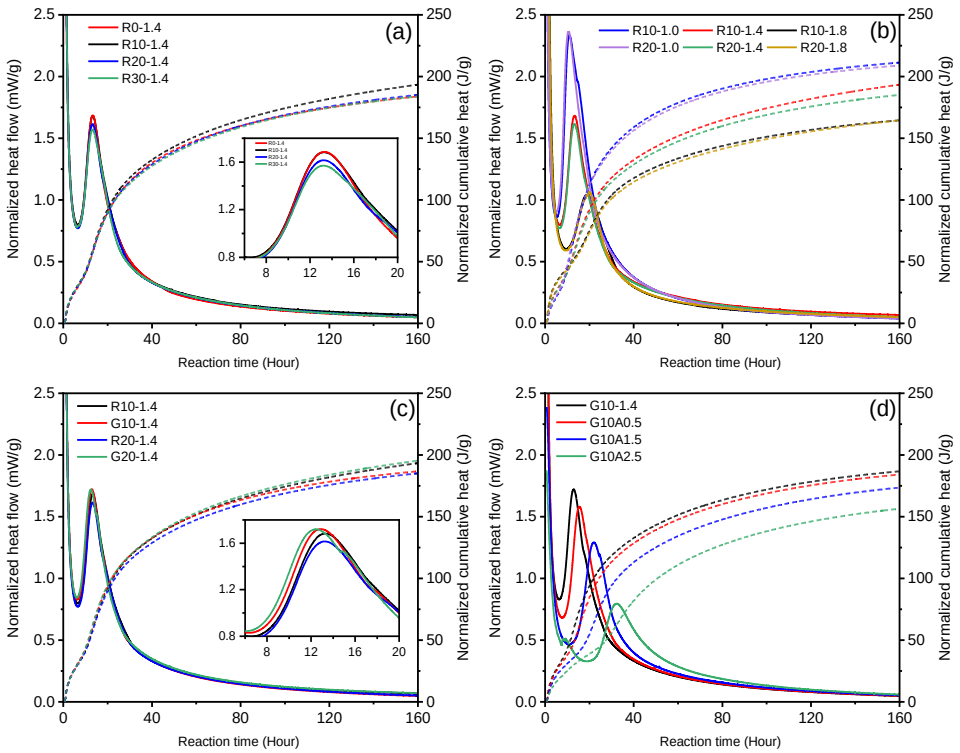

Fig. 6.4: normalized heat flow and cumulative heat flow of the blends within 7d (a): replacement levels of BBA, (b): silicate modulus, (c): particle size of BBA, (d): additional AAW.

6.3.3 Phase assemblages

- **XRD analysis**

The XRD patterns depicted in **Fig. 6.5(a)** illustrate the raw materials' mineralogical composition, while **Fig. 6.5(b-d)** offers a comparative analysis of the XRD patterns for all 28d samples. In the case of R0-1.4, the main crystalline phases identified include mullite ($Al_{4.8}O_{9.6}Si_{1.2}$), quartz (SiO_2), and calcite ($CaCO_3$), originating from raw CFA. The broad peaks around 34.2°(2θ) indicate the formation of amorphous C-(A)-S-H gel, which is considered the

main reaction product in AAMs [252]. For BBA-substituted samples (**Fig. 6.5(b)**), in addition to the phases observed in R0-1.4, traces of rutile (TiO_2) and calcium titanium oxide ($CaTiO_3$) originating from BBA are detected. Notably, minor peaks indicative of hydrotalcite-like phases are observed. As the BBA content increases, there is a corresponding augmentation in the intensity of these hydrotalcite-like phase peaks, suggesting the active involvement of BBA in their formation. In the GBBA-substituted samples G10-1.4 and G20-1.4, no substantial difference in crystalline phases is discernible when compared with the R10-1.4 and R20-1.4. This observation can be attributed to the similar chemical composition between GBBA and BBA.

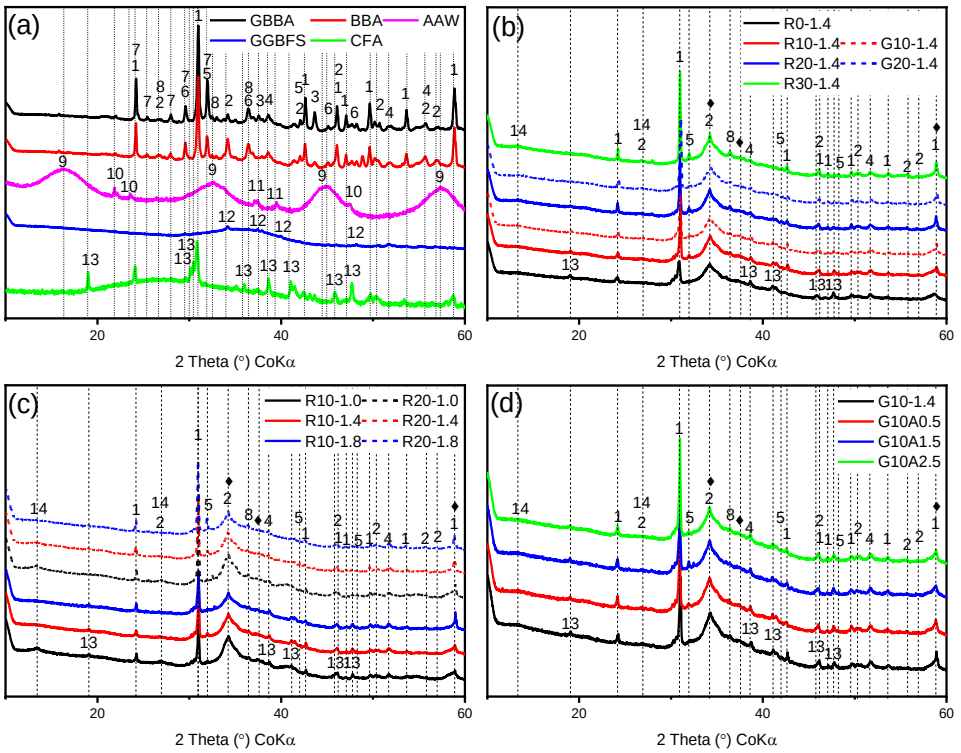

Fig. 6.5: XRD patterns of 28 d samples (Legend: 1- Quartz, 2- Calcite, 3- Lime, 4- Calcium titanium oxide, 5- Rutile, 6- Anhydrite, 7- Microcline, 8- Gehlenite, 9- Boehmite, 10- Bayerite, 11- Thenardite, 12- Hatrurite, 13- Mullite, 14- Hydrotalcite, ♦-C-(A)-S-H gel [247]).

When various activators are applied to the blends (**Fig. 6.5(c)**), discernible differences primarily manifest in the intensity of peaks corresponding to hydrotalcite-like phases and C-(A)-S-H gels. Activators with lower Ms exhibit heightened intensity, attributable to increased alkalinity accelerating the reaction process of the blends, as described in the reaction kinetics in **Section 6.3.2**. Consequently, an augmented formation of hydrotalcite-like phases and C-(A)-S-H gels at 28d is anticipated in R10-1.0 and R20-1.0. Notably, the lower proportion of SiO_2 in the activator directs a greater involvement of $Al(OH)_4$ in the solution toward the formation of a hydrotalcite-like phase rather than the formation of C-(A)-S-H gel [309].

In **Fig. 6.5(d)**, the incorporation of AAW into the blends is depicted, revealing no discernible new crystalline phase apart from those detected in G10-1.4. In summary, the main hydration products, including the hydrotalcite-like phase and C-(A)-S-H gel, persist regardless of BBA modification, activator modulus, and the introduction of additional AAW. In general, the hydrotalcite and related layered double hydroxides (LDHs) phases demonstrate the capacity for ion immobilization [310], making them widely applied in waste management [311]. The impact of these products on the leaching characteristics of the BBA-GGBFS-CFA system will be further addressed in **Section 6.3.5**.

- **FT-IR analysis**

In addition to the formation of a hydrotalcite-like phase, the gel products exhibit the capacity to adsorb the heavy metals on the surface and interlayer region [312,313]. Therefore, the impact of BBA content, fineness, activator modulus and additional AAW on gel characteristics was investigated using FT-IR, as depicted in **Fig. 6.6**. The FT-IR spectra of raw materials are presented in **Fig. 6.6(a)**. Two adsorption peaks are observed for raw GGBFS. The major band at around 900 cm^{-1} and 500 cm^{-1} corresponds to the asymmetric stretching vibration of Si-O-T bonds (T represents tetrahedral Si or Al units) [314]. The same vibration for CFA is shifted to around 1020 cm^{-1} due to the slightly different composition of the amorphous phase in the raw materials [78]. Bands at about 795 cm^{-1}, 776 cm^{-1} and 555 cm^{-1} confirm the presence of mullite and quartz in CFA [315]. For BBA and GBBA, the main adsorptions at 1418 cm^{-1} and 875 cm^{-1} are related to O-C-O bonds of carbonates [47], while the weak peaks at 612 cm^{-1} and 592 cm^{-1} are attributed to the vibrations of S-O from the anhydrite. AAW shows the bands around 3326 cm^{-1}, 1075 cm^{-1} and 482 cm^{-1}, corresponding to the O-H and Al-O vibrations from bayerite and colloidal boehmite. In **Fig. 6.6(b)**, which showcases the modified samples, all FTIR spectra show absorption bands around 3370 cm^{-1}, 1660 cm^{-1}, 1415 cm^{-1} and 950 cm^{-1}. These bands are associated with the stretching and bending vibration of H-O bonds, the stretching vibration of O-C-O bonds in carbonates, and the asymmetric and symmetric stretching vibration of Si-O-T bonds in $[SiO_4]$ and $[AlO_4]$, respectively [141].

The impact of BBA contents, fineness, Ms of activators and additional AAW on the structure of C-(A)-S-H gel is explored in **Fig. 6.6(c)** within a wavenumber range of 1200 – 600 cm^{-1}, recognized as a characteristic region for aluminosilicates [247]. The primary band centered around 950 cm^{-1} is commonly ascribed to Q^2 silica units within the C-(A)-S-H gel [263,316]. Notably, recent studies have posited that bands around 930 cm^{-1} and 1060 cm^{-1} may also contribute to Q^2- silicate species [317,318]. However, these potential adsorptions associated with Q^2-silicate are observed at 910 cm^{-1} in the BBA-GGBFS-CFA system, indicating a distinct degree of gel polymerization in AAMs compared to ordinary Portland cement. The signal at 810 cm^{-1} corresponds to the Si-O stretching of Q^1 tetrahedra [141], and the signal at 665 cm^{-1} is related to Si-O-Si bending vibrations [319]. The band at about 890 cm^{-1} has been correlated with the stretching vibration of Al-O-Si [320], while the band at 1050 cm^{-1} is associated with the symmetric bending of Al-O-H [141]. When BBA is incorporated, the intensities of Q^2 decrease with higher BBA content, particularly evident in R30-1.4, indicating shorter silica chains due to the release of more Ca^{2+} from the BBA. A similar decline is observed in the bands around 890 cm^{-1}, indicating less substitution of $[AlO_4]$ in C-(A)-S-H gel due to lower reactive aluminum content in BBA compared to CFA.

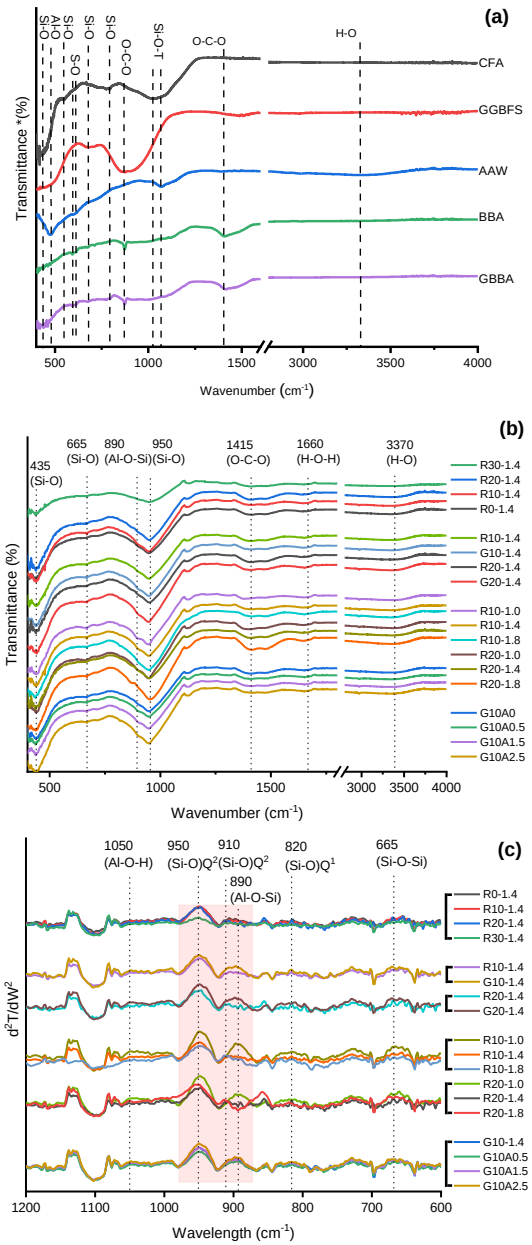

Fig. 6.6: FT-IR spectra of (a) the raw GGBFS, CFA, BBA, GBBA and AAW, and the 28 d samples with various BBA content, fineness, activator modulus and additional AAW: (b): transmittance vs wavelength, (c) 2nd derivative of the transmittance d^2T/dW^2 vs wavelength.

In comparison to BBA, the utilization of finer GBBA slightly enhances the intensity of Q^2 and the Al-O-Si bond owing to the presence of more reactive silicate and aluminum caused by the enhanced dissolution of the finer particles. These elements promote the polymerization of silica chains and the substitution of $[SiO_4]$ in the Q^2 sites by $[AlO_4]$. A similar intensified Q^2 bond is

observed when a smaller Ms activator is employed. Interestingly, despite the lower [SiO_2] content provided by the low Ms activator solution, heightened alkalinity enhances the dissolution of silicates from solid precursors, facilitating increased involvement in gel formation. This observation also aligns with the promoted heat of hydration, as discussed in **Section 6.3.2**. Furthermore, an enhanced Al-O-Si bond is observed, particularly in the low Ms activator, where the higher alkalinity also reinforces the dissolution of CFA and BBA particles, leading to an enhanced substitution of [AlO_4] in C-A-S-H gel.

Regarding the addition of AAW, no significant increase in the Al-O bond around 1075 cm^{-1} is observed, indicating sufficient dissolution of AAW in the system. The slightly growing absorption peak ascribed to the Si-O-Al bridge with increasing AAW confirms that [AlO_4] generated by AAW actively participates and displaces the Si-O-T tetrahedra within the gel. This process results in a negative charge within the gel, proving highly favorable for the adsorption and immobilization of heavy metals in the gel matrix [90]. To summarize, the outlined modifications, including grinding, lower Ms of activators, and additional AAW, can improve the incorporation of [AlO_4] in the gel products, which is beneficial for the solidification of heavy metals and ions within the matrix.

- **TG-DTG analysis**

Fig. 6.7 presents the TG and DTG curves of all 28d samples. The main mass loss peak (50 °C to 250 °C) is attributed to the dehydration of bound water from the C-(A)-S-H gel [57,321]. The shoulder around 250 °C and the broad peak around 400 °C in the DTG curves are associated with the dehydration of hydrotalcite-like phases [73]. Additionally, the decomposition of carbonates is observed at approximately 650 °C. While these carbonates mainly originate from raw materials, it is possible that some additional carbonates formed during the curing and preparation. Furthermore, a minor mass loss peak that occurs around 800 °C is related to the decomposition of C-(A)-S-H gel to wollastonite ($CaSiO_3$) [322].

To evaluate the quantity of reaction products, the mass loss attributed to dehydration was calculated using a tangential method and is presented in **Table 6.4** [164]. Compared with R0-1.4, the bound water content from gels decreases in the blends with BBA/GBBA substitutions, various activators and AAW additives. This decrease suggests a lower formation of C-(A)-S-H gel in the modified paste due to the replacement of CFA. It is important to note that the mass loss due to the dehydration of C-(A)-S-H gels overlaps with the dehydration of the hydrotalcite-like phases, making their separation difficult and potentially leading to deviations in the calculated bound water content of the gels. However, R0-1.4 exhibits the lowest bound water content between 250 °C to 500 °C, confirming the reduced formation of hydrotalcite-like phases in the referenced blend. In other words, after the modifications, more free water is bound in hydrotalcite-like phases, especially in samples with Ms of 1.0, aligning with the XRD patterns in **Fig. 6.5(c)**. Regarding the AAW-modified samples, there is less bound water in the gels, indicating that the reduced alkalinity weakens the gel formation due to the dissolution of AAW. However, it should be noted that the $Al(OH)_4^-$ contributes to the formation of hydrotalcite-like phases owing to the increase of $Al(OH)_4^-$ in the solution. In summary, the use of BBA/GBBA, activators with lower Ms, and additional AAW can promote the consumption of free water in the reaction system by forming hydrotalcite-like phases.

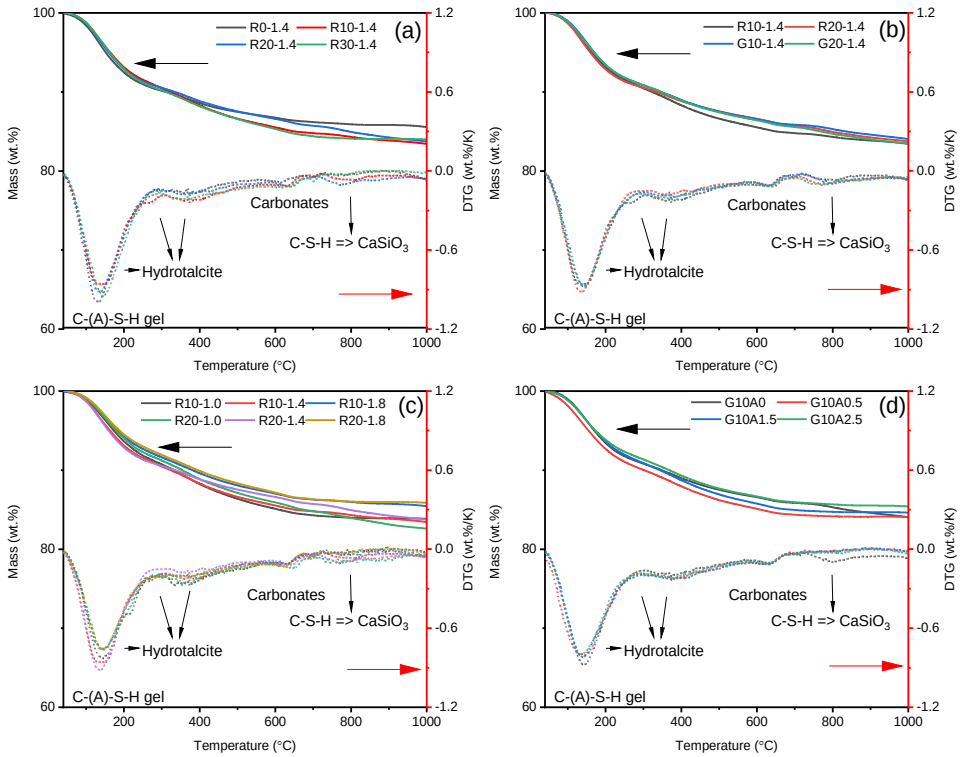

Fig. 6.7: Thermal analysis of the 28d pastes with different (a-b) BBA/GBBA content, (c) silicate modulus and (d) AAW content.

Table 6.4: Weight loss (%) at different temperature ranges in 28d samples.

Group	Weight Loss (%)		
	50-200°C Bound water from C-(A)-S-H gel	250-500°C Bound water from Hydrotalcite-like phases	(40-1000°C) Total weight loss
R0-1.4	8.94	3.51	14.38
R10-1.4	8.54	4.91	16.64
R20-1.4	8.72	4.80	16.33
R30-1.4	8.88	4.61	16.06
R10-1.0	8.08	5.48	16.07
R10-1.8	7.31	4.61	14.55
R20-1.0	7.79	5.16	17.45
R20-1.8	7.05	4.66	14.19
G10-1.4	8.60	4.55	16.04
G20-1.4	8.54	4.71	16.58
G10A0.5	8.94	4.85	15.92
G10A1.5	8.11	5.03	15.44
G10A2.5	7.66	4.66	14.60

6.3.4 Microstructure

The microstructural properties of the modified samples are associated with the physical encapsulation effect of heavy metals. MIP analysis of 28d samples was performed and the results are demonstrated in **Fig. 6.8(a-d)**. Pores in cementitious materials are typically classified as gel pores (< 10 nm), capillary pores (10 - 5000 nm) and macro-pores (> 5000 nm) [323]. The total porosity and the porosity of various size pores are summarized in **Fig. 6.8(e)**.

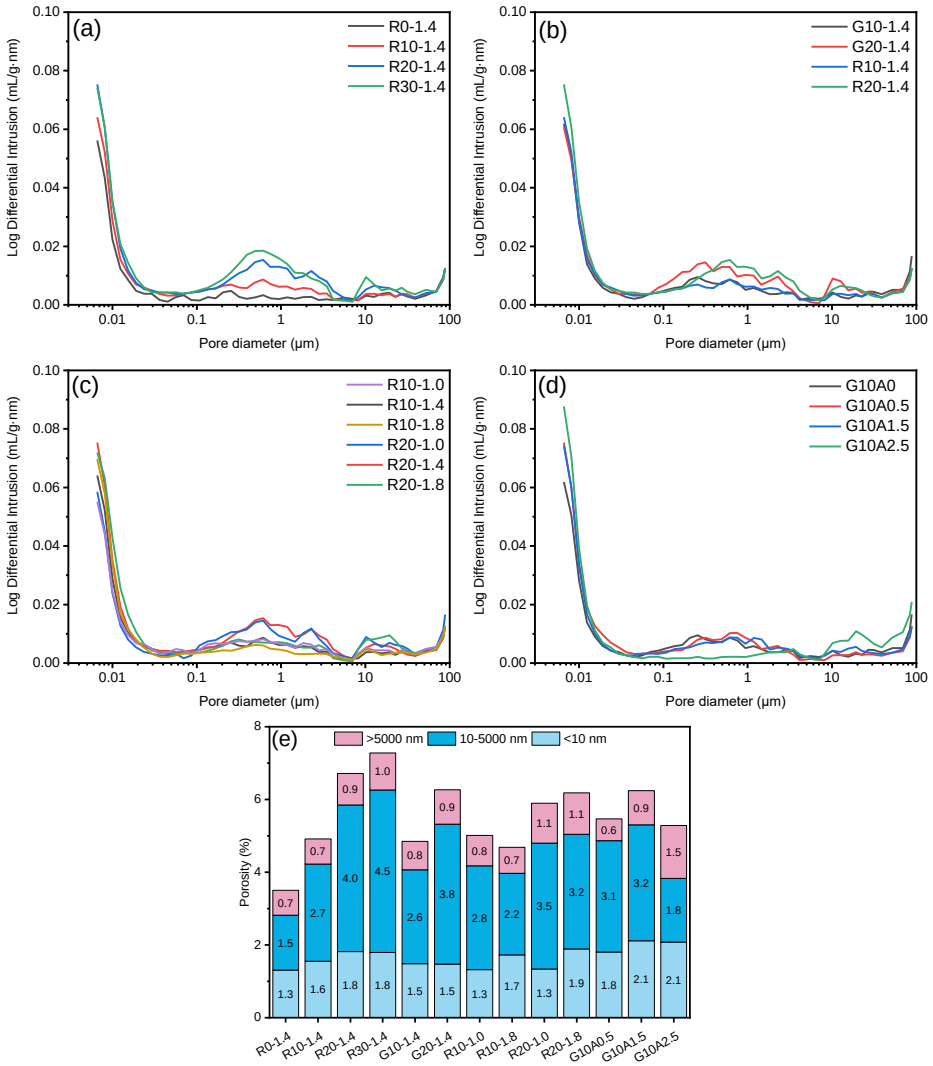

Fig. 6.8: (a-d) Pore size distribution and (e) Total porosity and the porosity of each type of pores in the prepared 28d pastes with various modifications.

Among the tested samples, R0-1.4 exhibits the lowest porosity of 3.5%, while the modifications increase the total porosity. This increase is mainly attributed to reduced workability after the incorporation of BBA/GBBA (**Table 6.2**), resulting in more capillary and macro-pores.

Nevertheless, the substitution of BBA promotes the gel pores, which is consistent with the increased amount of bound water from the C-(A)-S-H gel (**Table 6.4**). As demonstrated by Wang et al., the C-(A)-S-H gels with a higher Ca/Si ratio exhibit increased porosity and surface area [89]. Hence, the release of more soluble Ca^{2+} ions from BBA leads to their incorporation into C-(A)-S-H gel. Compared with BBA, GBBA has a less significant influence on gel pores, but there is a reduction in capillary pores and the total porosity, particularly evident in the G20-1.4 sample. This indicates that the finer particles act as a filler and refine the pore structure. Furthermore, a higher Ms activator leads to a reduction in capillary pores and the pore size due to the enhanced polymerization, as confirmed by the FT-IR spectra in **Fig. 6.6**. In the AAW-modified samples, the porosity of gel pore increases with more AAW, indicating that the dissolved $Al(OH)_4$ participates in the formation of gel products. However, excessive AAW addition also results in a higher content of macro-pores due to the worse workability. Overall, the modifications provide control over the pore size distribution of the matrix. In terms of reducing heavy metals leaching pathways, the use of GBBA and higher Ms activators can help reduce the capillary pores and macro-pores, while increasing Ms and AAW promotes the formation of gel pores.

6.3.5 Leaching behavior

From an environmental perspective, the leaching behavior of raw materials and BBA-GGBFS-CFA blends were characterized. **Table 6.5** summarizes the leaching values of raw BBA, GBBA, GGBFS, CFA and AAW, with limits established by the Dutch Soil Quality Decree (SQD) regarding the acceptable emissions for inorganic pieces [324].

Table 6.5: The leaching of BBA and AAW obtained via a one-batch leaching test (mg/kg dry mass of materials).

E/I	BBA	GBBA	AAW	GGBFS	CFA	SQD*
Cl^-	**4590**	**4640**	**3490**	406.3	4.85	616
SO_4^{2-}	**19270**	**19220**	**69910**	1226	2172	2430
As	UDL	UDL	0.04	UDL	UDL	0.90
Pb	**304.37**	**457.5**	0.12	UDL	UDL	2.30
Zn	**28.95**	**39.59**	0.01	0.14	UDL	4.50
Ba	1.76	3.70	0.05	2.25	15.4	22.0
Cr	**25.39**	**34.63**	**0.79**	0.26	**2.06**	0.63
Cu	0.16	0.35	0.05	UDL	UDL	0.90
Mo	**3.28**	**3.27**	0.17	UDL	**5.28**	1.00
Sb	UDL	UDL	0.04	UDL	UDL	0.32
B	2.85	2.39	45250	0.12	29.7	
Mg	0.03	0.04	13.28	0.19	UDL	
Sr	40.46	43.72	0.73	17.6	45.5	
Na	2430	2480	41280	246.9	255.5	
K	6070	6270	24	128.4	113.7	
Ca	6120	8470	133	1720	993.8	
Al	0.08	0.12	0.46	UDL	0.93	
pH	12.8	12.9	8.4	11.5	11.6	

Note: pH value of the leachate at L/S10, UDL: Under detect limitation <0.02 mg/kg, SQD*: Unshaped material as specified by the legislation: Soil Quality Decree [324], E/I: elements or ions, the values in **bold** are above the limits of SQD.

In the raw BBA and GBBA particles, the leaching contents of chloride (Cl^-), sulfate (SO_4^{2-}), lead (Pb), zinc (Zn), chromium (Cr) and molybdenum (Mo) significantly exceed their legal values, posing a primary concern for their use in building materials. It is noteworthy that GBBA exhibits a higher concentration of heavy metal concentration compared to BBA, indicating that these ions are more easily leached out from the finer particles. Additionally, the contents of Cl^-, SO_4^{2-}, and Cr in AAW, as well as the contents of the Cr and Mo in CFA, surpass the established limits. Therefore, this study focuses on solidifying the aforementioned heavy metals and anions in the BBA-GGBFS-CFA blends.

Table 6.6 summarizes the leaching contents of Cr, Mo, Zn, Pb, Cl^- and SO_4^{2-} from the 28d BBA-GBFS-CFA blends. A significant reduction in the leaching of heavy metals, chloride and sulfate is evident in all blends. For the leaching of Pb, its concentration falls below detection limits, showcasing remarkably low levels. The notable reduction in Pb leaching has been attributed to its precipitation as silicate species ($PbSiO_3$, Pb_2SiO_4, Pb_3SiO_5), a phenomenon well-established in previous studies [173,325,326]. Additionally, it has been reported that Pb was present in the form of $Pb(OH)_2$ in alkali-activated fly ash/blast furnace slag [327]. Within the BBA-GGBFS-CFA blends, the activators contain abundant silicate ions with high alkalinity, offering substantial capacity to immobilize the leached Pb. Moreover, recent studies have indicated that soluble Pb can be chemically bonded into the amorphous 3D network of the hydrates [90,313].

Concerning the leaching of Zn, its concentration is detectable solely in low Ms activators activated samples (R10-1.0 and R20-1.0). The lower Ms results in increased alkalinity of the solution [134], contributing to the formation of soluble oxyanionic $Zn(OH)_4^{2-}$ [84]. Consequently, Zn species are not easily immobilized through simple precipitation or ion exchange with alkali cations balancing the negatively charged Al tetrahedra. Overall, a reduction in Zn leaching can be observed, potentially attributed to Zn-bearing phases, such as the $Zn_4Si_2O_7(OH)_2 \cdot H_2O$, γ-$Zn(OH)_2$, $CaZn_2(OH)_6 \cdot 2H_2O$ [328,329]. Unfortunately, these phases could not be detected in the present XRD patterns due to the relatively low Zn concentration. Furthermore, previous studies have confirmed the incorporation of Zn within the matrix of C-S-H [330,331].

Regarding the leaching of Cr, its concentration exhibits an increase with a higher proportion of BBA, since Cr is mainly derived from BBA. The elevated leaching from finer particles of GBBA is understandable, attributing to the heightened surface area. However, a lower activator modulus contributes to a reduction in Cr leaching. Several factors may contribute to this observation. Firstly, the promoted formation of hydrotalcite-like phases in samples R10-1.0 and R20-1.0 plays a significant role in diminishing Cr leaching, as it could be incorporated into the hydrotalcite layer framework through isomorphic substitution for Mg and Al ions [332]. Secondly, the high alkalinity induces the precipitation of $Cr(OH)_3$, while the abundant Ca^{2+} promotes the formation of $CaCrO_4$ [333]. The introduction of additional AAW initially reduces Cr leaching, but a further increase in AAW leads to an increase in Cr leaching. This phenomenon can be attributed to the dissolution of AAW, which increases the substitution of $[AlO_4]$ in the silica chain, thereby enhancing the adsorption of Cr. Furthermore, previous studies [334,335] have suggested that boehmite has a remarkable adsorption capacity for Cr, indicating that the amorphous boehmite in the AAW used may contribute similarly. However, it is noteworthy that excess AAW reduces the alkalinity of the pore solution, adversely affects

workability, and induces more macro-pores (**Fig. 6.8**), facilitating the migration of Cr during leaching.

Table 6.6: One batch leaching test of 28d blends (mg/kg dry mass of materials).

E/I*	Cr	Mo	Zn	Pb	Cl^-	SO_4^{2-}	pH
R0-1.4	0.04	0.49	UDL	UDL	94	992	12.36
R10-1.4	0.15	0.44	UDL	UDL	165	1567	12.41
R20-1.4	0.2	0.4	UDL	UDL	255	**1984**	12.45
R30-1.4	0.33	0.33	UDL	UDL	344	**2992**	12.46
G10-1.4	0.24	0.38	UDL	UDL	185	1663	12.43
G20-1.4	0.33	0.31	UDL	UDL	258	**1987**	12.46
R10-1.0	0.14	0.5	0.09	UDL	189	1569	12.5
R10-1.8	0.18	0.44	UDL	UDL	161	1629	12.32
R20-1.0	0.19	0.41	0.12	UDL	267	**1980**	12.53
R20-1.8	0.33	0.37	UDL	UDL	237	**2090**	12.36
G10A0**	0.24	0.38	UDL	UDL	185	1663	12.43
G10A0.5	0.15	0.35	UDL	UDL	182	1510	12.42
G10A1.5	0.2	0.39	UDL	UDL	165	1598	12.4
G10A2.5	0.22	0.42	UDL	UDL	144	1702	12.38
Limit	1	0.63	4.5	2.3	616	1730	-

Note: UDL: Under detect limitation <0.02 mg/kg, *E/I: elements or ions, **G10A0 = G10-1.4, the values in **bold** are above the limits of SQD.

In contrast to Cr, the leached Mo concentration decreases with increasing substitution of BBA, as Mo is mainly sourced from CFA. Compared to BBA, an equivalent amount of GBBA reduces Mo leaching, indicating the positive effect of the increased reactivity of GBBA on the reaction products, as evidenced by the reduced capillary pores (**Fig. 6.8**). Moreover, increasing the Ms of activators leads to reduced leaching of Mo. This is due to the lower pH of the pore solution, which limits the solubility of Mo [336]. Additionally, the leaching of Mo oxyanions is assumed to be regulated by the dissolution of $CaMoO_4$ [337]. Therefore, a lower pH environment in the pore solution proves advantageous for controlling the leaching of Mo, as a decreased pH leads to a higher concentration of Ca^{2+}. A similar effect is achieved when AAW is added. However, excessive AAW results in adverse leaching of Mo due to the defective encapsulation caused by the increased pore structure (**Fig. 6.8**).

The leaching of Cl^- and SO_4^{2-} exhibits an increase with the BBA and GBBA content. This trend is consistent with the leaching behavior observed for Cr^-, where BBA serves as the primary source for the leaching of these ions. Nevertheless, the utilization of lower Ms activators leads to an increase in Cl^- leaching, accompanied by a reduction in SO_4^{2-} leaching in the blends. This observation aligns with the findings of Tao et al., who attributed such behavior to the distinct selectivity of hydrotalcite-like phases for SO_4^{2-} ions rather than Cl^- ions [338]. Furthermore, in comparison to G10-1.4, a higher addition of AAW induces a reduction in Cl^- leaching within the blends. Unlike Cl^- leaching, the leaching of SO_4^{2-} initially experiences a decline with the addition of AAW but subsequently increases with further increments in AAW content. The decrease in leached anions can be attributed to the capacity of AAW to promote the formation of additional gel pores (**Fig. 6.8**), facilitating the absorption and immobilization of anions within the matrix. However, it is crucial to note that AAW inherently contains leachable sulfate, and augmenting its dosage results in a concurrent elevation in SO_4^{2-} leaching. Overall, Cl^- leaching

remains significantly below its respective legal limits. However, substantial concentrations of SO_4^{2-} are notably observed in blends containing 20 wt% BBA/GBBA or higher, surpassing the legal threshold. This occurrence is attributed to the inherent anhydrite content, leading to an increased leachable sulfate. Consequently, addressing the leaching of sulfate in blends with high BBA dosage necessitates further consideration.

It is also noteworthy that the decrease in the leaching level of toxic elements can be partially attributed to the dilution effect, given the relatively lower proportion (10 wt% - 30 wt%) of effective BBA content in the binders. Hence, based on the above findings, it could be concluded that effective solidification of Cr, Mo, Pb, Zn, Cl^- and SO_4^{2-} can be achieved in the BBA-GGBFS-CFA blends through physical encapsulation, dilution, adsorption and precipitation. There are no leaching concerns when applying a 10 wt% BBA substitution in the hybrid blends.

6.3.6 Mechanical properties

To evaluate the mechanical properties of BBA-GGBFS-CFA blends as a building material, the compressive strength at 7d and 28d was tested, and the results are presented in **Fig. 6.9**. The compressive strength exhibits a decrease with BBA substitution in **Fig. 6.9(a)**. This decline can be attributed to the relatively larger particle size of BBA, leading to reduced flowability and a lower packing density of the fresh mortar. Furthermore, BBA shows relatively low reactivity, resulting in a weaker matrix with less gel production, which aligns with the observed increase in capillary pores within the matrix. However, GBBA slightly enhances the compressive strength in **Fig. 6.9(b)**. This improvement can be partially ascribed to the enhanced flowability, facilitating the expulsion of air voids and reducing capillary pores. The finer particles of GBBA also contribute to a significantly refined packing density of the matrix, as indicated by the observed decrease in the proportion of capillary pores within the matrix. Furthermore, as outlined in **Section 6.3.1**, more reactive [SiO_4] and [AlO_4] from GBBA can promote gel formation. Considering the influence of Ms on the blends in **Fig. 6.9(c)**, the activator with a higher Ms enhances the 7d compressive strength, regardless of the BBA replacement level. The high Ms activator solution provides more reactive [SiO_2] content, which can be integrated into the silica chain of the C-(A)-S-H gel. Notably, R10-1.0 and R20-1.0 exhibit better 28d compressive strength compared with R10-1.4 and R20-1.4. This enhancement could be attributed to the better hydration of CFA at a later age due to the higher alkalinity in activators. Upon introducing AAW in **Fig. 6.9(d)**, the compressive strength decreases with higher AAW dosage. This can be explained by the dissolution of AAW, which consumes alkaline ions and slows down the dissolution process of GGBFS, consequently reducing gel formation, as evidenced by the decreased bound water in the C-(A)-S-H gel (**Table 6.4**).

In conclusion, the compressive strength of the hybrid binder ranges from 36.8 MPa to 58.8 MPa at 28 d, making it suitable as a substitute for various types of cement in terms of mechanical performance according to BS EN 192-1. Furthermore, the mechanical property of the blends can be regulated by adjusting the BBA content, fineness, silicate modulus, and the addition of AAW, allowing customization to meet specific construction requirements.

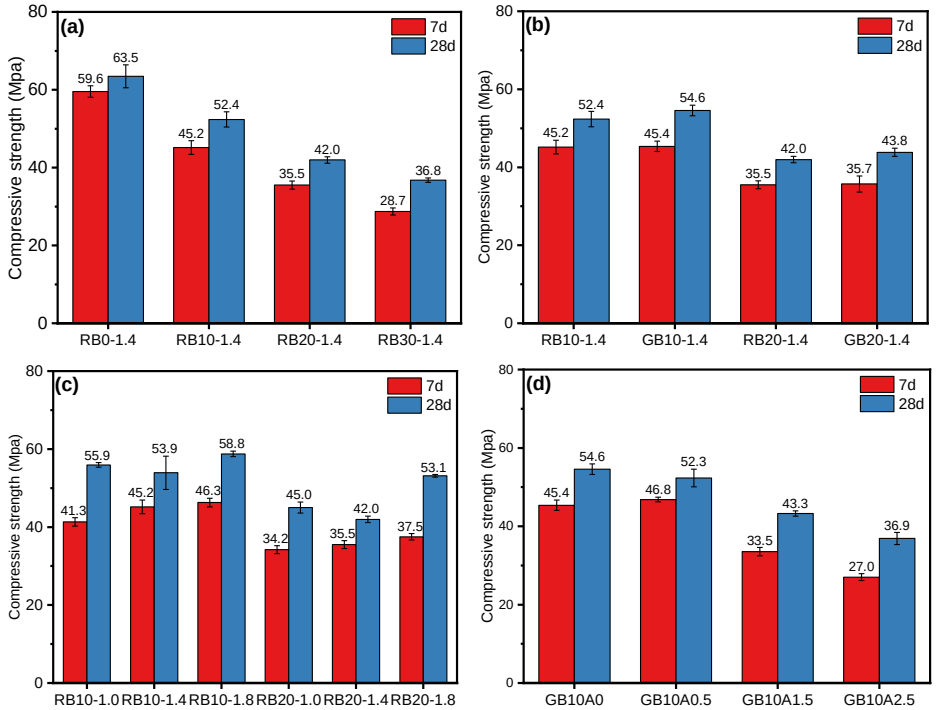

Fig. 6.9: Compressive strength of all blends at the age of 7d and 28d.

6.4 Discussions

In an effort to alleviate the environmental repercussions associated with landfill disposal and the substantial quantity of BBA (approximately 10,000 tons in the Netherlands), this chapter advocated for the utilization of BBA as construction materials, alongside GGBFS and CFA. Several factors, including the BBA content, fineness, silicate modulus of the activator, and the incorporation of additional AAW, were systematically investigated to optimize the solidification of BBA within alkali-activated materials. Studies have indicated that these factors can impact diverse final properties of the hybrid binders, making it unfeasible to achieve optimal performance across all properties with a singular mixing ratio. For instance, a higher modulus contributes to improved mechanical performance but it is also associated with higher Cr and sulfate leaching. Hence, optimizing the final properties of hybrid binders is a complex task that cannot solely rely on adjusting a single factor. This study delves into the individual impacts of these factors on the curing properties of hybrid binders to establish a theoretical foundation for practical applications. To provide clarity on these effects, the role of the mentioned factors in influencing the composition of reaction products and pore solutions is further explicated by comparing the variations in the leach solution concerning $[Al(OH)_4^-]$, $[Si(OH)_4^-]$, $[Ca^{2+}]$, and $[Na^+]$ ions (**Fig. 6.10**).

6.4.1 The effect of BBA content

In **Fig. 6.10(a)**, the concentrations of $[Al(OH)_4^-]$, $[Si(OH)_4^-]$, $[Ca^{2+}]$, and $[Na^+]$ exhibit a similar trend. Initially, the ion concentrations decrease with a 10 wt% BBA. However, a subsequent

increase in the BBA content leads to a higher concentration. This suggests that the 10 wt% BBA optimizes each ion in the precipitation of reaction products, consistent with the findings of promoted hydration heat (**Fig. 6.4**). The additional BBA mainly provides more Ca^{2+} and Na^{+} ions, while having less impact on $Si(OH)_4^-$ ions due its low reactivity, thereby making less contributions in compressive strength. On the contrary, the irregular shape of BBA particles induces more capillary pores (**Fig. 6.8**), resulting in the reduction of the mechanical performance.

6.4.2 The effect of BBA fineness

In **Fig. 6.10(b)**, an increase in fineness does elevate the concentration of $[Al(OH)_4^-]$, $[Si(OH)_4^-]$, $[Ca^{2+}]$, and $[Na^+]$, favoring the formation of reaction products. However, there is minimal growth in $[Si(OH)_4^-]$ concentration, suggesting that the improved mechanical properties of G10-1.4 and G20-1.4 are mainly due the filler effect of GBBA, enhancing particle packing and reducing the capillary pores within the binder (**Fig. 6.8**). It is crucial to note that the increased fineness induces higher leaching of toxic elements from BBA (**Table 6.6**). Additionally, the milling process of BBA incurs higher costs for raw material pre-treatment. Hence, the decision to grind BBA should be carefully weighed against the actual budget and performance indicators.

6.4.3 The effect of silicate modulus

Fig. 6.10(c) illustrates the impact of the silicate modulus of the activator on the concentration of $[Al(OH)_4^-]$, $[Si(OH)_4^-]$, $[Ca^{2+}]$, and $[Na^+]$ in the leachate. The rise in activator modulus correlates with an increased concentration of $[Si(OH)_4^-]$, leading to more leachable $[Si(OH)_4^-]$ in the pore solution. Interestingly, the concentrations of $[Al(OH)_4^-]$, $[Ca^{2+}]$, and $[Na^+]$ exhibit an inverse trend. One potential reason for this phenomenon is that the ample $[Si(OH)_4^-]$ in R20-1.8 contributes to the consumption of $[Al(OH)_4^-]$, $[Ca^{2+}]$, and $[Na^+]$, forming N/C-(A)-S-H gel. The enhanced production of gel leads to a reduction in capillary pores (**Fig. 6.8**), consequently improving the mechanical properties of the binder. Conversely, the insufficient $[Si(OH)_4^-]$ in R20-1.0 results in higher concentrations of $[Al(OH)_4^-]$, $[Ca^{2+}]$, and $[Na^+]$. This promotes the formation of hydrotalcite-like phases, as supported by the higher bound water derived from the hydrotalcite-like phases in TG results (**Table 6.4**). The selection of the modulus primarily relies on the desired mechanical properties and leaching performance.

6.4.4 The effect of additional AAW

The influence of AAW on the concentration of $[Al(OH)_4^-]$, $[Si(OH)_4^-]$, $[Ca^{2+}]$, and $[Na^+]$ in the leachate is summarized in **Fig. 6.10(d)**. The incorporation of AAW leads to relatively low concentrations of $[Ca^{2+}]$, which may impede the formation of the C-(A)-S-H gel, consistent with the decreased bound water observed in **Table 6.4**. This reduction in Ca^{2+} is linked to decreased alkalinity resulting from AAW dissolution, thereby contributing to the deterioration in mechanical performance. On the other hand, the high leaching of B from AAW (**Table 6.5**) may contribute to Ca^{2+} consumption through the precipitation of calcium borate ($CaO{\cdot}3B_2O_3{\cdot}8H_2O$, $CaO{\cdot}B_2O_3{\cdot}6H_2O$) or ulexite ($NaCa[B_5O_6(OH)_6]{\cdot}5H_2O$) [339]. Despite these effects, the co-disposal objective of BBA and AAW has been achieved, with acceptable leaching behavior and desirable mechanical performance for use as building materials.

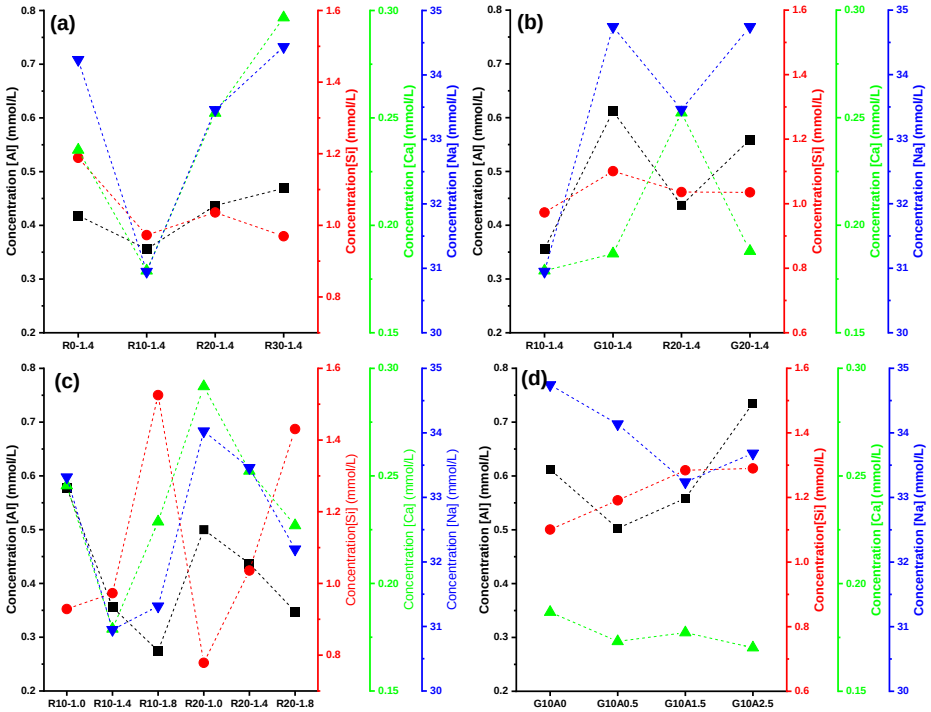

Fig. 6.10: Cation variation of the leachate from the 28d BBA-GGBFS-CFA blends ([Al], [Si], [Ca],[Na]).

6.5 Conclusions

This work investigates the hydration process in alkali-activated BBA-GGBFS-CFA blended binder and its potential for heavy metal immobilization. The effect of BBA content, BBA fineness, silicate modulus of activator and AAW on reaction kinetics, hydration products, microstructure and mechanical properties of the blends are investigated, as well as the leaching behavior of hybrid binders. The following conclusions can be drawn:

- BBA exhibits lower reactivity compared to CFA but still contains reactive minerals that can form hydrotalcite-like phases in highly alkaline solutions. The dissolution and polymerization of the hybrid blends are enhanced by 10 wt% BBA, as evidenced by a greater cumulative hydration heat release. The main hydration products are the C-(A)-S-H gels, with BBA replacement accelerating the reaction process and enhancing gel products.

- The compressive strength of the GGBFS-CFA-BBA blends ranges from 36.8 to 58.8 MPa at 28d, correlating with BBA substitution levels, fineness, silicate modulus and additional AAW, indicating their potential application as building materials.

- The hybrid blends effectively immobilize the high-leachable Cl^-, SO_4^{2-}, Cr, Mo, Pb, and Zn content from BBA/GBBA. No heavy metal leaching exceeding the Dutch legal limit

occurs within the 10 wt% G/BBA substitution level. However, high SO_4^{2-} leaching needs to be addressed when pursuing higher substitution levels of BBA.

- AAW retards the reaction process of GBBA-GGBFS-CFA blends, leading to strength degradation. However, a low AAW dosage enhances the immobilization efficiency of toxic ions. Co-disposal of AAW and BBA is feasible, exhibiting no new leaching problems and providing sufficient compressive strength for building material.

- This chapter offers insights into optimizing hybrid blends for sustainable alkali-activated materials, crucial for solidifying secondary industrial by-products. The proposed waste-to-resource model promotes circular economy principles by utilizing waste-combined AAMs as an alternative to ordinary Portland cement and effectively addresses heavy metals leaching from waste materials.

Chapter 7 Advancing self-cleaning performance in metakaolin-based geopolymers through in-situ zeolite formation and TiO_2 integration

The deterioration of self-cleaning properties of cementitious materials upon hydration was addressed by in-situ zeolite formation within metakaolin-based geopolymers. Pastes with varied in-situ zeolite content were formulated by adjusting the Si/Al ratio of initial raw materials and curing temperatures. The impact of in-situ zeolite formation on self-cleaning performance was systematically investigated through phase composition, optical property and microstructure analyses. Zeolite A formation notably enhances self-cleaning performance, despite contributing to higher band energy and lower Urbach energy. The increases in crystalline zeolite amount and matrix porosity enhance mass transfer capacity. The open pore structure of zeolite facilitates the formation of connective channels during particle growth, mitigating the "sheltering" effect of the surrounding media for photocatalysts and ensuring improved self-cleaning performance upon hydration. This chapter summarizes the synthesis conditions for zeolite A, providing mechanistic insights into in-situ zeolite formation in metakaolin-based geopolymers and emphasizing its promising potential for optimizing self-cleaning properties in cementitious materials.

This chapter is partially published elsewhere:

X. Ling, D.R. Liu, K. Schollbach, W. Chen, Advancing self-cleaning performance in metakaolin-based geopolymers through in-situ zeolite formation and TiO_2 integration, Cement and Concrete Composites, 150, 105567, 2024.

7.1 Introduction

Geopolymers, produced by mixing aluminosilicate precursors (e.g., fly ash, blast furnace slag and metakaolin) with an alkali solution, have gained extensive attention as sustainable binders due to their utilization of industrial by-products, leading to low CO_2 emissions compared to traditional Portland cement [30,340,341]. Using geopolymers as the carrier of photocatalysts offers an advantage in eliminating the retarding effect of OH^- generated during the PCO process, as OH^- would engage in the hydrolysis of aluminosilicate precursors. Sanalkumar et al. have proposed the incorporation of TiO_2 in metakaolin-based geopolymers (MKG), reporting the enhanced contaminate decomposition capacity with TiO_2 addition [342]. Moreover, Kaya-Özkiper et al. investigated the photocatalytic degradation of methylene blue in red mud and metakaolin-based geopolymers, determining an optimal TiO_2 dosage of 3.7 wt% [343]. Strini et al. tested the NO_X degradation capacity of fly ash/metakaolin-based and organic-modified

photocatalytic geopolymers at the film level and observed superior photocatalytic properties compared to the OPC-based matrix [344]. These studies have affirmed MKG's potential as a photocatalyst carrier for enhanced photocatalytic self-cleaning. Nevertheless, there is limited knowledge about the impact of various reaction products within MKG on photocatalytic performance despite the use of many different activators (modulus), concentrations and curing conditions resulting in diverse physicochemical properties of reaction products that can influence photocatalytic efficiency [340,345–347].

MKG predominantly yields amorphous sodium aluminosilicate hydrate (N-A-S-H) gel with a network structure consisting of Si-O and Al-O tetrahedra connected by shared oxygen atoms, closely resembling zeolites. The N-A-S-H gel is often considered a zeolite precursor with an amorphous structure, lacking long-range order [348]. Under specific conditions, such as a suitable Si/Al ratio in the initial raw materials and elevated curing temperature, crystalline zeolites with stable crystal structures and well-defined channels can be formed within geopolymers. Notably, both commercial zeolites and synthesized zeolites have demonstrated remarkable efficacy as supports for semiconductor photocatalysts in the removal of toxic organic pollutants [349]. Renowned for their highly porous structure, adsorption capabilities, and surface catalytic properties, these zeolites play a pivotal role in enhancing the overall performance of the photocatalytic process [350]. Yang et al. have proposed using synthesized-zeolite, obtained from the reaction of fly ash beads in an alkali solution, as a carrier for photocatalysts in the OPC. The outcomes show significantly improved photocatalytic efficiency and long-term performance of photocatalytic cementitious materials [351]. However, when applied in the MKG, the external zeolite phases may dissolve during the alkali-activation process [352,353], leading to a reduction in zeolite content within the matrix. This implies that the utilization of external zeolite as a photocatalyst carrier may not be effective in MKG. Hence, this study explores the in-situ formation of zeolite to enhance the photocatalytic properties of MKG. The phase composition of in-situ zeolite formation in MKG is influenced by the mole ratios of Si/Al and Na/Si in initial raw materials for polymerization, leading to distinct structures and properties of zeolites [350,354]. For instance, zeolite X, characterized by the faujasite structure, exhibits a high cation exchange capacity [340], making it highly adaptable for diverse applications such as heavy metal adsorption, separation of small molecules and serving as a catalyst in fluid catalysis cracking [355]. Conversely, zeolite with the Linde Type A (LTA) structure, distinguished by its hydrophilic nature and ion-exchange capabilities, is

extensively employed in household detergents and ion-exchange membranes [356,357]. Therefore, a compressive understanding of the contributions of in-situ zeolite with these distinct properties to the photocatalytic process could prove beneficial in designing MKG with enhanced photocatalytic performance [358].

With the potential of MKG for photocatalytic applications established, this chapter aims to answer the following questions: 1) the interactions between photocatalysts and reaction products within MKG, and 2) the role of in-situ zeolite formation in the photocatalytic process of TiO_2-modified MKG. Therefore, the primary objective of this chapter is to uncover the mechanisms behind photocatalytic performance attributed to in-situ zeolite formation. Sodium-based activators with various modulus were utilized to adjust the Si/Al ratio of initial raw materials and the subsequent reaction products (with/without zeolite formation). Meanwhile, different levels of zeolite formation were achieved under elevated curing temperatures (45°C), and their influences on the photocatalytic performance were quantitatively investigated. Multiple characterization techniques, including quantitative X-ray diffraction (Q-XRD), thermogravimetric analysis (TGA), mercury intrusion porosimetry (MIP), and scanning electron microscopy (SEM), were employed to characterize the physicochemical properties of the prepared MKG. Additionally, self-cleaning performance was assessed under UV light, measuring the discoloration process of Rhodamine B (RhB).

7.2 Materials and Experiments

7.2.1 Raw Materials

Metakaolin (METAMAX®, sourced from BASF) was utilized as the precursor for geopolymer preparation. The chemical composition of metakaolin is detailed in **Table 7.1**. The high reactive silica and aluminate contents enable comprehensive alkali activation. Two sodium-based alkali solutions were prepared as activators, both with an equivalent Na_2O of 27.2 wt% (Na/Al mole ratio=1.0). The first solution consisted of pure sodium hydroxide solution, prepared by dissolving the required amount of NaOH pellets (> 98.5%, sourced from VWR Chemicals) in deionized water. The second solution combined sodium silicate solution (Mass ratio 26.9% SiO_2, 8.0% Na_2O, 65.1% H_2O, sourced from Labshop) with NaOH pellets. Prior to casting, these alkaline solutions were prepared and retained in sealed glass bottles for 1 d to achieve equilibrium. Titanium dioxide nanoparticles (< 22.5 nm 120 particle size, 99.7 wt% trace metals basis, Sigma-Aldrich) were employed to confer photocatalytic properties to the geopolymers.

Table 7.1:Chemical and physical properties of metakaolin.

Oxides [%]	CaO	SiO_2	Al_2O_3	Fe_2O_3	K_2O	Na_2O	TiO_2	Others	LOI	Surface area [m^2/g]	d50 [μm]
Content	0.04	52.3	45.2	0.42	0.15	0.22	1.54	0.32	0.79	14.2	5.43

7.2.2 Specimen preparation

Table 7.2 shows the mix design of MKG. 5 wt% TiO_2 was utilized as the photocatalyst, a level that has demonstrated desirable photocatalytic performance for MKG in previous studies [342]. The water-to-binder (w/b) ratio was maintained at 1.0, consisting of 70 wt% free water and 30 wt% water from the activators. Initially, TiO_2 powder was dispersed in 70 wt% free water using ultrasonic dispersion for 15 min, with the addition of 0.5 wt% nonionic surfactant (Triton X-

405, Dow Chemical) to enhance TiO_2 dispersion [112,359]. Subsequently, this mixture was blended with metakaolin in a laboratory mixer at a low speed for 3 min, and a polycarboxylate-based superplasticizer (ViscoFlow-37, Sika) was employed to adjust the consistency of the fresh mixtures. Finally, the activator solution was introduced under medium-speed stirring for 5 min.

The fresh geopolymer was cast into 4 × 4 × 16 cm^3 plastic molds and covered with three layers of film, then cured at ambient temperature for 24 h. It is well-known that the polymerization process of geopolymer is highly sensitive to curing temperature [360]. Therefore, the demolded geopolymers were sealed in plastic bags and cured at 20 °C and 45 °C for 24 h, respectively. All samples were moved into a curing room (20 ± 2 °C, 90% RH) until the test ages.

Table 7.2: The mass ratio of each material in the designed mixtures.

Group	Metakaolin	NaOH	Waterglass	w/b	TiO_2	Si/Al	Na/Al	Temperature
RAr	100	35.05	-	1.0	-	1.0	1.0	20°C
RA1.0	100	35.05	-		5	1.0		20°C
RA1.2	100	31.63	42.80		5	1.2		20ºC
RHr	100	35.05	-		-	1.0		45°C
RH1.0	100	35.05	-		5	1.0		45°C
RH1.2	100	31.63	42.80		5	1.2		45°C

Note: The Si/Al and Na/Al mole ratio calculations include the Si or Na from the Metakaolin and activators, as well as Al from the metakaolin.

7.2.3 Methodology

- **Q-XRD and TGA analysis**

All the samples at the test age were crushed and immersed in isopropanol for 24 h to terminate hydration. Subsequently, the isopropanol was removed by using diethyl ether, followed by vacuum drying at 40 °C for 24 h. It should be noted that this process assumes the complete removal of surface and inter-pore free water [164].

The crystalline phases of the geopolymers after 7d and 28d curing were characterized by X-ray diffraction (XRD) analysis using a Bruker D4 PHASER equipped with a LynxEye detector and Co X-ray tube. The test was conducted with a step size of 0.02° and a 2θ range from 10° to 90° (40 kV, 30 mA). The Rietveld method was applied for the quantitative analysis. The test samples, mixed with 10 wt% Silicon Powder (Internal standard), were milled in an XRD-Mill McCrone for 10 min. The XRD patterns were analyzed with High-score plus and quantified using TOPAS Academic software v5.0. The crystal structural data used in the analysis are provided in **Table 7.3**.

Approximately 50 mg of powders from each mixture was used for TGA in a Jupiter STA 449 F1 from Netzsch. The samples were heated from 40 °C to 1000 °C at a heating rate of 10 K/min with N_2 as carrier gas.

Table 7.3: Structural data of the phases used for the XRD analysis.

Mineral name	Chemical formula	# PDF-reference	ICSD
Zeolite A	$Na_{12}(Al_{12}Si_{12}O_{48})(H_2O)_{27}$	01-089-8015	088329
Anatase	TiO_2	01-084-1285	202242
Silicon	Si	00-005-0565	-
Zeolite X	$Na_2Al_2Si_{2.4}O_{8.8}\cdot 6.7H_2O$	00-012-0246	-

- **FT-IR analysis**

The functional groups of the raw materials and the 7d and 28d cured MKG were analyzed with FT-IR spectroscopy. The analysis was conducted using a Varian 3100 instrument, and all samples were scanned 30 times at a resolution of 4 cm^{-1} within a wavenumber range of 4000 - 400 cm^{-1}.

- **MIP analysis**

The 7d and 28d paste samples were crushed into around 4 mm granular pieces. These pieces were then immersed in isopropanol to terminate the reaction and subsequently dried in a vacuum oven at 40 °C for 24 h. The porosity and pore size distribution of these pieces were analyzed using a mercury porosimeter (AutoPore IV 9500, Micromeritics) with an absolute pressure range from 0.7 kPa to 230 MPa and a contact angle of 130 °.

- **Optical properties**

After 7d and 28d of curing, the geopolymers were cut into pieces with a size of 4 ×4×1 cm^3. The top surface (4×4 cm) was then polished using a series of SiC sandpapers (P250, P400, P600, P1200 and P2500). The polished surface was washed with ethanol and cleaned using a high-pressure blower to remove any debris. The diffuse reflection spectra of the polished surface were measured by a UV-VIS-NIR spectrophotometer (Lambda 750, Perkin Elmer) equipped with a 150 mm integrating sphere. The test was conducted within a wavenumber range of 250-800 nm at a scanning speed of 2 nm/s [111,361].

- **Self-cleaning properties**

The self-cleaning properties were analyzed through the discoloration process of Rhodamine B (RhB) under UV irradiation. Initially, a 0.1 mM RhB solution was sprayed onto the polished surface of specimens for staining, which was subsequently left to naturally dry in a dark environment for 24 h at 22 ± 2 °C, 65% RH. Following the drying period, the RhB-stained surface was evaluated using Ocean Optics Spectrometers at four different times, with 16 evenly distributed points. The CIE Lab color parameter a^* was measured within a wavelength range of 380~780 nm. The average color value was used as the a_0^* for each group. The samples were then exposed to a UV lamp with a light intensity of 10 ±0.05 W/m^2 for various durations: 15, 45 105, 225, 420, 1275, 1800, 4300, and 7200 min. The average a^* value of the discolored surface was recorded, and the color change efficiency was calculated by:

$$\varphi = \left(a_0^* - a_t^*\right)/a_0^* \times 100 \quad \textbf{(7.1)}$$

Where φ is the color change efficiency of each geopolymer (%), a_0* is the value without UV irradiation, and a_t^* is the value of a^* after t min of UV irradiation.

- **Scanning electron microscope (SEM) and EDX analysis**

After the termination of hydration, flaky specimens from the crushed 28d samples were collected and coated with gold (Au) using a Quorum 150TS plus sputter coater. The micro-morphological structure of the reaction products was observed using a scanning electron microscope (SEM) equipped with an energy-dispersive X-ray diffraction (EDX) detector (Phenom Pro). For the elemental composition analysis of the reaction products, a bulk piece of the dried samples was selected and impregnated in epoxy resin. After hardening, the samples were polished with SiC sandpapers (P250, P400, P600, P1200 and P2500) and cleaned in an isopropanol ultrasonic bath. After slight vacuum drying, the surface was coated with Au, and spot analysis was conducted on each sample at a voltage of 15 kV.

7.3 Results

7.3.1 Phase assemblages analysis

Fig. 7.1 shows the XRD patterns of raw metakaolin, 7d and 28d cured MKG. Raw metakaolin often contains a trace amount (0.6 ~ 1.8 wt%) of anatase (TiO_2), as reported in some previous studies [190,362,363]. Therefore, the peaks belonging to anatase are inevitably observed in our raw MK and groups RAr and RHr. Since the surface self-cleaning property is generally affected by the effective exposure of TiO_2 particles, the contribution of both the original anatase and the added anatase to the self-cleaning property of MKG is then considered in the present work.

The broad hump observed around 25 - 30° (2θ) in raw metakaolin indicates the presence of the highly reactive amorphous aluminosilicate content. When the alkaline solution is incorporated, this broad hump shifts to 30 - 40° (2θ), indicating the formation of amorphous aluminosilicate gels (N-A-S-H gel) with a different structure [364]. N-A-S-H gel, as the predominantly amorphous product in geopolymers, has been suggested to be related to the precursor gel for zeolite formation [365,366]. However, to date, no studies have verified whether such precursors are equivalent to crystalline zeolite in terms of self-cleaning properties in geopolymers. Therefore, the in-situ formation of crystalline zeolite and amorphous gels will be discussed separately.

In the 7d RAr sample, alongside the N-A-S-H gel, zeolite A forms as one of the main hydration products, as expressed by

$$2Si(OH)_4 + 2Al(OH)_4^- + 2Na^+ \rightarrow 0.167\ Na_{12}(AlO_2)_{12}(SiO_2)_{12}\cdot 27H_2O(\text{Zeolite A}) + 3.5H_2O \quad \textbf{(7.2)}$$

in which the reactants are assumed to be the monomers. Zeolite A comprises sodalite cages formed by connecting to the six nearest neighboring sodalite cages through double four-membered rings [367], resulting in an excellent ion exchange capacity and satisfactory hydrophilic properties. Thus, the yield of zeolite A is of importance for the self-cleaning property, as summarized in **Fig. 7.2**. The formation of zeolite A in RAr is 5.3 wt%, whereas it increases to 15.2 wt% in RHr, indicating the promotion effect of the curing temperature on the reaction process [364]. A similar increase, from 9.0 wt% to 11.6 wt%, is also observed in RA1.0 and RH1.0. Notably, a higher content of zeolite A is formed in RA1.0 compared to RAr. Previous research has documented the role of TiO_2 nanoparticles in promoting hydration product formation in cement systems, with studies attributing this phenomenon to the nucleation effect of TiO_2 nanoparticles [368,369]. Drawing parallels from these findings, it is

reasonable to speculate that TiO_2 could have a similar influence on the hydration process of metakaolin. However, the opposite is the case in the RHr and RH1.0 concerning the production of zeolite. A. Oleksiak et al. have reported that the formation of zeolite in porous materials also is influenced by the confinement (pore size), where a higher energetic barrier for nucleation will exist in smaller pores [370]. Therefore, the group RHr, without the filling of TiO_2, may exhibit a higher pore size, contributing to nucleation and growth of zeolite. Notably, the peaks ascribed to zeolite A are not observed in the RA1.2 and RH1.2. This is mainly because the increased amount of silicate from the activators can form cages and rings, and their lability decreases, thereby slowing the exchange rate of cyclic- or cage-like oligomeric species for the zeolite formation [371,372]. It also proves the feasibility of adjusting the Si/Al ratio of the binder to control zeolite formation.

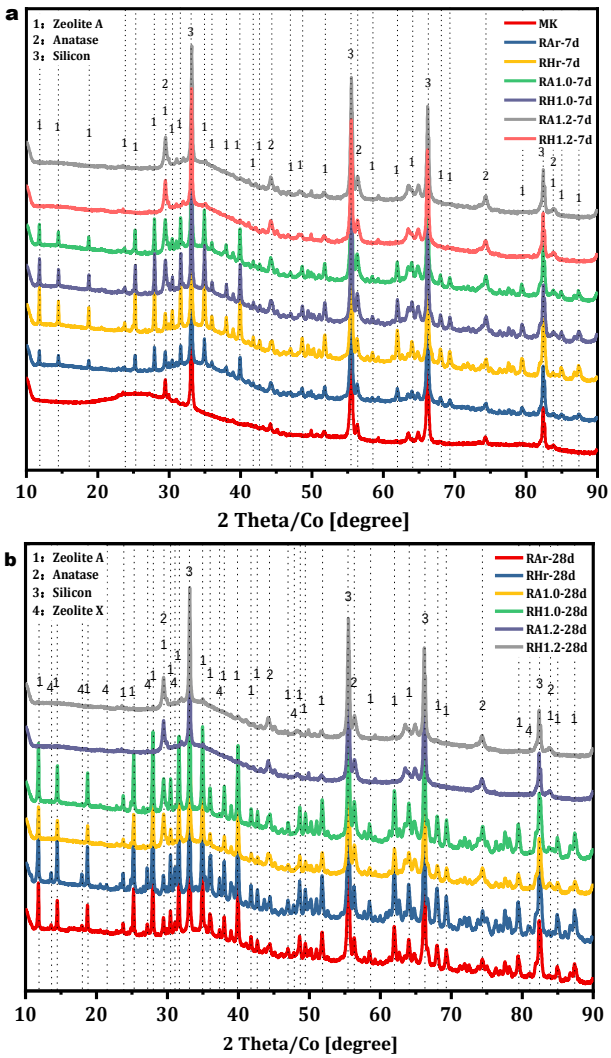

Fig. 7.1: XRD patterns of the raw metakaolin, 7d (a) and 28d (b) MKG. The patterns are displaced vertically for clarity. Silicon is externally incorporated as an internal standard for the Q-XRD analysis.

It should be noted that zeolite X forms in the 28d RAr and RHr samples as expressed by

$$2.4Si(OH)_4 + 2Al(OH)_4^- + 2Na^+ \rightarrow Na_2(AlO_2)_2(SiO_2)_{2.4}\cdot 6.7H_2O(\text{Zeolite X}) + 2.1H_2O \quad \textbf{(7.3)}$$

Zeolite X is also based on the sodalite cage structure and shows a high cation exchange capacity [340]. Different from zeolite A, the sodalite cage in Zeolite X is connected to the four nearest neighboring sodalite cages through double six-membered rings [367]. The formation of zeolite A and zeolite X highly depends on the NaOH concentration [367,373,374]. A high NaOH concentration is necessary for the formation of Zeolite A, while a lower one produces zeolite X. Similar results have been reported by Kuneki et al. in the synthesis of zeolite A and zeolite X using NaOH and Class C fly ash [375]. Thus, with the hydration process of MKG, the alkaline activator is gradually consumed for the reaction products, and the consequent concentration reduction leads to Zeolite X formation. Overall, based on the Q-XRD analysis, it is feasible to control the formation and yield of zeolite within MKG using the various Si/Al ratios of starting materials and curing temperatures, and greater zeolite formation is confirmed with the hydration progress.

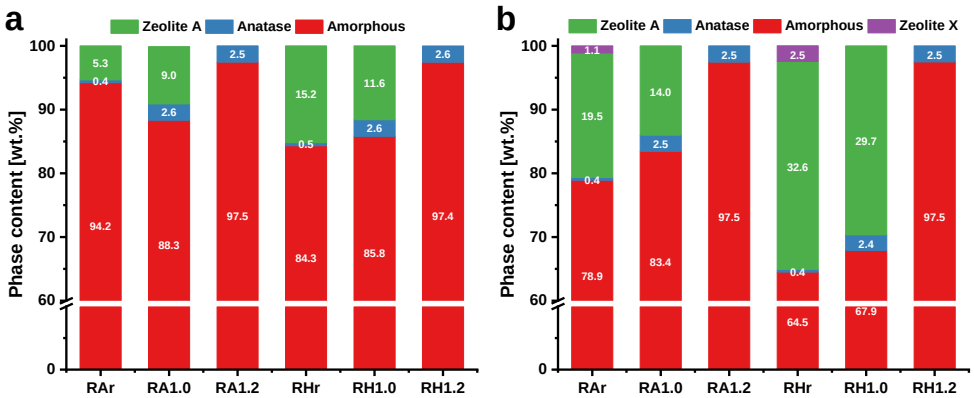

Fig. 7.2: The proportion of each mineral phase in the 7d (a) and 28d (b) geopolymers. (Note: the calculated proportion of anatase in MKG includes the added anatase and the original anatase from raw metakaolin. The amorphous content comprises the unreacted metakaolin and N-A-S-H gel.

Thermogravimetric analysis (TGA) and differential thermogravimetric analysis (DTG) were conducted on the 7d and 28d MKG samples, and the results are presented in **Fig. 7.3**. The major mass loss, occurring between 60-350 °C, is ascribed to the dehydration of N-A-S-H gel and zeolite phases [376–378]. Notably, due to the tightly bound nature of the water within the zeolite cage structure [379], there is an observed shift of dehydration peaks towards higher temperatures as the zeolite content increases. This shift is particularly evident in the 28d RA/Hr and RA/H1.0 samples. However, precisely quantifying the mass of bound water separately for N-A-S-H gel and zeolite is challenging due to the peak overlap in the DTG curves. Additionally, in our specific case, variations in the practical bound water content in zeolite may be influenced not only by temperature but also by distinct chemical compositions in different mixes [380]. Therefore, **Table 7.4** summarizes only the total bound water along with the free water content.

At 7d, all samples show an increased total bound water with higher curing temperature, indicating enhanced metakaolin reactivity due to elevated curing temperature. Notably, when comparing with RAr and RHr, the additional TiO_2 in RA1.0 and RH1.0 contributes to higher

total bound water, consistent with increased reaction products in **Fig. 7.2**. RA1.2 and RH1.2 samples exhibit a slight increase in total bound water content compared to RA1.0 and RH1.0, associated with the promoted release of silicate species from high Ms activators, fostering a more continuous gel network formation [376]. In simpler terms, the ordered structure of the crystalline zeolite restricts bound water retention, while the amorphous N-A-S-H gel structure retains more bound water. At 28d, the prolonged hydration process results in increased total bound water content, attributed to the higher reaction degree of the metakaolin. Interestingly, a higher increasing rate of bound water is observed in RAr and RHr in **Table 7.4**. This finding is associated with the formation of Zeolite X during the later stage of hydration, aligning with the Q-XRD results depicted in **Fig. 7.2**.

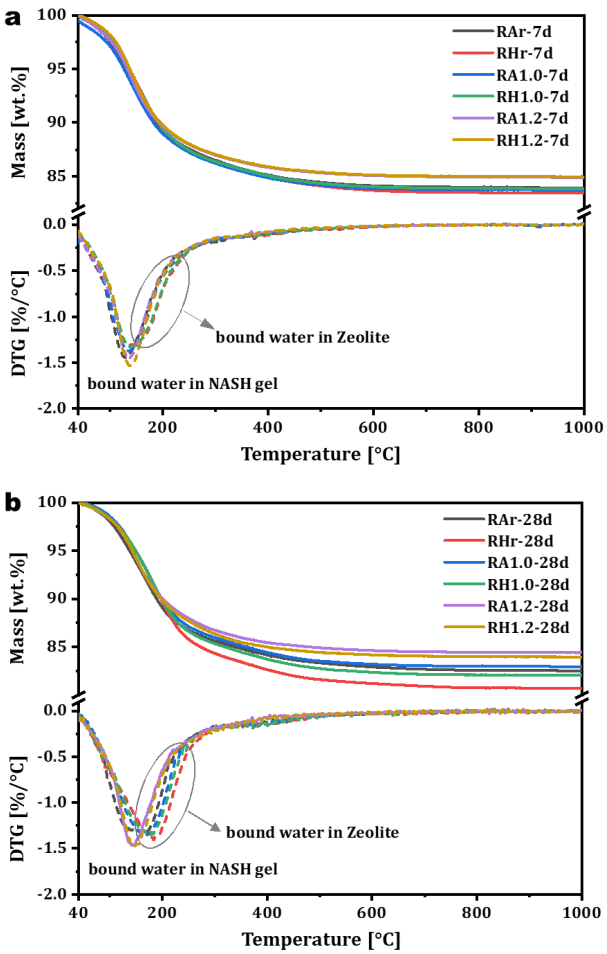

Fig. 7.3: TG and DTG curves of the 7d (a) and 28d (b) MKG.

In MKG, aside from chemically bound water, the predominant water state in the MKG is free water in pores [381]. Previous studies have noted the potential expulsion of interstitial water during curing [190,382]. However, no expelled water was observed during demolding, possibly due to the lower w/b ratio of 1.0, in contrast to the higher ratio used in the previous study [190],

facilitating free water retention within the matrix. Though a minor portion of this free water may evaporate during the curing process, this specific water content is not factored into the present calculation of free water. The calculation is simplified by subtracting the total bound water from the total added water, as shown in **Table 7.4**. Specimens of the same curing age exhibit a consistent level of pore water, crucial as a reaction medium in the photocatalytic process where the hydroxyl radicals (·OH) are generated through the reaction of photogenerated holes (h^+) and hydroxyl ions (OH^-). The uniform pore water level in all specimens implies an equivalent capacity to convert the resulting degradation byproducts under UV irradiation, eliminating the influence of free water on self-cleaning efficiency. It also explains the photocatalytic process on the matrix surface is influenced by the environmental humidity, leading to the self-cleaning performance test being conducted under controlled humidity conditions. Further analysis of the effect of the Si/Al ratio on the functional group, optical properties, and microstructure of MKG will be elaborated in the following sections.

Table 7.4: Detailed water content in the 7d and 28d MKG (wt%).

Group	7d		28d		Increasing rate of bound water from 7d to 28d (wt%)
	Bound water [a] Mass loss (60-350 °C)	Free water [b]	Bound water [a] Mass loss (60-350 °C)	Free water [b]	
RAr	21.40	78.60	23.59	76.41	10.3
RHr	21.96	78.04	26.39	73.61	20.2
RA1.0	21.64	78.36	23.85	76.15	10.2
RH1.0	22.22	77.78	25.19	74.81	13.4
RA1.2	22.00	78.00	23.10	76.90	5.0
RH1.2	22.34	77.66	24.03	75.97	7.6

Note: all values are normalized by the mass of the initial metakaolin.

a. The total bound water is calculated with the weight loss between 60 to 350 °C

b. Free water = Total water – Total bound water.

7.3.2 Function group identification

Fourier-transformed infrared spectra of the raw materials and MKG are shown in **Fig. 7.4**. In the infrared spectrum of the raw metakaolin (**Fig. 7.4(a)**), three adsorption peaks are observed. The major bands at 1062 cm^{-1} and 434 cm^{-1} correspond to the Si-O-Si stretching vibration and bending vibration, respectively. Additionally, a minor band at 792 cm^{-1} is assigned to the Al-O-Si stretching vibration [383]. Raw anatase exhibits its primary adsorption peak at 428 cm^{-1}, attributed to the Ti-O-Ti bonds within the TiO_2 lattice [384].

Upon the incorporation of the alkaline solution in 7d samples **Fig. 7.4(b)**, the main band shifts from 1062 cm^{-1} to a lower wavenumber at around 960 cm^{-1}. This shift has been reported as an indicator of aluminosilicate dissolution and restructuring due to the polymerization of N-A-S-H gel [385]. It should be noted that the Si-O-Al bonds in TO_4 tetrahedra in zeolites may overlap with this absorption [386,387]. Furthermore, with an increase in the Si/Al ratio in the starting materials, the bandwidth of this adsorption widens in RA1.2 and RH1.2. According to Ozer's study characterizing MKG with different Si/Al ratios in the starting materials [383], the difference in bandwidth is primarily induced by variations in the crystallinity level of

geopolymers. Consequently, groups with more amorphous phase formation, as indicated by Q-XRD analysis (**Fig. 7.2**), exhibit a broader bandwidth.

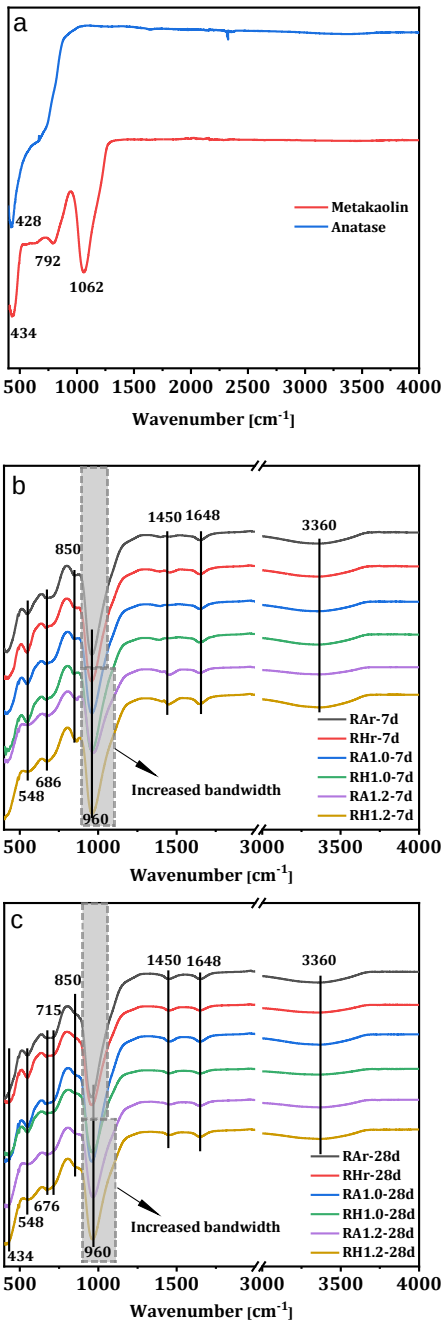

Fig. 7.4: FT-IR spectra of the (a) raw metakaolin and anatase, (b) 7d and (c) 28d MKG. The spectra are displaced vertically for clarity.

Meanwhile, the band centered around 548 cm^{-1} in RAr, RHr, RA1.0 and RH1.0 is a characteristic feature attributed to the formation of double four-membered rings in zeolites [386,388]. However, this absorption is absent in the RA1.2 and RH1.2 samples, confirming limited crystalline zeolite formation when the Si/Al ratio increases to 1.2. The adsorption at around 3360 cm^{-1} and 1648 cm^{-1} is assigned to the stretching and bending vibrations of chemically bound water, respectively. Additionally, slight peaks of the O-C-O bond are observed around 1450 cm^{-1} and 850 cm^{-1}, potentially due to carbonation during curing and testing [47].

In the 28d samples in **Fig. 7.4(c)**, similar differences in increased bandwidth around 960 cm^{-1} and decreased intensity of the peaks around 548 cm^{-1} are observed for the same reason as explained earlier. Additionally, the intensified adsorption around 434 cm^{-1} and 715 cm^{-1} in RAr and RHr is associated with zeolite X, as evidenced by Q-XRD results [388]. Overall, the incorporation of TiO_2 in RA1.0 and RH1.0 does not lead to any significant changes when compared to RAr and RHr. This might be due to the overlap between the Ti-O-Ti adsorption around 428 cm^{-1} and the Si-O-Si bending vibration around 434 cm^{-1}. Besides, while some researchers have reported the synthesis of composite photocatalysts using TiO_2 hydrosols and detected Si-O-Ti bonds located at approximately 950 cm^{-1} [111,389,390], these bonds are not evident in the present spectra. This absence could be attributed to the overlap with the Si-O-Al bonds in the geopolymer. Additionally, it may be related to the fact that crystalline TiO_2 does not participate in the polymerization reaction process of the geopolymers. Nevertheless, based on the FT-IR results, the cage structure of zeolite in the RAr, RHr, RA1.0 and RH1.0 is verified.

7.3.3 Optical band gap energy and Urbach energy

UV-VIS-NIR reflection spectra of 7d and 28d MKG were measured. The band gap energy (E_g) of each sample can be determined using Tauc's plot method with the following equations [391]:

$$\alpha = (1 - R)^2/2R \quad \textbf{(7.4)}$$

$$\alpha \cdot hp \cdot \nu = \left(hp \cdot \nu - E_g\right)^n \quad \textbf{(7.5)}$$

Where R is the reflectance of MKG (%), α is the Kubelka-Munk optical absorption coefficient (%), hp is the Planck constant ≈ 6.626×10^{-34} $J \cdot Hz^{-1}$, ν is the photon's frequency (s^{-1}) and n is the exponent that depends on the nature of the transition. Typically, n = 2 is used for indirect band gap calculation according to previous literature [392,393]. Finally, E_g is derived from the plotted graphs by extrapolating the linear region to the abscissa.

Fig. 7.5 illustrates Tauc's plot of the 7d and 28d MKG, and the corresponding optical band gap energy is summarized in **Table 7.5**. All samples exhibit a band gap energy ranging from 2.7 to 3.2 eV, falling within the semiconductor range [394]. This phenomenon can be attributed to the substitution of $[AlO_4]$ in the N-A-S-H gel, which introduces a negative charge, resulting in localized defect states within the band gap. These defect states can act as trapping or recombination centers for electrons, thereby influencing the overall electronic behavior of the geopolymers.

With an increase in curing temperature, the associated band gap decreases in all samples. This decrease can be explained as the formation of more defects in the amorphous phases at higher temperatures, introducing energy levels within the band gap. Meanwhile, the addition of TiO_2

in RA1.0 and RH1.0 leads to an increased optical band gap in MKG, primarily due to the higher band gap of anatase (approximately 3.2 eV [384]). The increased formation of crystalline zeolite also contributes to the higher band gap energy, supported by the observation of increased band gap energy with longer curing age, where more zeolite is formed. Additionally, an increase in the Si/Al ratio in the RA/H1.2 samples results in a decreased band gap energy due to the higher prevalence of amorphous phases in RA/H1.2, as indicated by the Q-XRD results in **Fig. 7.2**. The amorphous phase lacks long-range order and possesses a disordered atomic structure, leading to a reduction of band gap energy.

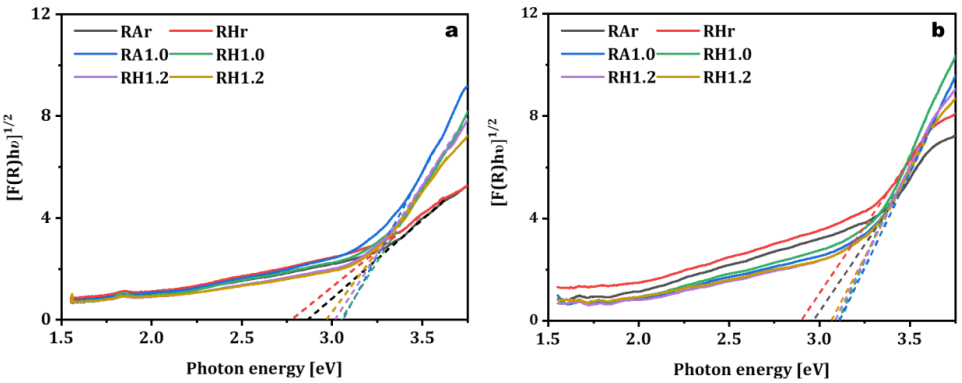

Fig. 7.5: Tauc's plot of the 7d (a) and 28d (b) MKG.

The localized states within the band gap, which are caused by structural disorder, defects and impurities, often induce the Urbach tail in a material. The associated band tail width is referred to as the Urbach energy (E_u), and its calculation follows the empirical Urbach rule as expressed by [395]:

$$\alpha = a_0 \exp(hp \cdot \nu / E_u) \quad \textbf{(7.6)}$$

$$\ln F(R) = (1/E_u) hp \cdot \nu + \ln a_0 \quad \textbf{(7.7)}$$

Where a_0 is a constant, E_u is the Urbach energy (eV), hν is the incident photon energy (eV), and α is the Kubelka-Munk optical absorption coefficient (%). The Eu for all geopolymers is calculated from the reciprocal gradient of the straight line in **Appendix Fig. E.1** and is summarized in **Table 7.5**.

When TiO_2 is integrated into RA1.0 and RH1.0, the Eu decreases compared to RAr and RHr. The reduction in Eu mainly results from the enhanced formation of crystalline zeolite A. Conversely, the increased Eu in RA1.2 and RH1.2 is associated with the amorphous N-A-S-H gel content, as inferred in the Q-XRD results in **Fig. 7.2**. Meanwhile, the E_u of MKG increases with higher curing temperature. This is because elevated temperature enhances the hydration process, leading to a greater formation of amorphous products. Consequently, more structural defects are present in the matrix. On the contrary, the Eu of MKG decreases at 28d in comparison with the 7d samples. This reduction is attributed to the improved crystalline quality and structure of geopolymer, as more zeolites are formed, and some structural defects and disorders may gradually diminish or be repaired over time.

A higher Urbach energy generally indicates superior photocatalytic activity of the materials, resulting in improved self-cleaning performance. Based on the current results, RAr and RHr, without the modification of TiO_2, exhibit the highest photocatalytic activity among the tested geopolymers. This contrasts with the TiO_2-modified OPC system, where TiO_2 addition introduces more localized defect states and increases the E_u of the cement paste [111]. This suggests that MKG is better suited for use as a cementitious carrier for photocatalysts. However, it is worth mentioning that the self-performance of hardened cement paste is not solely governed by structural or crystalline defects [111], a point reinforced by the self-cleaning performance of MKG detailed in the following sections.

Table 7.5: Optical band energy and Urbach energy of the 7d and 28d MKG.

Group	Band gap energy [eV]		Urbach energy [eV]	
	7d	28d	7d	28d
RAr	2.87	2.97	0.91	0.75
RHr	2.78	2.90	0.93	0.85
RA1.0	3.06	3.11	0.83	0.77
RH1.0	3.05	3.10	0.86	0.78
RA1.2	3.02	3.09	0.85	0.69
RH1.2	2.97	3.06	0.91	0.74

7.3.4 Self-cleaning performance

The self-cleaning performance of 7d and 28d MKG is evaluated through the discoloration process of RhB-stained surfaces under UV exposure, and the discoloration evolution is depicted in **Fig. 7.6**. Regardless of the curing temperature, curing age, the addition of TiO_2 and Si/Al ratios, three stages of the discoloration process are observed: a) rapid color change during the first 4 h of UV exposure, b) slight color change between 4 h and 72 h of UV exposure, c) a stable stage after 72 h of UV exposure. The early rapid color change may be attributed to the initially higher RhB concentration. As the photocatalytic process advances, RhB concentration decreases, and decomposed RhB remains on the matrix surface, potentially hindering further oxidation. Similar trends in color changes have been reported in studies of TiO_2-modified cement systems [111,112]. However, the detailed discoloration rates and efficiencies of the prepared MKG vary based on the modifications, as summarized in **Table 7.6**.

At 7d, the rate of color change is in the order of RA1.0 > RA1.2 > RAr. Though no TiO_2 is added, RAr exhibits a certain level of self-cleaning performance, likely attributed to the original TiO_2 in the metakaolin. The additional TiO_2 in the RA1.0 and RH1.0 promotes their discoloration rate and efficiency as more TiO_2 joins in the photocatalytic process. Meanwhile, the increased Si/Al ratio leads to a reduction of the discoloration rate in the RA/H1.2 samples. This suggests that the in-situ formation of zeolite in RA1.0 and RH1.0 is more beneficial in the photocatalytic process than the formation of N-A-S-H in RA1.2 and RH1.2. Further supporting this conclusion is the finding that a higher curing temperature enhances the color change rate in RH1.0 but diminishes the rate in RH1.2. This differential effect can be attributed to the promoted zeolite in RH1.0, which does not lead to the sheltering effect of the photocatalysts due to its porous structure. In contrast, the promoted N-A-S-H formation in RH1.2 enhances

the sheltering effect, hindering the photocatalytic process, similar to the behavior observed in the OPC system with the formation of C-(A)-S-H gel [111].

Importantly, it is observed that samples with a higher curing age exhibit a higher color change rate, which differs from OPC-based systems, where hydration products form on the surface of photocatalysts and induce a sheltering effect, leading to a deterioration in self-cleaning performance over time [112]. Besides, the reference samples show a significantly improved color change rate at 28d, which is even comparable with RA1.2 and RH1.2. This confirms that the formation of zeolite at later stages in RAr and RHr plays an essential role in improved self-cleaning performance. RA1.0 and RH1.0 always demonstrated the best performance, even though the band energy and Urbach energy in RA1.0 and RH1.0 are not optimal. This suggests that the self-cleaning performance in MKG is not directly correlated with its band energy and Urbach energy, indicating that other factors influence the self-cleaning performance of MKG [111]. Overall, the in-situ formation of zeolite leads to a significant enhancement of photocatalytic properties, surpassing even the TiO_2-modified OPC system, as indicated in **Table 7.6**. This underscores its promising potential for application in functional building materials.

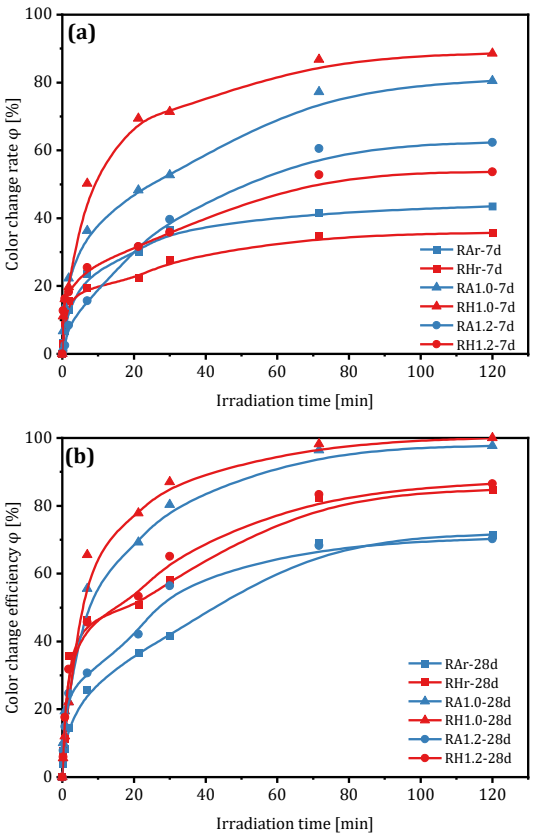

Fig. 7.6: Discoloration process of 7d (a) and 28d (b) MKG with UV irradiation.

Table 7.6: The color change rate of different geopolymers and cement systems from literature (%).

Group	Colour change rate (%)			Literature
	7d (* h)	28d (* h)	-Other curing age (*h)	
OPC+5wt% TiO_2	86.1 (~47h)	80.1 (~47h)	-	[112]
OPC+0.1wt%TiO_2	42.1 (~24h)	48.0 (~24h)	-	[111]
OPC+5wt%TiO_2	-	-	64.0 - 1d (26h)	[396]
OPC+10wt%TiO_2-N,C/300	-	55.0 – (60h)	-	[397]
OPC+5wt%TiO_2	-	-	~95.0 - 4 years (30h)	[398]
RAr	42.0 (72h)	69.5 (72h)		This study
RHr	34.9 (72h)	82.1 (72h)		
RA1.0	77.4 (72h)	96.2 (72h)		
RH1.0	86.8 (72h)	98.2 (72h)		
RA1.2	60.1 (72h)	68.3 (72h)		
RH1.2	52.7 (72h)	83.3 (72h)		

Note: * degradation time under UV (h).

7.3.5 Microstructure of geopolymers

- **Porosity and pore size distribution**

The photocatalytic performance of pure TiO_2 is limited by its low specific surface area and high scattering, which hinders incident light from reaching the active sites on the catalyst surface [349]. Consequently, the microstructure of the carrier plays a crucial role in enhancing the overall performance of the photocatalytic system [112]. The evolution of the pore size distribution for MKG is shown in **Table 7.7** and **Fig. 7.7**, illustrating the influence of curing time, added TiO_2, and Si/Al ratio of starting materials on the microstructure. MKG exhibits a relatively high porosity of approximately 45 ~ 50% compared to hydrated OPC [112], which is beneficial for improving photocatalytic efficiency [399]. Since MIP analysis cannot detect the closed pores within the matrix, the actual porosity may be higher. The difference in porosity between hydrated OPC and MKG can be attributed to two factors: a) N-A-S-H gel contains less bound water than C-(A)-S-H gel [400], and b) the w/b ratio used in MKG is 1.0, which is significantly higher than that used for OPC hydration.

The incorporation of TiO_2 in RA1.0 and RH1.0 leads to a slight increase in porosity and a decrease in the average pore diameter compared to RAr and RHr. This differs from the role of TiO_2 in the OPC system, where it can act as a filler in the matrix and help preserve porosity and pore volume [111]. In MKG, it works as nucleating seeds and promotes the formation of zeolite A, which exhibits higher porosity than the N-A-S-H gel, thereby increasing the overall porosity of the matrix. This effect was also observed in the study of Lolli et al. [401]. Meanwhile, the increased formation of reaction products significantly fills the voids and reduces the average pore size. When increasing the Si/Al ratio, the porosity of the MKG diminishes due to a greater amount of water that is bound in the amorphous N-A-S-H gel in RA1.2 and RH1.2, which fills the capillary pores. This reduction is also a consequence of the morphological structural differences between crystalline zeolite A and amorphous gel. Accordingly, an elevated curing temperature reduces the porosity and pore volume of the MKG due to the accelerated reaction kinetics, leading to a rapid formation of the geopolymers network [364].

The porosity of the MKG decreases with a longer curing age, indicating that more products are formed as curing progresses, allowing the pore structure in the matrix to be filled. Notably, an increase in the average pore size is also observed, particularly in the RAr, RHr and RA1.0, RH1.0 samples. Yang and White have considered this increase to be a result of the dissolution of metakaolin during the curing, leading to the formation of N-A-S-H gel and associated mesopores [402]. Moreover, it cannot be discounted that the formation of zeolite during the curing process also leads to chemical expansion, which may create new pores and enlarge the existing pores [190]. Overall, it can be concluded that the formed zeolite induces a higher total pore area and refines the pore size distribution through its own porous structure and volume expansion effect, which is conducive to improving the photocatalytic efficiency of MKG [399].

Table 7.7: Microstructure of the 7d and 28d MKG.

Sample	Curing age	Porosity (%)	Total pore volume (ml/g)	Total pore area (m^2/g)	Average pore diameter (nm)
RAr	7d	50.99	0.5193	8.809	235.8
RHr		49.39	0.4409	7.093	248.6
RA1.0		51.90	0.5109	10.231	199.8
RH1.0		49.68	0.4789	9.566	200.3
RA1.2		45.44	0.4149	8.690	191.0
RH1.2		44.55	0.4098	8.053	203.5
RAr	28d	48.89	0.4869	6.443	302.2
RHr		44.55	0.4491	4.745	354.4
RA1.0		45.89	0.4380	6.660	263.1
RH1.0		46.97	0.4546	6.086	298.8
RA1.2		44.15	0.4068	8.602	189.2
RH1.2		44.99	0.4036	7.817	206.5

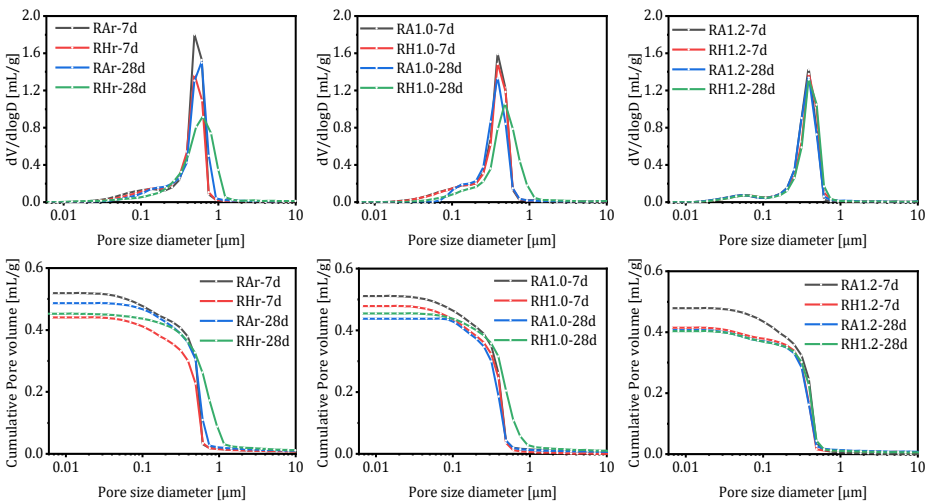

Fig. 7.7: The differential pore size distribution and cumulative pore volume of the 7d and 28d geopolymers.

- **SEM and EDX analysis**

The morphology of the reaction products within the 7d and 28d MKG is presented in **Fig. 7.8**. At 7d, the formation of zeolite A in the RAr and RA1.0 samples is confirmed, based on the characteristic cubic crystal habit. The average crystallite diameter is around 3 µm. The curing temperature does not significantly influence the size of the formed zeolite in RHr and RH1.0. However, a slight growth in the particle size of zeolite is observed at 28d, particularly in the RAr and RHr samples. This may be one of the reasons for the greater enhancement of the photocatalytic performance for these samples at a later stage (**Fig. 7.6**). Additionally, the zeolite X detected in the XRD patterns of RAr and RHr is scarcely distinguishable in SEM images due to its low content. Moreover, zeolite X often exhibits an octahedral habit [403], further complicating the distinction between zeolite X and zeolite A in the samples.

Interestingly, a minute population of particles with similar shapes of zeolites (indicated by red circles) becomes visible in the RA1.2 and RH1.2 samples at 28d. These particles are currently considered potential zeolite precursors, characterized by low crystallinity, which makes them undetectable in XRD analysis. Additionally, it is worth noting that these precursors do not exhibit significant changes in particle dimensions when exposed to elevated curing temperatures or extended curing durations. Overall, based on SEM images, we can infer a limited formation of zeolite precursors in RA1.2 and RH1.2.

The chemical composition of the precursor mixture and the reaction products in the 7d and 28d MKG is elucidated in ternary phase diagrams at fixed Si/Al ratios of 1.0 and 1.2, as depicted in **Fig. 7.9**. The primary elements involved are Na, Al and Si. A linear correlation can be observed between the Si/Al ratio in the reaction products and the used activators modulus, resulting in values ranging from 0.72 to 0.74 for RAr, RHr, RA1.0 and RH1.0, and 0.89 to 0.92 for RA1.2 and RH1.2, This relationship is attributed to the distinct formation of N-A-S-H gel and zeolite. While both N-A-S-H gel and zeolite contain tetrahedrons linked by oxygen bridges as primary building units, a high [SiO_4] content facilitates the formation of silicate chains, whereas an insufficient [SiO_4] content results in the formation of single or double four-membered and six-membered ring. These membered ring structures contribute to the zeolite framework and ensure the formation of micropores, channels and cavities [404]. Consequently, the in-situ formed zeolite surrounding TiO_2 photocatalysts does not hinder their effectiveness; instead, the porous structure of zeolite aids in enhancing the transport of the catalysis products.

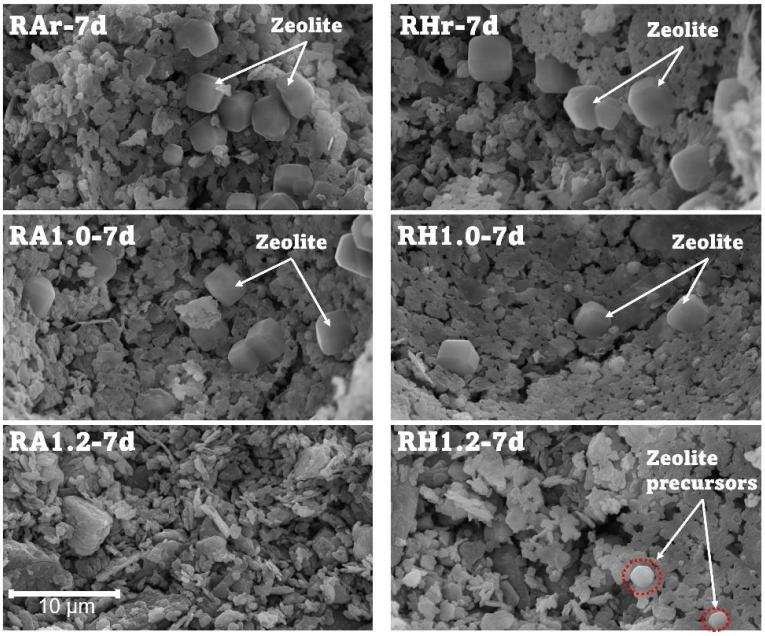

(a)

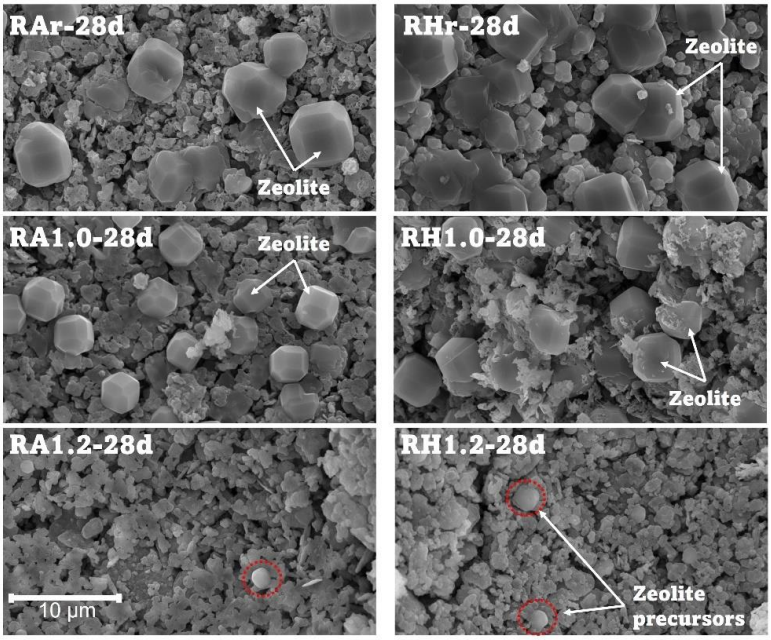

(b)

Fig. 7.8: SEM-SE image of the (a) 7d and (b) 28d MKG.

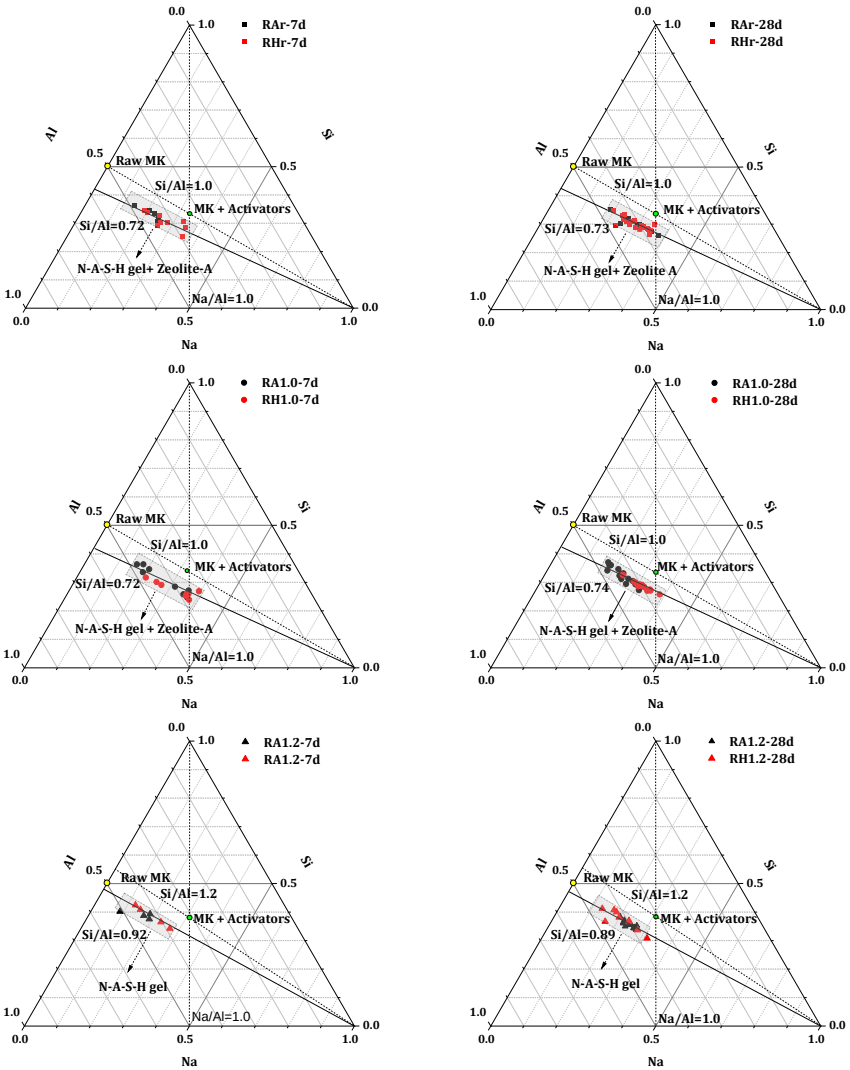

Fig. 7.9: The elemental composition (Na, Al, Si in mol ratio) of the 7d and 28d MKG obtained through the EDX spot analysis. (Theoretical lines representing a Si/Al ratio of 1.0 are graphed for the 7d and 28d RAr, RHr, RA1.0, and RH1.0 samples. Similarly, for the 7d and 28d RA1.2 and RH1.2 samples, theoretical lines corresponding to a Si/Al ratio of 1.2 are plotted. The positioning of the raw metakaolin point is determined through the calculation of its chemical composition.

7.4 Discussions

In this study, the pivotal variables considered among the samples encompass the incorporation of TiO_2, the Si/Al ratio in the raw materials, and the curing temperature. The investigation focuses on understanding their respective impacts on the photocatalytic properties of MKG. It is easy to understand that a matrix incorporating TiO_2 facilitates photocatalytic properties, owing to the increased exposure of TiO_2, thereby fostering a more effective photocatalytic process. Furthermore, the presence of TiO_2 accelerates the polymerization process of

aluminosilicate precursors, as evidenced by the enhanced formation of zeolite A in RA1.0. This observation aligns with prior studies highlighting the role of TiO_2 in promoting hydration products within cement systems, a phenomenon often linked to the nucleation effect of TiO_2 nanoparticles during the hydration of C_3S [368,369]. Hence, it can be inferred that TiO_2 particles may exert a similar nucleation effect on the hydration process of metakaolin. However, further systematic analysis is required to definitively verify the nucleation effect of TiO_2.

Another noteworthy observation pertains to the distinct zeolite formation in samples with a Si/Al ratio of 1.0. They exhibit superior photocatalytic properties compared to those with a Si/Al ratio of 1.2. Significantly, the discoloration analysis of MKG establishes that its self-cleaning performance is not intricately linked to the optical characteristics of the cementitious matrix. Contrary to expectations, the higher optical band gap of specimens RA1.0 and RH1.0 does not adversely affect their self-cleaning efficacy, as observed experimentally. The in-situ zeolite formation emerges as a significant contributor to the photocatalytic process. Moreover, the augmentation in the quantity of in-situ formed zeolite adhered to the surface of the photocatalysts during the hydration process does not result in a sheltering effect, thus preventing any deterioration in the self-cleaning properties of MKG. Instead, enhanced photocatalytic efficiency is attained after 28d compared to 7d old samples, as depicted in **Fig. 7.6**, illustrating a divergence from the OPC system.

7.4.1 Enhanced mechanism of self-cleaning performance upon zeolite formation

The schematic diagram of the self-cleaning mechanism of MKG is presented in **Fig. 7.10**. Taking RA1.0 as an example, zeolite A is generated within the MKG matrix and adheres to the surface of TiO_2 particles with the hydration process. Owing to the transparency of zeolite to UV-Vis radiation above 240 nm [405], there is a permissible penetration of photons into the solid opaque powder, reaching the TiO_2 photocatalysts situated at intraparticle positions. Subsequently, the TiO_2 photocatalysts generate electron-hole pairs and create active oxygen radicals O_2^- and hydroxy radicals HO·, thereby facilitating the degradation of pollutants [342].

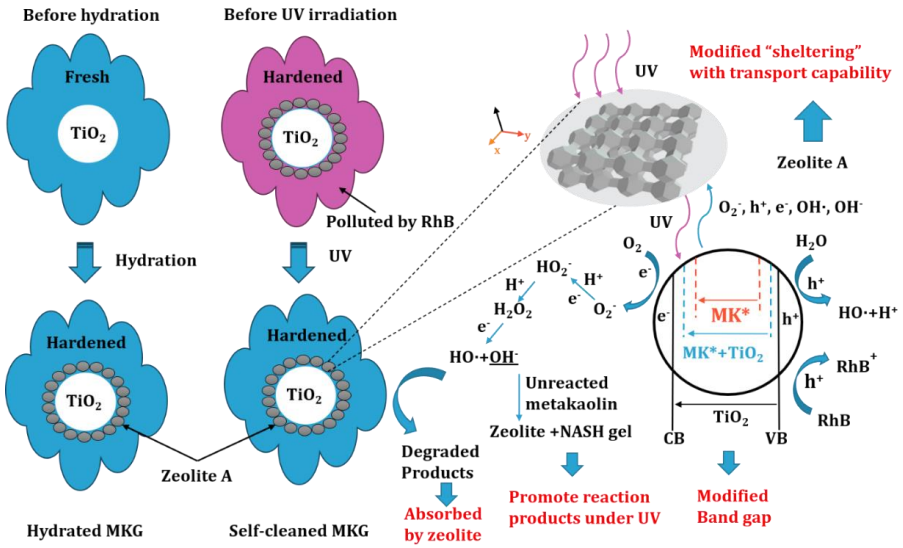

Fig. 7.10: Schematic diagram of the self-cleaning mechanism of TiO_2 modified MKG.

Many previous investigations have attributed the stronger photoactivity of TiO_2 in cement-based materials to an increased concentration of oxygen vacancies or other defects[111,406,407]. However, the observed increase in optical bandgap and decrease in Urbach energy within the matrix due to zeolite formation renders the explanation based on surface defects illogical. During the photocatalytic process, the beneficial impact of the zeolite can be summarized as follows: 1) The porous structure inherent to zeolite provides sufficient space for the photocatalytic process. Meanwhile, it elevates mass transfer capacities, which help to transfer the generated reactive radicals ($HO\cdot$, O_2^-), thereby enhancing photocatalytic efficiency. 2) The extensive surface area of zeolite facilitates the adsorption of the degraded pollutants, mitigating the accumulation of the pollutants and subsequent degradation of photocatalytic performance. 3) Through the hydration process, more crystalline zeolite structures are generated, overlaying the surface and promoting the growth of the zeolite particles, as observed in **Fig. 7.8**. The resultant zeolite formations ensure the porosity of the matrix. Consequently, the in-situ zeolite formations as the surrounding media for photocatalysts serve to diminish their "sheltering" effect.

7.4.2 Analysis of in-situ formation conditions of zeolites in geopolymers

In light of the substantive contribution of porous zeolite to the enhanced self-cleaning properties of geopolymers, effective control over their production becomes a crucial factor in the utilization of MKG for functional build materials. This study reveals that three factors (TiO_2 content, Si/Al ratio of the initial materials, and curing temperature) influence the in-situ zeolite formation and validates the in-situ formation of Zeolite A and Zeolite X within the MKG. Significantly, the predominant form identified in this study is zeolite A, and its crucial role in enhancing self-cleaning properties is well established. However, it remains uncertain whether zeolite X has a similar effect due to its lower formation in the process, as substantiated in **Section 7.3.4**. Therefore, the reported reaction conditions from the literature that govern the formation of zeolite A are comprehensively delineated in **Table 7.8**. The current investigation systematically examines the impact of the Si/Al ratio in the initial materials on crystalline zeolite formation, a phenomenon manifesting at an optimal Si/Al of 1.0. It is noteworthy that traces of crystalline zeolite formation have been documented at Si/Al of 1.2 or 1.25 [354,408,409]. The variance in the Si/Al ratio may be attributed to the higher curing temperature (70 ~ 90 °C) in these studies, which potentially instigates the crystallization of amorphous zeolite precursors. This observation also implies the potential for crystalline zeolite formation in RA1.2 under elevated curing temperatures. Additionally, when alternative reactive precursors such as microsilica, geothermal silica, rice hull ash, and fly ash are employed [348,410–412] an increased Si/Al ratio in the raw materials is required for the generation of crystalline zeolites. This is likely due to the relatively lower reactive silica (in detail, the dissolved Si-O tetrahedra) content within these alternative precursors. To conclude, the Si/Al ratio of the reactive content in the initial materials assumes an essential role in dictating the formation condition, with the design of this ratio contingent upon the specifics of the reaction system.

Table 7.8: Literature overview of synthesis and curing conditions of Zeolite A formed in geopolymers.

Starting materials				Curing conditions	Zeolite Structure type	Ref.
Precursor	Activator	Si/Al	Na/Al			
MK	SH	0.95	1.2	60°C, 24 h	LTA	[413]
MK	SH	0.96	1.1	60°C, 24 h	LTA	[414]
MK	SH	0.96	1.2	60°C, 24 h	LTA	[414]
MK	SH	0.96	1.3	60°C, 24 h	LTA	[414]
MK	SH	0.97	-	80°C, 24 h	LTA	[415]
MK	SH	1.0	1.0	20°C, 24	LTA + FAU	This study
MK	SH	1.0	1.0	45°C, 24	LTA + FAU	This study
MK	SH	1.0	1.0	95 °C, 24 h	LTA	[416]
MK	SH	1.0	1.13	80 °C, 24 h	LTA	[416]
MK	SH	1.0	1.0	60 °C, 6 h	LTA	[417]
MK+SF	SH+WG	1.01	1.0	60°C, 24 h	LTA + FAU	[418]
MK	SH	1.03	0.85	60 °C, 24 h	LTA	[419]
MK	SH	1.04	0.6	70°C, 2h	LTA	[408]
MK	SH	1.04	0.8	70°C, 2h	LTA	[408]
MK	SH	1.04	1.0	70°C, 2h	LTA	[408]
MK	SH	1.1	1.0	95 °C, 24 h	LTA+FAU	[416]
MK	SH	1.1	1.13	80 °C, 24 h	LTA	[416]
MK	SH	1.12	1.0	60 °C, 24 h	LTA + FAU	[383]
MK	SH	1.2	1.0	80 °C, 24 h	LTA	[354]
MK	SH	1.25	0.8	70°C, 2h	LTA	[408]
MK	SH	1.25	1.0	90 °C, 48 h	LTA	[409]
MS	SA	1.01	0.98	80 °C, 3 d	LTA + HS	[348]
MS	SA	1.76	0.98	80 °C, 3 d	LTA + HS	[348]
MS	SA	3.01	0.98	80 °C, 3 d	LTA + HS	[348]
RHA	SA	1.5	1.27	40 °C, 21 d	LTA + FAU	[410]
GS	WG	1.5	1.29	40 °C, 4, 21 d	LTA + FAU	[411]
GS	WG	1.5	1.38	40 °C, 4, 21 d	LTA + FAU	[411]
FA	SH+WG	1.29	1.0	80°C, 24h	LTA	[412]
FA	SH+WG	1.41	1.0	80°C, 24h	LTA	[412]

MK: metakaolin, SH: sodium hydroxide, SA: sodium aluminate, WG: waterglass, RHA: rice hull ash, GS: geothermal silica, SF: silica fume, MS: microsilica, FA: fly ash, LTA: Zeolite A, FAU: Zeolite X, HS: hydroxy-sodalite zeolite.

Meanwhile, based on the findings in **Fig. 7.1**, the employment of high-temperature curing is deemed non-essential for zeolite A production. Although high-temperature curing expedites zeolite formation and augments early photocatalytic performance, as shown in **Fig. 7.6(a)**, considering the associated equipment requirement and heightened energy consumption, an elevated-temperature curing process is not recommended, particularly when the later-stage photocatalytic performance is anticipated to be comparable, as depicted in **Fig. 7.6(b)**. While most investigations in **Table 7.8** do not explicitly explore the photocatalytic properties of the engineered geopolymers, the in-situ formation of Zeolite A within the matrix suggests their

potential utility as carriers for photocatalysts in construction materials, with the expectation of corresponding enhancements upon the incorporation of photocatalysts into these composite blends. Certainly, when fabricating geopolymers using alternative raw material precursors like fly ash, it is anticipated that the in-situ formation of zeolites could enhance the eventual self-cleaning characteristics. However, it is important to recognize that other common hydration products (such as hydrotalcite, C-(A)-S-H, and inherent minerals) may also exert influence. Therefore, comprehensive investigations are necessary to elucidate the feasibility of applying other geopolymers in self-cleaning applications. In summary, this study presents a method for achieving high self-cleaning performance in MKG at ambient temperatures, offering convenience in fabrications and leading to associated energy cost savings.

7.5 Conclusions

This chapter attempts to provide a comprehensive understanding of the impact of in-situ zeolite formation on the self-cleaning performance of metakaolin-based geopolymers. Paste samples with two different Si/Al ratios in the initial materials were formulated, incorporating TiO_2 nanoparticles. The evolution of phase composition, functional groups, optical properties, self-cleaning performance and microstructure of the MKG under varying curing temperatures and curing ages was systematically investigated. Based on the obtained results, the following conclusions can be drawn.

- The Si/Al ratio of the initial raw materials significantly influences the hydration products of metakaolin-based geopolymers. Notably, at a Si/Al ratio of 1.0, the concurrent formation of Zeolite A and N-A-S-H is observed. At a ratio of 1.2, the prevalence of available Si-O tetrahedron content directs the formation of N-A-S-H gel, precluding zeolite.

- Elevated curing temperature (45°C) promotes the hydration process of metakaolin-based geopolymers, resulting in increased quantities of hydration products. Importantly, this acceleration does not alter the categorization of geopolymer hydration products no matter the Si/Al ratio in the initial raw materials.

- The incorporation of TiO_2 induces more zeolite formation within the geopolymer at ambient temperature based on 7d Q-XRD analysis of RAr and RA1.0. However, under accelerated hydration conditions at a higher curing temperature, TiO_2 acts as the filler, diminishing average pore size within the matrix and restricting zeolite growth and formation.

- Zeolite formation in geopolymers enhances the matrix with a higher optical band and lower Urbach energy, driven by increased crystallinity. This confirms that the improved photocatalytic properties observed in metakaolin-based geopolymers cannot be solely attributed to heightened surface defects.

- The self-cleaning performance of metakaolin-based geopolymers can be improved by the in-situ formation of Zeolite A, characterized by cage structures. This formation not only enhances the total pore area but also refines pore size distribution within

geopolymers. The resulting modified microstructure amplifies the mass transfer capacity of the matrix, thereby intensifying the photoactivity of TiO_2.

- The deterioration of self-cleaning properties of cementitious materials during hydration can be effectively alleviated through in-situ zeolite formation within metakaolin-based geopolymers. The growth of crystalline zeolite A with strict dimensions ensures the establishment of internal pores. As these porous zeolite structures develop and adhere to the surface of photocatalysts, the sheltering effect of the reaction products is diminished. The in-situ formation of porous minerals in cementitious materials emerges as a viable strategy for improving photocatalytic properties, promising an extended lifespan.

Chapter 8 Pentasodium diethylenetriamine pentaacetate (DTPA-5Na) activated basic oxygen furnace slag

In this chapter, the use of waste gypsum as calcium sulfate source in Portland cement and Basic Oxygen Furnace (BOF) slag system has been investigated. The prepared cement with waste gypsum and clinker shows promising properties according to EN196& EN 197. However, the reactivity of BOF slag is relatively low and currently underutilized or landfilled. This chapter explores a novel method to enhance the reactivity of BOF slag for construction materials applications through chemical activation using pentasodium diethylenetriamine pentaacetate (DTPA-5Na). Significant insights are gained by investigating the activation mechanism, hydration kinetics, and mechanical properties of BOF slag-based binders, coupled with mineralogical, thermal, and microstructural analyses. Results demonstrate that DTPA-5Na substantially boosts the reactivity of brownmillerite and accelerates the formation of monocarboaluminate and C-S-H gel, leading to improved mechanical performance. Moreover, the addition of flue gas desulphurization (FGD) gypsum alongside DTPA adjusts the hydration process by influencing the release of calcium and sulfate ions, thereby impacting the kinetics of hydration and promoting ettringite formation. This combined approach results in enhanced mechanical performance and reduced porosity in BOF slag pastes, meeting Dutch Soil Quality Decree limits on heavy metal leaching, and contributing to recovering sulfate residues.

The chapter is partially from the following article:

X. Ling, Z. H. Jiang, K. Schollbach, W. Chen, H.J.H. Brouwers, Pentasodium diethylenetriamine pentaacetate (DTPA-5Na) activated basic oxygen furnace slag (in preparation).

8.1 Introduction

Since the dicalcium silicate in BOF slag exhibits low reactivity, efforts have been made to formulate pure BOF slag-based binders based on activating brownmillerite, the second most abundant hydraulically reactive component in BOF slag (~20 wt%) [30,420]. Brownmillerite is a solid solution with the formula $Ca_2(Al_xFe_{2-x})O_5$. In Portland cement, this phase is typically characterized by x approaching 1, denoted as Ca_2FeAlO_5. Its hydration occurs in the early stages of cement hydration, leading to the formation of the Fe-containing AFm phase and hydrogarnets [421,422]. When only brownmillerite is exposed to the water, it forms a metastable gel identified as C-(A, F)-H, which subsequently converts to a hydrogarnet phase over time [423,424]. However, the hydraulic activity of brownmillerite diminishes as the iron content increases [425] and the iron-rich brownmillerite in BOF slag is anticipated to exhibit lower hydraulic activity, thereby limiting its effective strength development.

Chelating agents are compounds with multiple coordination atoms (sites) that can form stable complexes with metal ions, such as ethylenediaminetetraacetic acid (EDTA), diethylenetriaminepentaacetic acid (DTPA), and oxalate [426,427]. Owning to their ability to bond with metal ions, these agents have been widely employed in the stabilization and extraction of metal ions. Additionally, chelating agents facilitate the dissolution of metal salts. For instance, EDTA boosts the dissolution rate of calcite by up to one order of magnitude compared to rates measured in its absence [428]. Recently, Chang et al. investigated the effect of ethanol-diisopropanolamine (EDIPA) on the hydration and mechanical properties of BOF slag pastes at a water to binder (w/b) ratio of 0.35 [429]. Their study demonstrated an accelerated hydration process attributed to the chelating ability of EDIPA with Ca^{2+}, Al^{3+} and Fe^{3+}. Despite this acceleration, the resulting compressive strength of BOF slag pastes remained low, typically around 4.5 MPa at 28d, thus limiting its application as a promising substitute for Portland cement. In contrast, Kaja et al. developed a tri-potassium citrate monohydrate-activated BOF slag binder, achieving a compressive strength of 75 MPa at 28d [30]. The superior mechanical performance has been attributed to the enhanced hydration of brownmillerite facilitated by the chelating properties of tri-potassium citrate monohydrate. Furthermore, its superplasticizing properties reduce the water demand of slag paste, ensuring desirable workability at a lower w/b ratio of 0.16. Similar strength enhancements have also been observed using sodium oxalate as the activator for BOF slag at a w/b ratio of 0.18 [420]. These studies have established the effective activation of BOF slag using chelating agents, showcasing their potential for recycling BOF slag into construction materials. Nevertheless, a comprehensive understanding of the interactions between chelating agents and the minerals in BOF slag is still needed. This knowledge is essential for identifying more suitable agents to enhance the activation process of BOF slag, as well as providing theoretical support for the use of additives to improve its overall performance.

In this chapter, pentasodium diethylenetriaminepentaacetic acid (DTPA-5Na), a chelating agent commonly used in agriculture, water treatment and healthcare [430,431], was chosen as the activator to investigate its effect on the hydration kinetics, mechanical properties, and potential environmental implications of the BOF slag pastes. The study explored the correlation between the accelerated hydration process and the reaction products, as well as elucidated the enhanced mechanical performance through phase assemblage and microstructure analysis. A multi-technique approach was employed, including calorimetric analysis, mechanical performance

testing, qualitative and quantitative XRD analysis, thermogravimetric (TG) analysis, porosimetry (MIP), and SEM/EDX analysis. Furthermore, while the chelating effect accelerates the dissolution of minerals in BOF slag, the study also investigated the addition of sulfate to regulate the hydration process. Sulphate was added in the form of flue gas desulphurization (FGD) gypsum, as the hydration of brownmillerite in the presence of gypsum leads to the formation of ettringite [432]. The influence of FGD gypsum was then compared to sodium sulfate. The findings present a new approach to recycling sulfur-containing industrial residues. Moreover, the use of waste gypsum in cement production was investigated, and its feasibility was confirmed based on compliance with EN 196 and EN 197 standards.

8.2 Materials and methods

8.2.1 Raw materials

In the cement preparation process, two types of waste gypsum from NOAH (Norway) were used alongside bulk clinker sourced from Heidelberg Materials. The waste gypsum, generated through the neutralization of spent sulfuric acid with limestone, was classified as gypsum-white and gypsum-yellow. The cement mixture contained 95 wt% clinker and 5 wt% waste gypsum, with CEM 52.5R chosen as the reference cement. To achieve a comparable particle size distribution, the received bulk clinker was milled using a Disc Mill for varying durations. This ensured that particle size distribution would not negatively affect the final performance of the resulting cement. After milling the clinker for 8 min, it was mixed with waste gypsum in a mass ratio of 95:5. Mortar samples were then prepared using this binder and standard sand in a 1:3 ratio, followed by curing in water until the designated testing ages.

Two types of raw materials, BOF slag and FGD gypsum, were used in the preparation of BOF-based pastes. BOF slag was supplied by Tata Steel (IJmuiden, The Netherlands). The received BOF slag with a size of < 5.6 mm was stored in air-tight plastic drums to prevent carbonation. In order to apply the BOF slag as a binder material, it was further ground using a Retsch RS 300 XL disc mill at a speed of 912 min^{-1} for 15 min. FGD gypsum was provided by NOAH (Norway). All the raw materials were vacuum-dried at 60°C for one day to remove the moisture content. DTPA-5Na, purchased from Sigma Aldrich (CAS 140-01-2, 40% aqueous solution), was used as the activator of the BOF slag. The chemical structure of DTPA-5Na is presented in **Fig. 8.1**.

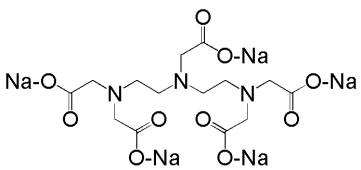

Fig. 8.1: Chemical structure of DTPA-5Na ($C_{14}H_{23}N_3Na_5O_{10}$).

The chemical composition of raw materials was determined by X-ray Fluorescence analysis (XRF, PANalytical Epsilon 3) using a fused bead method, and the results are given in oxide weight percentages in **Table 8.1**. The BOF slag mainly comprises CaO, Fe_2O_3, SiO_2, MgO and MnO. Notably, all Fe in the BOF slag is reported as Fe_2O_3; but Fe can occur in the form of Fe^0, Fe^{2+}, and Fe^{3+} in the BOF slag. The oxidation of metallic or divalent iron leads to increased mass when the BOF slag is heated up to 1000°C for the loss on ignition (LOI) test. Meanwhile,

the mineralogical composition of the raw materials was investigated on Bruker D4 diffractometer with CoKα radiation. Reflections were measured in a 2 Theta (2θ) range of 10° to 90° with a step size of 0.02°. The phase identification was conducted with Highscore Plus using the ICDD PDF-2 database. The main phases in BOF slag, as shown in **Fig. 8.2**, are (α'+β) C_2S, wüestite, magnetite, and brownmillerite. A high concentration of gypsum (≥ 95%) is also confirmed in the FGD gypsum. The particle size distribution of the milled BOF slag and FGD gypsum is characterized using a Mastersizer2000 from Malvern, as illustrated in **Fig. 8.3(b)**. Isopropanol was used as the solvent during the measurement to prevent the dissolution or hydration reaction. The d(50) of the milled BOF slag and FGD gypsum are 15.4 and 31.9 μm, respectively.

Table 8.1: Chemical composition of raw materials (%).

Oxides	MgO	Al_2O_3	SiO_2	P_2O_5	SO_3	CaO	TiO_2	V_2O_5	Cr_2O_3	MnO	Fe_2O_3	Br	LOI
CEM 52.5R	2.2	4.8	22.1	/	3.2	65.5	0.3	/	/	/	4.1	/	1.9
Clinker	1.7	7.3	19.8	/	1.8	64.4	0.2	/	/	/	2.6	/	0.3
Gypsum-w	/	0.7	0.2	/	44.6	29.2	0.3	/	/	/	0.1	/	21.3
Gypsum-y	/	2.9	4.0	/	40.8	27.2	0.2	/	/	/	0.5	/	20.8
BOF	7.8	2.0	14.2	1.6	/	40.5	1.4	1.0	0.3	4.7	26.9	/	-0.6*
FGD	/	1.0	0.5	/	45.6	28.9	/	/	/	/	0.1	2.6	21.3

*: The oxidation of metallic or divalent iron induces an increased mass during the LOI test.

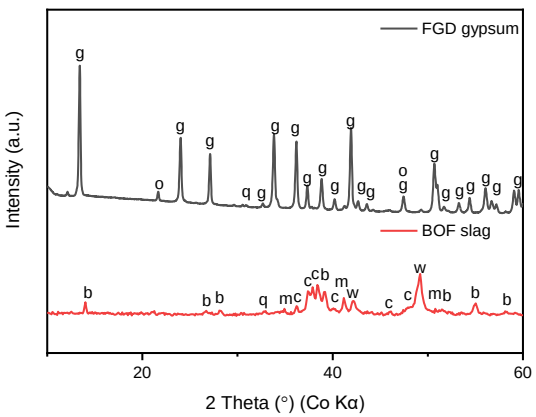

Fig. 8.2: XRD patterns of the raw BOF slag and FGD gypsum. (b- brownmillerite $Ca_2Fe_2O_5$, c- alpha' and beta dicalcium silicate Ca_2SiO_4, g- gypsum $CaSO_4 \cdot 2H_2O$, m- magnetite Fe_3O_4, o- bayerite $Al(OH)_3$, q- quartz SiO_2, w- wüestite, FeO.)

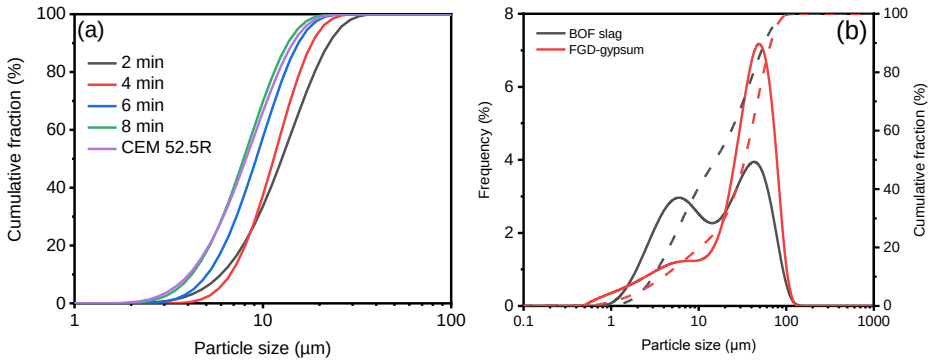

Fig. 8.3: Particle size distribution of (a) clinker after 2, 4, 6, 8 min of milling and CEM 52.5R, (b) BOF slag and FGD gypsum.

8.2.2 Specimen preparation

The BOF-based mixes are designed in two sets (**Table 8.2**). The pure BOF slag was activated with 0, 0.5, and 1.0 wt% DTPA-5Na (relative to BOF slag) to investigate the effect of the dosage on the activation. Although higher dosages of DTPA-5Na enhance the hydration of BOF slag, their use should be minimized to maintain cost-effectiveness. Consequently, higher dosages of DTPA-5Na were not included in this study. Secondly, to reveal the impact of the FDG gypsum on the performance of BOF slag binder, 0.5, 1.5, 2.5, 3.5 wt% FGD gypsum (relative to BOF slag) was added in the 1.0 wt% DTPA-5Na-activated BOF slag system. The samples are named with the percentage of DTPA-5Na and FDG gypsum, e.g., D1F1.5 represents 1.0 wt% DTPA-5Na and 1.5 wt% FGD gypsum.

As mentioned earlier, the chelating agents can act as plasticizers, contributing to a reduced water demand [30]. According to a preliminary study, all pastes were prepared with a water-to-solid (w/s) ratio of 0.18, which is the minimum ratio required to achieve sufficient workability when mixing and casting the pastes. The activator solution was prepared by mixing the required DTPA-5Na and deionized water, prepared one day before the preparation of the pastes. All pastes were prepared according to EN196-1, casting in styrofoam molds with a size of 40*40*160 mm. Subsequently, the samples were sealed with layers of cling film to prevent moisture loss and carbonation and stored in a curing room with a temperature of 20 ± 1 °C and RH of 60% until the test ages.

Table 8.2: The mass ratio of each material in the designed mixtures.

Group	BOF slag	DTPA-5Na	FGD	w/s
D0F0	100	0	0	
D0.5F0	100	0.5	0	
D1.0F0	100	1.0	0	
D1.0F0.5	100	1.0	0.5	0.18
D1.0F1.5	100	1.0	1.5	
D1.0F2.5	100	1.0	2.5	
D1.0F3.5	100	1.0	3.5	
D1.0S1.5	100	1.0	1.24*	

Note: * sodium sulfate (Na_2SO_4) with an equivalent sulfate content to FGD gypsum in D1.0F1.5 was used, and the bound water in FGD gypsum was equivalently replaced by 0.32g of free water.

8.2.3 Methodology

- **Clinker-waste gypsum cement**

The setting time, fineness, hydration kinetics, and mechanical performance of the prepared cement and CEM52.5 R were characterized according to EN-196.

- **BOF-Based binder materials**

Hydration kinetics and reaction process at an early age

The hydration kinetics of BOF slag-based binder was investigated using an isothermal calorimeter (TAM Air, Thermometric) maintained at a constant temperature of 20 °C. Paste samples, as listed in **Table 8.2**, were prepared, injected into sealed glass ampoules and promptly placed within the calorimeter channels. The initial peak occurring within the first 30 min, attributed to the dissolution of raw materials, was excluded from the analysis. Measurements of heat flow and cumulative heat were recorded over 7d after sample mixing. The heat flow and cumulative heat were normalized by the mass of the solid.

To study the early reaction progress of BOF slag-based binder, the evolution of mineralogical compositions was analyzed through X-ray diffraction (XRD) analysis. Specifically, samples D0F0 and D1F0 were selected to examine the effect of DTPA-5Na on the early hydration process of BOF slag at various curing ages: 0 min, 15 min, 1 h, 3 h, 8 h, 15 h, 24 h and 48 h. Additionally, samples D1F0.5 and D1F2.5 were chosen to study the effect of FGD gypsum on the early hydration process of DTPA-5Na-activated BOF slag at curing ages of 0 min, 15 min, 45 min, 2 h, 4 h, 6h, 8 h, 15 h. These curing ages were designated based on the hydration behavior of each paste. Before the XRD analysis, the hydration of the investigated samples was terminated at the designated curing ages. The samples were crushed into fractions smaller than 1 mm, immersed in isopropanol for 24 h, and subsequently flushed with diethyl ether for 30 min. The samples were then vacuum dried at 40°C for 30 min. The dried samples were ground to pass through a 80 μm for XRD analysis. XRD analysis was performed on a Bruker D2 PHASER using Co Kα radiation (30 kV, 10 mA) with a scanning rate of 0.02º (2θ) per step from 10º to 60º (2θ). The obtained XRD patterns were analyzed using High-score plus software.

Mechanical properties and microstructural analysis

The compressive strength of the paste specimens was assessed after 7d and 28d of hydration, following the protocol outlined in EN196-1, with a loading rate of 2400 N/s. Six duplicates for each mixture were used to determine compressive strength.

To elucidate the mechanism of strength enhancement in BOF slag-based binder via DTPA-5Na and FGD gypsum, a series of microstructural analyses were conducted. These included quantitative X-ray diffraction (Q-XRD) analysis, thermogravimetric analysis (TGA), mercury intrusion porosimetry (MIP), and scanning electron microscope (SEM) and energy dispersive X-Ray (EDX) analysis.

Q-XRD analysis was performed on both raw materials and hydrated samples using the Rietveld method [433]. The testing samples were mixed with 10 wt% Silicon Powder (used as an Internal standard) and milled for 5 min in an XRD-Mill McCrone. The Q-XRD tests were conducted with a step size of 0.02° over a 2θ range from 5° to 90°. The resulting XRD patterns were analyzed using High-score plus and quantified using TOPAS Academic software v5.0 [434]. The crystal structural data used for quantitative analysis are detailed in **Table 8.3**.

Thermogravimetric analysis was conducted on 28d samples using a Jupiter STA 449 F1 instrument from Netzsch. Approximately 50 mg of dried powder was used for each test, which was performed at a heating rate of 10 K/min from 40 °C to 1000 °C under a N_2 environment.

For MIP analysis, 28d paste samples were crushed into granular pieces approximately 4 mm in size. The total porosity and pore volume distribution of these granular pieces were analyzed using a mercury porosimeter (AutoPore IV 9500, Micromeritics). The analysis was conducted over an absolute pressure range from 0.7 kPa to 230 MPa, with a contact angle of 130º.

Powder samples obtained from the crushed 28d samples were also prepared for SEM and EDX analysis (Phenom Pro). The samples were initially spread on a carbon conductive adhesive tap and then coated with gold (Au) for 30 seconds using a Quorum 150TS plus sputter coater at 30 mA. The morphology of the reaction products was observed in secondary electron mode at a magnification of 15000. Spot EDS analysis was performed at a voltage of 15 kV to characterize the chemical composition of reaction products.

Table 8.3: Structural data of the phases used for the quantitative XRD analysis.

Mineral name	Cement notation	Chemical formula	ICSD	Space group
Silicon	-	Si	43610	Fd-3m
Fe-rich wüestite	RO	$Fe_{0.8}Mn_{0.2}O$	67199	Fm-3m
Mg-rich wüestite	RO	$Fe_{0.3}Mg_{0.7}O$	67200	Fm-3m
Magnetite	Ff	Fe_3O_4	30860	Fd-3mZ
Brownmillerite	C_2(A, F)	$Ca_2Al_{0.79}Ti_{0.61}Fe_{1.59}O_5$ *	9197	Pnma
Larnite	βC_2S	Ca_2SiO_4	81096	P121/n1
Alpha'-belite	$\alpha'C_2S$	Ca_2SiO_4	81097	Pnma
Lime	-	CaO	28905	Fm-3m
Portlandite	CH	$Ca(OH)_2$	64950	P-3m1
Calcite	Cc	$CaCO_3$	80869	R-3c
Quartz	-	SiO_2	90145	P3221
Monocarboaluminate	AFm	$3CaO{\cdot}Al_2O_3{\cdot}CaCO_3{\cdot}11H_2O$	00-054-0848***	P-1
Hydrocalumite	AFm	$Ca_4Al_2(OH)_{12}(Cl, CO_3, OH)_2{\cdot}4H_2O$	00-016-0333***	P21
Ettringite	AFt	$Ca_6Al_2(SO_4)_3(OH)_{12}{\cdot}26H_2O$	16045	P31c

*: The chemical formular used for brownmillerite was derived from the chemical composition determined through large area phase mapping analysis conducted on BOF slag samples sourced from the Tata Steel Plant IJmuiden [435,436].

Leaching behavior of heavy metals

One batch leaching test was conducted on both the raw materials and cured paste samples according to EN 12347-2. The cured samples were first crushed to a size smaller than 4 mm and then mixed with deionized water in polyethylene bottles at a liquid-to-solid (L/S) ratio of 10. These bottles were sealed and horizontally placed on a linear reciprocating shaking device (Stuart SSL2) for 24 h, with a constant shaking rate of 250 rpm. Afterward, the liquids were filtered through a 0.2 µm polyether sulfone membrane and acidified with nitric acid to prevent potential precipitation. The resulting leachate was analyzed using an inductively coupled plasma optical emission spectrometer (ICP-OES Spectral Blue) according to NEN 6966.

8.3 Results of the clinker and waste gypsum cement

8.3.1 Setting time

The initial and final setting time of the prepared cement, clinker, and CEM 52.5R were characterized, with the results presented in **Fig. 8.4**. Compared to the commercial CEM 52.5R, the clinker exhibited a faster setting time. This difference can be attributed to the additional gypsum typically used in the production of CEM 52.5R, which reacts with tricalcium aluminate (C_3A). The hydration products from this reaction form a coating on the C_3A, preventing its rapid interaction with water. A similar phenomenon occurs with the waste gypsum used in the prepared cement, as it also acts to retard the setting time by controlling the C_3A hydration. However, the cement prepared with waste gypsum demonstrated a prolonged setting time, likely due to the impurities introduced by the waste gypsum. Furthermore, the cement containing gypsum-w, which has a higher concentration of gypsum, exhibited an even longer setting time. This observation is consistent with the role of gypsum in delaying the setting process. Importantly, the setting time of the cement prepared with waste gypsum meets the requirements of EN 196, exceeding the minimum threshold of 45 minutes, indicating its suitability for practical use.

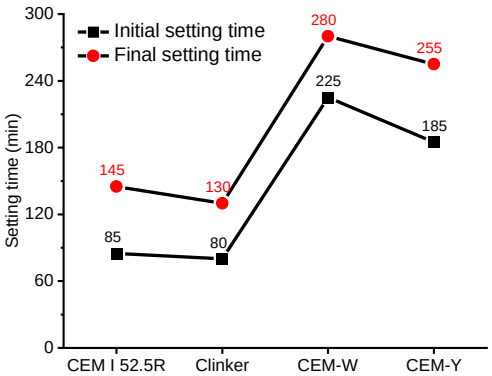

Fig. 8.4: The initial and final setting time of CEM-52.5R, Clinker and the prepared cement.

8.3.2 Hydration kinetics

The influence of different types of waste gypsum on the hydration kinetics of clinker was investigated, as illustrated in **Fig. 8.5**. In the pure clinker system, the main hydration heat peak occurs around 12 h, corresponding to the hydration process of alite (C_3S). The additional waste gypsum results in a more pronounced heat flow peak. Although similar observations about the enhancement of gypsum on C_3S hydration have been widely reported in previous studies, there is no universally accepted explanation for this phenomenon. Several hypotheses have been proposed, including the seeding effect of the formed ettringite and an interaction between gypsum and C_3S. Overall, the cumulative heat release of pure clinker within the first 168 h is approximately 180 J/g. The presence of waste gypsum enhances clinker hydration, increasing the cumulative heat to 215 J/g. However, the cumulative heat of the prepared cement is lower than that of CEM 52.5R, potentially due to impurities in the waste gypsum. Despite efforts to control the particle size of the clinker, some variation remains compared to commercial-grade cement, contributing to differences in the exothermic hydration process. Nevertheless, based

on the present results, this variation is considered acceptable. Additionally, the hydration behavior of clinker with the two types of waste gypsum did not show significant differences, indicating a consistent effect of the waste gypsum on hydration.

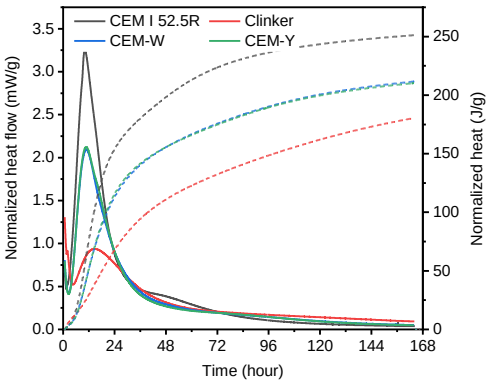

Fig. 8.5: Cumulative heat and heat flow during the initial 168 h of hydration.

8.3.3 Mechanical performance

The mechanical performance of the prepared cement was evaluated through flexural and compressive strength tests at 7, 28 and 91d, with the results summarized in **Fig. 8.6**. Notably, the pure clinker samples exhibit the lowest strength at all ages, consistent with the hydration heat results at an early age in **Fig. 8.5**. The addition of waste gypsum significantly improves both flexural and compressive strength, which can be attributed to the formation of ettringite during hydration. Furthermore, gypsum regulates the setting behavior, preventing rapid setting and facilitating proper strength development over time. In summary, the 28d flexural strength and compressive strength of the prepared cement are approximately 9 MPa and 52.5 MPa, respectively, meeting the strength requirements of the EN197 standard. Therefore, the waste gypsum generated by NOAH is highly recommended for cement production, offering a sustainable solution by recycling waste materials, conserving natural resources, and providing economic benefits.

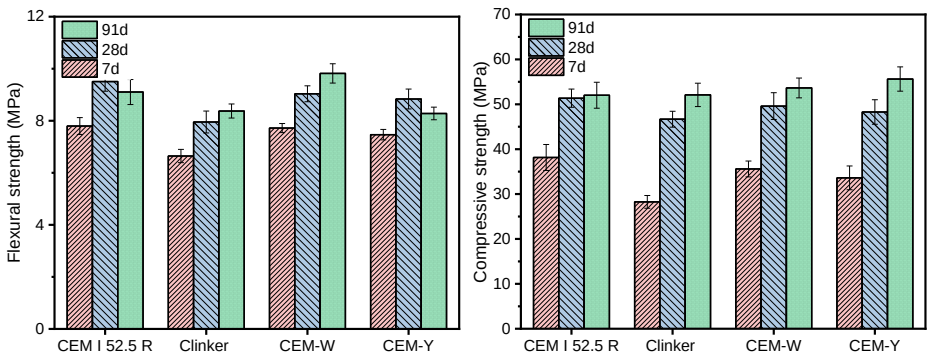

Fig. 8.6: Flexural and compressive strength of the mortar samples.

8.4 Results of the BOF slag-based binder materials

8.4.1 Hydration kinetics and its correlation with hydration products

The 7d hydration heat release of BOF slag with water and DTPA-5Na (0.5 wt.% and 1.0 wt.%) were monitored via isothermal calorimetry to understand the effect of the DTPA-5Na concentration on the early hydration kinetics of BOF slag, as shown in **Fig. 8.7**. In D0F0, the heat flow decreases continuously for the first 15 h, and then a broad peak of low intensity around 19.5 h, which demonstrates the low reactivity of BOF slag at the early age. After that, a second peak of relatively high intensity occurs around 40.0 h. In order to correlate the reaction process for each exothermic peak, the mineralogical composition of the BOF slag after hydration with water for 15 min, 1h, 3h, 8h, 15h, 24h, and 48h hydration was characterized by XRD analysis, and the results are illustrated in **Fig. 8.8**. During this period, the (0 2 0) peak associated with brownmillerite (2θ = 13.94°, d = 7.30 Å) gradually diminishes, suggesting its dissolution. Conversely, the (0 0 2) peak of monocarboaluminate (2θ = 13.60°, d = 7.80 Å) increases significantly after 8h hydration. This observation suggests that the early reaction produces monocarboaluminate, contributing to the exothermic peak observed in D0F0 around 19.5 h. Similar formations have been reported in previous studies, which attributed them to the reactions of aluminate (C_3A and $C_{12}A_7$) and $CaCO_3$ [429]. However, the BOF slag used in this study has relatively low aluminum content. Therefore, we propose that some of Al (III) is likely to be substituted by Fe (III) in the monocarboaluminate [437]. Determining the specific composition of the reaction products is challenging since these minerals are layered double hydroxides, and the exchange of interlayer metal ions, particularly iron and aluminum, is highly probable. Hereinafter, we refer to it as monocarboaluminate. Subsequently, the (0 0 2) peak ascribed to hydrocalumite (2θ=13.05°, d = 7.86 Å) emerges after 15h hydration, corresponding to the second exothermic peak. It is worth noting that the formation of C-S-H gel resulting from the hydration of C_2S also generates heat. However, this heat release is believed to be comparatively lower due to the limited extent of early hydration of C_2S [438].

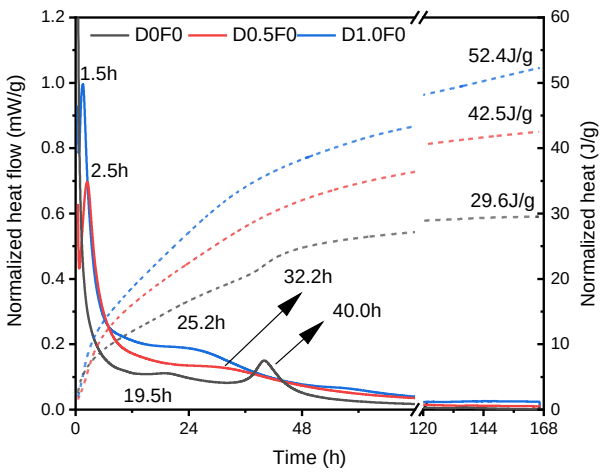

Fig. 8.7: Cumulative heat and heat flow during the initial 168 h of hydration: 0, 0.5 and 1.0 wt% DTPA-5Na-activated BOF slag binder.

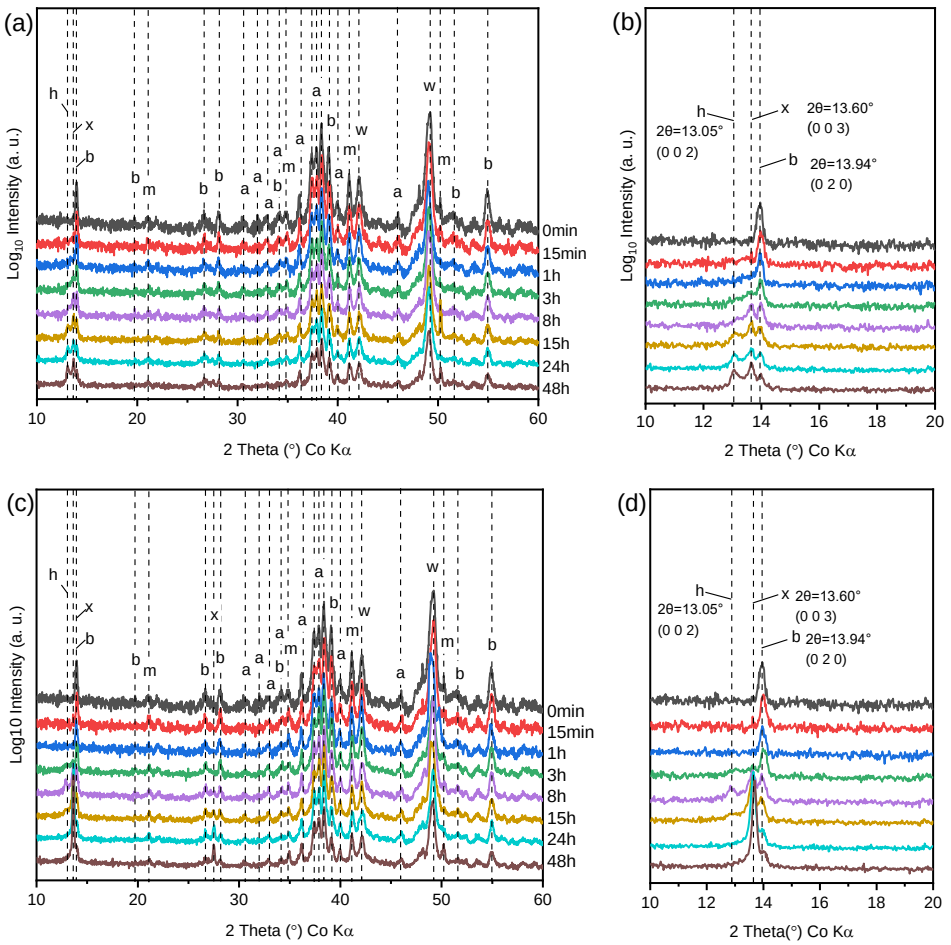

Fig. 8.8: Phases evolution of D0F0 (a-b) and D1F0 (c-d) after 0min, 15min, 1, 3, 8, 15, 24 and 48h. (a, c) 2θ ranges from 10° to 60°, and (b, d) 2θ ranges from 10° to 20°. The patterns are displaced vertically for clarity. (a- alpha' and beta dicalcium silicate, b- brownmillerite, m- magnetite, p- portlandite w- wüestite, h- hydrocalumite, x- monocarboaluminate).

The incorporation of DTPA-5Na induces a different heat release behavior in the early ages. Specifically, it leads to an intense peak within the first few hours, followed by another broad peak of lower intensity. For 0.5 wt% DTPA-5Na, the times to reach the two heat peaks are 2.5 h and 32.2 h, respectively. For 1.0 wt% DTPA-5Na, the peaks occur at 1.5 h and 25.2 h. It should be noted that the phase composition of D1.0F0 does not exhibit significant change after 1h and 3h of hydration, as depicted in **Fig. 8.8(c)**. Consequently, the initial intense peak observed around 1.5h in the calorimetry test is likely attributed to the dissolution of brownmillerite, facilitated by the chelating effect of DTPA-5Na. Certainly, a minor portion of the heat may also be associated with the formation of monocarboaluminate, as indicated by the tiny peaks observed in **Fig. 8.8(d)**. The primary hydration product in DTPA-5Na-activated BOF slag is monocarboaluminate, while the formation of hydrocalumite is limited. This limitation is potentially due to the competition between the two minerals for calcium and aluminum. Additionally, there is a demonstrable promotion in the total heat released during the first 168 h

of hydration with the introduction of DTPA-5Na, from 29.6 J/g for D0F0 to 42.5 J/g with 0.5 wt% DTPA-5Na, and further to 52.4 J/g with 1.0 wt% DTPA-5Na. This underscores the pronounced acceleration of BOF slag hydration facilitated by DTPA-5Na, with the acceleration extent intricately contingent upon the dosage of DTPA-5Na.

The 7d hydration heat release of 1.0 wt% DTPA-5Na-activated BOF slag with the incorporation of different concentrations of FGD gypsum is depicted in **Fig. 8.9**. It is evident that the hydration peaks of the binder are significantly delayed with increasing dosage of the FGD gypsum. Specifically, the time required to reach the hydration peaks extends from 1.5h and 24.2 h to 4.3 h and 45.8h, respectively, for 0.5 wt% FGD gypsum incorporation. Notably, as the FGD gypsum increases to 1.5 wt% or above, the evolution of hydration peaks displays distinct patterns compared with those in D0F0 and D1F0.5. Initially, a peak emerges at approximately 3.3 h with diminished intensity, succeeded by subsequent peaks occurring at 8.4 h, 14.0 h, and 24.2 h for 1.5 wt%, 2.5 wt%, and 3.5 wt% FGD gypsum incorporation, respectively. In order to elucidate the underlying reasons for these differing isothermal calorimetry patterns, the evolution of reaction products of D1F0.5 and D1F2.5 at 15 min, 45 min, 2 h, 4 h, 6 h, 8 h, and 15 h were characterized through XRD analysis, as illustrated in **Fig. 8.10**.

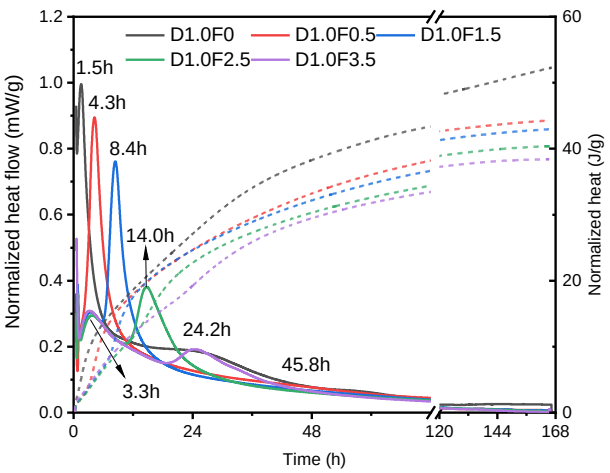

Fig. 8.9: Cumulative heat and heat flow during the initial 168 h of hydration: 1.0 wt% DTPA-5Na -activated BOF slag binder with varying dosages of FGD gypsum (0 to 3.5 wt%).

In the XRD patterns of D1F0.5, the peak of incorporated FGD gypsum is visible at 2θ = 13.45° (d = 7.61 Å) and continuously decreases in intensity and has disappeared entirely at 2h, indicating the early-stage dissolution in the hydration process. Subsequently, distinct peaks ascribed to the monocarboaluminate emerge after 4h hydration, identified as the primary contributor to the exothermic peak around 4.3h in **Fig. 8.9** for D1F0.5. Remarkably, the entire exothermic peak in D1F0.5 is attributed to the combined effects of FGD gypsum dissolution and monocarboaluminate generation, as well as the dissolution of brownmillerite.

In the case of D1F2.5, the gypsum is completely consumed after 6h, consistent with the anticipated prolonged dissolution duration for a higher gypsum dosage. Consequently, the initial exothermic peak around 3.3 h in **Fig. 8.9** for D1F2.5 is associated with the dissolution of FGD gypsum. The subsequent exothermic peak around 14.0 h corresponds to the monocarboaluminate formation, supported by the emergence of its distinctive peaks after 15 h

hydrations. This finding also indicates that the addition of FGD gypsum retards the dissolution of brownmillerite. Additionally, a small peak (2θ=13.05°), indicative of ettringite, is discernible after 8h hydration in the XRD patterns of D1F2.5. In summary, both DTPA-5Na and FGD gypsum significantly influence the hydration process of BOF slag binder and the associated hydration products, thereby opening up the possibility of modifying the overall properties of this binder.

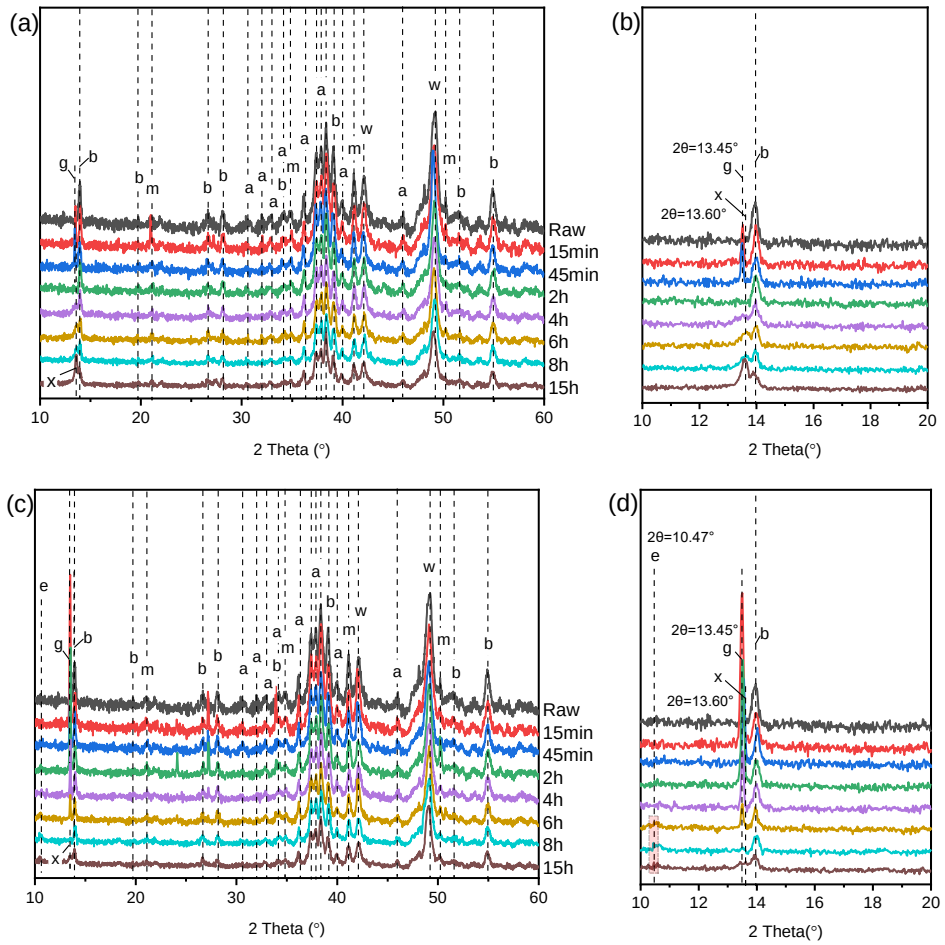

Fig. 8.10: Phases evolution of D1.0F0.5 and D1.0F2.5 after 15min, 45min, 2, 4, 6, 8 and 15h (a) 2θ ranges from 10° to 60° (b) 2θ ranges from 10° to 16°. The patterns are displaced vertically for clarity. (a- alpha' and beta dicalcium silicate, b- brownmillerite, e- ettringite, g-gypsum, m- magnetite, p- portlandite, w- wüestite, x- monocarboaluminate).

8.4.2 Effects of DTPA-5Na and FGD gypsum on mechanical properties

The compressive strength development for each paste is illustrated in **Fig. 8.11**. As anticipated, the paste containing only water exhibits relatively low compressive strength at 7 and 28 days, measuring around 5.0 and 9.8 MPa, respectively, due to the limited reactive phase contents within BOF slag. In comparison, a notable increase in compressive strength is observed with the addition of DTPA-5Na as an activator. For instance, at 28 days, D1F0 reaches 23.5 MPa,

indicating a significant enhancement in the hydration degree of the BOF slag. Furthermore, the incorporation of FGD gypsum leads to an even more substantial enhancement in mechanical performance. The compressive strength increases with a higher dosage of FGD gypsum, with D1F3.5 achieving a compressive strength of 37.5 MPa at 28 days. This significantly improved compressive strength underscores the synergistic effect of DTPA-5Na activation and FGD gypsum incorporation on BOF slag hydration, highlighting its great potential as a supplement to Portland cement binder. The mechanism behind the mechanical enhancement facilitated by DTPA-5Na and FGD gypsum will be discussed in the next Section through a systematic analysis of hydration products and microstructure characteristics.

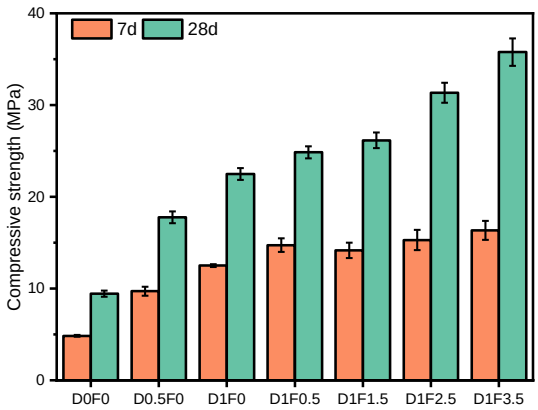

Fig. 8.11: Effect of DTPA-5Na and FGD gypsum content on compressive strength development.

8.4.3 Enhancement mechanism of DTPA-5Na and FGD gypsum

- **Q-XRD analysis**

To figure out the enhancement mechanism of DTPA-5Na and FGD gypsum on BOF slag hydration, their effects on the phase composition were evaluated through the XRD analysis. **Fig. 8.12** shows the mineralogical compositions of 28d DTPA-5Na activated BOF slag pastes. When the BOF slag was hydrated with only water, only traces of hydrocalumite and monocarboaluminate were detected, consistent with the phase evolution observed in **Fig. 8.8** during the early stages. Notably, the specific peak corresponding to hydrocalumite shifts from $2\theta = 13.05^{o}$ (**Fig. 8.8**) to 12.95^{o} (**Fig. 8.12**). This shift in layered double hydroxides suggests an expansion in the interlayer spacing, likely due to the substitution of hydroxides with carbonate ions with ages [231]. Upon activation of DTPA-5Na, there is a notable increase in the intensity of the peak associated with the monocarboaluminate, accompanied by a significant decrease in the intensity of peaks related to brownmillerite. Additionally, the peak attributed to hydrocalumite becomes invisible, indicating that DTPA-5Na facilitates monocarboaluminate formation while hindering hydrocalumite production. This phenomenon could be explained by the consumption of calcium and aluminum elements due to the formation of monocarboaluminate.

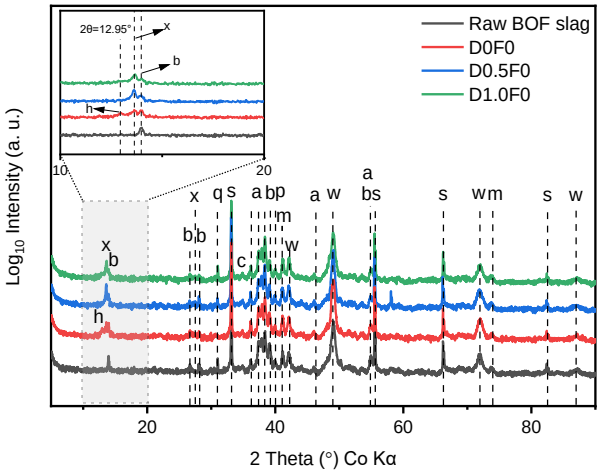

Fig. 8.12: XRD patterns of the raw BOF slag and 28d BOF slag (D0F0, D0.5F0 and D1.0F0). The patterns are displaced vertically for clarity. (a - alpha' and beta dicalcium silicate, b - brownmillerite, c - calcite, e - ettringite, m - magnetite, p - portlandite, w - wüestite, h - hydrocalumite, q - quartz, x - monocarboaluminate).

Table 8.4 presents a comprehensive overview of phase variations in the 28d BOF slag pastes under the activation of various DTPA-5Na and FGD gypsum dosages. It should be noted that the raw BOF slag used contains 9.9 wt% of amorphous content, largely introduced during the milling process of the raw materials. This amorphous fraction is primarily comprised of the C_2S phase, as identified by Kaja et al. in their investigation of the chemical composition of the BOF slag via Phase Recognition and Characterization (PARC) analysis and XRD Rietveld refinement [30]. Compared to raw BOF slag, the brownmillerite content in D0F0 decreases to 13.7 wt% and amorphous content decreases to 8.9 wt%, suggesting that, without any activation, the reactivity of BOF slag primarily resides in brownmillerite and amorphous C_2S. Notably, though the hydration of amorphous C_2S triggers the formation of C-S-H gel [125], part of it may contribute to the formation of monocarboaluminate and hydrocalumite, thereby decreasing the overall amorphous content. After the activation of DTPA-5Na, the brownmillerite content decreases to 12.2 wt% (with 1.0 wt% DTPA-5Na), while the monocarboaluminate content increases to 7.3 wt%, confirming its efficacy in promoting brownmillerite hydration. Meanwhile, the amorphous content declines with the incorporation of DTPA-5Na. This reduction can be attributed to two potential reasons: DTPA-5Na may facilitate the dissolution of amorphous C_2S, or the samples tested contain more crystalline C_2S.

Fig. 8.13 reveals the mineralogical composition of 1.0 wt% DTPA-5Na activated BOF slag pastes with various FGD gypsum dosages. The incorporation of FGD gypsum leads to the emergence of the peak associated with hydrocalumite, with its intensity escalating in proportion to the FGD gypsum dosages. Detailly, the hydrocalumite increases to 2.6~3.1 wt%, while monocarboaluminate decreases to 3.5 wt%, as shown in **Table 8.4**. This observation can be explained by FGD gypsum supplying adequate Ca^{2+} ions, thereby facilitating the formation of hydrocalumite. Notably, compared with the hydrocalumite formed in D0F0, the formed hydrocalumite in FGD gypsum-modified samples shows the specific peaks at a lower 2θ = 12.77 °. The shift is potentially induced by the incorporation of sulfate ions in the interlayer

[439]. Moreover, the addition of FGD gypsum promotes the formation of ettringite, reaching up to 7.2 wt% when combined with 3.5 wt% FGD gypsum. This observation is consistent with the results obtained during the early hydration stage of D1.0F2.5, as illustrated in **Fig. 8.10**. More importantly, the FGD gypsum-modified BOF slag binders activated by DTPA-5Na exhibit a comparatively lower residual amount of brownmillerite than those without incorporating the FGD gypsum, implying that gypsum facilitates the dissolution of brownmillerite. This effect could be attributed to the precipitations of ettringite, along with a decrease in calcium and aluminum concentrations in the aqueous environment, subsequently enhancing the dissolution process.

Table 8.4: The phase composition of the hydrated samples normalized to 100 g of anhydrous raw BOF slag (g).

Phase	Raw BOF	D0 F0	D0.5 F0	D1.0 F0	D1.0 F0.5	D1.0 F1.5	D1.0 F2.5	D1.0 F3.5
Wüestite*	31.0 (2.0)	29.4 (1.2)	29.8 (2.4)	30.5 (2.8)	29.7 (2.1)	27.8 (2.2)	27.4 (2.3)	30.4 (2.3)
Belite **	36.5 (2.0)	40.4 (2.0)	42.9 (2.0)	39.0 (2.9)	37.1 (2.1)	37.0 (2.3)	34.5 (2.2)	35.5 (3.0)
Magnetite	6.0 (0.3)	6.0 (0.2)	5.9 (0.3)	6.7 (0.3)	5.9 (0.3)	6.6 (0.3)	5.6 (0.3)	5.2 (0.3)
Brownmillerite	14.9 (0.5)	13.7 (0.5)	12.2 (0.4)	12.2 (0.7)	10.7 (0.9)	10.0 (0.6)	10.2 (0.6)	10.9 (0.6)
Lime	0.5 (0.1)	-	-	-	-	-	-	-
Calcite	0.4 (0.3)	1.1 (0.3)	1.4 (0.4)	1.4 (0.4)	2.7 (0.4)	0.7 (0.3)	0.4 (0.3)	0.9 (0.3)
Portlandite	0.04 (0.02)	-	0.06 (0.08)	0.15 (0.08)	0.02 (0.20)	0.04 (0.21)	0.30 (0.12)	0.47 (0.17)
Monocarboaluminate	-	4.1 (0.7)	5.2 (0.7)	7.3 (0.8)	6.7 (0.7)	3.9 (0.7)	5.8 (0.7)	3.5 (0.7)
Hydrocalumite	-	1.9 (0.3)	1.3 (0.4)	1.4 (0.4)	2.6 (0.4)	3.1 (0.4)	2.7 (0.4)	2.8 (0.4)
Ettringite	-	-	-	-	-	1.0 (0.3)	3.6 (0.4)	7.2 (0.4)
Amorphous	9.9 (2.3)	8.9 (2.2)	6.7 (2.7)	6.6 (3.3)	11.6 (2.7)	18.2 (2.7)	17.9 (2.7)	12.5 (3.1)

* : Total of the Fe-rich wüestite and Mg-rich wüestite. **: Total of the Larnite and Alpha'-belite. (): Errors derived from the TOPAS calculation.

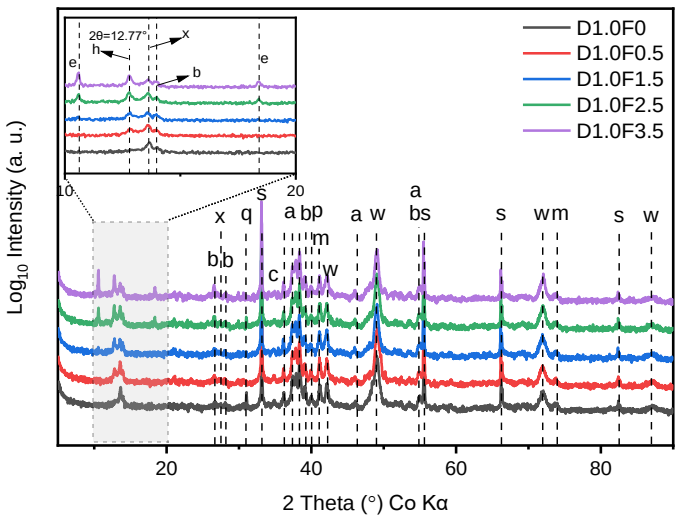

Fig. 8.13: XRD patterns of the 28d BOF slag (D1.0F0, D1.0F0.5, D1.0F1.5, D1.0F2.5 and D1.0F3.5). The patterns are displaced vertically for clarity. (a - alpha' and beta dicalcium silicate, b - brownmillerite, c - calcite, e - ettringite, m - magnetite, p - portlandite, w - wüestite, h - hydrocalumite, q - quartz, x - monocarboaluminate).

- **Thermogravimetric analysis**

Thermogravimetric analysis (TGA) and differential thermogravimetric analysis (DTG) were performed on 28d samples, with the results depicted in **Fig. 8.14**. For D0F0, a total mass loss of approximately 4 wt% can be observed over the temperature range, mainly attributed to the release of bound water within the hydrates and CO_2 within the carbonates. Specifically, the primary mass loss, occurring notably between 120 – 180 °C, is associated with the dehydration of monocarboaluminate [264,440]. Given the relatively low formation content of hydrocalumite in D0F0, its dehydration peak likely overlaps with that of monocarboaluminate. Additionally, minor peaks around 100 °C and 460°C are observed. These peaks are typically identified as the dehydration of C-S-H gel and portlandite based on the previous studies [420,438], confirming the hydration of a certain amount of C_2S within the BOF slag, as described by [441]:

$$C_2S + (2\text{-}x\text{-}y)H \rightarrow C_x\text{-}S\text{-}H_y + (2\text{-}x)CH \quad \textbf{(8.1)}$$

However, these products are formed in limited quantities, contributing to the low compressive strength of D0F0. Furthermore, a broad peak spanning 680 – 720 °C (labeled as (2) in **Fig. 8.14**) is observed, originating from the decomposition of carbonates like calcite and monocarboaluminate. The presence of carbonates indicates some carbonation occurring during the preparation and curing processes despite careful sealing and vacuum drying of the samples.

The introduction of DTPA-5Na and FGD gypsum in the BOF slag system induces an increased total mass loss over the temperature range, approximately ranging from 6% to 10%, suggesting an enhanced hydration degree of the BOF slag. Detailly, applying DTPA-5Na to the BOF slag results in an increased mass loss attributed to the dehydration of monocarboaluminate and C-S-H gel, indicating a higher content of hydration products. Additionally, in comparison with D0F0, a mass loss around 620 °C (labeled as (1) in **Fig. 8.14**) is observed when DTPA-5Na is incorporated. This mass loss is typically attributed to the decarbonation of magnesite ($MgCO_3$)

[442,443], although magnesite was not detected in our XRD analysis due to its low content and overlap with other phases. Consequently, magnesite is not included in **Table 8.4**. Notably, previous studies on the chemical composition of BOF slag indicate that magnesium predominantly exists in the forms of wüestite and magnetite [444]. Therefore, the observed mass loss due to the decarbonation of $MgCO_3$ indirectly confirms that DTPA-5Na promotes the dissolution of these minerals, aligning with the phase evolution findings presented in **Table 8.4**.

Incorporation of FGD gypsum into 1.0 wt% DTPA-5Na activated BOF slag induces a significant additional mass loss around 100-130 °C, ascribed to the dehydration of ettringite. Notably, this mass loss increases with higher FGD dosages, providing further evidence of its correlation with ettringite formation. Therefore, the enhanced mechanical performance resulting from the extra formation of ettringite can be inferred. The peak associated with portlandite initially increases with 0.5% FGD gypsum but declines with further increases in FGD gypsum content. This trend may be attributed to the extra consumption of Ca^{2+} by the formation of ettringite than portlandite, as the equilibrium formation of C-S-H gel with C_2S dissolution would permit a certain concentration of Ca^{2+}, sufficient for transforming low FGD dosages into ettringite. However, higher FGD dosages consume more Ca^{2+}, consequently inhibiting portlandite formation. This reduction in portlandite parallels findings in the hydration of C_3S with additional gypsum [445]. Unfortunately, identifying the mass loss attributed to the dehydration of C-S-H gel in the FGD-modified BOF slag system poses challenges, as it overlaps with the dehydration of ettringite.

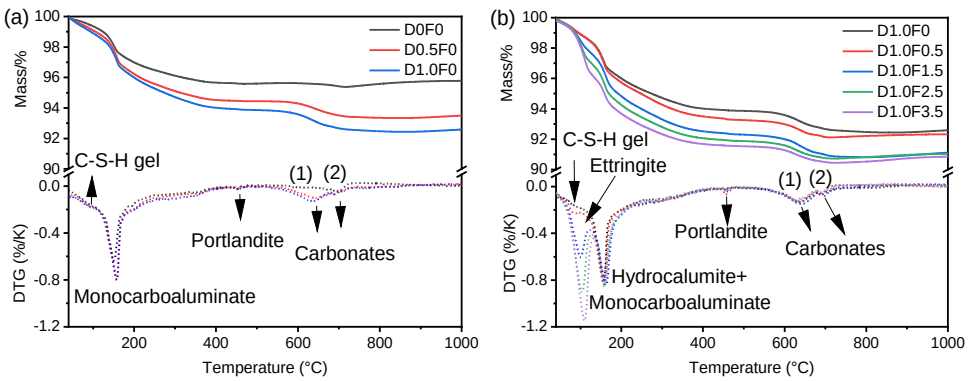

Fig. 8.14: TG and DTG curves of the 28d BOF slag (a) 0 - 1.0 wt% DTPA-5Na (b) 0 - 3.5 wt% FGD gypsum. (1) The mass loss is attributed to the decarbonation of the calcite from the BOF slag. (2) The mass loss is attributed to the decarbonation of the formed monocarboaluminate.

- **Pore structure**

Fig. 8.15(a) shows the total porosity and average pore size of BOF slag pastes after 28 d hydration obtained by MIP test. The BOF slag paste hydrated with water (D0F0) has the highest total porosity of 27.1% and an average pore size of 68.0 nm. Significant improvements are observed when DTPA-5Na is introduced as the activator, with 1.0 wt% DTPA-5Na, the total porosity decreases to 23.0%, and the average pore size reduces to 39.1 nm. Furthermore, upon adding FGD gypsum to the DTPA-5Na-activated BOF slag, additional enhancements are noted. Specifically, with the incorporation of 3.5 wt% FGD gypsum, the total porosity is diminished to 18.7%, and the average porosity is reduced to 23.7 nm. The decrease in total porosity aligns

with the enhanced mechanical performance depicted in **Fig. 8.11**, suggesting a correlation between reduced porosity and improved mechanical properties.

To elucidate the effect of DTPA-5Na and FGD gypsum on the pore structure in detail, the evolution of four types of pores - macro-pore (> 100 nm), capillary pore (50 – 100 nm), middle capillary pore (10 – 50 nm), and gel and mesopore (<10 nm) was investigated, based on classification from literature studies [56]. The pore volume distribution of each paste is illustrated in **Fig. 8.15(b)**. It is observed that the paste D0F0 exhibits the highest volume of pores >100 nm, which explains its low strength properties. Upon the activation of DTPA-5Na, pores (> 100 nm) become filled with more reaction products, forming additional capillary pores. A similar reduction in the macro-pores volume is noted after the incorporation of FGD gypsum, indicating the filling effect of the formed ettringite. Notably, a significant increase in gel pores and mesopores is observed when 3.5% FGD gypsum is utilized, which suggests a refinement in the pore structure, contributing to improved mechanical properties and overall performance of the paste.

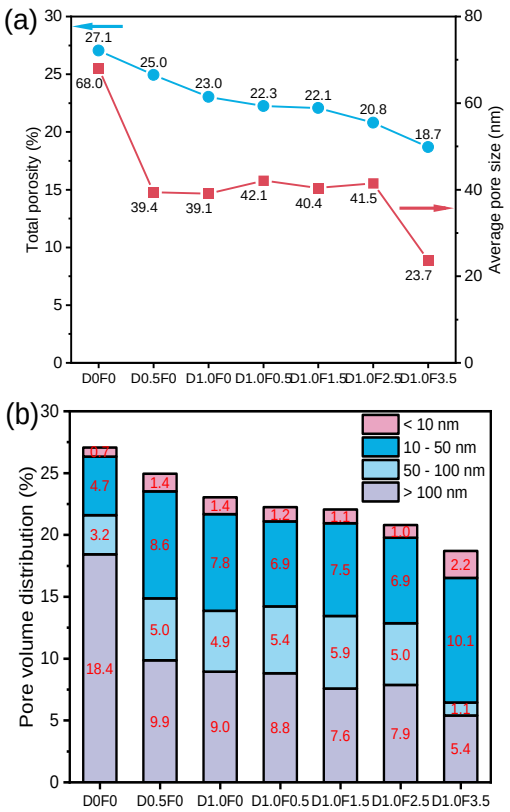

Fig. 8.15: (a) Total porosity and average pore size and (b) pore volume distribution of 28d samples.

- **SEM and EDX analysis**

To reveal the effect of DTPA-5Na and FGD gypsum on the microstructure of BOF slag pastes, specimens of D0F0, D1.0F0 and D1.0F3.5 after 28d hydration were examined using a scanning electron microscope (SEM). The secondary electron images on the fresh surface of these

samples are presented in **Fig. 8.16**. In the D0F0 sample, only irregular particles were observed. According to the previously mentioned results, the BOF slag hydrated only with water exhibits a low degree of reactivity. Consequently, the irregular polygonal morphology of these particles represents the BOF slag with a low degree of hydration. In comparison, the incorporation of 1.0 wt% DTPA-5Na in the D1.0F0 sample results in the formation of well-distributed flaky crystals throughout the matrix. These flaky particles are attributed to the formation of the minerals with a layered structure (e.g. monocarboaluminate and hydrocalumite), indicating increased reactivity facilitated by DTPA-5Na, as confirmed by XRD results. Furthermore, in the D1.0F3.5 sample, some rod-like crystals intercalated with the flaky crystals can be observed. These rod-like crystals are the newly formed ettringite. These observations are consistent with XRD results, which confirm the formation of both ettringite and monocarboaluminate. Their formation also aligns with the pore structure analysis, indicating that the addition of FGD gypsum contributes to ettringite formation, which fills the pores and refines the microstructure of the pastes, thereby enhancing their mechanical properties.

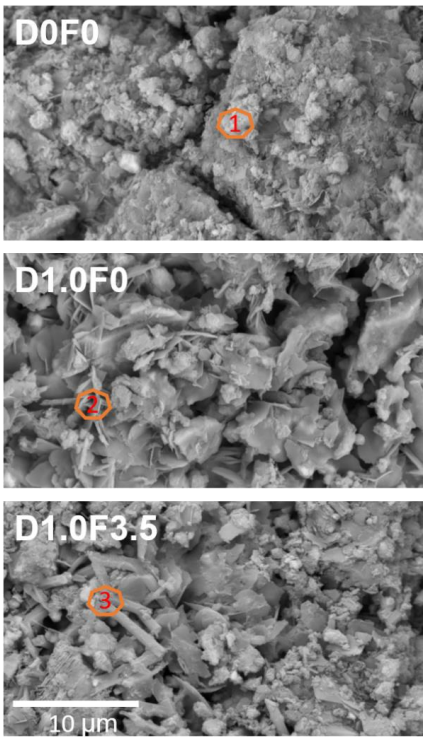

Fig. 8.16: SEM-SE image of the 28d D0F0, D1.0F0 and D1.0F3.5. Particles with representative morphology were selected for EDS spot analysis (1) irregular particles, (2) flaky particles, and (3) rod-like particles.

A detailed EDS spot analysis was conducted on crystals with various shapes, as observed in **Fig. 8.16**. The chemical compositions of these crystals are analyzed and summarized in **Table 8.5**, presented in terms of atomic concentration. Compared to the composition of D0F0, D1.0F0 reveals notable increases in aluminum and calcium elements, which is consistent with the composition of the formed monocarboaluminate. Meanwhile, D1.0F0 exhibits increased iron

content. This increase is attributable to Fe (III) dissolved from brownmillerite, which contributes to the formation of Fe-monocarboaluminate, where Al(III) is substituted by Fe(III) [437]. Additionally, since the formation of monocarboaluminate relies on the dissolution of brownmillerite, it is likely that monocarboaluminate precipitates on the surface of brownmillerite, resulting in a higher iron content due to this overlapping.

In the case of the FGD gypsum-modified samples D1.0F3.5, the heightened presence of aluminum and sulfate elements provides compelling evidence for ettringite formation. Additionally, the rod-like particles in D1.0F3.5 exhibit a high concentration of Fe. Similar with the Fe-monocarboaluminate, Fe(III) can partially substitute for Al(III) in ettringite, leading to the formation of Fe-ettringite ($Ca_6[Al_{1-x}Fe_x(OH)_6]_2(SO_4)_3 \cdot 26H_2O$) [446]. Studies have shown that Fe-ettringite forms much slower than Al-ettringite [447]. Therefore, the Fe-ettringite phases are more likely to form at later stages of hydration, contributing to the stability of the iron within the matrix.

Table 8.5: Spot analysis of the D0C0, D1.0F0, and D1.0F3.5 (the positions are marked in **Fig. 8.16**).

Element symbol		O	Mg	Al	Si	S	Ca	Ti	V	Cr	Fe
Atomic Concentration	(1)	72.49	1.76	0.19	3.41	N.D.	15.92	0.47	0.54	N.D.	4.02
	(2)	65.39	1.03	1.55	2.28	N.D.	17.57	3.54	0.87	0.69	6.23
	(3)	67.32	2.00	1.59	2.65	2.68	16.23	0.23	0.32	0.11	5.23

N.D.- not detected.

8.4.4 Environmental impact

Certain heavy metals can persist during steel manufacture in BOF slag, raising concerns about their leaching potential and resulting environmental impacts when utilized as building materials. The leaching behavior of raw materials and 28d cured paste samples have been characterized, with findings detailed in **Table 8.6**. The heavy metals found in raw BOF slag are Chromium (Cr), Molybdenum (Mo) and Vanadium (V), while only V is detected in FGD gypsum. The leaching of these elements is below the permissible limit set by the Dutch soil quality decree.

Upon 28d hydrated BOF slag with only water (D0F0), there is increased leaching of Cobalt (Co), Mo and V. This heightened leaching is attributed to mineral dissolution during the hydration process. Santos et al. have revealed the distribution of Cr and V within the BOF slag mineral phases, with Cr mostly incorporated in wüestite and brownmillerite and V predominantly found in C_2S and brownmillerite [444]. Hence, the dissolution of brownmillerite, as indicated by the XRD patterns in **Fig. 8.8**, likely contributes to these increased leaching levels.

Meanwhile, the addition of DTPA-5Na results in increased leaching of most heavy metals, likely due to DTPA-5Na accelerating the mineral dissolution, thereby releasing internal heavy metals. However, the leaching of V decreases, possibly due to the formation of solid $Ca_3(VO_4)_2$ ($\log K_{SP}$ = -17.97), which precipitates dominantly at pH around 12 [448]. The equilibrium formation of C-S-H phases with C_2S dissolution would allow for high Ca^{2+} concentration in the leachate and limit the solubility of $Ca_3(VO_4)_2$ [449]. Hence, more V is solidified and remains embedded within the matrix, as corroborated by the chemical composition analysis of reaction products in D1.0F0 (**Table 8.5**).

Incorporating FGD gypsum in DTPA-5Na-activated BOF slag diminishes Cr leaching. Previous studies have indicated that Cr(VI) is the predominant form in BOF slag leachate, as opposed to Cr(III) [450]. At a pH of around 12, Cr(VI) primarily exists as CrO_4^{2-}. Consequently, the addition of $CaSO_4$ promotes the precipitation of $CaCrO_4$ (logKsp = -5.29). Moreover, it has been reported that the ettringite formed in FGD-modified BOF slag can immobilize CrO_4^{2-} within its molecular structure [451]. Enhanced ettringite formation consequently leads to greater immobilization of Cr. It should also be mentioned that Cr(III) precipitates as $Cr(OH)_3$ under high pH conditions, further contributing to the reduction of Cr leaching. However, the leaching of V increases as ettringite formation consumes Ca^{2+}, resulting in less $Ca_3(VO_4)_2$ precipitation. In the case of Co, Cu, Mo and Ni, their leaching levels vary with increased FGD gypsum, likely due to altered equilibrium formation of hydrocalumite, ettringite and C-S-H gel, which have different immobilization capacities of heavy metals [332,452–455]. Overall, the prepared BOF slag pastes exhibit satisfactory levels of heavy metals leaching, thus validating their suitability as environmentally friendly binders. Further investigation, particularly concerning Mo leaching near the threshold, is necessary to understand the influence of higher gypsum levels on the retention of contaminants in the BOF slag hydration products.

Table 8.6: The leaching behavior of the heavy metals from the raw BOF slag, FGD gypsum and 28d paste samples obtained through one batch leaching test at a liquid to solid of 10, and the SQD legal limit values. All values are in mg/kg dry raw materials. (L.D. - Lower than the detection limits).

Elements	Co	Cr	Cu	Mo	Ni	V
Raw BOF	L.D	0.07	L.D	0.17	L.D	0.29
Raw FGD	L.D	L.D	L.D	L.D	L.D	0.01
D0F0	0.01	0.04	L.D	0.27	L.D	0.68
D0.5F0	0.36	0.13	0.13	0.43	0.24	0.63
D1.0F0	0.41	0.14	0.26	0.44	0.25	0.05
D1.0F0.5	0.37	0.03	0.68	0.42	0.21	0.36
D1.0F1.5	0.39	0.02	0.49	0.47	0.22	0.41
D1.0F2.5	0.41	0.02	0.77	0.55	0.21	0.52
D1.0F3.5	0.18	0.01	0.43	0.71	0.17	0.41
Limits	0.54	0.63	0.9	1.0	0.44	1.8

8.4.5 BOF slag hydration model: theoretical water demand and chemical shrinkage

Based on the Q-XRD and TG analysis, the primary reactive components in BOF slag are C_2S and brownmillerite, leading to the formation of monocarboaluminate, hydrocalumite and C-S-H gel. It is noteworthy that BOF slag contains limited C_3S content, resulting in a hydration process distinctly different from that of Portland cement. Overall, the reactivity of C_2S is low, and early strength development is highly dependent on the hydration of brownmillerite. After the activation of DTPA-5Na, the dissolution of brownmillerite is accelerated, while other minerals such as wüestite and magnetite exhibit limited significant changes. Hence, we simplify the hydration of BOF slag post-DTPA-5Na activation to the hydration of C_2S and brownmillerite, assuming the other minerals are inert phases. The theoretical water demand required for the full hydration of BOF slay is thereby calculated according to the following reactions [456]:

$$C_2S + 3.5H_2O \rightarrow C_{1.7}SH_{3.2} + 0.3CH \quad \textbf{(8.2)}$$

$$2C_2(A, F) + Cc + CH + 10H \rightarrow C_4(A, F)cH_{11}(\text{Monocarboaluminate}) \quad \textbf{(8.3)}$$

$$2C_2(A, F) + Cc + CH + 9H \rightarrow C_4(A, F)cH_{10}\ (\text{Hydrocalumite-carbonate}) \quad \textbf{(8.4)}$$

$$2C_2(A, F) + CsH_2 + CH + 7H \rightarrow C_4(A, F)sH_{10}\ (\text{Hydrocalumite-sulphate}) \quad \textbf{(8.5)}$$

$$2C_2(A, F) + 3CsH_2 + 34H \rightarrow C_6(A, F)s_3H_{36}\ (\text{Ettringite}) + CH + (A, F)H_3 \quad \textbf{(8.6)}$$

whereby the reaction products (monocarboaluminate and hydrocalumite) are modified based on the findings in the present study. Assuming that the amorphous phase in the raw BOF slag accounts for the XRD-amorphous C_2S (as determined in a previous study on the chemical composition of BOF slag via XRD Rietveld analysis and Phase Recognition and Characterization analysis [30]), and considering that only monocarboaluminate or hydrocalumite can be formed (due to various water content is needed for the formation of monocarboaluminate and hydrocalumite), the calculated water demand for pure BOF slag, expressed as water/slag mass ratio, is 0.22 ~ 0.23.

When the gypsum is included, the total formation of ettringite is restricted by its dosage, given that the brownmillerite content is relatively higher than that of gypsum. Therefore, assuming that all the gypsum contributes to the ettringite formation, the calculated water demand for 3.5 wt% gypsum modified BOF slag, expressed as water/slag mass ratio, is 0.25 ~ 0.26.

Table 8.7: Mineralogical composition of BOF slag and phase properties.

Phase	Mass content in BOF slag [wt%]	Density (TOPAS) [g/cm^3]	Molar mass of pure phases [g/mole]	Molar volume [cm^3/mole]
Wüstite	27.4	4.600	71.85	15.62
Magnetite	3.7	5.119	55.85	10.91
C_2S	24.5	3.307	172.24	52.08
Brownmillerite	14.3	3.810	271.85	71.35
Lime	0.7	3.432	56.08	16.34
Calcite	0.4	2.813	100.09	36.34
Gypsum	-	2.960	172.16	58.16
Amorphous	18.2			
Portlandite		2.211	74.09	33.51
Monocarboaluminate		2.173	568.46	261.60
Hydrocalumite		1.652	289.46	175.22
Ettringite		1.791	1255.11	700.79
C-S-H		2.25 [456]	213.09	94.70

Assuming that C_2S and brownmillerite are the only reactive phases in the BOF slag, the total chemical shrinkage can be calculated based on the proposed hydration reactions and data presented in **Table 8.7**. As the distinction between amorphous content originating from raw BOF slag and that due to the precipitation of C-S-H gel could not be made through Q-XRD analysis in this study, the quantity of C-S-H gel was determined based on the bound water in 28d hydrated samples (from the thermogravimetric analysis, 4.52g for D0F0, 6.54g for D1.0F0 and 9.19g for D1.0F3.5 per 100 g_{slag}). Specifically, the amount of water bound in hydrocalumite, monocarboaluminate, portlandite and ettringite was calculated, with all remaining water assumed to be incorporated into C-S-H gel. The amount of C-S-H gel was then calculated and subsequently subtracted from the total amorphous content to estimate the content of unreacted

XRD-amorphous C_2S. After 28d hydration, the total chemical shrinkage of D0F0 is 2.1 ml/100 g_{slag}, which translates to 5% volume reduction. This value is substantially lower than that for OPC (6 ~ 9 ml/100 g_{cement}) [457] or GGBFS slag (11 ~ 15 ml/100 g_{slag}) [458]. The low chemical shrinkage is attributed to the low hydration degree of C_2S after 28d, as well as the high level of inerts in the BOF slag. The detailed phase composition of BOF slag (D0F0, D1.0F0 and D1.5F0) hydrated for 28d is presented in **Fig. 8.17**. Upon activation of DTPA-5Na, the chemical shrinkage increases to 3.3 ml/ 100 g_{slag} due to the enhanced reaction degree of brownmillerite and amorphous C_2S. Integration of gypsum further elevates the chemical shrinkage to 3.9 ml/ 100 g_{slag}. Interestingly, the addition of gypsum facilitates the hydration of amorphous C_2S and brownmillerite. As a result, a greater amount of free water is bound into the hydration products, aligning with the observed increase in chemical shrinkage.

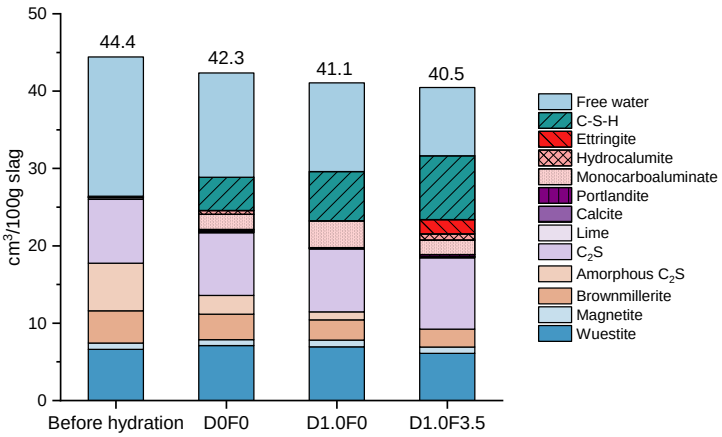

Fig. 8.17: Composition of BOF slag paste before and 28d of hydration – D0F0, D1.0F0 and D1.0F3.5 (measured).

To verify the proposed hydration reaction, the calculated phase composition of hydrated BOF slag is depicted in **Fig. 8.18**. A hydration degree of $\alpha = 0.3$ was employed, based on the reaction degree of the C_2S phase after 28d according to **Fig. 8.17**. It must be noted that the various water content required for the formation of monocarboaluminate and hydrocalumite influences the calculation of consumed free water, as indicated in **Eq. (8.3)** and **Eq. (8.4)**. Hence, the hydrated BOF slag with only monocarboaluminate or hydrocalumite formation was calculated separately. Comparing the volume of D0F0 (42.3 cm^3/ 100 g_{slag}) in **Fig. 8.17**, the range of 42.7 to 42.1 cm^3/ 100 g_{slag} confirms the desirable outcomes from the hydration model of BOF slag.

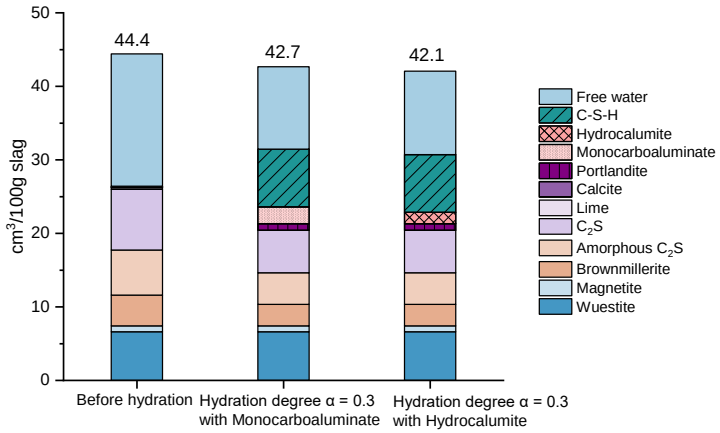

Fig. 8.18: Composition of BOF slag paste before hydration and D0F0 with only monocarboaluminate or hydrocalumite at the hydration degree of α = 0.3 (modeled).

However, some discrepancies in the volume ratios of hydration products, as calculated according to the proposed hydration reaction, can be observed between D0F0 in **Fig. 8.17** and **Fig. 8.18**. Several factors may contribute to these variations. 1) The formation of monocarboaluminate and hydrocalumite could be influenced by the localized w/b ratio, which is likely to be lowered during the hydration process. 2) The bound water content in C-S-H gel may differ from the Ca/Si ratio, likely influenced by the dissolution process of the minerals, such as brownmillerite, lime and C_2S. 3) The bound water content might be overestimated, as the termination of the hydration process by isopropanol and diethyl ether cannot exchange all free water [459]. Certainly, there are some additional aspects that could be further considered to improve the hydration model of BOF slag. 1) Enhancing measurement techniques to accurately identify the amorphous content present in the raw BOF slag. 2) Developing methods to effectively differentiate between unreacted amorphous content and newly formed C-S-H gel in hydrated BOF slag. 3) Considering the potential dissolution of wüestite during the hydration process of BOF slag. 4) Various bound water content in monocarboaluminate due to Fe(III) substitution.

To validate the effect of DTPA-5Na on the activation of brownmillerite, the proposed hydration reaction of BOF slag was employed, and the chemical shrinkage was calculated at a hydration degree of 0.35 for C_2S (as per **Fig. 8.17**). **Fig. 8.19** presents the theoretical volume of D1.0F0 at various hydration degrees of brownmillerite. Comparing these theoretical results with the measured results of D1.0F0, the hydration degree of brownmillerite ranges from 0.45 to 0.69 (> 0.3), confirming that the DTPA-5Na promotes the hydration of brownmillerite. Similar calculations were conducted with hydrated D1.0F3.5 to validate the impact of FGD gypsum on the hydration of brownmillerite. **Fig. 8.20** presents the theoretical volume of D1.0F3.5 at various hydration degrees of brownmillerite. Combining these theoretical results with the measured results of D1.0F3.5, the hydration degree of brownmillerite ranges from 0.75 to 1.0, confirming that FGD gypsum also contributes to the hydration of brownmillerite. However, it should be noted that the hydration degree of brownmillerite in both D1.0F0 and D1.0F3.5 may be overestimated due to several factors mentioned earlier in this Section. Further efforts are required to improve the hydration modeling of BOF slag.

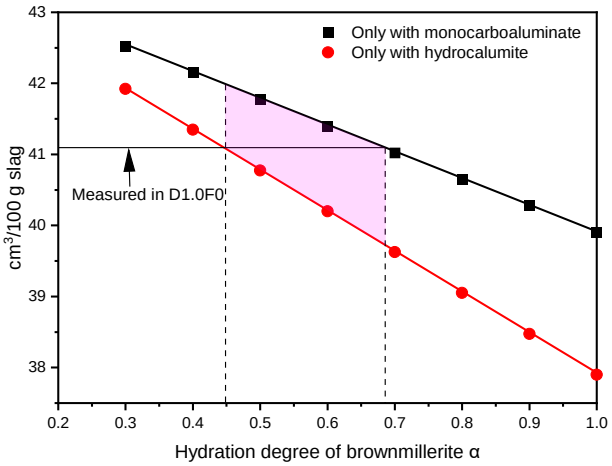

Fig. 8.19: Theoretical volume of D1.0F0 at various hydration degrees of brownmillerite (Hydration degree of C_2S was set as 0.35 according to **Fig. 8.17**).

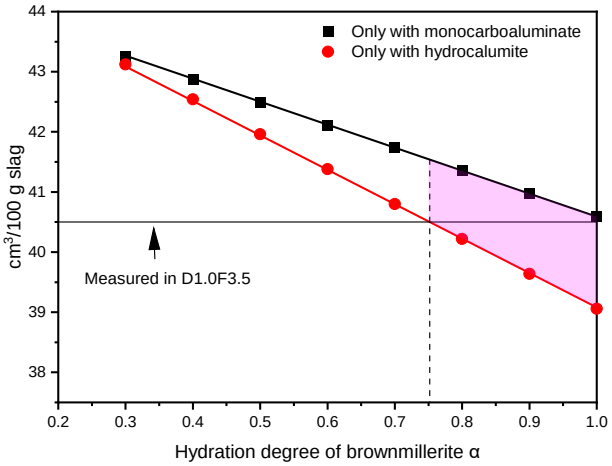

Fig. 8.20: Theoretical volume of D1.0F3.5 at various hydration degrees of brownmillerite (Hydration degree of C_2S was set as 0.35 according to **Fig. 8.17**).

8.5 Discussions of BOF slag-based binder materials

8.5.1 Activation mechanism of DTPA-5Na

In this study, DTPA-5Na was employed to promote the hydration process of BOF slag. Based on the findings in the hydration kinetics and mechanical performance of the formulated BOF slag pastes, DTPA-5Na demonstrates its promising potential for activating BOF slag and promoting the monocarboaluminate formation. More insight into the chelating reaction between DTPA-5Na and the ions from the BOF slag is provided herein to elucidate the activations mechanism of DTPA-5Na.

In accordance with cement hydration theory [460], the precipitation of hydration products involves several sequential stages, including dissolution, saturation, nucleation, and growth.

Similarly, it is expected that the hydration products of the binder made from basic oxygen furnace (BOF) slag would follow a similar pattern. Subsequently, the leachable [Ca], [Al], [Fe], [Na] elements, major elements involved in the chelation process, were analyzed in both raw materials and DTPA-5Na activated BOF slag via one-batch leaching tests, as illustrated in **Fig. 8.21**. The raw BOF slag exhibited a leachable [Al] of 31.63 mg/Kg, [Fe] of 0.04 mg/Kg, [Na] of 14.5 mg/Kg and [Ca] of 4130 mg/Kg. With relatively sufficient [Al] and [Ca], it is reasonable to observe the formation of monocarboaluminate and hydrocalumite, as verified in **Fig. 8.8**. After the 28d hydration, due to the formation of these products in D0F0, the leachable [Al] and [Ca] reduce correspondingly.

When 0.5 wt% DTPA-5Na is incorporated, there is an increase in the leachable [Na] content, confirming the dissolution of DTPA-5Na, as represented by:

$$\text{DTPA-5Na} + 5H_2O \leftrightarrow [\text{DTPA-5H}] + 5Na^+ + 5OH^- \quad \textbf{(8.7)}$$

Similarly, the incorporation of 1.0 wt% DTPA-5Na in D1.0F0 results in almost twice the [Na] content, consist with the doubled amount of DTPA-5Na, indicating desirable test accuracy. It is noteworthy that there is an increase in the leachable [Ca], while leachable [Al] shows a slight decrease and leachable Fe content remains extremely low. This observation contrasts with the expected stability constants of DTPA chelating agents for different ions, which are typically Fe(III) > Al(III) > Ca(II) [461]. Similar findings have been reported for the chelating ability of EDIPA when tested with $CaCl_2$, $AlCl_3$, and $FeCl_3$ solutions, respectively [33]. Therefore, this conflicting phenomenon suggests that relying solely on the known chelating abilities of chelators is insufficient to elucidate the mechanisms of their interactions with multiple metal ions within the BOF slag binder system. The effect of the pH of the pore solution on the stability of chelates should be taken into consideration, as the hydration of C_2S in BOF slag provides an alkaline environment [438]. Fe(III) and Al(III) are likely precipitates, thereby reducing the stability of the chelate. Hence, DTPA more likely chelates with Ca(II), as expressed by:

$$\text{DTPA-5H} + Ca^{2+} \leftrightarrow [\text{Ca-DTPA-3H}] + 2H^+ \quad \textbf{(8.8)}$$

Importantly, chelated metal ions do not participate in the dissolution balance [429]. Chelation is equivalent to reducing calcium concentration in the aqueous phase. According to Le Chatelier's principle, this promotes forward dissolution progress until a new value of the dissolution equilibrium constant K is reached [462]. Consequently, the dissolution of brownmillerite is promoted, as expressed by:

$$Ca_2(Al_x,Fe_{1-x})_2O_5 + 5H_2O \leftrightarrow 2Ca^{2+} + 2xAl(OH)_4^- + (2-2x)Fe^{3+} + (10-8x)OH^- \quad \textbf{(8.9)}$$

However, it is essential to acknowledge that certain heavy metals, which may be physically or chemically encapsulated within the BOF slag [463], are also released during the dissolution process. Therefore, when increasing DTPA-5Na dosages, further consideration should be given to leaching, as this could lead to increased release of heavy metals, raising environmental and safety concerns.

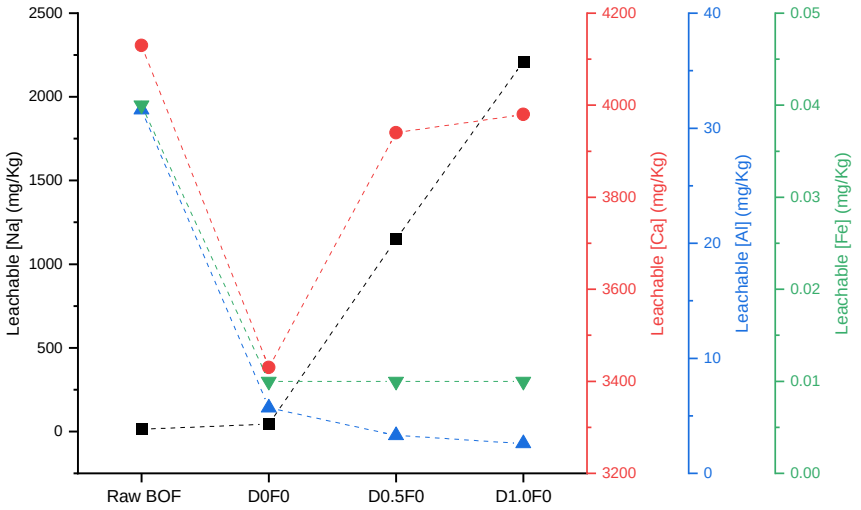

Fig. 8.21: Leachable Na, Ca, Al and Fe elements from the Raw BOF slag, D0F0, D0.5F0 and D1.0F0. Values are normalized by the amount of BOF slag in the samples.

8.5.2 Effect of calcium and sulfate on the enhanced mechanism

This study proposed the integration of FGD gypsum into DTPA-5Na-activated BOF slag binder in order to augment its recovery and utilization in construction materials and simultaneously improve the overall performance of the binder. It has been found that FGD gypsum can delay the hydration (**Fig. 8.9**) and influence the hydration reaction products (**Fig. 8.13**). Enhancing the understanding of the impact of calcium and sulfate would be beneficial for regulating the final performance of the BOF slag binder system. As observed in **Fig. 8.10**, the formation of monocarboaluminate is only observed after the dissolution of FGD gypsum. Hence, the delay effect of FGD gypsum on the hydration of BOF slag is likely related to the dissolution equilibrium. Taking into account the DTPA-5Na activation mechanism outlined in **Section 8.4.1**, the more [Ca] in the aqueous phase via chelation facilitates the dissolution of brownmillerite. Reasonably, the dissolution of brownmillerite could be influenced by the concentration of [Ca] in the aqueous phase, according to **Eq. (8.9)**. Therefore, the [Ca] released from the FGD gypsum plays a vital role in the hydration process of DTPA-5Na activated BOF slag.

To elucidate the impact of [Ca], sodium sulfate with an equivalent sulfate content to D1.0F1.5 was integrated into 1.0 wt% DTPA-5Na activated BOF slag (named D1.0S1.5). **Fig. 8.22** illustrates the hydration behavior of D1.0F1.5 and D1.0S1.5 over the initial 168 h. D1.0S1.5 demonstrates a pronounced heat flow at the beginning of the calorimetry test and a significant peak at 8.5 h, while D1.0F1.5 displays a minor peak at 3.3 h followed by a prominent peak at 8.4 h. This discrepancy can be partially attributed to the distinct dissolution properties between FGD gypsum and sodium sulfate. FGD gypsum has low solubility (Ksp = 2.4×10^{-5}), whereas sodium sulfate readily dissolves in water, leading to a higher heat release during mineral dissolution. Besides, the more rapidly dissolved sulfate in D1.0S1.5 promptly engages in hydration, resulting in a higher cumulative heat within 168 h. Notably, the sulfate in D1S1.5 contributes to the formation of hydrocalumite at 7d (indicated by a tiny broad peak at 2θ=13.07° in **Fig. 8.23**), while ettringite is rarely detected. However, the opposite phenomenon is observed

in 7d D1.0F1.5. The disparity may be attributed to insufficient [Ca] for ettringite formation when sodium sulfate is used. Moreover, sulfate ions are likely solidified in the interlayer of the hydrocalumite, hindering further reaction to form the ettringite.

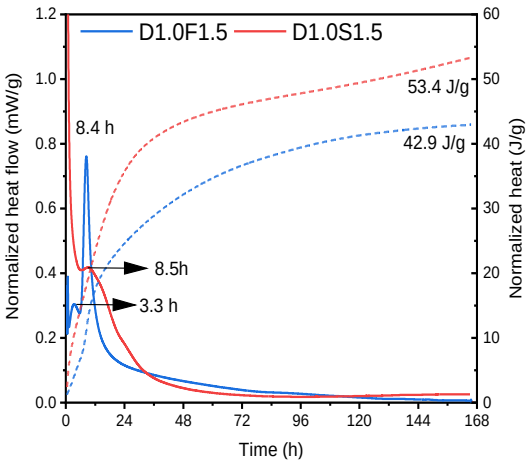

Fig. 8.22: Cumulative heat and heat flow of D1.0F1.5 and D1.0S1.5 during the initial 168 h of hydration.

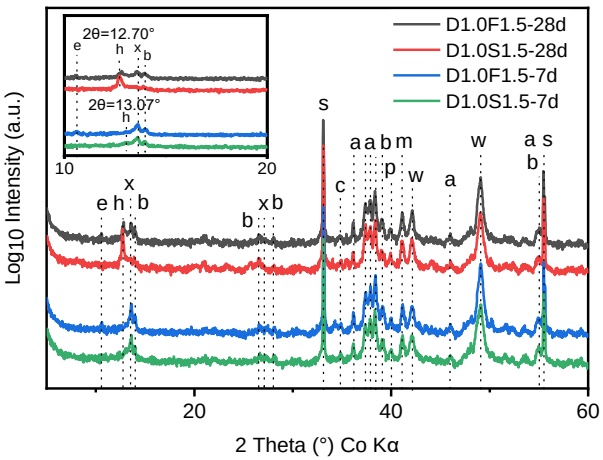

Fig. 8.23: XRD pattern of 28d D1.0F1.5 and D1.0S1.5. (a - alpha' and beta dicalcium silicate, b - brownmillerite, c - calcite, e - ettringite, m - magnetite, p - portlandite, w - wüestite, h - hydrocalumite, q - quartz, x - monocarboaluminate).

Interestingly, the 7d compressive strength of D1.0S1.5 measures 19.0 MPa (**Fig. 8.24**), surpassing that of D1.0F1.5. However, this does not imply that hydrocalumite is more effective than ettringite in strength development. Instead, it suggests that the refined pore structure of the matrix, filled with more reaction products in D1.0S1.5, contributes to its higher strength, as supported by the greater cumulative heat released from the hydration reaction, as shown in **Fig. 8.22**. Overall, sodium sulfate and FGD gypsum exert a similar effect on the 28d compressive strength (**Fig. 8.24**). Consequently, regardless of the formation of sulfate-containing

hydrocalumite or ettringite, the level of reaction product formation remains limited by the sulfate content, thus affecting the strength development.

In summary, owning to the chelation effect of DTPA-5Na, introducing additional sulfate emerges as a viable strategy to promote hydration products in the DTPA-5Na-activated BOF slag system, while the release of Ca(II) facilitates the regulation of early hydration process. Therefore, industrial residues with high soluble sulfate content, such as phosphogypsum [464], electrolytic manganese residues [465], and gypsum residues generated in copper and zinc-making processes [466,467], represent promising candidates for inclusion in the design of DTPA-5Na-activated BOF slag-based binders. Moreover, the early strength of these binders can be modulated by the sulfate dissolution rate, allowing for the customization of early strength characteristics tailored for applications in rapid repairs and specialized concretes.

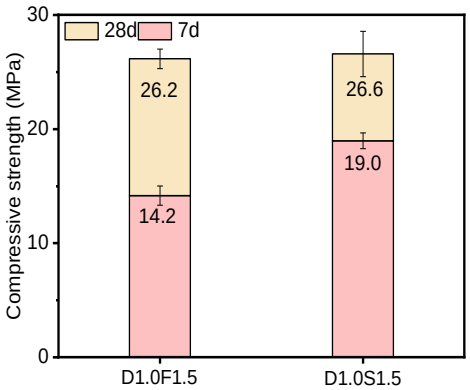

Fig. 8.24: Compressive strength of 7d and 28d D1.0F1.5 and D1.0S1.5.

8.6 Conclusions

This chapter evaluated the feasibility of using waste gypsum in cement production, focusing on setting time, hydration kinetics, and mechanical performance. The results indicated that the waste gypsum showed promising potential for use in cement formulations.

Meanwhile, this chapter aims to use BOF slag to prepare a sustainable cement-free binder with activation of DTPA-5Na and FGD gypsum incorporation. The hydration kinetics, mechanical performance and the potential environmental impact of this novel binder were evaluated. Meanwhile, to provide a comprehensive understanding of the role of DTPA-5Na on the activation of the BOF slag and the enhanced performance by FGD gypsum, the evolution of phase composition, pore structure and microstructure of the BOF slag binder under varying DTPA-5Na and FGD gypsum dosages were investigated. Based on the obtained results, the following conclusions can be drawn.

- DTPA-5Na effectively activates the hydration of BOF slag with 1wt% DTPA-5Na increasing the cumulative hydration heat from 29.6 J/g to 52.4 J/g in the first 168 h. The activation mechanism of DTPA-5Na involves promoting the dissolution of brownmillerite through chelating effects, thereby contributing to the formation of monocarboaluminate. The increased hydration products enhance the 28d compressive strength from 10 MPa to 23.5 MPa.

- The inclusion of FGD gypsum in the DTPA-5Na-activated BOF slag retards the hydration process and increases the setting time from 0.5h to 2.5h with 3.5wt% FGD gypsum. It results in a lower cumulative heat at early ages due to the partial occupation of DTPA-5Na by Ca ions released from FGD gypsum. Nonetheless, it is advantageous for promoting the ettringite formation, leading to a denser structure of the BOF slag binders. 3.5 wt% FGD gypsum enhances the 28d compressive strength from 23.5 MPa for D1.0F0 to 37.5 MPa for D1.0F3.5.

- The proposed FGD-DTPA-5Na-BOF slag binders have no leaching issues, with toxic elements such as Co, Cr, Cu, Mo, Ni, and V fully complying with leaching criteria. However, it is important to note that an increased activation degree of BOF slag may result in the release of more heavy metal ions originally embedded in the minerals. Therefore, the hydration degree and long-term durability of the formulated innovative BOF slag binders should be carefully addressed for each new formulation design.

- The additional sulfate from sulfate salts is the key factor influencing the formation of ettringite in DTPA-5N-activated BOF slag binder. Importantly, the diverse dissolution properties of sulfate salts can be leveraged to modify the hydration process. Furthermore, rapid ettringite and hydrocalumite formation facilitates early-age strength development.

Chapter 9 Conclusions and recommendations

This thesis focuses on the recycling and recovery of industrial solid waste within construction materials, aiming to devise economically and environmentally sustainable solutions. The investigated industrial solid wastes are readily available in the Netherlands and produced in significant quantities. Drawing upon the distinctive attributes of diverse waste types, this project proposes promising high-end applications, including sludge-based sealing materials (Chapter 2-3), alkali-activated materials (Chapter 4-7), and cement-free binders utilizing basic oxygen furnace slag (Chapter 8). The benefits from these newly developed materials for varying applications are summarized in **Table 9.1**. The newly developed materials can primarily be used for landfill sealing and as cementitious materials. By utilizing industrial solid waste, these materials promote recycling, reduce resource consumption, and offer enhanced sustainability with a lower carbon footprint compared to traditional materials. It is important to note that while the potential for CO_2 emission reduction is significant, a comprehensive life cycle assessment will be necessary in future research to fully quantify these environmental benefits.

Table 9.1: Summary of the newly developed materials for different applications.

Applications	Traditional materials	Newly developed materials	Benefits
Landfill sealing materials	Clay or clay-containing materials	Digested sewage sludge incineration fly ash aluminum-anodizing waste	- Reduced reliance on clay-based mineral resources and Ordinary Portland cement -Promotes recycling of industrial solid waste - Lowers CO_2 emissions during the cementitious materials productions, leading to cost-saving - Provides additional functionalities, such as self-cleaning properties.
Cementitious materials	Ordinary Portland cement	WIFD and sodium carbonate-activated materials	
		Biomass bottom ash-modified alkali-activated materials	
		Self-cleaning alkali-activated materials	
		Basic oxygen furnace slag-based binder materials	

Furthermore, to ensure the viability of the end products, a comprehensive array of properties is systematically evaluated. This research explores the potential enhancements in product performance through the regulation of admixture and additives, as well as the intricate interactions between components on both physical and chemical aspects. The major findings and corresponding recommendations for future research are outlined below.

9.1 Conclusions

9.1.1 Sludge-based sealing materials and their carbonation behavior

With the aim to eliminate the need for natural clay and promote the recycling of sludge materials, a proposal was made for sludge-based sealing materials to be used in landfill cover systems.

Through experimental investigation, it was found that a formulation consistent with digested sewage sludge (DSS) (46 wt%) with aluminum anodizing waste (AAW) (9 wt%) as additives and aggregates (45 wt%), alongside waterglass (Na_2SiO_3) (1.5 wt%), demonstrated the lowest permeability (k value = 3.78×10^{-12} m/s). The colloidal boehmite present in AAW played a significant role in filling voids and reducing total porosity, thereby enhancing the impermeability of the matrix. The formation of gypsum within the sealing materials was attributed to leachable sulfate from the additives. Considering the low pH of the pore solution, the low dosage of waterglass (1.5 wt%) tended to form silica gel rather than the C-S-H gel.

Due to substantial greenhouse emissions in landfills stemming from the decomposition of organic waste, the potential impact of CO_2 on landfill sealing materials was evaluated. Following CO_2 diffusion, their permeability values increase, accompanied by the formation of carbonates and monohydrocalcite. The formation of monohydrocalcite is influenced by the leachable magnesium content in the raw materials. The degradation in impermeability is due to volume alterations induced by mineral carbonation processes. The organic content from the sludge remains stable during the carbonation process. A higher dosage of waterglass mitigates the increase in permeability resulting from carbonation, attributed to the formed silica gel, which is less carbonated and actively participates in filling the void spaces. Additionally, the impact of carbonation on the leachability of toxic elements is intricately linked to the nature of the raw materials employed.

9.1.2 Recycling industrial solid waste in alkali-activated materials

Sustainable building materials with low CO_2 emissions are increasingly sought after in the cement industry. Alkali-activated materials represent one such alternative, formulated by mixing aluminosilicate precursors with alkali solutions. Common activators include sodium/potassium-based hydroxides and silicates, known for their high alkalinity and cost. However, the development of sodium carbonate-based activated materials has been limited by slow strength development at an early age. To address this, Waste incineration filter dust (WIFD), containing portlandite and calcite, has been proposed as an activator in sodium carbonate-activated materials. The synergistic effect of portlandite and sodium carbonate enhances the activation of GGBFS, as evidenced by the incorporation of 5 wt.% WIFD reduces the time to reach the heat flow peak from 58 hours to 10 hours. The main hydration products are C-(A)-S-H gel and hydrotalcite, with calcite from WIFD contributing to Hemicarboaluminate formation. However, higher WIFD dosage reduces the mechanical performance due to a decreased proportion of GGBFS.

To further improve the mechanical performance of the hybrid binder with high-volume recycling of WIFD, additional silica fume (SF) and nano-silica (NS) were introduced. SF slightly increases the compressive strength of the blended mortar at early ages but decreases it at longer ages due to a lower reactivity. In contrast, NS enhances compressive strength at all ages due to better pozzolanic reactivity, refining pore structure through improved formation of C-(A)-S-H gels. However, NS retards the reaction process and inhibits the formation of Hemicarboaluminate and hydrotalcite by consuming more Ca^{2+} and Al^{3+} in gel formation. It is important to note that despite the enhanced mechanical properties, NS induces a lower carbonation resistance of the matrix. Instead, incorporating 2 wt.% SF and reducing WIFD dosage prove beneficial for improving carbonation resistance. Overall, the proposed hybrid binder shows advantages in CO_2 emission reduction and cost saving.

Recycling industrial solid wastes presents significant challenges, primarily due to the presence of heavy metal ions. The immobilization of biomass bottom ash (BBA) within alkali-activated materials is explored, leveraging their well-known solidification ability. The investigation focused on the effects of BBA content, BBA fineness, silicate modulus of activator and aluminum anodizing waste (AAW) on reaction kinetics, hydration products, microstructure and mechanical properties. BBA exhibits lower reactivity compared to other components. However, the inclusion of 10 wt% BBA enhances the dissolution and polymerization of the hybrid blends. The main hydration products are the C-(A)-S-H gels and hydrotalcite-like phases, with higher BBA replacement accelerating the reaction process and enhancing gel products. The compressive strength of the hybrid blends ranges from 36.8 to 58.8 MPa at 28d, correlating with BBA substitution levels, fineness, silicate modulus and additional AAW. Moreover, the hybrid blends effectively immobilize the high-leachable Cl^-, SO_4^{2-}, Cr, Mo, Pb, and Zn content from BBA. Within the 10 wt% G/BBA substitution level, no heavy metal leaching exceeds the Dutch legal limit. Co-disposal of AAW and BBA proves feasible, exhibiting no new leaching problems and providing sufficient compressive strength for building material applications.

Furthermore, the exploration of functional alkali-activated materials has extended to the integration of TiO_2. To clarify, metakaolin was employed as the precursor, and no additional waste material was introduced, as the current investigation primarily focused on the advancing self-cleaning properties through the in-situ formation of zeolite, with a greater emphasis on mechanistic studies. The findings reveal that crystalline Zeolite A forms when the Si/Al ratio reaches 1.0 within the initial materials. This zeolite formation induces a matrix with a higher optical band and lower Urbach energy, driven by enhanced crystallinity. These results confirm that the improvement in photocatalytic properties in metakaolin-based geopolymers cannot be solely attributed to increased surface defects. The in-situ formation of zeolite enhances the self-cleaning performance of the matrix by refining the pore structure and enhancing the mass transfer capacity, thereby intensifying the photoactivity of TiO_2.

9.1.3 Development of BOF slag-based cement-free binder

In pursuit of developing a cement-free binder, basic oxygen furnace (BOF) slag, a solid by-product generated during the steel-making process, was utilized. DTPA-5Na was employed as an activator for the hydration of BOF slag. The addition of 1.0 wt% DTPA-5Na resulted in a notable reduction in setting time, from 4.2 h to 0.5 h, and an increase in cumulative hydration heat, from 29.6 J/g to 52.4 J/g. The activation mechanism of DTPA-5Na involves facilitating the dissolution of brownmillerite through the chelation of metal ions, thereby promoting the formation of monocarboaluminate. The augmented hydration products subsequently led to a substantial enhancement in 28 d compressive strength, from 10 MPa to 23.5 MPa.

Meanwhile, the effect of flue gas desulfurization (FGD) gypsum on DTPA-5Na-activated BOF slag was investigated. The incorporation of FGD gypsum in DTPA-5Na-activated BOF slag retards the hydration process, extending the setting time from 0.5 hours to 2.5 hours with a 3.5 wt% FGD gypsum content. This delay results in a reduced cumulative heat at early ages, potentially attributed to the partial occupation of DTPA-5Na by calcium ions released from FGD gypsum. However, it proves advantageous in promoting ettringite formation, consequently contributing to a denser structure of the BOF slag binders. Remarkably, the inclusion of 3.5 wt% FGD gypsum leads to an enhancement in 28d compressive strength, elevating it from 23.5 MPa to 37.5 MPa.

9.2 Recommendations

With the goal of expanding the recycling and recovery of industrial solid waste, we have proposed the concept of valorization of waste materials in construction materials. As demonstrated in this thesis, various construction materials tailored for diverse applications have been engineered with different levels of waste substitution/incorporation. The performance of these formulated materials has been assessed based on specific application requirements, e.g., low permeability for sealing materials. However, it must be noted that the present findings are confined to laboratory-scale investigations, and transitioning to larger practical applications requires addressing additional considerations including environmental impact, practicability and economic advantages. In this context, general recommendations for future research, derived from the insights gained in this dissertation, are provided, followed by specific suggestions for each analyzed material system.

In the context of landfill sealing materials, compaction during the installation process is typically carried out using heavy machinery like compactors or rollers in practical landfills. It is crucial to adjust the compaction parameters based on the specific method used to prepare the sealing materials. Moreover, when choosing sludge or other solid waste materials for recycling or reclamation purposes, it is essential to take into account various factors. These include the cost of acquiring the feedstock and the expenses associated with transporting it to the processing or recycling facility. Additionally, the suitability and adequacy of the feedstock for the intended application must be carefully evaluated.

For alkali-activated materials, the use of sodium or potassium-based hydroxide and silicate solutions as common alkaline activators presents a significant technological barrier to large-scale application due to environmental concerns and production costs. Additionally, the large-scale preparation of alkaline solutions necessitates careful consideration of several factors, including the safety of personnel, the environment, and equipment. In this thesis, we proposed the use of a mixture of sodium carbonate and WIFD as activators, demonstrating advantages in both cost and safety. Nevertheless, the utilization of sodium carbonate and WIFD, which are in powder form, introduces the challenge of achieving uniform mixing of the raw materials and powder activators, particularly in large-scale applications.

Currently, research on the properties of cement replacement materials has primarily focused on pastes and mortars. However, it is essential to extend this research to the preparation of concrete and conduct comprehensive studies. The overall performance of the formulated concrete should be thoroughly assessed, including its mechanical properties, shrinkage behavior, creep, and durability.

More specific recommendations related to this work are as follows.

9.2.1 Sludge-based sealing materials and their carbonation behavior

In the sealing materials, additives with fine particle size (like AAW), contribute to the desired impermeability. Therefore, fine industrial solid waste is recommended to potentially improve the impermeability of sealing materials. However, due to the limited formation of binder materials, only silica gel may form. As a result, the leaching behavior of the resulting sealing materials is highly dependent on the initial materials. Hence, the leaching behavior of industrial solid waste is another crucial aspect in terms of potential environmental impact, which must be addressed before their application in sealing materials. This does not imply that wastes

containing leached heavy metal ions are unsuitable, but rather emphasizes the need for appropriate immobilization of heavy metal ions using suitable additives. For instance, the reduced arsenic (As) leaching from DSS can be attributed to the coagulation of sulfates from additives. Furthermore, despite a slight reduction in impermeability, PDSS-based sealing materials still comply with Dutch requirements for soil capping, supporting the recycling of pre-treated DSS in sealing material. The Thermal Pressure Hydrolysis process offers additional advantages by enhancing biogas production and dewaterability in WWTPs. This dual benefit underscores the sustainability and practicality of employing such materials in environmental engineering applications. Moreover, the fact that the permeability of DS-based specimens slightly exceeds limits does not necessarily disqualify DS as a viable raw material for sealing materials. Numerous factors influence permeability, including mix design, additives, and compaction degree. Therefore, further optimizing sealing material properties by adjusting mixing ratios to meet regulatory requirements can facilitate the inclusion of DS in sealing material applications.

The impact of CO_2 on the sealing materials was investigated using an accelerated carbonation process. However, it is worth noting that the accelerated carbonation process differs from natural carbonation processes in several aspects, such as CO_2 concentration, pressure, temperature, etc. This suggests there is potential for further refinement to achieve more accurate results. These variations could not only influence the resulting reaction products but also affect the dynamic process of carbonation. Consequently, refining the dynamic simulation process is essential for more precise predictions regarding the durability of sealing materials.

9.2.2 Recycling industrial solid waste in AAMs

The portlandite in WIFD plays a significant role in accelerating the hydration of sodium carbonate-activated GGBFS. This insight offers the opportunity to recycle portlandite-containing waste in the activation process of GGBFS with sodium carbonate. Not only does this approach contribute to waste reduction and environmental sustainability, but it also provides cost savings by minimizing the need for additional activator materials.

In efforts to increase the utilization of WIFD in sodium carbonate-activated GGBFS, there is an inevitable reduction in the percentage of precursors. Since the WIFD itself lacks an inherent silicate source, this indirectly dilutes the silicate source involved in gel production, thus diminishing the overall matrix performance. To address this, we proposed leveraging silica fume and nano-silica to explore their potential for enhancing performance. Results indicate that nano-silica exhibits higher reactivity and leads to significant strength enhancement. This outcome suggests that similar waste systems could benefit from such enhancement strategies. Moreover, this research highlights that the carbonation resistance of alkali-activated materials does not necessarily correlate positively with their strength. Other factors, including gel composition and pore structure, also play crucial roles in carbonation resistance, underscoring the importance of considering these factors when designing for optimal carbonation resistance.

With the utilization of biomass fuels emerging as a prominent trend in new energy source development, the solidification of their by-products, specifically biomass bottom ash (BBA), within alkali-activated materials has been explored. Based on the findings, it can be concluded that the optimal substitution level of BBA is 10 wt% in terms of heavy metals leaching and mechanical performance. Notably, higher substitutions lead to strength reduction, a challenge that could potentially be addressed by incorporating additional nano-silica, as suggested by

previous conclusions. Moreover, the potential effect of BBA fineness on the overall performance of the hybrid binder was investigated. Using finer particles can indeed enhance the strength of the matrix and accelerate the hydration process. However, it also tends to increase the leaching of heavy metal ions. Considering the elevated costs and energy consumption associated with the milling process, it may be of more practical engineering interest to minimize the degree of milling.

The self-cleaning performance of the metakaolin-based geopolymers can be significantly improved by the in-situ zeolite formation. The formation of zeolite is achieved by adjusting the initial Si/Al ratio of raw materials. This opens up the possibility of using waste materials, such as aluminum anodizing waste, to adjust the initial Si/Al. However, it is crucial to address the potential effect of abundant impurities present in industrial solid waste on the self-cleaning performance upon their inclusion in the matrix. On the other hand, the findings introduce innovative approaches to address the regression of photocatalytic properties caused by the hydration process of cementitious materials through porous zeolite formation. Consequently, the in-situ formation of porous minerals in cementitious materials emerges as a promising strategy for enhancing photocatalytic properties and ensuring an extended lifespan.

9.2.3 Development of BOF slag-based cement-free binder

The development of basic oxygen furnace (BOF) slag-based binder has been achieved by the activation of DTPA-5Na and the modification of flue gas desulfurization (FGD) gypsum. The activation mechanism of DTPA-5Na entails facilitating the dissolution of brownmillerite through metal ion chelation, thus supporting the activation strategy of BOF slag by the chelating agent. Consequently, it may be inferred that other chelating agents could have similar effects on BOF slag hydration, warranting further optimization for the enhanced overall performance of the BOF slag binder, alongside considerations regarding the cost-effectiveness of chelating agents. Meanwhile, the chelation effect of DTPA-5Na results in a significant concentration of [Al] and [Ca] in the aqueous phases during dissolution equilibrium. Introducing additional sulfate emerges as a viable strategy to enhance hydration products in the DTPA-5Na-activated BOF slag system. Industrial residues with high soluble sulfate content, such as phosphogypsum, electrolytic manganese residues, and gypsum residues generated in copper and zinc-making processes, represent promising candidates for incorporation in the formulation of BOF slag-based binders.

Bibliography

[1] Eurostat, Generation of waste by waste category, hazardousness and NACE Rev. 2 activity, (2023). https://doi.org/10.2908/ENV_WASGEN.

[2] W.Y. Lin, W.C. Ng, B.S.E. Wong, S.L.M. Teo, G. d/o Sivananthan, G.H. Baeg, Y.S. Ok, C.H. Wang, Evaluation of sewage sludge incineration ash as a potential land reclamation material, J. Hazard. Mater. 357 (2018) 63–72. https://doi.org/10.1016/j.jhazmat.2018.05.047.

[3] M. Barjenbruch, O. Kopplow, Enzymatic, mechanical and thermal pre-treatment of surplus sludge, Adv. Environ. Res. 7 (2003) 715–720. https://doi.org/10.1016/S1093-0191(02)00032-1.

[4] B. Wett, P. Phothilangka, A. Eladawy, Systematic comparison of mechanical and thermal sludge disintegration technologies, Waste Manag. 30 (2010) 1057–1062. https://doi.org/10.1016/j.wasman.2009.12.011.

[5] H. Yu, M. Adriaenssens, J. Bakx, V. Hartan, J. Qu, X. Ji, L. de Gier, Sewage sludge management in a circular economy: Exploring technologies applied in the Netherlands, 2020.

[6] J. Namie, P. Konieczka, Review of sewage sludge management : standards, regulations and analytical methods, J. Clean. Prod. 90 (2015) 1–15. https://doi.org/10.1016/j.jclepro.2014.11.031.

[7] D. Sandy, Final implementation report for Directive 86/278/EEC on sewage sludge: 2013 – 2015, Portugal, 2018. https://policycommons.net/artifacts/1976397/final-implementation-report-for-directive-86278eec-on-sewage-sludge/2728162/ on 19 Jun 2023.

[8] S.N. (CBS), Urban waste water treatment per province and river basin district 2020, (2023). https://opendata.cbs.nl/#/CBS/en/dataset/7477eng/table?dl=91C32 (accessed June 16, 2023).

[9] W. Peng, A. Pivato, Sustainable management of digestate from the organic fraction of municipal solid waste and food waste under the concepts of back to earth alternatives and circular economy, Waste and Biomass Valorization. 10 (2019) 465–481. https://doi.org/10.1007/s12649-017-0071-2.

[10] C. Hung, W. Tsai, J. Chen, Y. Lin, Y. Chang, Characterization of biochar prepared from biogas digestate, Waste Manag. 66 (2017) 53–60. https://doi.org/10.1016/j.wasman.2017.04.034.

[11] F. Agrela, M. Cabrera, M.M. Morales, M. Zamorano, M. Alshaaer, Biomass fly ash and biomass bottom ash, in: J. de Brito, F. Agrela (Eds.), New Trends Eco-Efficient Recycl. Concr., Woodhead Publishing, 2019: pp. 23–58. https://doi.org/https://doi.org/10.1016/B978-0-08-102480-5.00002-6.

[12] M. Cabrera, A.P. Galvin, F. Agrela, M.D. Carvajal, J. Ayuso, Characterisation and technical feasibility of using biomass bottom ash for civil infrastructures, Constr. Build. Mater. 58 (2014) 234–244. https://doi.org/10.1016/j.conbuildmat.2014.01.087.

[13] R. Melotti, E. Santagata, M. Bassani, M. Salvo, S. Rizzo, A preliminary investigation into the physical and chemical properties of biomass ashes used as aggregate fillers for bituminous mixtures, Waste Manag. 33 (2013) 1906–1917. https://doi.org/10.1016/j.wasman.2013.05.015.

[14] I. Obernberger, K. Supancic, Possibilities of ash utilisation from biomass combustion plants., in: Proc. 17th Eur. Biomass Conf. Exhib., Hamburg, 2009.

[15] J. Cuenca, J. Rodríguez, M. Martín-morales, Z. Sánchez-roldán, M. Zamorano, Effects of olive residue biomass fly ash as filler in self-compacting concrete, Constr. Build. Mater. 40 (2013) 702–709. https://doi.org/10.1016/j.conbuildmat.2012.09.101.

[16] A. Correia, T. Chambino, L. Gonçalves, A. Franco, R. Gonçalves, A. Gonçalves, V. Limpo, F. Delmas, C. Nogueira, F. Bartolomeu, Municipal wastewater treatment with anodizing solid waste, Desalination. 185 (2005) 341–350. https://doi.org/10.1016/j.desal.2005.04.043.

[17] E.M.M. Ewais, N.H.A. Besisa, A. Ahmed, Aluminum titanate based ceramics from aluminum sludge waste, Ceram. Int. 43 (2017) 10277–10287. https://doi.org/10.1016/j.ceramint.2017.05.057.

[18] M.J. Ribeiro, S. Blackburn, J.A. Labrincha, Single screw extrusion of mullite-based tubes containing Al-rich anodising sludge, Ceram. Int. 35 (2009) 1095–1101. https://doi.org/10.1016/j.ceramint.2008.04.024.

[19] J. Corker, I. Marques, S. Resalati, T. Okoroafor, A. Maalouf, Z. Fu, M. Fan, Al-rich industrial waste as new alternative of fumed silica for the manufacture of vacuum insulation panels for building energy conservation, J. Clean. Prod. 415 (2023). https://doi.org/10.1016/j.jclepro.2023.137854.

[20] G.G. de Moraes, B.G. Oliveira, C. Siligardi, M.D. de M. Innocentini, A.A.M. Oliveira Jr., J.B.R. Neto, D. Hotza, A.P.N. de Oliveira, Production of foundry filters using Al_2O_3 from the Al-anodizing process, Adv. Sci. Technol. 62 (2010) 119–124. https://doi.org/10.4028/www.scientific.net/ast.62.119.

[21] I. Marques, V. Neto, I. Grilo, M.. Vieira, E. Júlio, Recycling of residual sludge from aluminium anodizing and lacquering in clay brinks - Case study of portuguese industries, Cincos'12. (2012) 249–255.

[22] J. Lederer, V. Trinkel, J. Fellner, Wide-scale utilization of MSWI fly ashes in cement production and its impact on average heavy metal contents in cements : The case of Austria, Waste Manag. 60 (2017) 247–258. https://doi.org/10.1016/j.wasman.2016.10.022.

[23] C. Ferreira, A. Ribeiro, L. Ottosen, Possible applications for municipal solid waste fly ash, J. Hazard. Mater. 96 (2003) 201–216. https://doi.org/10.1016/S0304-3894(02)00201-7.

[24] T. Sabbas, A. Polettini, R. Pomi, T. Astrup, O. Hjelmar, P. Mostbauer, G. Cappai, G. Magel, S. Salhofer, C. Speiser, S. Heuss-Assbichler, R. Klein, P. Lechner, Management of municipal solid waste incineration residues, Waste Manag. 23 (2003) 61–88. https://doi.org/10.1016/S0956-053X(02)00161-7.

[25] M.J. Quina, J.C. Bordado, R.M. Quinta-Ferreira, Treatment and use of air pollution control residues from MSW incineration: An overview, Waste Manag. 28 (2008) 2097–2121. https://doi.org/10.1016/j.wasman.2007.08.030.

[26] R. Shirley, L. Black, Alkali activated solidification/stabilisation of air pollution control residues and co-fired pulverised fuel ash, J. Hazard. Mater. 194 (2011) 232–242. https://doi.org/10.1016/j.jhazmat.2011.07.100.

[27] A.H. Kanhar, S. Chen, F. Wang, Incineration fly ash and its treatment to possible utilization: a review, Energies. 13 (2020) 6681. https://doi.org/10.3390/en13246681.

[28] S.Z. Carvalho, F. Vernilli, B. Almeida, M. Demarco, S.N. Silva, The recycling effect of BOF slag in the portland cement properties, Resour. Conserv. Recycl. 127 (2017) 216–220. https://doi.org/10.1016/j.resconrec.2017.08.021.

[29] E. Gartner, H. Hirao, A review of alternative approaches to the reduction of CO_2 emissions associated with the manufacture of the binder phase in concrete, Cem. Concr. Res. 78 (2015) 126–142. https://doi.org/10.1016/j.cemconres.2015.04.012.

[30] A.M. Kaja, K. Schollbach, S. Melzer, S.R. van der Laan, H.J.H. Brouwers, Q. Yu, Hydration of potassium citrate-activated BOF slag, Cem. Concr. Res. 140 (2021) 106291. https://doi.org/10.1016/j.cemconres.2020.106291.

[31] A. van Zomeren, S.R. van der Laan, H.B.A. Kobesen, W.J.J. Huijgen, R.N.J. Comans, Changes in mineralogical and leaching properties of converter steel slag resulting from accelerated carbonation at low CO_2 pressure, Waste Manag. 31 (2011) 2236–2244. https://doi.org/10.1016/j.wasman.2011.05.022.

[32] E. Belhadj, C. Diliberto, A. Lecomte, Characterization and activation of basic oxygen furnace slag, Cem. Concr. Compos. 34 (2012) 34–40. https://doi.org/10.1016/j.cemconcomp.2011.08.012.

[33] F. Han, Z. Zhang, D. Wang, P. Yan, Hydration heat evolution and kinetics of blended cement containing steel slag at different temperatures, Thermochim. Acta. 605 (2015) 43–51. https://doi.org/10.1016/j.tca.2015.02.018.

[34] Y. Jiang, T.C. Ling, C. Shi, S.Y. Pan, Characteristics of steel slags and their use in cement and concrete—A review, Resour. Conserv. Recycl. 136 (2018) 187–197. https://doi.org/10.1016/j.resconrec.2018.04.023.

[35] Y. Xue, S. Wu, H. Hou, J. Zha, Experimental investigation of basic oxygen furnace slag used as aggregate in asphalt mixture, J. Hazard. Mater. 138 (2006) 261–268. https://doi.org/10.1016/j.jhazmat.2006.02.073.

[36] B. Das, S. Prakash, P.S.R. Reddy, V.N. Misra, An overview of utilization of slag and sludge from steel industries, Resour. Conserv. Recycl. 50 (2007) 40–57. https://doi.org/10.1016/j.resconrec.2006.05.008.

[37] W. Franco Santos, High-end applications of basic oxygen furnace slag as a cementitious binder: Phase Assemblage, Mechanical & Chemical Activation, Composites Application, Ph.D Thesis, Eindhoven University of Technology, 2024.

[38] Aakriti, S. Maiti, N. Jain, J. Malik, A comprehensive review of flue gas desulphurized gypsum: Production, properties, and applications, Constr. Build. Mater. 393 (2023) 131918. https://doi.org/10.1016/j.conbuildmat.2023.131918.

[39] Eurostat, Generation of waste by waste category, hazardousness and NACE Rev. 2 activity, (2021). https://ec.europa.eu/eurostat/databrowser/view/ENV_WASGEN/default/table?lang=en.

[40] O. Radley-Gardner, H. Beale, R. Zimmermann, eds., Directive 2008/122/EC of the European Parliament and of the Council, in: Fundam. Texts Eur. Priv. Law, 2nd ed., Hart Publishing, Oxford, 2016: pp. 593–605. http://www.bloomsburycollections.com/book/fundamental-texts-on-european-private-law-1/directive-2008-122-ec-of-the-european-parliament-and-of-the-council/.

[41] A.A. Brian, H.B. Craig, Effect of desiccation on compacted natural clays, J. Geotech. Geoenvironmental Eng. 127 (2001) 67–75. https://doi.org/10.1061/(ASCE)1090-0241(2001)127:1(67).

[42] D. Koch, Bentonites as a basic material for technical base liners and site encapsulation cut-off walls, Appl. Clay Sci. 21 (2002) 1–11. https://doi.org/10.1016/S0169-1317(01)00087-4.

[43] Rijkswaterstaat Bodem+, Guidelines for the implementation of the landfill decree on soil protection, (1991) 88. https://www.bodemplus.nl/@132149/richtlijnen-uitvoeringsregeling-stortbesluit/.

[44] B.Y. Sadasivam, K.R. Reddy, Adsorption and transport of methane in landfill cover soil amended with waste-wood biochars, J. Environ. Manage. 158 (2015) 11–23. https://doi.org/10.1016/j.jenvman.2015.04.032.

[45] K. Spokas, J. Bogner, J.P. Chanton, M. Morcet, C. Aran, C. Graff, Y.M.-L. Golvan, I. Hebe, Methane mass balance at three landfill sites : What is the efficiency of capture by gas collection systems ?, Waste Manag. 26 (2006) 516–525. https://doi.org/10.1016/j.wasman.2005.07.021.

[46] M.A. Barlaz, J.P. Chanton, R.B. Green, Controls on landfill gas collection efficiency: instantaneous and lifetime performance, J. Air Waste Manag. Assoc. 59 (2009) 1399–1404. https://doi.org/10.3155/1047-3289.59.12.1399.

[47] S.A. Bernal, J.L. Provis, V. Rose, R. Mejía De Gutierrez, Evolution of binder structure in sodium silicate-activated slag-metakaolin blends, Cem. Concr. Compos. 33 (2011) 46–54. https://doi.org/10.1016/j.cemconcomp.2010.09.004.

[48] B. Walkley, R. San Nicolas, M.A. Sani, G.J. Rees, J. V. Hanna, J.S.J. van Deventer, J.L. Provis, Phase evolution of C-(N)-A-S-H/N-A-S-H gel blends investigated via alkali-activation of synthetic calcium aluminosilicate precursors, Cem. Concr. Res. 89 (2016) 120–135. https://doi.org/10.1016/j.cemconres.2016.08.010.

[49] M.C.G. Juenger, R. Siddique, Recent advances in understanding the role of supplementary cementitious materials in concrete, Cem. Concr. Res. 78 (2015) 71–80. https://doi.org/10.1016/j.cemconres.2015.03.018.

[50] C. Li, H. Sun, L. Li, A review: The comparison between alkali-activated slag (Si + Ca) and metakaolin (Si + Al) cements, Cem. Concr. Res. 40 (2010) 1341–1349. https://doi.org/10.1016/j.cemconres.2010.03.020.

[51] N. Ye, Y. Chen, J. Yang, S. Liang, Y. Hu, J. Hu, S. Zhu, W. Fan, B. Xiao, Transformations of Na, Al, Si and Fe species in red mud during synthesis of one-part geopolymers, Cem. Concr. Res. 101 (2017) 123–130. https://doi.org/10.1016/j.cemconres.2017.08.027.

[52] B. Yuan, S. Yuan, C. Straub, W. Chen, Activation of binary binder containing fly ash and portland cement using red mud as alkali source and its application in controlled low-strength materials, J. Mater. Civ. Eng. 32 (2020) 1–11. https://doi.org/10.1061/(ASCE)MT.1943-5533.0003023.

[53] E. Altan, S.T. Erdoğan, Alkali activation of a slag at ambient and elevated temperatures, Cem. Concr. Compos. 34 (2012) 131–139. https://doi.org/10.1016/j.cemconcomp.2011.08.003.

[54] Z. Shi, C. Shi, S. Wan, N. Li, Z. Zhang, Effect of alkali dosage and silicate modulus on carbonation of alkali-activated slag mortars, Cem. Concr. Res. 113 (2018) 55–64. https://doi.org/10.1016/j.cemconres.2018.07.005.

[55] X. Ke, S.A. Bernal, J.L. Provis, Controlling the reaction kinetics of sodium carbonate-activated slag cements using calcined layered double hydroxides, Cem. Concr. Res. 81 (2016) 24–37. https://doi.org/10.1016/j.cemconres.2015.11.012.

[56] N. Li, C. Shi, Z. Zhang, Understanding the roles of activators towards setting and hardening control of alkali-activated slag cement, Compos. Part B Eng. 171 (2019) 34–45. https://doi.org/10.1016/j.compositesb.2019.04.024.

[57] M. Ben Haha, B. Lothenbach, G. Le Saout, F. Winnefeld, Influence of slag chemistry on the hydration of

alkali-activated blast-furnace slag - Part II: Effect of Al_2O_3, Cem. Concr. Res. 42 (2012) 74–83. https://doi.org/10.1016/j.cemconres.2011.08.005.

[58] M. Schneider, M. Romer, M. Tschudin, H. Bolio, Sustainable cement production-present and future, Cem. Concr. Res. 41 (2011) 642–650. https://doi.org/10.1016/j.cemconres.2011.03.019.

[59] B. Yuan, C. Straub, S. Segers, Q.L. Yu, H.J.H. Brouwers, Sodium carbonate activated slag as cement replacement in autoclaved aerated concrete, Ceram. Int. 43 (2017) 6039–6047. https://doi.org/10.1016/j.ceramint.2017.01.144.

[60] I. Garcia-Lodeiro, A. Palomo, A. Fernández-Jiménez, D.E. MacPhee, Compatibility studies between N-A-S-H and C-A-S-H gels. Study in the ternary diagram Na_2O-CaO-Al_2O_3-SiO_2-H_2O, Cem. Concr. Res. 41 (2011) 923–931. https://doi.org/10.1016/j.cemconres.2011.05.006.

[61] N.K. Lee, H.K. Lee, Setting and mechanical properties of alkali-activated fly ash/slag concrete manufactured at room temperature, Constr. Build. Mater. 47 (2013) 1201–1209. https://doi.org/10.1016/j.conbuildmat.2013.05.107.

[62] X.H. Yuan, W. Chen, Z.A. Lu, H. Chen, Shrinkage compensation of alkali-activated slag concrete and microstructural analysis, Constr. Build. Mater. 66 (2014) 422–428. https://doi.org/10.1016/j.conbuildmat.2014.05.085.

[63] B. Yuan, Q.L. Yu, H.J.H. Brouwers, Time-dependent characterization of Na_2CO_3 activated slag, Cem. Concr. Compos. 84 (2017) 188–197. https://doi.org/10.1016/j.cemconcomp.2017.09.005.

[64] C. Duran Atiş, C. Bilim, Ö. Çelik, O. Karahan, Influence of activator on the strength and drying shrinkage of alkali-activated slag mortar, Constr. Build. Mater. 23 (2009) 548–555. https://doi.org/10.1016/j.conbuildmat.2007.10.011.

[65] T. Yang, Z. Zhang, H. Zhu, W. Zhang, Y. Gao, X. Zhang, Q. Wu, Effects of calcined dolomite addition on reaction kinetics of one-part sodium carbonate-activated slag cements, Constr. Build. Mater. 211 (2019) 329–336. https://doi.org/10.1016/j.conbuildmat.2019.03.245.

[66] X. Gao, X. Yao, T. Yang, S. Zhou, H. Wei, Z. Zhang, Calcium carbide residue as auxiliary activator for one-part sodium carbonate-activated slag cements: compressive strength, phase assemblage and environmental benefits, Constr. Build. Mater. 308 (2021) 125015. https://doi.org/10.1016/j.conbuildmat.2021.125015.

[67] D. Jeon, Y. Jun, Y. Jeong, J.E. Oh, Microstructural and strength improvements through the use of Na_2CO_3 in a cementless Ca(OH)2-activated Class F fly ash system, Cem. Concr. Res. 67 (2015) 215–225. https://doi.org/10.1016/j.cemconres.2014.10.001.

[68] K.H. Yang, A.R. Cho, J.K. Song, S.H. Nam, Hydration products and strength development of calcium hydroxide-based alkali-activated slag mortars, Constr. Build. Mater. 29 (2012) 410–419. https://doi.org/10.1016/j.conbuildmat.2011.10.063.

[69] Y. Zhao, T. Shi, L. Cao, L. Kan, M. Wu, Influence of steel slag on the properties of alkali-activated fly ash and blast-furnace slag based fiber reinforced composites, Cem. Concr. Compos. 116 (2021) 103875. https://doi.org/10.1016/j.cemconcomp.2020.103875.

[70] G. Liu, M.V.A. Florea, H.J.H. Brouwers, The role of recycled waste glass incorporation on the carbonation behaviour of sodium carbonate activated slag mortar, J. Clean. Prod. 292 (2021) 126050. https://doi.org/10.1016/j.jclepro.2021.126050.

[71] Y. Liu, W. Zhu, E.H. Yang, Alkali-activated ground granulated blast-furnace slag incorporating incinerator fly ash as a potential binder, Constr. Build. Mater. 112 (2016) 1005–1012. https://doi.org/10.1016/j.conbuildmat.2016.02.153.

[72] X. Gao, B. Yuan, Q.L. Yu, H.J.H. Brouwers, Characterization and application of municipal solid waste incineration (MSWI) bottom ash and waste granite powder in alkali activated slag, J. Clean. Prod. 164 (2017) 410–419. https://doi.org/10.1016/j.jclepro.2017.06.218.

[73] M. Ben Haha, G. Le Saout, F. Winnefeld, B. Lothenbach, Influence of activator type on hydration kinetics, hydrate assemblage and microstructural development of alkali activated blast-furnace slags, Cem. Concr. Res. 41 (2011) 301–310. https://doi.org/10.1016/j.cemconres.2010.11.016.

[74] V. Živica, Effects of type and dosage of alkaline activator and temperature on the properties of alkali-activated slag mixtures, Constr. Build. Mater. 21 (2007) 1463–1469. https://doi.org/10.1016/j.conbuildmat.2006.07.002.

[75] Q. Yuan, D. Zhou, B. Li, H. Huang, C. Shi, Effect of mineral admixtures on the structural build-up of cement paste, Constr. Build. Mater. 160 (2018) 117–126. https://doi.org/10.1016/j.conbuildmat.2017.11.050.

[76] J.L. Provis, J.S.J. van Deventer, Geopolymers and other alkali-activated materials, 5th ed., Elsevier Ltd., 2019. https://doi.org/10.1016/b978-0-08-100773-0.00016-2.

[77] B.S. Gebregziabiher, R.J. Thomas, S. Peethamparan, Temperature and activator effect on early-age reaction kinetics of alkali-activated slag binders, Constr. Build. Mater. 113 (2016) 783–793. https://doi.org/10.1016/j.conbuildmat.2016.03.098.

[78] X. Gao, Q.L. Yu, H.J.H. Brouwers, Reaction kinetics, gel character and strength of ambient temperature cured alkali activated slag–fly ash blends, Constr. Build. Mater. 80 (2015) 105–115. https://doi.org/10.1016/j.conbuildmat.2015.01.065.

[79] S.A. Bernal, R. Mejía De Gutiérrez, J.L. Provis, Engineering and durability properties of concretes based on alkali-activated granulated blast furnace slag/metakaolin blends, Constr. Build. Mater. 33 (2012) 99–108. https://doi.org/10.1016/j.conbuildmat.2012.01.017.

[80] J.X. Lu, C.S. Poon, Use of waste glass in alkali activated cement mortar, Constr. Build. Mater. 160 (2018) 399–407. https://doi.org/10.1016/j.conbuildmat.2017.11.080.

[81] A.M. Rashad, D.M. Sadek, Behavior of alkali-activated slag pastes blended with waste rubber powder under the effect of freeze/thaw cycles and severe sulfate attack, Constr. Build. Mater. 265 (2020) 120716. https://doi.org/10.1016/j.conbuildmat.2020.120716.

[82] W. Ten Kuo, T.C. Hou, Engineering properties of alkali-activated binders by use of desulfurization slag and GGBFS, Constr. Build. Mater. 66 (2014) 229–234. https://doi.org/10.1016/j.conbuildmat.2014.05.056.

[83] Z. Abdollahnejad, T. Luukkonen, M. Mastali, P. Kinnunen, M. Illikainen, Development of one-part alkali-activated ceramic/slag binders containing recycled ceramic aggregates, J. Mater. Civ. Eng. 31 (2019) 04018386. https://doi.org/10.1061/(asce)mt.1943-5533.0002608.

[84] B.I. El-eswed, Chemical evaluation of immobilization of wastes containing Pb , Cd , Cu and Zn in alkali-activated materials : A critical review, J. Environ. Chem. Eng. 8 (2020) 104194. https://doi.org/10.1016/j.jece.2020.104194.

[85] R.A. Antunes, B. Santa, C. Soares, H.G. Riella, Geopolymers with a high percentage of bottom ash for solidification / immobilization of different toxic metals, J. Hazard. Mater. 318 (2016) 145–153. https://doi.org/10.1016/j.jhazmat.2016.06.059.

[86] Y. Luna, X. Querol, D. Antenucci, J. Vale, Waste stabilization / solidification of an electric arc furnace dust using fly ash-based geopolymers, Fuel. 88 (2009) 1185–1193. https://doi.org/10.1016/j.fuel.2008.01.021.

[87] X. Chen, Y. Guo, S. Ding, H. Zhang, F. Xia, J. Wang, Utilization of red mud in geopolymer-based pervious concrete with function of adsorption of heavy metal ions, J. Clean. Prod. 207 (2019) 789–800. https://doi.org/10.1016/j.jclepro.2018.09.263.

[88] Q. Tian, S. Nakama, K. Sasaki, Immobilization of cesium in fly ash-silica fume based geopolymers with different Si/Al molar ratios, Sci. Total Environ. 687 (2019) 1127–1137. https://doi.org/10.1016/j.scitotenv.2019.06.095.

[89] Z. Wang, Y. Chen, L. Xu, Z. Zhu, Y. Zhou, F. Pan, K. Wu, Insight into the local C-S-H structure and its evolution mechanism controlled by curing regime and Ca/Si ratio, Constr. Build. Mater. 333 (2022) 127388. https://doi.org/10.1016/j.conbuildmat.2022.127388.

[90] B. Guo, D. Pan, B. Liu, A.A. Volinsky, M. Fincan, J. Du, S. Zhang, Immobilization mechanism of Pb in fly ash-based geopolymer, Constr. Build. Mater. 134 (2017) 123–130. https://doi.org/10.1016/j.conbuildmat.2016.12.139.

[91] J. Chen, Y. Wang, H. Wang, S. Zhou, H. Wu, Detoxification / immobilization of hexavalent chromium using metakaolin-based geopolymer coupled with ferrous chloride, J. Environ. Chem. Eng. 4 (2016) 2084–2089. https://doi.org/10.1016/j.jece.2016.03.038.

[92] Z. Zheng, Y. Li, Z. Zhang, X. Ma, The impacts of sodium nitrate on hydration and microstructure of Portland cement and the leaching behavior of Sr^{2+}, J. Hazard. Mater. 388 (2020) 121805. https://doi.org/10.1016/j.jhazmat.2019.121805.

[93] Y. Zhu, Z. Zheng, Y. Deng, C. Shi, Z. Zhang, Advances in immobilization of radionuclide wastes by alkali activated cement and related materials, Cem. Concr. Compos. 126 (2022) 104377. https://doi.org/10.1016/j.cemconcomp.2021.104377.

[94] J. Rosales, M. Cabrera, M.G. Beltrán, M. López, F. Agrela, Effects of treatments on biomass bottom ash applied to the manufacture of cement mortars, J. Clean. Prod. 154 (2020) 424–435. https://doi.org/10.1016/j.jclepro.2017.04.024.

[95] M.J.R. Hinojosa, A.P. Galvín, F. Agrela, M. Perianes, A. Barbudo, Potential use of biomass bottom ash as alternative construction material : Conflictive chemical parameters according to technical regulations, FUEL. 128 (2014) 248–259. https://doi.org/10.1016/j.fuel.2014.03.017.

[96] M.G. Beltrán, F. Agrela, A. Barbudo, J. Ayuso, A. Ramírez, Mechanical and durability properties of concretes manufactured with biomass bottom ash and recycled coarse aggregates, Constr. Build. Mater. 72 (2014) 231–238. https://doi.org/10.1016/j.conbuildmat.2014.09.019.

[97] M. Cabrera, A.P. Galvin, F. Agrela, M.G. Beltran, J. Ayuso, Reduction of leaching impacts by applying biomass bottom ash and recycled mixed aggregates in structural layers of roads, Materials (Basel). 9 (2016) 228. https://doi.org/10.3390/ma9040228.

[98] M. Sleiman, T.W. Kirchstetter, P. Berdahl, H.E. Gilbert, S. Quelen, L. Marlot, C. V Preble, S. Chen, A. Montalbano, O. Rosseler, H. Akbari, R. Levinson, H. Destaillats, Soiling of building envelope surfaces and its effect on solar reflectance – Part II : Development of an accelerated aging method for roofing materials, Sol. Energy Mater. Sol. Cells. 122 (2014) 271–281. https://doi.org/10.1016/j.solmat.2013.11.028.

[99] C. Ferrari, A.G. Touchaei, M. Sleiman, A. Libbra, A. Muscio, C. Siligardi, H. Akbari, Effect of aging processes on solar reflectivity of clay roof tiles, Adv. Build. Energy Res. 8 (2014) 28–40. https://doi.org/10.1080/17512549.2014.890535.

[100] A. Fujishima, K. Honda, Electrochemical photolysis of water at a semiconductor electrode, Nature. 238 (1972) 37–38. https://doi.org/10.1038/238037a0.

[101] L. Zhong, F. Haghighat, Photocatalytic air cleaners and materials technologies - Abilities and limitations, Build. Environ. 91 (2015) 191–203. https://doi.org/10.1016/j.buildenv.2015.01.033.

[102] M.V. Diamanti, M. Ormellese, M. Pedeferri, Characterization of photocatalytic and superhydrophilic properties of mortars containing titanium dioxide, Cem. Concr. Res. 38 (2008) 1349–1353. https://doi.org/10.1016/j.cemconres.2008.07.003.

[103] A. Folli, C. Pade, T. Bæk, T. De Marco, D.E. Macphee, TiO_2 photocatalysis in cementitious systems: Insights into self-cleaning and depollution chemistry, Cem. Concr. Res. 42 (2012) 539–548. https://doi.org/10.1016/j.cemconres.2011.12.001.

[104] Y. Li, W. Ma, Chemosphere Photocatalytic oxidation technology for indoor air pollutants elimination : A review, Chemosphere. 280 (2021) 130667. https://doi.org/10.1016/j.chemosphere.2021.130667.

[105] J. Yuenyongsuwan, S. Sinthupinyo, E.A.O. Rear, T. Pongprayoon, Hydration accelerator and photocatalyst of nanotitanium dioxide synthesized via surfactant-assisted method in cement mortar, Cem. Concr. Compos. 96 (2019) 182–193. https://doi.org/10.1016/j.cemconcomp.2018.11.024.

[106] A. Alonso-tellez, R. Masson, D. Robert, N. Keller, V. Keller, Comparison of Hombikat UV100 and P25 TiO_2 performance in gas-phase photocatalytic oxidation reactions, J. Photochem. Photobiol. A Chem. 250 (2012) 58–65. https://doi.org/10.1016/j.jphotochem.2012.10.008.

[107] R.A.R. Monteiro, S.M. Miranda, C. Rodrigues-silva, J.L. Faria, A.M.T. Silva, R.A.R. Boaventura, V.J.P. Vilar, Gas phase oxidation of n-decane and PCE by photocatalysis using an annular photoreactor packed with a monolithic catalytic bed coated with P25 and PC500, Appl. Catal. B, Environ. 165 (2015) 306–315. https://doi.org/10.1016/j.apcatb.2014.10.026.

[108] J.M. Don, A. Pen, FTIR study of photocatalytic degradation of 2-propanol in gas phase with different TiO_2 catalysts, Appl. Catal. B, Environ. 89 (2009) 204–213. https://doi.org/10.1016/j.apcatb.2008.11.027.

[109] S.W. Verbruggen, K. Masschaele, E. Moortgat, T.E. Korany, B. Hauchecorne, A. Martens, S. Lenaerts, Factors driving the activity of commercial titanium dioxide powders towards gas phase photocatalytic oxidation of acetaldehyde, Catal. Sci. Technol. 2 (2012) 2311–2318. https://doi.org/10.1039/c2cy20123b.

[110] M. V Diamanti, F. Lollini, M.P. Pedeferri, L. Bertolini, Mutual interactions between carbonation and titanium dioxide photoactivity in concrete, Build. Environ. 62 (2013) 174–181.

https://doi.org/10.1016/j.buildenv.2013.01.023.

[111] Z. Wang, Q. Yu, F. Gauvin, P. Feng, R. Qianping, H.J.H. Brouwers, Nanodispersed TiO_2 hydrosol modified Portland cement paste: The underlying role of hydration on self-cleaning mechanisms, Cem. Concr. Res. 136 (2020) 106156. https://doi.org/10.1016/j.cemconres.2020.106156.

[112] D. Liu, A. Kaja, Y. Chen, H.J.H. Brouwers, Q. Yu, Self-cleaning performance of photocatalytic cement mortar: Synergistic effects of hydration and carbonation, Cem. Concr. Res. 162 (2022) 107009. https://doi.org/10.1016/j.cemconres.2022.107009.

[113] J. Chen, C.S. Poon, Photocatalytic cementitious materials: Influence of the microstructure of cement paste on photocatalytic pollution degradation, Environ. Sci. Technol. 43 (2009) 8948–8952. https://doi.org/10.1021/es902359s.

[114] E. Benhelal, G. Zahedi, E. Shamsaei, A. Bahadori, Global strategies and potentials to curb CO_2 emissions in cement industry, J. Clean. Prod. 51 (2013) 142–161. https://doi.org/10.1016/j.jclepro.2012.10.049.

[115] M. Schneider, Process technology for efficient and sustainable cement production, Cem. Concr. Res. 78 (2015) 14–23. https://doi.org/10.1016/j.cemconres.2015.05.014.

[116] R.M. Andrew, Global CO_2 emissions from cement production, 1928--2018, Earth Syst. Sci. Data. 11 (2019) 1675–1710. https://doi.org/10.5194/essd-11-1675-2019.

[117] W. Shen, L. Cao, Q. Li, W. Zhang, G. Wang, C. Li, Quantifying CO_2 emissions from China's cement industry, Renew. Sustain. Energy Rev. 50 (2015) 1004–1012. https://doi.org/10.1016/j.rser.2015.05.031.

[118] T. Luukkonen, Z. Abdollahnejad, J. Yliniemi, P. Kinnunen, M. Illikainen, One-part alkali-activated materials: A review, Cem. Concr. Res. 103 (2018) 21–34. https://doi.org/10.1016/j.cemconres.2017.10.001.

[119] N. Elfami, H. Ez-zaki, A. Diouri, O. Sassi, A. Boukhari, Improvement of hydraulic and mechanical properties of dicalcium silicate by alkaline activation, Constr. Build. Mater. 247 (2020) 118589. https://doi.org/10.1016/j.conbuildmat.2020.118589.

[120] E. Belhadj, C. Diliberto, A. Lecomte, Characterization and activation of basic oxygen furnace slag, Cem. Concr. Compos. 34 (2012) 34–40. https://doi.org/10.1016/j.cemconcomp.2011.08.012.

[121] Q. Wang, J.W. Yang, P.Y. Yan, Influence of initial alkalinity on the hydration of steel slag, Sci. China Technol. Sci. 55 (2012) 3378–3387. https://doi.org/10.1007/s11431-012-4830-9.

[122] A. Bouregba, H. Ez-zaki, A. Diouri, O. Sassi, Dicalcium silicate hydration behavior in the presence of Na_2CO_3 and water glass, Asian J. Civ. Eng. 20 (2019) 857–867. https://doi.org/10.1007/s42107-019-00150-0.

[123] A. Cuesta, E.R. Losilla, M.A.G. Aranda, J. Sanz, Á.G. De La Torre, Reactive belite stabilization mechanisms by boron-bearing dopants, Cem. Concr. Res. 42 (2012) 598–606. https://doi.org/10.1016/j.cemconres.2012.01.006.

[124] H.El-Didamony, A.M. Sharara, I.M. Helmy, S.A. El-Aleem, Hydration characteristic of β-C_2S in the presence of some accelerators, Cem. Concr. Res. 26 (1996) 1179–1187. https://doi.org/10.1016/0008-8846(96)00103-2.

[125] M.J. Ahmed, K. Lambrechts, X. Ling, K. Schollbach, H.J.H. Brouwers, Effect of hydroxide, carbonate, and sulphate anions on the β-dicalcium silicate hydration rate, Cem. Concr. Res. 173 (2023) 107302. https://doi.org/10.1016/j.cemconres.2023.107302.

[126] M.J. Ahmed, W.F. Santos, H.J.H. Brouwers, Air granulated basic Oxygen furnace (BOF) slag application as a binder: Effect on strength, volumetric stability, hydration study, and environmental risk, Constr. Build. Mater. 367 (2023) 130342. https://doi.org/10.1016/j.conbuildmat.2023.130342.

[127] M. Jawad, S. Durand, M. Antoun, F. Gauvin, S. Amziane, H.J.H. Brouwers, Utilization of air granulated basic oxygen furnace slag as a binder in belite calcium sulfoaluminate cement : A sustainable alternative, J. Clean. Prod. 436 (2024) 140539. https://doi.org/10.1016/j.jclepro.2023.140539.

[128] European Commission, Directorate-General for Research and Inovation, European Green Deal – Research & innovation call, Publications Office of the European Union, 2021. https://doi.org/doi/10.2777/33415.

[129] Y.L. Li, J.W. Liu, J.Y. Chen, Y.F. Shi, W. Mao, H. Liu, Y. Li, S. He, J.K. Yang, Reuse of dewatered sewage sludge conditioned with skeleton builders as landfill cover material, Int. J. Environ. Sci. Technol.

11 (2014) 233–240. https://doi.org/10.1007/s13762-013-0199-y.

[130] S. Oh, W.S. Shin, Applicability of solidified/stabilized dye sludge char as a landfill cover material, KSCE J. Civ. Eng. 21 (2017) 2573–2583. https://doi.org/10.1007/s12205-017-0064-5.

[131] N.A. Rosli, H.A. Aziz, M.R. Selamat, L.L.P. Lim, A mixture of sewage sludge and red gypsum as an alternative material for temporary landfill cover, J. Environ. Manage. 263 (2020) 110420. https://doi.org/10.1016/J.JENVMAN.2020.110420.

[132] E.H. Kim, J.K. Cho, S. Yim, Digested sewage sludge solidification by converter slag for landfill cover, Chemosphere. 59 (2005) 387–395. https://doi.org/10.1016/j.chemosphere.2004.10.038.

[133] M. Liu, H. Lu, Q. Deng, S. Ji, L. Qin, Y. Wan, Shear strength, water permeability and microstructure of modified municipal sludge based on industrial solid waste containing calcium used as landfill cover materials, Waste Manag. 145 (2022) 20–28. https://doi.org/10.1016/j.wasman.2022.04.031.

[134] X. Gao, Q.L. Yu, A. Lazaro, H.J.H. Brouwers, Investigation on a green olivine nano-silica source based activator in alkali activated slag-fly ash blends: Reaction kinetics, gel structure and carbon footprint, Cem. Concr. Res. 100 (2017) 129–139. https://doi.org/10.1016/j.cemconres.2017.06.007.

[135] M. Wiśniewska, W. Stępniewski, The influence of lime, water-glass and clay addition on sealing properties of waste rock from Bogdanka, in: Environ. Eng. Proc. 2nd Natl. Congr. Environ. Eng. 4-8 Sept. 2005, CRC Press, 2006: p. 271.

[136] M. Tramontin, L. Simão, O. Rubem, K. Montedo, F. Raupp, A. Pedro, N. De Oliveira, Aluminum anodizing waste and its uses : An overview of potential applications and market opportunities, Waste Manag. 84 (2019) 286–301. https://doi.org/10.1016/j.wasman.2018.12.003.

[137] M.J. Ribeiro, J.A. Labrincha, Properties of sintered mullite and cordierite pressed bodies manufactured using Al-rich anodising sludge, 34 (2008) 593–597. https://doi.org/10.1016/j.ceramint.2006.12.005.

[138] C.A. Grattoni, X.D. Jing, R.W. Zimmerman, Disproportionate permeability reduction when a silicate gel is formed in-situ to control water production, SPE Lat. Am. Caribb. Pet. Eng. Conf. (2001). https://doi.org/10.2118/69534-MS.

[139] D. Boels, J. Bril, E. Hummelink, O. Boersma, Durability of Hydrostab; a field investigation and prognosis, Wageningen, 2005. https://edepot.wur.nl/25573.

[140] S. Brunauer, P.H. Emmett, E. Teller, Adsorption of gases in multimolecular Layers, J. Am.Chem.Soc. 60 (1938) 309–319. https://doi.org/10.1021/ja01269a023.

[141] S. Barzgar, M. Tarik, C. Ludwig, B. Lothenbach, The effect of equilibration time on Al uptake in C-S-H, Cem. Concr. Res. 144 (2021) 106438. https://doi.org/10.1016/j.cemconres.2021.106438.

[142] Z. Jinhong, L. Qimei, Z. Xiaorong, The hydrochar characters of municipal sewage sludge under different hydrothermal temperatures and durations, J. Integr. Agric. 13 (2014) 471–482. https://doi.org/10.1016/S2095-3119(13)60702-9.

[143] M. Horgnies, J.J. Chen, C. Bouillon, Overview about the use of fourier transform infrared spectroscopy to study cementitious materials, WIT Trans. Eng. Sci. 77 (2013) 251–262. https://doi.org/10.2495/MC130221.

[144] P. Thipkhunthod, V. Meeyoo, P. Rangsunvigit, T. Rirksomboon, Describing sewage sludge pyrolysis kinetics by a combination of biomass fractions decomposition, J. Anal. Appl. Pyrolysis. 79 (2007) 78–85. https://doi.org/10.1016/j.jaap.2006.10.005.

[145] J. De Oliveira Silva, G.R. Filho, C. Da Silva Meireles, S.D. Ribeiro, J.G. Vieira, C.V. Da Silva, D.A. Cerqueira, Thermal analysis and FTIR studies of sewage sludge produced in treatment plants. the case of sludge in the city of Uberlândia-MG, Brazil, Thermochim. Acta. 528 (2012) 72–75. https://doi.org/10.1016/j.tca.2011.11.010.

[146] L. Tourneret, F. Berger, C. Mavon, A. Chambaudet, Calcium sulphate formation during the heat-up period: some essential parameters, Appl. Clay Sci. 14 (1999) 299–317. https://doi.org/10.1016/S0169-1317(99)00005-8.

[147] M.A. Tantawy, M.R. Shatat, M.A. Taher, M.A. Taher, M. Abd-El-Hamed, Low temperature synthesis of belite cement based on silica fume and lime, Int. Sch. Res. Not. 2014 (2014) 10. https://doi.org/10.1155/2014/873215.

[148] T. Sun, Q. Zhuo, Y. Chen, Z. Wu, Synthesis of boehmite and its effect on flame retardancy of epoxy resin, High Perform. Polym. 27 (2015) 100–104. https://doi.org/10.1177/0954008314540312.

[149] M. Li, B. Xiao, X. Wang, J. Liu, Consequences of sludge composition on combustion performance derived from thermogravimetry analysis, Waste Manag. 35 (2015) 141–147. https://doi.org/10.1016/j.wasman.2014.10.004.

[150] P. Gahlot, G. Balasundaram, V.K. Tyagi, A.E. Atabani, S. Suthar, A.A. Kazmi, L. Štěpanec, D. Juchelková, A. Kumar, Principles and potential of thermal hydrolysis of sewage sludge to enhance anaerobic digestion, Environ. Res. 214 (2022). https://doi.org/10.1016/j.envres.2022.113856.

[151] C. Rodriguez-Navarro, E. Ruiz-Agudo, A. Luque, A.B. Rodriguez-Navarro, M. Ortega-Huertas, Thermal decomposition of calcite: Mechanisms of formation and textural evolution of CaO nanocrystals, Am. Mineral. 94 (2009) 578–593. https://doi.org/10.2138/am.2009.3021.

[152] M. Park, S. Lee, H. Kim, I. Park, J. Choy, Tailoring porosity of colloidal boehmite sol by controlling crystallite size, Bull. Korean Chem. Soc. 33 (2012) 1962–1966. https://doi.org/10.5012/bkcs.2012.33.6.1962.

[153] K. Miao, Z. Wang, R. He, L. Jin, Z. Song, R. Yu, Z. Lu, D. Li, Effects of boehmite on the calcination shrinkage and mechanical properties of gypsum-bonded molds, Adv. Eng. Mater. 24 (2022). https://doi.org/10.1002/adem.202100683.

[154] H.B. Nagaraj, B. Reesha, M. V. Sravan, M.R. Suresh, Correlation of compaction characteristics of natural soils with modified plastic limit, Transp. Geotech. 2 (2015) 65–77. https://doi.org/10.1016/j.trgeo.2014.09.002.

[155] Rijkswaterstaat, Guidelines implementing the landfill decision on soil protection, (1991) 88. https://www.bodemplus.nl/@132149/richtlijnen-uitvoeringsregeling-stortbesluit/.

[156] I. Herrmann, M. Svensson, H. Ecke, J. Kumpiene, C. Maurice, L. Andreas, A. Lagerkvist, Hydraulic conductivity of fly ash–sewage sludge mixes for use in landfill cover liners, Water Res. 43 (2009) 3541–3547. https://doi.org/10.1016/j.watres.2009.04.052.

[157] H. Zhang, B. Yang, G. Zhang, X. Zhang, Sewage sludge as barrier material for heavy metals in waste landfill, Arch. Environ. Prot. 42 (2016) 52–58. https://doi.org/10.1515/aep-2016-0020.

[158] D.A. Rubinos, G. Spagnoli, Utilization of waste products as alternative landfill liner and cover materials–A critical review, Crit. Rev. Environ. Sci. Technol. 48 (2018) 376–438. https://doi.org/10.1080/10643389.2018.1461495.

[159] J.Q. Chen, T.R. Liu, M.M. Sun, Y.Z. Zhao, H.H. Ge, Inhibition of poly(Ethylenediaminetetraacetic acid-diethanolamine) on deposition of calcium sulfate crystal in simulated industrial water, Crystals. 10 (2020) 1–15. https://doi.org/10.3390/cryst10060544.

[160] A.M.B. Silva, D.O. Junot, L.V.E. Caldas, D.N. Souza, Structural, optical and dosimetric characterization of $CaSO_4$:Tb, $CaSO_4$:Tb, Ag and $CaSO_4$:Tb,Ag(NP), J. Lumin. 224 (2020). https://doi.org/10.1016/j.jlumin.2020.117286.

[161] I. García-Lodeiro, A. Fernández-Jiménez, M.T. Blanco, A. Palomo, FTIR study of the sol-gel synthesis of cementitious gels: C-S-H and N-A-S-H, J. Sol-Gel Sci. Technol. 45 (2008) 63–72. https://doi.org/10.1007/s10971-007-1643-6.

[162] Y. Pan, S. He, X. Cheng, Z. Li, C. Li, Y. Huang, L. Gong, A fast synthesis of silica aerogel powders-based on water glass via ambient drying, J. Sol-Gel Sci. Technol. 82 (2017) 594–601. https://doi.org/10.1007/s10971-017-4312-4.

[163] F. Paulik, J. Paulik, M. Arnold, Thermal decomposition of gypsum, Thermochim. Acta. 200 (1992) 195–204. https://doi.org/10.1016/0040-6031(92)85115-C.

[164] K. Scrivener, R. Snellings, B. Lothenbach, A practical guide to microstructural analysis of cementitious materials, Crc Press Boca Raton, FL, USA, 2016. https://doi.org/10.1201/b19074.

[165] Y. Ma, J. Hu, G. Ye, The pore structure and permeability of alkali activated fly ash, Fuel. 104 (2013) 771–780. https://doi.org/10.1016/j.fuel.2012.05.034.

[166] A.A. Amadi, A.O. Eberemu, Potential application of lateritic soil stabilized with cement kiln dust (CKD) as liner in waste containment structures, Geotech. Geol. Eng. 31 (2013) 1221–1230. https://doi.org/10.1007/s10706-013-9645-3.

[167] J. Sung, H. Song, G. Yim, S. Woo, J. Kim, An engineered cover system for mine tailings using a hardpan layer : A solidification / stabilization method for layer and field performance evaluation, J. Hazard. Mater. 197 (2011) 153–160. https://doi.org/10.1016/j.jhazmat.2011.09.069.

[168] S.A. Stronach, F.P. Glasser, Modelling the impact of abundant geochemical components on phase stability and solubility of the CaO-SiO_2-H_2O system at 25 °C: Na^+, K^+, SO_4^{2-}, Cl^- and CO_3^{2-}, Adv. Cem. Res. 9 (1997) 167–181. https://doi.org/10.1680/adcr.1997.9.36.167.

[169] H. Song, S. Kwon, Permeability characteristics of carbonated concrete considering capillary pore structure, 37 (2007) 909–915. https://doi.org/10.1016/j.cemconres.2007.03.011.

[170] R.W. Zuhl, Z. Amjad, Solution chemistry impact on silica polymerization by inhibitors, in: Miner. Scales Biol. Ind. Syst., 2013: p. 173. https://doi.org/10.1201/b15606-13.

[171] P. Singh, A. Borthakur, R. Singh, R. Bhadouria, A critical review on the research trends and emerging technologies for arsenic decontamination from water, Groundw. Sustain. Dev. 14 (2021) 100607. https://doi.org/10.1016/j.gsd.2021.100607.

[172] C.H. Weng, C.P. Huang, H.E. Allen, A.H. Cheng, P.F. Sanders, Chromium leaching behavior in soil derived from chromite ore processing waste, Sci. Total Environ. 154 (1994) 71–86. https://doi.org/10.1016/0048-9697(94)90615-7.

[173] C.E. Halim, S.A. Short, J.A. Scott, R. Amal, G. Low, Modelling the leaching of Pb, Cd, As, and Cr from cementitious waste using PHREEQC, J. Hazard. Mater. 125 (2005) 45–61. https://doi.org/10.1016/j.jhazmat.2005.05.046.

[174] L.A. Mendes, L. Felipe, P. Bucater, M.D. Landgraf, M. Olímpia, O. Rezende, Role of organic matter in the adsorption / desorption of Cr , Cu and Pb in competitive systems in two different soils, Open Access Libr. J. 1 (2014) 1–5. https://doi.org/10.4236/oalib.1101022.

[175] J.J.G. Costa, M.J. Reigosa, J.M. Matías, E.F. Covelo, Soil Cd , Cr , Cu , Ni , Pb and Zn sorption and retention models using SVM : Variable selection and competitive model, Sci. Total Environ. 593–594 (2017) 508–522. https://doi.org/10.1016/j.scitotenv.2017.03.195.

[176] Rijkswaterstaat, Landfills in the Netherlands, (2022). https://www.bodemplus.nl/onderwerpen/bodem-ondergrond/verwerking-grond/stortplaatsen/stortplaatsen/ (accessed March 29, 2022).

[177] X. Ling, W. Chen, K. Schollbach, H.J.H. Brouwers, Low permeability sealing materials based on sewage , digestate and incineration industrial by-products in the final landfill cover system, Constr. Build. Mater. 412 (2024) 134889. https://doi.org/10.1016/j.conbuildmat.2024.134889.

[178] G.M. Ayininuola, I.O. Ayodeji, Influence of sludge ash on soil shear strength, J. Civ. Eng. Reseach. 6 (2016) 72–77. https://doi.org/10.5923/j.jce.20160603.04.

[179] M.R. Iqbal, K. Hashimoto, S. Tachibana, K. Kawamoto, Geotechnical properties of sludge blended with crushed concrete and incineration ash, Int. J. GEOMATE. 16 (2019) 116–123. https://doi.org/10.21660/2019.57.8130.

[180] D. Lin, K. Lin, M. Hung, H. Luo, Sludge ash / hydrated lime on the geotechnical properties of soft soil, 145 (2007) 58–64. https://doi.org/10.1016/j.jhazmat.2006.10.087.

[181] S. Lim, W. Jeon, J. Lee, K. Lee, N. Kim, Engineering properties of water/wastewater-treatment sludge modified by hydrated lime, fly ash and loess, Water Res. 36 (2002) 4177–4184. https://doi.org/10.1016/S0043-1354(02)00150-1.

[182] N.T. Dung, T.J.N. Hooper, C. Unluer, Improving the carbonation resistance of Na_2CO_3-activated slag mixes via the use of reactive MgO and nucleation seeding, Cem. Concr. Compos. 115 (2021) 103832. https://doi.org/10.1016/j.cemconcomp.2020.103832.

[183] S.Y. Wang, E. McCaslin, C.E. White, Effects of magnesium content and carbonation on the multiscale pore structure of alkali-activated slags, Cem. Concr. Res. 130 (2020) 105979. https://doi.org/10.1016/j.cemconres.2020.105979.

[184] E. Gartung, W.-U. Henken-Mellies, J. Kanitz, H.-G. Ramke, Geotechnical aspects of landfill closure and aftercare, in: Y. Chen, L. Zhan, X. Tang (Eds.), Adv. Environ. Geotech., Springer Berlin Heidelberg, Berlin, Heidelberg, 2010: pp. 188–203. https://doi.org/10.1007/978-3-642-04460-1_12.

[185] A. Leemann, F. Moro, Carbonation of concrete: the role of CO_2 concentration, relative humidity and CO_2 buffer capacity, Mater. Struct. Constr. 50 (2017) 1–14. https://doi.org/10.1617/s11527-016-0917-2.

[186] S.A. Bernal, J.L. Provis, B. Walkley, R. San Nicolas, J.D. Gehman, D.G. Brice, A.R. Kilcullen, P. Duxson, J.S.J. Van Deventer, Gel nanostructure in alkali-activated binders based on slag and fly ash, and effects of accelerated carbonation, Cem. Concr. Res. 53 (2013) 127–144. https://doi.org/10.1016/j.cemconres.2013.06.007.

[187] H. Grénman, T. Salmi, D. Yu, J. Addai-mensah, Dissolution of boehmite in sodium hydroxide at ambient pressure : Kinetics and modelling, Hydrometallurgy. 102 (2010) 22–30. https://doi.org/10.1016/j.hydromet.2010.01.005.

[188] M. Olszak-Humienik, On the thermal stability of some ammonium salts, Thermochim. Acta. 378 (2001) 107–112. https://doi.org/10.1016/S0040-6031(01)00585-8.

[189] K. Serafeimidis, G. Anagnostou, On the crystallisation pressure of gypsum, Environ. Earth Sci. 72 (2014) 4985–4994. https://doi.org/10.1007/s12665-014-3366-7.

[190] Z. Li, S. Zhang, Y. Zuo, W. Chen, Chemical deformation of metakaolin based geopolymer, Cem. Concr. Res. 120 (2019) 108–118. https://doi.org/10.1016/j.cemconres.2019.03.017.

[191] M.S. Churio, M.A. Brusa, M.A. Grela, S.G. Bertolotti, C.M. Previtali, Time-resolved photoacoustic calorimetry of aqueous peroxodisulfate photolysis in the presence of nitrite anions, Phys. Chem. Chem. Phys. 5 (2003) 902–906. https://doi.org/10.1039/b209334k.

[192] I.W. Duedall, The partial molal volume of calcium carbonate in sea water, Geochim. Cosmochim. Acta. 36 (1972) 729–734. https://doi.org/10.1016/0016-7037(72)90083-X.

[193] A.G. Turnbull, A thermochemical study of monohydrocalcite, Geochim. Cosmochim. Acta. 37 (1973) 1593–1601. https://doi.org/10.1016/0016-7037(73)90093-8.

[194] C.N. Singman, Atomic volume and allotropy of the elements, J. Chem. Educ. 61 (1984) 137. https://doi.org/10.1021/ed061p137.

[195] Q. Yao, G. Zhou, Transformation of amorphous calcium carbonate into Monohydrocalcite in aqueous solution : A biomimetic mineralization study Transformation of amorphous calcium carbonate into monohydrocalcite in aqueous solution : a biomimetic mineralization study, (2015). https://doi.org/10.1127/ejm/2015/0027-2486.

[196] B. Li, J. Xiong, C. Peng, M. Li, H. Liu, W. Wang, S. Peng, Hierarchical porous AlOOH hollow microspheres for efficient CO_2 capture, Ceram. Int. 49 (2023) 38226–38236. https://doi.org/10.1016/j.ceramint.2023.09.154.

[197] C.N. Singman, Atomic volume and allotropy of the elements, J. Chem. Educ. 61 (1984) 137. https://doi.org/10.1021/ed061p137.

[198] H. Böke, S. Akkurt, S. Özdemir, E.H. Göktürk, E.N. Caner Saltik, Quantification of $CaCO_3$–$CaSO_3 \cdot 0.5H_2O$–$CaSO_4 \cdot 2H_2O$ mixtures by FTIR analysis and its ANN model, Mater. Lett. 58 (2004) 723–726. https://doi.org/10.1016/j.matlet.2003.07.008.

[199] N. V. Chukanov, Infrared spectra of mineral species: Extended library, 1st ed., Springer, Dordrecht, 2014. http://link.springer.com/10.1007/978-94-007-7128-4.

[200] M. Hua, B. Wang, L. Chen, Y. Wang, V.M. Quynh, B. He, X. Li, Verification of lime and water glass stabilized FGD gypsum as road sub-base, Fuel. 89 (2010) 1812–1817. https://doi.org/10.1016/j.fuel.2009.11.029.

[201] K.-I. Song, J.-K. Song, B.Y. Lee, K.-H. Yang, Carbonation characteristics of alkali-activated blast-furnace slag mortar, Adv. Mater. Sci. Eng. 2014 (2014) 326458. https://doi.org/10.1155/2014/326458.

[202] N. Li, N. Farzadnia, C. Shi, Microstructural changes in alkali-activated slag mortars induced by accelerated carbonation, Cem. Concr. Res. 100 (2017) 214–226. https://doi.org/10.1016/j.cemconres.2017.07.008.

[203] K.S.W. Sing, Reporting physisorption data for gas/solid systems with special reference to the determination of surface area and porosity (Recommendations 1984), Pure Appl. Chem. 57 (1985) 603–619. https://doi.org/doi:10.1351/pac198557040603.

[204] Z. Zhang, G.W. Scherer, Evaluation of drying methods by nitrogen adsorption, Cem. Concr. Res. 120 (2019) 13–26. https://doi.org/10.1016/j.cemconres.2019.02.016.

[205] A. Morandeau, M. Thiéry, P. Dangla, Impact of accelerated carbonation on OPC cement paste blended with fly ash, Cem. Concr. Res. 67 (2015) 226–236. https://doi.org/10.1016/j.cemconres.2014.10.003.

[206] M.S. Bin Shafique, J.C. Walton, N. Gutierrez, R.W. Smith, A.J. Tarquin, Influence of carbonation on leaching of cementitious wasteforms, J. Environ. Eng. 124 (1998) 463–467. https://doi.org/10.1061/(ASCE)0733-9372(1998)124:5(463).

[207] S. Valls, E. Vàzquez, Accelerated carbonatation of sewage sludge-cement-sand mortars and its environmental impact, Cem. Concr. Res. 31 (2001) 1271–1276. https://doi.org/10.1016/S0008-8846(01)00573-7.

[208] N. Alba, E. Vázquez, S. Gassó, J.M. Baldasano, Stabilization/solidification of MSW incineration residues from facilities with different air pollution control systems: Durability of matrices versus carbonation, Waste Manag. 21 (2001) 313–323. https://doi.org/10.1016/S0956-053X(00)00082-9.

[209] F. Sanchez, C. Gervais, A.C. Garrabrants, R. Barna, D.S. Kosson, Leaching of inorganic contaminants from cement-based waste materials as a result of carbonation during intermittent wetting, Waste Manag. 22 (2002) 249–260. https://doi.org/10.1016/S0956-053X(01)00076-9.

[210] Council of the European Union, Council decision of 19 December 2002 establishing criteria and procedures for the acceptance of waste at landfills pursuant to Article 16 of and Annex II to Directive 1999/31/EC, Off. J. Eur. Communities. (2003) 27–49.

[211] R. Nishiyama, T. Munemoto, K. Fukushi, Formation condition of monohydrocalcite from $CaCl_2$–$MgCl_2$–Na_2CO_3 solutions, Geochim. Cosmochim. Acta. 100 (2013) 217–231. https://doi.org/10.1016/j.gca.2012.09.002.

[212] P.J. Gunning, C.D. Hills, P.J. Carey, Accelerated carbonation treatment of industrial wastes, Waste Manag. 30 (2010) 1081–1090. https://doi.org/10.1016/j.wasman.2010.01.005.

[213] X. Ling, K. Schollbach, Y. Chen, H.J.H. Brouwers, The effect of nano-silica and silica fume on the sodium carbonate-activated slag system containing air pollution control residues, Waste Manag. 176 (2024) 52–63. https://doi.org/10.1016/j.wasman.2024.01.028.

[214] S. Sabrin, R. Nazari, M.G.R. Fahad, M. Karimi, J.W. Everett, R.W. Peters, Investigating effects of landfill soil gases on landfill elevated subsurface temperature, Appl. Sci. 10 (2020). https://doi.org/10.3390/APP10186401.

[215] N.H. Jafari, T.D. Stark, T. Thalhamer, Progression of elevated temperatures in municipal solid waste landfills, J. Geotech. Geoenvironmental Eng. 143 (2017) 05017004. https://doi.org/10.1061/(asce)gt.1943-5606.0001683.

[216] S.A. Walling, S.A. Bernal, L.J. Gardner, H. Kinoshita, J. Provis, Blast furnace slag-$Mg(OH)_2$ cements activated by sodium carbonate, RSC Adv. 8 (2018) 23101–23118. https://doi.org/10.1039/c8ra03717e.

[217] A. Abdalqader, F. Jin, A. Al-Tabbaa, Performance of magnesia-modified sodium carbonate-activated slag/fly ash concrete, Cem. Concr. Compos. 103 (2019) 160–174. https://doi.org/10.1016/j.cemconcomp.2019.05.007.

[218] B. Yuan, Q.L. Yu, H.J.H. Brouwers, Assessing the chemical involvement of limestone powder in sodium carbonate activated slag, Mater. Struct. Constr. 50 (2017) 0–14. https://doi.org/10.1617/s11527-017-1003-0.

[219] Y. Jeong, J.E. Oh, Y. Jun, J. Park, J.H. Ha, S.G. Sohn, Influence of four additional activators on hydrated-lime [$Ca(OH)_2$] activated ground granulated blast-furnace slag, Cem. Concr. Compos. 65 (2016) 1–10. https://doi.org/10.1016/j.cemconcomp.2015.10.007.

[220] A. Moropoulou, A. Bakolas, E. Aggelakopoulou, The effects of limestone characteristic, granulation and calcination temperature to the reactivity of quicklime, Cem. Concr. Res. 31 (2001) 633–639. https://doi.org/10.1016/S0008-8846(00)00490-7.

[221] M. Khachani, A. El Hamidi, M. Halim, S. Arsalane, Non-isothermal kinetic and thermodynamic studies of the dehydroxylation process of synthetic calcium hydroxide $Ca(OH)_2$, J. Mater. Environ. Sci. 5 (2014) 615–624.

[222] B. Yuan, Q.L. Yu, H.J.H. Brouwers, Evaluation of slag characteristics on the reaction kinetics and mechanical properties of Na_2CO_3 activated slag, Constr. Build. Mater. 131 (2017) 334–346. https://doi.org/10.1016/j.conbuildmat.2016.11.074.

[223] A. Fernandez-Jimenez, F. Puertas, Setting of alkali-activated slag cement. Influence of activator nature, Adv. Cem. Res. 13 (2001) 115–121. https://doi.org/10.1680/adcr.13.3.115.39288.

[224] S.A. Bernal, J.L. Provis, R.J. Myers, R. San Nicolas, J.S.J. van Deventer, Role of carbonates in the chemical evolution of sodium carbonate-activated slag binders, Mater. Struct. Constr. 48 (2014) 517–529. https://doi.org/10.1617/s11527-014-0412-6.

[225] K.H. Yang, J. Il Sim, S.H. Nam, Enhancement of reactivity of calcium hydroxide-activated slag mortars by the addition of barium hydroxide, Constr. Build. Mater. 24 (2010) 241–251. https://doi.org/10.1016/j.conbuildmat.2009.09.001.

[226] M.S. Kim, Y. Jun, C. Lee, J.E. Oh, Use of CaO as an activator for producing a price-competitive non-cement structural binder using ground granulated blast furnace slag, Cem. Concr. Res. 54 (2013) 208–214. https://doi.org/10.1016/j.cemconres.2013.09.011.

[227] I. Ismail, S.A. Bernal, J.L. Provis, R. San Nicolas, S. Hamdan, J.S.J. Van Deventer, Modification of phase evolution in alkali-activated blast furnace slag by the incorporation of fly ash, Cem. Concr. Compos. 45 (2014) 125–135. https://doi.org/10.1016/j.cemconcomp.2013.09.006.

[228] I. García Lodeiro, D.E. Macphee, A. Palomo, A. Fernández-Jiménez, Effect of alkalis on fresh C-S-H gels. FTIR analysis, Cem. Concr. Res. 39 (2009) 147–153. https://doi.org/10.1016/j.cemconres.2009.01.003.

[229] Y. Kocak, S. Nas, The effect of using fly ash on the strength and hydration characteristics of blended cements, Constr. Build. Mater. 73 (2014) 25–32. https://doi.org/10.1016/j.conbuildmat.2014.09.048.

[230] S.A. Bernal, E.D. Rodríguez, R. Mejia De Gutiérrez, J.L. Provis, S. Delvasto, Activation of metakaolin/slag blends using alkaline solutions based on chemically modified silica fume and rice husk ash, Waste and Biomass Valorization. 3 (2012) 99–108. https://doi.org/10.1007/s12649-011-9093-3.

[231] X. Ke, S.A. Bernal, J.L. Provis, Uptake of chloride and carbonate by Mg-Al and Ca-Al layered double hydroxides in simulated pore solutions of alkali-activated slag cement, Cem. Concr. Res. 100 (2017) 1–13. https://doi.org/10.1016/j.cemconres.2017.05.015.

[232] N.T. Dung, T.J.N. Hooper, C. Unluer, Accelerating the reaction kinetics and improving the performance of Na_2CO_3-activated GGBS mixes, Cem. Concr. Res. 126 (2019) 105927. https://doi.org/10.1016/j.cemconres.2019.105927.

[233] K. Wang, D. Han, P. Zhao, X. Hu, Z. Yin, D. Wu, Role of $Mg_xCa_{1-x}CO_3$ on the physical-chemical properties and cyclic CO_2 capture performance of dolomite by two-step calcination, Thermochim. Acta. 614 (2015) 199–206. https://doi.org/10.1016/j.tca.2015.06.033.

[234] H.Y. Zeng, X. Deng, Y.J. Wang, K.B. Liao, Preparation of mg-ai hydrotalcite by urea method and its catalytic activity for transesterification, AIChE J. 55 (2009) 1229–1235. https://doi.org/10.1002/AIC.11722.

[235] F. Puertas, M. Palacios, H. Manzano, J.S. Dolado, A. Rico, J. Rodríguez, A model for the C-A-S-H gel formed in alkali-activated slag cements, J. Eur. Ceram. Soc. 31 (2011) 2043–2056. https://doi.org/10.1016/j.jeurceramsoc.2011.04.036.

[236] B. Akturk, A.B. Kizilkanat, N. Kabay, Effect of calcium hydroxide on fresh state behavior of sodium carbonate activated blast furnace slag pastes, Constr. Build. Mater. 212 (2019) 388–399. https://doi.org/10.1016/j.conbuildmat.2019.03.328.

[237] C. Shi, R.L. Day, A calorimetric study of early hydration of alkali-slag cement, Cem. Concr. Res. 25 (1995) 1333–1346. https://doi.org/10.1016/0008-8846(95)00126-W.

[238] S. Song, H.M. Jennings, Pore solution chemistry of alkali-activated ground granulated blast-furnace slag, Cem. Concr. Res. 29 (1999) 159–170. https://doi.org/10.1016/S0008-8846(98)00212-9.

[239] N. Mobasher, S.A. Bernal, J.L. Provis, Structural evolution of an alkali sulfate activated slag cement, J. Nucl. Mater. 468 (2016) 97–104. https://doi.org/10.1016/j.jnucmat.2015.11.016.

[240] T. Meng, Y. Qiang, A. Hu, C. Xu, L. Lin, Effect of compound nano-$CaCO_3$ addition on strength development and microstructure of cement-stabilized soil in the marine environment, Constr. Build. Mater. 151 (2017) 775–781. https://doi.org/10.1016/j.conbuildmat.2017.06.016.

[241] X. Liu, B. Ma, H. Tan, H. Li, J. Mei, T. Zhang, P. Chen, B. Gu, Chloride immobilization of cement-based material containing nano-Al_2O_3, Constr. Build. Mater. 220 (2019) 43–52. https://doi.org/10.1016/j.conbuildmat.2019.05.148.

[242] M. Nikravan, A.A. Ramezanianpnour, R. Maknoon, Technological and environmental behavior of petrochemical incineration bottom ash (PI-BA) in cement-based using nano-SiO_2 and silica fume (SF),

Constr. Build. Mater. 191 (2018) 1042–1052. https://doi.org/10.1016/j.conbuildmat.2018.09.135.

[243] X. Gao, Q.L. Yu, H.J.H. Brouwers, Characterization of alkali activated slag–fly ash blends containing nano-silica, Constr. Build. Mater. 98 (2015) 397–406. https://doi.org/10.1016/j.conbuildmat.2015.08.086.

[244] G. Quercia, G. Hüsken, H.J.H. Brouwers, Water demand of amorphous nano silica and its impact on the workability of cement paste, Cem. Concr. Res. 42 (2012) 344–357. https://doi.org/10.1016/j.cemconres.2011.10.008.

[245] L.P. Singh, W. Zhu, T. Howind, U. Sharma, Quantification and characterization of C-S-H in silica nanoparticles incorporated cementitious system, Cem. Concr. Compos. 79 (2017) 106–116. https://doi.org/10.1016/j.cemconcomp.2017.02.004.

[246] A.A. Ramezanianpour, M.A. Moeini, Mechanical and durability properties of alkali activated slag coating mortars containing nanosilica and silica fume, Constr. Build. Mater. 163 (2018) 611–621. https://doi.org/10.1016/j.conbuildmat.2017.12.062.

[247] E. Kapeluszna, Ł. Kotwica, A. Różycka, Ł. Gołek, Incorporation of Al in C-A-S-H gels with various Ca/Si and Al/Si ratio: Microstructural and structural characteristics with DTA/TG, XRD, FTIR and TEM analysis, Constr. Build. Mater. 155 (2017) 643–653. https://doi.org/10.1016/j.conbuildmat.2017.08.091.

[248] G. Renaudin, J. Russias, F. Leroux, F. Frizon, C. Cau-dit-Coumes, Structural characterization of C-S-H and C-A-S-H samples-Part I: Long-range order investigated by Rietveld analyses, J. Solid State Chem. 182 (2009) 3312–3319. https://doi.org/10.1016/j.jssc.2009.09.026.

[249] F. Pacheco Torgal, S. Miraldo, J.A. Labrincha, J. De Brito, An overview on concrete carbonation in the context of eco-efficient construction: Evaluation, use of SCMs and/or RAC, Constr. Build. Mater. 36 (2012) 141–150. https://doi.org/10.1016/j.conbuildmat.2012.04.066.

[250] S.A. Bernal, J.L. Provis, D.G. Brice, A. Kilcullen, P. Duxson, J.S.J. Van Deventer, Accelerated carbonation testing of alkali-activated binders significantly underestimates service life: The role of pore solution chemistry, Cem. Concr. Res. 42 (2012) 1317–1326. https://doi.org/10.1016/j.cemconres.2012.07.002.

[251] A. Lázaro García, Nano-silica production at low temperatures from the dissolution of olivine: Synthesis, tailoring and modeling, Eindhoven University of Technology, 2014. https://doi.org/10.6100/IR774494.

[252] X. Ling, K. Schollbach, G. Liu, H.J.H. Brouwers, The utilization of waste incineration filter dust (WIFD) in sodium carbonate activated slag mortars, Constr. Build. Mater. 313 (2021) 125494. https://doi.org/10.1016/j.conbuildmat.2021.125494.

[253] C.B. Cheah, L.E. Tan, M. Ramli, The engineering properties and microstructure of sodium carbonate activated fly ash/ slag blended mortars with silica fume, Compos. Part B Eng. 160 (2019) 558–572. https://doi.org/10.1016/j.compositesb.2018.12.056.

[254] S. Brunauer, P.H. Emmett, E. Teller, Adsorption of Gases in Multimolecular Layers, J. Am. Chem. Soc. 60 (1938) 309–319. https://doi.org/10.1021/ja01269a023.

[255] Y. Qing, Z. Zenan, K. Deyu, C. Rongshen, Influence of nano-SiO_2 addition on properties of hardened cement paste as compared with silica fume, Constr. Build. Mater. 21 (2007) 539–545. https://doi.org/10.1016/j.conbuildmat.2005.09.001.

[256] H. Li, H.G. Xiao, J. Yuan, J. Ou, Microstructure of cement mortar with nano-particles, Compos. Part B Eng. 35 (2004) 185–189. https://doi.org/10.1016/S1359-8368(03)00052-0.

[257] C. Shi, R.L. Day, A calorimetric study of early hydration of alkali-slag cements, Cem. Concr. Res. 25 (1995) 1333–1346. https://doi.org/10.1016/0008-8846(95)00126-W.

[258] D. Krizan, B. Zivanovic, Effects of dosage and modulus of water glass on early hydration of alkali–slag cements, Cem. Concr. Res. 32 (2002) 1181–1188. https://doi.org/10.1016/S0008-8846(01)00717-7.

[259] M. Criado, A. Fernández-Jiménez, A. Palomo, I. Sobrados, J. Sanz, Effect of the SiO_2/Na_2O ratio on the alkali activation of fly ash. Part II: ^{29}Si MAS-NMR Survey, Microporous Mesoporous Mater. 109 (2008) 525–534. https://doi.org/10.1016/j.micromeso.2007.05.062.

[260] M. Rupasinghe, R. San Nicolas, P. Mendis, M. Sofi, T. Ngo, Investigation of strength and hydration characteristics in nano-silica incorporated cement paste, Cem. Concr. Compos. 80 (2017) 17–30. https://doi.org/10.1016/j.cemcncomp.2017.02.011.

[261] X. Gao, Q.L. Yu, H.J.H. Brouwers, Properties of alkali activated slag–fly ash blends with limestone addition, Cem. Concr. Compos. 59 (2015) 119–128. https://doi.org/10.1016/j.cemconcomp.2015.01.007.

[262] K. De Weerdt, K.O. Kjellsen, E. Sellevold, H. Justnes, Synergy between fly ash and limestone powder in ternary cements, Cem. Concr. Compos. 33 (2011) 30–38. https://doi.org/10.1016/j.cemconcomp.2010.09.006.

[263] P. Yu, R.J. Kirkpatrick, B. Poe, P.F. McMillan, X. Cong, Structure of Calcium Silicate Hydrate (C-S-H): Near-, Mid-, and Far-Infrared Spectroscopy, J. Am. Ceram. Soc. 82 (1999) 742–748. https://doi.org/https://doi.org/10.1111/j.1151-2916.1999.tb01826.x.

[264] B. Lothenbach, G. Le Saout, E. Gallucci, K. Scrivener, Influence of limestone on the hydration of Portland cements, Cem. Concr. Res. 38 (2008) 848–860. https://doi.org/10.1016/j.cemconres.2008.01.002.

[265] Fernández, J.L. García Calvo, M.C. Alonso, Ordinary Portland Cement composition for the optimization of the synergies of supplementary cementitious materials of ternary binders in hydration processes, Cem. Concr. Compos. 89 (2018) 238–250. https://doi.org/10.1016/j.cemconcomp.2017.12.016.

[266] S. Crosby, D. Tran, D. Cocke, E.S.M. Duraia, G.W. Beall, Effect of isomorphous substitution on the thermal decomposition mechanism of hydrotalcites, Materials (Basel). 7 (2014) 7048–7058. https://doi.org/10.3390/ma7107048.

[267] W.W. Focke, D. Molefe, F.J.W. Labuschagne, S. Ramjee, The influence of stearic acid coating on the properties of magnesium hydroxide, hydromagnesite, and hydrotalcite powders, J. Mater. Sci. 44 (2009) 6100–6109. https://doi.org/10.1007/s10853-009-3844-6.

[268] S.Y. Wang, E. McCaslin, C.E. White, Effects of magnesium content and carbonation on the multiscale pore structure of alkali-activated slags, Cem. Concr. Res. 130 (2020) 105979. https://doi.org/10.1016/j.cemconres.2020.105979.

[269] P. Hou, J. Qian, X. Cheng, S.P. Shah, Effects of the pozzolanic reactivity of nanoSiO_2 on cement-based materials, Cem. Concr. Compos. 55 (2015) 250–258. https://doi.org/10.1016/j.cemconcomp.2014.09.014.

[270] P.K. Mehta, P.J.M. Monteiro, Concrete: Microstructure, Properties, and Materials, Third ed., McGraw-Hill, 2006.

[271] H. Ye, Z. Chen, L. Huang, Mechanism of sulfate attack on alkali-activated slag : The role of activator composition, Cem. Concr. Res. 125 (2019) 105868. https://doi.org/10.1016/j.cemconres.2019.105868.

[272] I.G. Richardson, The calcium silicate hydrates, Cem. Concr. Res. 38 (2008) 137–158. https://doi.org/10.1016/j.cemconres.2007.11.005.

[273] C. Shi, P. V. Krivenko, D. Roy, alkali-activated cements and concretes, 1st Edition, London, 2003. https://doi.org/10.1201/9781482266900.

[274] D. Kong, H. Pan, L. Wang, D.J. Corr, Y. Yang, S.P. Shah, J. Sheng, Effect and mechanism of colloidal silica sol on properties and microstructure of the hardened cement-based materials as compared to nano-silica powder with agglomerates in micron-scale, Cem. Concr. Compos. 98 (2019) 137–149. https://doi.org/10.1016/j.cemconcomp.2019.02.015.

[275] S.A. Bernal, J.L. Provis, R. Mejı, J.S.J. Van Deventer, Accelerated carbonation testing of alkali-activated slag / metakaolin blended concretes : effect of exposure conditions, (2015) 653–669. https://doi.org/10.1617/s11527-014-0289-4.

[276] A. El-Turki, R.J. BaLL, G.C. Allen, The influence of relative humidity on structural and chemical changes during carbonation of hydraulic lime, Cem. Concr. Res. 37 (2007) 1233–1240. https://doi.org/10.1016/j.cemconres.2007.05.002.

[277] F. Colangelo, I. Farina, M. Travaglioni, C. Salzano, R. Cioffi, A. Petrillo, Eco-efficient industrial waste recycling for the manufacturing of fibre reinforced innovative geopolymer mortars: Integrated waste management and green product development through LCA, J. Clean. Prod. 312 (2021) 127777. https://doi.org/10.1016/j.jclepro.2021.127777.

[278] D.M.J. Sumajouw, D. Hardjito, S.E. Wallah, B. V. Rangan, Fly ash-based geopolymer concrete: Study of slender reinforced columns, J. Mater. Sci. 42 (2007) 3124–3130. https://doi.org/10.1007/s10853-006-0523-8.

[279] M. Weil, K. Dombrowski, A. Buchwald, Life-cycle analysis of geopolymers, in: J.L. Provis, J. van Deventer (Eds.), Geopolymers Struct. Process. Prop. Ind. Appl., Woodhead Publishing, 2009: pp. 194–

210. https://doi.org/10.1533/9781845696382.2.194.

[280] D.J.M. Flower, J.G. Sanjayan, Green house gas emissions due to concrete manufacture, Int. J. Life Cycle Assess. 12 (2007) 282–288. https://doi.org/10.1065/lca2007.05.327.

[281] F. Collins, Inclusion of carbonation during the life cycle of built and recycled concrete : influence on their carbon footprint, Int. J. Life Cycle Assess. 15 (2010) 549–556. https://doi.org/10.1007/s11367-010-0191-4.

[282] A. Adesina, Performance and sustainability overview of sodium carbonate activated slag materials cured at ambient temperature, Resour. Environ. Sustain. 3 (2021) 100016. https://doi.org/10.1016/j.resenv.2021.100016.

[283] M. Valente, M. Sambucci, M. Chougan, S. Hamidreza, Reducing the emission of climate-altering substances in cementitious materials : A comparison between alkali-activated materials and Portland cement-based composites incorporating recycled tire rubber, J. Clean. Prod. 333 (2022) 130013. https://doi.org/10.1016/j.jclepro.2021.130013.

[284] A. Gholizadeh-Vayghan, M.-H. Nofallah, A. Khaloo, Technoeconomic study of alkali-activated slag concrete with a focus on strength, CO_2 Emission, and material cost, J. Mater. Civ. Eng. 33 (2021) 1–12. https://doi.org/10.1061/(asce)mt.1943-5533.0003763.

[285] P. Van Den Heede, N. De Belie, Environmental impact and life cycle assessment (LCA) of traditional and ' green' concretes : Literature review and theoretical calculations, Cem. Concr. Compos. 34 (2012) 431–442. https://doi.org/10.1016/j.cemconcomp.2012.01.004.

[286] A.L. García, Nano-silica production at low temperatures from the dissolution of olivine: Synthesis, tailoring and modeling, Eindhoven University of Technology, Eindhoven, 2014. https://doi.org/10.6100/IR774494.

[287] F. Uddin, A. Shaikh, A. Hosan, Effect of nano silica on compressive strength and microstructures of high volume blast furnace slag and high volume blast furnace slag- fly ash blended pastes, Sustain. Mater. Technol. 17 (2019) e00111. https://doi.org/10.1016/j.susmat.2019.e00111.

[288] R.J. Myers, E. L'Hôpital, J.L. Provis, B. Lothenbach, Effect of temperature and aluminium on calcium (alumino)silicate hydrate chemistry under equilibrium conditions, Cem. Concr. Res. 68 (2015) 83–93. https://doi.org/10.1016/j.cemconres.2014.10.015.

[289] T.F. Sevelsted, J. Skibsted, Carbonation of C–S–H and C–A–S–H samples studied by ^{13}C, ^{27}Al and ^{29}Si MAS NMR spectroscopy, Cem. Concr. Res. 71 (2015) 56–65. https://doi.org/10.1016/j.cemconres.2015.01.019.

[290] X. Gao, Q.L. Yu, H.J.H. Brouwers, Reaction kinetics, gel character and strength of ambient temperature cured alkali activated slag-fly ash blends, Constr. Build. Mater. 80 (2015) 105–115. https://doi.org/10.1016/j.conbuildmat.2015.01.065.

[291] S. Chithiraputhiran, N. Neithalath, Isothermal reaction kinetics and temperature dependence of alkali activation of slag, fly ash and their blends, Constr. Build. Mater. 45 (2013) 233–242. https://doi.org/10.1016/j.conbuildmat.2013.03.061.

[292] Z. Shi, C. Shi, S. Wan, Z. Zhang, Effects of alkali dosage and silicate modulus on alkali-silica reaction in alkali-activated slag mortars, Cem. Concr. Res. 111 (2018) 104–115. https://doi.org/10.1016/J.CEMCONRES.2018.06.005.

[293] W. Zhang, X. Yao, T. Yang, Z. Zhang, Effect of calcined dolomite addition on sodium carbonate-activated slag cements with different curing methods, Adv. Cem. Res. 31 (2019) 370–381. https://doi.org/10.1680/jadcr.17.00204.

[294] M. Komljenoć, Z. Baščarević, V. Bradić, Mechanical and microstructural properties of alkali-activated fly ash geopolymers, J. Hazard. Mater. 181 (2010) 35–42. https://doi.org/10.1016/j.jhazmat.2010.04.064.

[295] M.T. Souza, L. Onghero, W.L. Repette, F. Raupp Pereira, A.P.N. de Oliveira, Sustainable cement with Al-anodizing waste: Evaluating reactivity and feasibility as a shrinkage-compensating admixture, J. Build. Eng. 30 (2020) 101233. https://doi.org/10.1016/j.jobe.2020.101233.

[296] A. Rungchet, P. Chindaprasirt, S. Wansom, K. Pimraksa, Hydrothermal synthesis of calcium sulfoaluminate e belite cement from industrial waste materials, J. Clean. Prod. 115 (2016) 273–283. https://doi.org/10.1016/j.jclepro.2015.12.068.

[297] E.B. da Costa, E.D. Rodríguez, S.A. Bernal, J.L. Provis, L.A. Gobbo, A.P. Kirchheim, Production and hydration of calcium sulfoaluminate-belite cements derived from aluminium anodising sludge, Constr. Build. Mater. 122 (2016) 373–383. https://doi.org/10.1016/j.conbuildmat.2016.06.022.

[298] O.M. Jensen, Thermodynamic limitation of self-desiccation, Cem. Concr. Res. 25 (1995) 157–164. https://doi.org/10.1016/0008-8846(94)00123-G.

[299] C. Ma, B. Chen, L. Chen, Effect of organic matter on strength development of self-compacting earth-based construction stabilized with cement-based composites, Constr. Build. Mater. 123 (2016) 414–423. https://doi.org/10.1016/j.conbuildmat.2016.07.018.

[300] X. Gao, Q.L. Yu, H.J.H. Brouwers, Assessing the porosity and shrinkage of alkali activated slag-fly ash composites designed applying a packing model, Constr. Build. Mater. 119 (2016) 175–184. https://doi.org/10.1016/j.conbuildmat.2016.05.026.

[301] X. Gao, Q.L. Yu, H.J.H. Brouwers, Properties of alkali activated slag-fly ash blends with limestone addition, Cem. Concr. Compos. 59 (2015) 119–128. https://doi.org/10.1016/j.cemconcomp.2015.01.007.

[302] T. Williamson, M.C.G. Juenger, The role of activating solution concentration on alkali – silica reaction in alkali-activated fly ash concrete, Cem. Concr. Res. 83 (2016) 124–130. https://doi.org/10.1016/j.cemconres.2016.02.008.

[303] A. Fernández-Jiménez, Á. Palomo, T. Vazquez, R. Vallepu, T. Terai, K. Ikeda, Alkaline activation of blends of metakaolin and calcium aluminate, J. Am. Ceram. Soc. 91 (2008) 1231–1236. https://doi.org/10.1111/j.1551-2916.2007.02002.x.

[304] Y. Luo, K.M. Klima, H.J.H. Brouwers, Q. Yu, Effects of ladle slag on Class F fly ash geopolymer : Reaction mechanism and high temperature behavior, Cem. Concr. Compos. 129 (2022) 104468. https://doi.org/10.1016/j.cemconcomp.2022.104468.

[305] E. Bernard, B. Lothenbach, D. Rentsch, I. Pochard, A. Dauzères, Formation of magnesium silicate hydrates (M-S-H), Phys. Chem. Earth. 99 (2017) 142–157. https://doi.org/10.1016/j.pce.2017.02.005.

[306] E. Deir, B.S. Gebregziabiher, S. Peethamparan, Influence of starting material on the early age hydration kinetics, microstructure and composition of binding gel in alkali activated binder systems, Cem. Concr. Compos. 48 (2014) 108–117. https://doi.org/10.1016/j.cemconcomp.2013.11.010.

[307] E. Najafi Kani, A. Allahverdi, J.L. Provis, Calorimetric study of geopolymer binders based on natural pozzolan, J. Therm. Anal. Calorim. 127 (2017) 2181–2190. https://doi.org/10.1007/s10973-016-5850-7.

[308] T. Luukkonen, H. Sreenivasan, Z. Abdollahnejad, J. Yliniemi, A. Kantola, V.V. Telkki, P. Kinnunen, M. Illikainen, Influence of sodium silicate powder silica modulus for mechanical and chemical properties of dry-mix alkali-activated slag mortar, Constr. Build. Mater. 233 (2020) 117354. https://doi.org/10.1016/j.conbuildmat.2019.117354.

[309] T. Schade, F. Bellmann, B. Middendorf, Quantitative analysis of C-(K)-A-S-H-amount and hydrotalcite phase content in finely ground highly alkali-activated slag/silica fume blended cementitious material, Cem. Concr. Res. 153 (2022) 106706. https://doi.org/10.1016/j.cemconres.2021.106706.

[310] P. Koilraj, Y. Kamura, K. Sasaki, Synergetic co-immobilization of SeO_4^{2-} and Sr^{2+} from aqueous solution onto multifunctional graphene oxide and carbon-dot based layered double hydroxide nanocomposites and their mechanistic investigation, J. Mater. Chem. A. 6 (2018) 10008–10018. https://doi.org/10.1039/c8ta01605d.

[311] H. Asiabi, Y. Yamini, M. Shamsayei, Highly selective and efficient removal of arsenic(V), chromium(VI) and selenium(VI) oxyanions by layered double hydroxide intercalated with zwitterionic glycine, J. Hazard. Mater. 339 (2017) 239–247. https://doi.org/10.1016/j.jhazmat.2017.06.042.

[312] N.D.M. Evans, Binding mechanisms of radionuclides to cement, Cem. Concr. Res. 38 (2008) 543–553. https://doi.org/10.1016/j.cemconres.2007.11.004.

[313] G. Qiao, D. Hou, W. Li, B. Yin, Y. Zhang, P. Wang, Molecular insights into migration of heavy metal ion in calcium silicate hydrate (CSH) surface and intra-CSH (Ca/Si = 1.3), Constr. Build. Mater. 365 (2023) 130097. https://doi.org/10.1016/j.conbuildmat.2022.130097.

[314] P. Rovnaník, P. Bayer, P. Rovnaníková, Characterization of alkali activated slag paste after exposure to high temperatures, Constr. Build. Mater. 47 (2013) 1479–1487. https://doi.org/10.1016/j.conbuildmat.2013.06.070.

[315] M. Criado, A. Palomo, A. Ferna, Alkali activation of fly ashes. Part 1: Effect of curing conditions on the carbonation of the reaction products, Fuel. 84 (2005) 2048–2054. https://doi.org/10.1016/j.fuel.2005.03.030.

[316] L. Fernandez, C. Alonso, A. Hidalgo, C. Andrade, The role of magnesium during the hydration of C_3S and C-S-H formation. Scanning electron microscopy and mid-infrared studies, Adv. Cem. Res. 17 (2005) 9–21. https://doi.org/10.1680/adcr.2005.17.1.9.

[317] J. Higl, D. Hinder, C. Rathgeber, B. Ramming, M. Lindén, Detailed in situ ATR-FTIR spectroscopy study of the early stages of C-S-H formation during hydration of monoclinic C_3S, Cem. Concr. Res. 142 (2021). https://doi.org/10.1016/j.cemconres.2021.106367.

[318] A. Vidmer, G. Sclauzero, A. Pasquarello, Infrared spectra of jennite and tobermorite from first-principles, Cem. Concr. Res. 60 (2014) 11–23. https://doi.org/10.1016/j.cemconres.2014.03.004.

[319] N.Y. Mostafa, A.A. Shaltout, H. Omar, S.A. Abo-El-Enein, Hydrothermal synthesis and characterization of aluminium and sulfate substituted 1.1 nm tobermorites, J. Alloys Compd. 467 (2009) 332–337. https://doi.org/10.1016/j.jallcom.2007.11.130.

[320] J. Partyka, M. Les, Raman and infrared spectroscopy study on structure and microstructure of glass – ceramic materials from SiO_2–Al_2O_3–Na_2O–K_2O–CaO system modified by variable molar ratio of SiO_2/Al_2O_3, Spectrochim. Acta Part A Mol. Biomol. Spectrosc. Biomol. Spectrosc. 152 (2016) 82–91. https://doi.org/10.1016/j.saa.2015.07.045.

[321] H.A. Abdel Gawwad, S. Abd El-Aleem, A.S. Ouda, Preparation and characterization of one-part non-Portland cement, Ceram. Int. 42 (2016) 220–228. https://doi.org/10.1016/j.ceramint.2015.08.096.

[322] R.J. Myers, E. L'Hôpital, J.L. Provis, B. Lothenbach, Effect of temperature and aluminium on calcium (alumino)silicate hydrate chemistry under equilibrium conditions, Cem. Concr. Res. 68 (2015) 83–93. https://doi.org/10.1016/j.cemconres.2014.10.015.

[323] J. Liu, N. Farzadnia, C. Shi, Microstructural and micromechanical characteristics of ultra-high performance concrete with superabsorbent polymer (SAP), Cem. Concr. Res. 149 (2021) 106560. https://doi.org/10.1016/j.cemconres.2021.106560.

[324] Soil Quality Decree, The Soil Quality Regulation, 2009. https://rwsenvironment.eu/subjects/soil/legislation-and/soil-quality-decree/.

[325] J. Zhang, J.L. Provis, D. Feng, J.S.J. Van Deventer, Geopolymers for immobilization of Cr^{6+}, Cd^{2+}, and Pb^{2+}, J. Hazard. Mater. 157 (2008) 587–598. https://doi.org/10.1016/j.jhazmat.2008.01.053.

[326] A. Palomo, M. Palacios, Alkali-activated cementitious materials: Alternative matrices for the immobilisation of hazardous wastes Part II. Stabilisation of chromium and lead, Cem. Concr. Res. 33 (2003) 289–295. https://doi.org/10.1016/S0008-8846(02)00964-X.

[327] J. Koplík, L. Kalina, The characterization of fixation of Ba, Pb, and Cu in alkali-activated fly ash/blast furnace slag matrix, Materials (Basel). 9 (2016) 533. https://doi.org/10.3390/ma9070533.

[328] F. Ziegler, A.M. Scheidegger, C.A. Johnson, R. Dähn, E. Wieland, Sorption mechanisms of zinc to calcium silicate hydrate: X-ray absorption fine structure (XAFS) investigation, Environ. Sci. Technol. 35 (2001) 4556–4561. https://doi.org/10.1021/es001768m.

[329] J. Tan, Z. Sierens, B. Vandevyvere, H. Dan, J. Li, Zinc oxide in alkali-activated slag (AAS): retardation mechanism, reaction kinetics and immobilization, Constr. Build. Mater. 371 (2023) 130739. https://doi.org/10.1016/j.conbuildmat.2023.130739.

[330] C.E. Tommaseo, M. Kersten, Aqueous solubility diagrams for cementitious waste stabilization systems. 3. Mechanism of zinc immobilizaton by calcium silicate hydrate, Environ. Sci. Technol. 36 (2002) 2919–2925. https://doi.org/10.1021/es0102484.

[331] I. Moulin, A. Masion, P.M. Bertsch, M.R. Wiesner, J. Bottero, F. Mosnier, C. Haehnel, X-ray absorption spectroscopy study of immobilization processes for heavy metals in calcium silicate hydrates. 2. zinc, Langmuir. 17 (2001) 3658–3665. https://doi.org/10.1021/la001302h.

[332] B. Li, S. Zhang, Q. Li, N. Li, B. Yuan, W. Chen, H.J.H. Brouwers, Q. Yu, Uptake of heavy metal ions in layered double hydroxides and applications in cementitious materials: Experimental evidence and first-principle study, Constr. Build. Mater. 222 (2019) 96–107. https://doi.org/10.1016/j.conbuildmat.2019.06.135.

[333] D. Wang, Q. Wang, S. Zhuang, J. Yang, Evaluation of alkali-activated blast furnace ferronickel slag as a cementitious material : Reaction mechanism , engineering properties and leaching behaviors, Constr. Build. Mater. 188 (2018) 860–873. https://doi.org/10.1016/j.conbuildmat.2018.08.182.

[334] W. Cui, X. Zhang, C.I. Pearce, M.H. Engelhard, H. Zhang, Y. Wang, S.M. Heald, S. Zheng, Y. Zhang, S.B. Clark, P. Li, Z. Wang, K.M. Rosso, Effect of Cr(III) Adsorption on the dissolution of boehmite nanoparticles in caustic solution, Environ. Sci. Technol. 54 (2020) 6375–6384. https://doi.org/10.1021/acs.est.9b07881.

[335] J. Li, M. Li, X. Yang, Y. Zhang, X. Liu, F. Liu, Morphology-controlled synthesis of boehmite with enhanced efficiency for the removal of aqueous Cr(VI) and nitrates, Nanotechnology. 30 (2019). https://doi.org/10.1088/1361-6528/aaff21.

[336] M. Izquierdo, X. Querol, Leaching behaviour of elements from coal combustion fly ash: An overview, Int. J. Coal Geol. 94 (2012) 54–66. https://doi.org/10.1016/j.coal.2011.10.006.

[337] Q. Alam, M.V.A. Florea, K. Schollbach, H.J.H. Brouwers, A two-stage treatment for Municipal Solid Waste Incineration (MSWI) bottom ash to remove agglomerated fine particles and leachable contaminants, Waste Manag. 67 (2020) 181–192. https://doi.org/10.1016/j.wasman.2017.05.029.

[338] T. Liu, S. Li, Y. Chen, H.J.H. Brouwers, Q. Yu, In-situ formation of layered double hydroxides in MgO – $NaAlO_2$-activated GGBS/ MSWI BA: Impact of Mg^{2+} on reaction mechanism and leaching behavior, Cem. Concr. Compos. 140 (2023) 105114. https://doi.org/10.1016/j.cemconcomp.2023.105114.

[339] W. Chen, X. Ling, Q. Li, B. Yuan, B. Li, H. Ma, Experimental evidence on formation of ulexite in sulfoaluminate cement paste mixed with high concentration borate solution and its retarding effects, Constr. Build. Mater. 215 (2019) 777–785. https://doi.org/10.1016/j.conbuildmat.2019.04.242.

[340] P. Rożek, M. Król, W. Mozgawa, Geopolymer-zeolite composites : A review, J. Clean. Prod. 230 (2019) 557–579. https://doi.org/10.1016/j.jclepro.2019.05.152.

[341] S. Qaidi, A. Yahia, B.A. Tayeh, H. Unis, R. Faraj, A. Mohammed, 3D printed geopolymer composites: A review, Mater. Today Sustain. 20 (2022) 100240. https://doi.org/10.1016/j.mtsust.2022.100240.

[342] K.U. Ambikakumari Sanalkumar, E.H. Yang, Self-cleaning performance of nano-TiO_2 modified metakaolin-based geopolymers, Cem. Concr. Compos. 115 (2021) 103847. https://doi.org/10.1016/j.cemconcomp.2020.103847.

[343] K. Kaya-Özkiper, A. Uzun, S. Soyer-Uzun, Red mud- and metakaolin-based geopolymers for adsorption and photocatalytic degradation of methylene blue: Towards self-cleaning construction materials, J. Clean. Prod. 288 (2021). https://doi.org/10.1016/j.jclepro.2020.125120.

[344] A. Strini, G. Roviello, L. Ricciotti, C. Ferone, F. Messina, L. Schiavi, D. Corsaro, R. Cioffi, TiO_2-based photocatalytic geopolymers for nitric oxide degradation, Materials (Basel). 9 (2016) 1–13. https://doi.org/10.3390/ma9070513.

[345] D. Zhao, Y. Gao, S. Nie, Z. Liu, F. Wang, P. Liu, S. Hu, Self-assembly of honeycomb-like calcium-aluminum-silicate-hydrate (C-A-S-H) on ceramsite sand and its application in photocatalysis, Chem. Eng. J. 344 (2018) 583–593. https://doi.org/10.1016/j.cej.2018.03.074.

[346] M. Nagao, K. Kobayashi, Y. Jin, I. Maruyama, T. Hibino, Ionic conductive and photocatalytic properties of cementitious materials: Calcium silicate hydrate and calcium aluminoferrite, J. Mater. Chem. A. 8 (2020) 15157–15166. https://doi.org/10.1039/d0ta04866f.

[347] A.F. Gualtieri, E. Marchi, E. Passaglia, Zeolite content and cation exchange capacity of zeolite-rich rocks, in: Porous Mater. Environ. Friendly Pocesses, 1999: pp. 707–713. https://doi.org/10.1016/s0167-2991(99)80277-8.

[348] P. Sturm, G.J.G. Gluth, S. Simon, H.J.H. Brouwers, H.C. Kühne, The effect of heat treatment on the mechanical and structural properties of one-part geopolymer-zeolite composites, Thermochim. Acta. 635 (2016) 41–58. https://doi.org/10.1016/j.tca.2016.04.015.

[349] G. Hu, J. Yang, X. Duan, R. Farnood, C. Yang, J. Yang, Recent developments and challenges in zeolite-based composite photocatalysts for environmental applications, Chem. Eng. J. 417 (2021) 129209. https://doi.org/10.1016/j.cej.2021.129209.

[350] P. Rożek, M. Król, W. Mozgawa, Geopolymer-zeolite composites: A review, J. Clean. Prod. 230 (2019) 557–579. https://doi.org/10.1016/j.jclepro.2019.05.152.

[351] L. Yang, F. Wang, D. Du, P. Liu, W. Zhang, S. Hu, Enhanced photocatalytic efficiency and long-term performance of TiO_2 in cementitious materials by activated zeolite fly ash bead carrier, Constr. Build. Mater. 126 (2016) 886–893. https://doi.org/10.1016/j.conbuildmat.2016.09.062.

[352] J. Luis, V. Lynch, H. Baykara, M. Cornejo, G. Soriano, N.A. Ulloa, Preparation , characterization , and determination of mechanical and thermal stability of natural zeolite-based foamed geopolymers, Constr. Build. Mater. 172 (2018) 448–456. https://doi.org/10.1016/j.conbuildmat.2018.03.253.

[353] N.A. Ulloa, H. Baykara, M.H. Cornejo, A. Rigail, C. Paredes, J. Luis, Application-oriented mix design optimization and characterization of zeolite-based geopolymer mortars, Constr. Build. Mater. 174 (2018) 138–149. https://doi.org/10.1016/j.conbuildmat.2018.04.101.

[354] E. Papa, V. Medri, S. Amari, J. Manaud, P. Benito, A. Vaccari, E. Landi, Zeolite-geopolymer composite materials: Production and characterization, J. Clean. Prod. 171 (2018) 76–84. https://doi.org/10.1016/j.jclepro.2017.09.270.

[355] Y. Liu, C. Yan, X. Qiu, D. Li, H. Wang, A. Alshameri, Preparation of faujasite block from fly ash-based geopolymer via in-situ hydrothermal method, J. Taiwan Inst. Chem. Eng. 59 (2016) 433–439. https://doi.org/10.1016/j.jtice.2015.07.012.

[356] J. Duan, J. Li, Z. Lu, One-step facile synthesis of bulk zeolite A through metakaolin-based geopolymer gels, J. Porous Mater. 22 (2015) 1519–1526. https://doi.org/10.1007/s10934-015-0034-6.

[357] H. Yan, C. Xue-min, L. Le-ping, L. Xing-dong, C. Jin-yu, The hydrothermal transformation of solid geopolymers into zeolites, Microporous Mesoporous Mater. 161 (2012) 187–192. https://doi.org/10.1016/j.micromeso.2012.05.039.

[358] R. Zouzelka, J. Rathousky, Photocatalytic abatement of NOx pollutants in the air using commercial functional coating with porous morphology, Appl. Catal. B Environ. 217 (2017) 466–476. https://doi.org/10.1016/j.apcatb.2017.06.009.

[359] Y. Sargam, K. Wang, A. Tsyrenova, F. Liu, S. Jiang, Effects of anionic and nonionic surfactants on the dispersion and stability of nanoSiO_2 in aqueous and cement pore solutions, Cem. Concr. Res. 144 (2021) 106417. https://doi.org/10.1016/j.cemconres.2021.106417.

[360] B.H. Mo, H. Zhu, X.M. Cui, Y. He, S.Y. Gong, Effect of curing temperature on geopolymerization of metakaolin-based geopolymers, Appl. Clay Sci. 99 (2014) 144–148. https://doi.org/10.1016/j.clay.2014.06.024.

[361] A. Castillo, M. Castellote, Characteristics and efficiency of photocatalytic cementitious materials: Type of binder, roughness and microstructure, Cem. Concr. Res. 71 (2015) 124–131. https://doi.org/10.1016/j.cemconres.2015.02.003.

[362] S. Chen, Y. Zhang, D. Yan, J. Jin, Y. Tian, Y. Liu, X. Qian, The influence of Si/Al ratio on sulfate durability of metakaolin-based geopolymer, Constr. Build. Mater. 265 (2020) 120735. https://doi.org/10.1016/j.conbuildmat.2020.120735.

[363] L. Hou, J. Li, Z. Lu, Effect of Na/Al on formation, structures and properties of metakaolin based Na-geopolymer, Constr. Build. Mater. 226 (2019) 250–258. https://doi.org/10.1016/j.conbuildmat.2019.07.171.

[364] J. Yuan, P. He, D. Jia, C. Yang, S. Yan, Effect of curing temperature and SiO_2/K_2O molar ratio on the performance of metakaolin-based geopolymers, Ceram. Int. 42 (2016) 16184–16190. https://doi.org/10.1016/j.ceramint.2016.07.139.

[365] J.L. Provis, G.C. Lukey, J.S.J. van Deventer, Do geopolymers actually contain nanocrystalline zeolites? A reexamination of existing results, Chem. Mater. 17 (2005) 3075–3085. https://doi.org/10.1021/cm050230i.

[366] J. Eun, P.J.M. Monteiro, S. Sun, S. Choi, S.M. Clark, The evolution of strength and crystalline phases for alkali-activated ground blast furnace slag and fly ash-based geopolymers, Cem. Concr. Res. 40 (2010) 189–196. https://doi.org/10.1016/j.cemconres.2009.10.010.

[367] A. Buchwald, H. Zellmann, C. Kaps, Condensation of aluminosilicate gels — model system for geopolymer binders, J. Non. Cryst. Solids. 357 (2011) 1376–1382. https://doi.org/10.1016/j.jnoncrysol.2010.12.036.

[368] J. Chen, S. Kou, C. Poon, Hydration and properties of nano-TiO_2 blended cement composites, Cem. Concr. Compos. 34 (2012) 642–649. https://doi.org/10.1016/j.cemconcomp.2012.02.009.

[369] B.Y. Lee, K.E. Kurtis, Influence of TiO_2 Nanoparticles on Early C_3S Hydration, J. Am. Ceram. Soc. 93 (2010) 3399–3405. https://doi.org/10.1111/j.1551-2916.2010.03868.x.

[370] M.D. Oleksiak, J.A. Soltis, M.T. Conato, R.L. Penn, J.D. Rimer, Nucleation of FAU and LTA zeolites from heterogeneous aluminosilicate precursors, Chem. Mater. 28 (2016) 4906–4916. https://doi.org/10.1021/acs.chemmater.6b01000.

[371] C.L. Schaffer, K.T. Thomson, Density functional theory investigation into structure and reactivity of prenucleation silica species, J. Phys. Chem. C. 112 (2008) 12653–12662. https://doi.org/10.1021/jp066534p.

[372] P. Duxson, J.L. Provis, G.C. Lukey, S.W. Mallicoat, W.M. Kriven, J.S.J. Van Deventer, Understanding the relationship between geopolymer composition, microstructure and mechanical properties, Colloids Surfaces A Physicochem. Eng. Asp. 269 (2005) 47–58. https://doi.org/10.1016/j.colsurfa.2005.06.060.

[373] T.B. Reed, D.W. Breck, Crystalline zeolites. II. Crystal structure of synthetic zeolite, type A, J. Am. Chem. Soc. 78 (1956) 5972–5977. https://doi.org/10.1021/ja01604a002.

[374] D.W. Breck, Zeolite molecular sieves: structure, chemistry, and use, Wiley, New York, 1973. https://cir.nii.ac.jp/crid/1130282269601488512.

[375] P. Kunecki, M. Wdowin, W. Franus, Synthesis of faujasite (FAU) and tschernichite (LTA) type zeolites as a potential direction of the development of lime Class C fly ash, Int. J. Miner. Process. 166 (2017) 69–78. https://doi.org/10.1016/j.minpro.2017.07.007.

[376] J.L. Provis, S.A. Bernal, Geopolymers and related alkali-activated materials, Annu. Rev. Mater. Res. 44 (2014) 299–327. https://doi.org/10.1146/annurev-matsci-070813-113515.

[377] C. Martins, G.M. Barbosa, A. Landesmann, M. Antonio, C. Nascimento, R. Sandra, V. Nascimento, Influence of the zeolite acidity on its synergistic action with a flame-retarding polymeric intumescent formulation, (2020) 619–630. https://doi.org/10.1007/s10853-019-04047-w.

[378] A. Kuhnt, W. Schwieger, Thermal stability studies of zeolites A and X synthesized from South African coal fly ash, (2015) 575–582. https://doi.org/10.1007/s11164-013-1211-3.

[379] P. Duxson, G.C. Lukey, J.S.J. Van Deventer, Physical evolution of Na-geopolymer derived from metakaolin up to 1000 ° C, J. Mater. Sci. 42 (2007) 3044–3054. https://doi.org/10.1007/s10853-006-0535-4.

[380] Y. Wang, Measurements and modeling of water adsorption isotherms of zeolite linde-type A crystals, Ind. Eng. Chem. Res. 59 (2020) 8304–8314. https://doi.org/10.1021/acs.iecr.9b06891.

[381] S. Park, M. Pour-ghaz, What is the role of water in the geopolymerization of metakaolin?, Constr. Build. Mater. 182 (2018) 360–370. https://doi.org/10.1016/j.conbuildmat.2018.06.073.

[382] R.M.Barrer, Hydrothermal chemistry of zeolites, Academic Press, London, 1982.

[383] I. Ozer, S. Soyer-uzun, Relations between the structural characteristics and compressive strength in metakaolin based geopolymers with different molar Si/Al ratios, Ceram. Int. 41 (2015) 10192–10198. https://doi.org/10.1016/j.ceramint.2015.04.125.

[384] E.A. Al, O. Firas, Photocatalytic activity of anatase titanium dioxide nanostructures prepared by reactive magnetron sputtering technique, Opt. Quantum Electron. 51 (2019) 1–11. https://doi.org/10.1007/s11082-018-1738-z.

[385] C.A. Rees, J.L. Provis, G.C. Lukey, J.S.J. van Deventer, Attenuated total reflectance fourier transform infrared analysis of fly ash geopolymer gel aging, Langmuir. 23 (2007) 8170–8179. https://doi.org/10.1021/la700713g.

[386] W. Kim, D. Choi, S. Kim, Sonochemical synthesis of zeolite a from metakaolinite in NaOH solution, Mater. Trans. 51 (2010) 1694–1698. https://doi.org/10.2320/matertrans.M2010191.

[387] E.M. Flanigen, H. Khatami, H.A. Szymanski, Infrared structural studies of zeolite frameworks, in: Mol. Sieve Zeolites-I, American Chemical Society, Washington, DC, 1974: pp. 201–229. https://doi.org/10.1021/ba-1971-0101.ch016.

[388] L. Heller-Kallai, I. Lapides, Reactions of kaolinites and metakaolinites with NaOH-comparison of different samples (Part 1), Appl. Clay Sci. 35 (2007) 99–107. https://doi.org/10.1016/j.clay.2006.06.006.

[389] L. Yang, A. Hakki, L. Zheng, M.R. Jones, F. Wang, D.E. Macphee, Photocatalytic concrete for NOx

abatement: Supported TiO_2 efficiencies and impacts, Cem. Concr. Res. 116 (2019) 57–64. https://doi.org/10.1016/j.cemconres.2018.11.002.

[390] J. Jiang, X. Dong, H. Wang, F. Wang, Y. Li, Z. Lu, Enhanced mechanical and photocatalytic performance of cement mortar reinforced by nano-TiO_2 hydrosol-coated sand, Cem. Concr. Compos. 137 (2023) 104906. https://doi.org/10.1016/j.cemconcomp.2022.104906.

[391] P.R. Jubu, F.K. Yam, V.M. Igba, K.P. Beh, Tauc-plot scale and extrapolation effect on bandgap estimation from UV–vis–NIR data – A case study of β-Ga_2O_3, J. Solid State Chem. 290 (2020) 121576. https://doi.org/10.1016/j.jssc.2020.121576.

[392] M. Kang, S.W. Kim, H.Y. Park, Optical properties of TiO_2 thin films with crystal structure, J. Phys. Chem. Solids. 123 (2018) 266–270. https://doi.org/10.1016/j.jpcs.2018.08.009.

[393] R. López, R. Gómez, Band-gap energy estimation from diffuse reflectance measurements on sol – gel and commercial TiO_2: a comparative study, J. Sol-Gel Sci. Technol. (2012) 1–7. https://doi.org/10.1007/s10971-011-2582-9.

[394] T. Huang, Z. Sun, Advances in multifunctional graphene-geopolymer composites, Constr. Build. Mater. 272 (2021) 121619. https://doi.org/10.1016/j.conbuildmat.2020.121619.

[395] I.P. Studenyak, M. V Kurik, M. Kranjc, On the Urbach rule in non-crystalline solids, J. Non. Cryst. Solids. 355 (2009) 54–57. https://doi.org/10.1016/j.jnoncrysol.2008.03.051.

[396] M. Vittoria, R. Paolini, M. Rossini, A. Basak, M. Zinzi, T. Poli, M. Pia, Long term self-cleaning and photocatalytic performance of anatase added mortars exposed to the urban environment, Constr. Build. Mater. 96 (2015) 270–278. https://doi.org/10.1016/j.conbuildmat.2015.08.028.

[397] M. Janus, J. Zatorska, A. Czy, K. Bubacz, E. Kusiak-nejman, A.W. Morawski, Self-cleaning properties of cement plates loaded with N,C-modified TiO_2 photocatalysts, Appl. Surf. Sci. 330 (2015) 200–206. https://doi.org/10.1016/j.apsusc.2014.12.113.

[398] B. Ruot, A. Plassais, L. Guillot, L. Bonafous, TiO_2-containing cement pastes and mortars : Measurements of the photocatalytic efficiency using a rhodamine B-based colourimetric test, 83 (2009) 1794–1801. https://doi.org/10.1016/j.solener.2009.05.017.

[399] M. Pérez-Nicolás, J. Balbuena, M. Cruz-Yusta, L. Sánchez, I. Navarro-Blasco, J.M. Fernández, J.I. Alvarez, Photocatalytic NOx abatement by calcium aluminate cements modified with TiO_2: Improved NO_2 conversion, Cem. Concr. Res. 70 (2015) 67–76. https://doi.org/10.1016/j.cemconres.2015.01.011.

[400] C.E. White, J.L. Provis, T. Proffen, J.S.J. van Deventer, The effects of temperature on the local structure of metakaolin-based geopolymer binder: A neutron pair distribution function investigation, J. Am. Ceram. Soc. 93 (2010) 3486–3492. https://doi.org/10.1111/j.1551-2916.2010.03906.x.

[401] F. Lolli, H. Manzano, J.L. Provis, M.C. Bignozzi, E. Masoero, Atomistic simulations of geopolymer models: The impact of disorder on structure and mechanics, ACS Appl. Mater. Interfaces. 10 (2018) 22809–22820. https://doi.org/10.1021/acsami.8b03873.

[402] K. Yang, C.E. White, Multiscale pore structure determination of cement paste via simulation and experiment: The case of alkali-activated metakaolin, Cem. Concr. Res. 137 (2020) 106212. https://doi.org/10.1016/j.cemconres.2020.106212.

[403] W. Li, H. Jin, H. Xie, D. Wang, E. Lei, Utilization of electrolytic manganese residue to synthesize zeolite A and zeolite X for Mn ions adsorption, J. Ind. Eng. Chem. 120 (2023) 147–158. https://doi.org/10.1016/j.jiec.2022.12.021.

[404] E. Erdogmus, M. Sutcu, S. Hossain, M. Bayram, A. Sarı, Effect of molding pressure and firing temperature on the properties of ceramics from natural zeolite, Constr. Build. Mater. 402 (2023) 132960. https://doi.org/10.1016/j.conbuildmat.2023.132960.

[405] A. Corma, H. Garcia, Zeolite-based photocatalysts, Chem. Commun. (2004) 1443–1459. https://doi.org/10.1039/B400147H.

[406] M.M. Khan, S.A. Ansari, D. Pradhan, M.O. Ansari, D.H. Han, J. Lee, M.H. Cho, Band gap engineered TiO_2 nanoparticles for visible light induced photoelectrochemical and photocatalytic studies, J. Mater. Che. 2 (2014) 637–644. https://doi.org/10.1039/c3ta14052k.

[407] B. Choudhury, A. Choudhury, Oxygen defect dependent variation of band gap, Urbach energy and luminescence property of anatase, anatase – rutile mixed phase and of rutile phases of TiO_2 nanoparticles,

Phys. E Low-Dimensional Syst. Nanostructures. 56 (2014) 364–371. https://doi.org/10.1016/j.physe.2013.10.014.

[408] Subaer, H. Fansuri, The formation and properties of Zeolite-A and Zeolite-X through geopolymerisation of metakaolin, Solid State Phenom. 273 (2018) 167–174. https://doi.org/10.4028/www.scientific.net/SSP.273.167.

[409] H.R. Rasouli, F. Golestani-fard, A.R. Mirhabibi, G.M. Nasab, K.J.D. Mackenzie, Fabrication and properties of microporous metakaolin-based geopolymer bodies with polylactic acid (PLA) fibers as pore generators, Ceram. Int. 41 (2015) 7872–7880. https://doi.org/10.1016/j.ceramint.2015.02.125.

[410] A. Hajimohammadi, J.S.J. Van Deventer, Solid reactant-based geopolymers from rice hull ash and sodium aluminate, Waste and Biomass Valorization. 8 (2017) 2131–2140. https://doi.org/10.1007/s12649-016-9735-6.

[411] A. Hajimohammadi, J.L. Provis, J.S.J. Van Deventer, The effect of silica availability on the mechanism of geopolymerisation, Cem. Concr. Res. 41 (2011) 210–216. https://doi.org/10.1016/j.cemconres.2011.02.001.

[412] L. Han, X. Wang, B. Wu, S. Zhu, J. Wang, Y. Zhang, In-situ synthesis of zeolite X in foam geopolymer as a CO2 adsorbent, J. Clean. Prod. 372 (2022) 133591. https://doi.org/10.1016/j.jclepro.2022.133591.

[413] Y. Liu, X. Yang, C. Yan, H. Wang, S. Zhou, Solvent-free synthesis of zeolite LTA monolith with hierarchically porous structure from metakaolin, Mater. Lett. 248 (2019) 28–31. https://doi.org/10.1016/j.matlet.2019.03.135.

[414] X. Yang, Y. Liu, C. Yan, G. Chen, Solvent-free preparation of hierarchical 4A zeolite monoliths: Role of experimental conditions, J. Cryst. Growth. 528 (2019) 125286. https://doi.org/10.1016/j.jcrysgro.2019.125286.

[415] Q. Su, Y. He, S. Yang, H. Wan, S. Chang, X. Cui, Synthesis of NaA-zeolite microspheres by conversion of geopolymer and their performance of Pb(II) removal, Appl. Clay Sci. 200 (2021) 105914. https://doi.org/10.1016/j.clay.2020.105914.

[416] J. Minkiewicz, W. Mozgawa, M. Kr, IR spectroscopy studies of zeolites in geopolymeric materials derived from kaolinite, J. Mol. Struct. 1126 (2016) 200–206. https://doi.org/10.1016/j.molstruc.2016.02.027.

[417] Q. Wan, F. Rao, S. Song, R.E. García, R.M. Estrella, C.L. Pati, Geopolymerization reaction , microstructure and simulation of metakaolin-based geopolymers at extended Si/Al ratios, Cem. Concr. Compos. 79 (2017) 45–52. https://doi.org/10.1016/j.cemconcomp.2017.01.014.

[418] F. Oshani, A. Allahverdi, A. Kargari, R. Norouzbeigi, Effect of preparation parameters on properties of metakaolin-based geopolymer activated by silica fume- sodium hydroxide alkaline blend, J. Build. Eng. 60 (2022) 104984. https://doi.org/10.1016/j.jobe.2022.104984.

[419] W. Li, P.N. Lemougna, K. Wang, Y. He, Z. Tong, X. Cui, Effect of vacuum dehydration on gel structure and properties of metakaolin-based geopolymers, Ceram. Int. 43 (2017) 14340–14346. https://doi.org/10.1016/j.ceramint.2017.07.190.

[420] W. Franco Santos, J.J. Botterweg, S. Chaves, K. Schollbach, S.R. Van Der Laan, H.J.H. Brouwers, Sodium oxalate activation of basic oxygen furnace slag for building materials, Resour. Conserv. Recycl. 198 (2023) 107174. https://doi.org/10.1016/j.resconrec.2023.107174.

[421] A. Cuesta, I. Santacruz, S.G. Sanfélix, F. Fauth, M.A.G. Aranda, A.G. De La Torre, Hydration of C_4AF in the presence of other phases: A synchrotron X-ray powder diffraction study, Constr. Build. Mater. 101 (2015) 818–827. https://doi.org/10.1016/j.conbuildmat.2015.10.114.

[422] B.Z. Dilnesa, E. Wieland, B. Lothenbach, R. Dähn, K.L. Scrivener, Fe-containing phases in hydrated cements, Cem. Concr. Res. 58 (2014) 45–55. https://doi.org/10.1016/j.cemconres.2013.12.012.

[423] N. Meller, C. Hall, A.C. Jupe, S.L. Colston, S.D.M. Jacques, J. Phipps, The paste hydration of brownmillerite with and without gypsum: a time resolved synchrotron diffraction study at 30, 70, 100 and 150 °C, J. Mater. Chem. 14 (2004) 428–435. https://doi.org/10.1039/B313215C.

[424] G. Zhang, Q. Ren, J. He, S. Jiang, X. Cheng, Y. Yu, S. Huang, C. Zhang, M. Zhou, New understanding of early hydration of C_4AF under surface vitrification, Powder Technol. 377 (2021) 372–378. https://doi.org/10.1016/j.powtec.2020.08.098.

[425] W. Kurdowski, Cement and Concrete Chemistry, Springer, Dordrecht, 2014. https://doi.org/10.1007/978-

94-007-7945-7.

[426] J. Pastor, A.M. Aparicio, A. Gutierrez-Maroto, A.J. Hernández, Effects of two chelating agents (EDTA and DTPA) on the autochthonous vegetation of a soil polluted with Cu, Zn and Cd, Sci. Total Environ. 378 (2007) 114–118. https://doi.org/10.1016/j.scitotenv.2007.01.022.

[427] V. Vallet, U. Wahlgren, I. Grenthe, Chelate effect and thermodynamics of metal complex formation in solution: A quantum chemical study, J. Am. Chem. Soc. 125 (2003) 14941–14950. https://doi.org/10.1021/ja036646j.

[428] T.D. Perry IV, O.W. Duckworth, T.A. Kendall, S.T. Martin, R. Mitchell, Chelating ligand alters the microscopic mechanism of mineral dissolution, J. Am. Chem. Soc. 127 (2005) 5744–5745. https://doi.org/10.1021/ja042737k.

[429] L. Chang, H. Liu, J. Wang, L. Song, Y. Wang, S. Cui, Effect of chelation via ethanol-diisopropanolamine on hydration of pure steel slag, Constr. Build. Mater. 357 (2022) 129372. https://doi.org/10.1016/j.conbuildmat.2022.129372.

[430] Y. Huang, H. Zheng, X. Hu, Y. Wu, X. Tang, Q. He, S. Peng, Enhanced selective adsorption of lead(II) from complex wastewater by DTPA functionalized chitosan-coated magnetic silica nanoparticles based on anion-synergism, J. Hazard. Mater. 422 (2022) 126856. https://doi.org/10.1016/j.jhazmat.2021.126856.

[431] A. Singh, Y.S. Shivay, Effects of green manures and zinc fertilizer sources on DTPA-extractable zinc in soil and zinc content in basmati rice plants at different growth stages, Pedosphere. 29 (2019) 504–515. https://doi.org/10.1016/S1002-0160(17)60442-9.

[432] X. Huang, F. Wang, S. Hu, Y. Lu, M. Rao, Y. Mu, Brownmillerite hydration in the presence of gypsum: The effect of Al/Fe ratio and sulfate ions, J. Am. Ceram. Soc. 102 (2019) 5545–5554. https://doi.org/10.1111/jace.16384.

[433] G. Le Saoût, V. Kocaba, K. Scrivener, Application of the Rietveld method to the analysis of anhydrous cement, Cem. Concr. Res. 41 (2011) 133–148. https://doi.org/10.1016/j.cemconres.2010.10.003.

[434] A.A. Coelho, TOPAS and TOPAS-Academic: An optimization program integrating computer algebra and crystallographic objects written in C++, J. Appl. Crystallogr. 51 (2018) 210–218. https://doi.org/10.1107/S1600576718000183.

[435] K. Schollbach, S.R. van der Laan, Microstructure analysis with quantitative phase mapping using SEM-EDS and Phase Recognition and Characterization (PARC) Software: applied to steelmaking slag, in: H. Pöllmann (Ed.), Charact. Modif. Appl. Residues, De Gruyter, Berlin, Boston, 2021: pp. 57–96. https://doi.org/doi:10.1515/9783110674941-003.

[436] J.C.O. Zepper, S.R. van der Laan, K. Schollbach, H.J.H. Brouwers, A Bogue approach applied to basic oxygen furnace slag, Cem. Concr. Res. 175 (2024) 107344. https://doi.org/10.1016/j.cemconres.2023.107344.

[437] B. Lothenbach, D.A. Kulik, T. Matschei, M. Balonis, L. Baquerizo, B. Dilnesa, G.D. Miron, R.J. Myers, Cemdata18: A chemical thermodynamic database for hydrated Portland cements and alkali-activated materials, Cem. Concr. Res. 115 (2019) 472–506. https://doi.org/10.1016/j.cemconres.2018.04.018.

[438] M.J. Ahmed, K. Lambrechts, X. Ling, K. Schollbach, H.J.H. Brouwers, Effect of hydroxide, carbonate, and sulphate anions on the β-dicalcium silicate hydration rate, Cem. Concr. Res. 173 (2023) 107302. https://doi.org/10.1016/j.cemconres.2023.107302.

[439] Y. Gao, J. Wu, Z. Zhang, R. Jin, X. Zhang, X. Yan, A. Umar, Z. Guo, Q. Wang, Synthesis of polypropylene/Mg_3Al-X (X = CO_3^{2-}, NO_3^-, Cl^-, SO_4^{2-}) LDH nanocomposites using a solvent mixing method: Thermal and melt rheological properties, J. Mater. Chem. A. 1 (2013) 9928–9934. https://doi.org/10.1039/c3ta11695f.

[440] L. Alarcon-Ruiz, G. Platret, E. Massieu, A. Ehrlacher, The use of thermal analysis in assessing the effect of temperature on a cement paste, Cem. Concr. Res. 35 (2005) 609–613. https://doi.org/10.1016/j.cemconres.2004.06.015.

[441] S. Krishnan, F. Zunino, S. Bishnoi, K. Scrivener, Characterisation and hydration kinetics of β-C_2S synthesised with K_2SO_4 as dopant, Cem. Concr. Res. 167 (2023). https://doi.org/10.1016/j.cemconres.2023.107119.

[442] A. Ismailov, N. Merilaita, S. Solismaa, M. Karhu, E. Levänen, Utilizing mixed-mineralogy ferroan magnesite tailings as the source of magnesium oxide in magnesium potassium phosphate cement, Constr.

Build. Mater. 231 (2020) 117098. https://doi.org/10.1016/j.conbuildmat.2019.117098.

[443] R. Zhang, Z. Liu, J. Yu, Exploring microfine magnesite based on thermal decomposition and sintering kinetics: A new direction in the one-step preparation of high-density sintered magnesia, Ceram. Int. 50 (2024) 29108–29119. https://doi.org/10.1016/j.ceramint.2024.05.136.

[444] W. Franco Santos, K. Schollbach, S. Melzer, S.R. van der Laan, H.J.H. Brouwers, Quantitative analysis and phase assemblage of basic oxygen furnace slag hydration, J. Hazard. Mater. 450 (2023) 131029. https://doi.org/10.1016/j.jhazmat.2023.131029.

[445] J.S. Andrade Neto, E.D. Rodríguez, P.J.M. Monteiro, A.G. De la Torre, A.P. Kirchheim, Hydration of C_3S and Al-doped C_3S in the presence of gypsum, Cem. Concr. Res. 152 (2022). https://doi.org/10.1016/j.cemconres.2021.106686.

[446] G. Möschner, B. Lothenbach, F. Winnefeld, A. Ulrich, R. Figi, R. Kretzschmar, Solid solution between Al-ettringite and Fe-ettringite ($Ca_6[Al_{1-x}Fe_x(OH)_6]_2(SO_4)_3 \cdot 26H_2O$), Cem. Concr. Res. 39 (2009) 482–489. https://doi.org/10.1016/j.cemconres.2009.03.001.

[447] G. Möschner, B. Lothenbach, J. Rose, A. Ulrich, R. Figi, R. Kretzschmar, Solubility of Fe-ettringite ($Ca_6[Fe(OH)_6]_2(SO_4)_3 \cdot 26H_2O$), Geochim. Cosmochim. Acta. 72 (2008) 1–18. https://doi.org/10.1016/j.gca.2007.09.035.

[448] J. Spooren, E. Kim, L. Horckmans, K. Broos, P. Nielsen, M. Quaghebeur, In-situ chromium and vanadium recovery of landfilled ferrochromium and stainless steel slags, Chem. Eng. J. 303 (2016) 359–368. https://doi.org/10.1016/j.cej.2016.05.128.

[449] S. Neuhold, A. van Zomeren, J.J. Dijkstra, H.A. van der Sloot, P. Drissen, D. Algermissen, D. Mudersbach, S. Schüler, T. Griessacher, J.G. Raith, R. Pomberger, D. Vollprecht, Investigation of possible leaching control mechanisms for chromium and vanadium in electric arc furnace (EAF) slags using combined experimental and modeling approaches, Minerals. 9 (2019) 1–19. https://doi.org/10.3390/min9090525.

[450] I. Reijonen, H. Hartikainen, Risk assessment of the utilization of basic oxygen furnace slag (BOFS) as soil liming material: Oxidation risk and the chemical bioavailability of chromium species, Environ. Technol. Innov. 11 (2018) 358–370. https://doi.org/10.1016/j.eti.2018.05.004.

[451] S. Peysson, J. Péra, M. Chabannet, Immobilization of heavy metals by calcium sulfoaluminate cement, Cem. Concr. Res. 35 (2005) 2261–2270. https://doi.org/10.1016/j.cemconres.2005.03.015.

[452] J.L. Milagres, C.R. Bellato, S.O. Ferreira, L. de M. Guimarães, G.J. Gabriel, A. Bolandini, Simultaneous removal process of divalent metal and anionic and cationic dyes by layered reconstruction with hydrocalumite intercalated with dodecyl sulfate, Colloids Surfaces A Physicochem. Eng. Asp. 582 (2019) 123890. https://doi.org/10.1016/j.colsurfa.2019.123890.

[453] A. Baldermann, V. Preissegger, S. Šimić, I. Letofsky-Papst, F. Mittermayr, M. Dietzel, Uptake of aqueous heavy metal ions (Co^{2+}, Cu^{2+} and Zn^{2+}) by calcium-aluminium-silicate-hydrate gels, Cem. Concr. Res. 147 (2021) 106521. https://doi.org/10.1016/j.cemconres.2021.106521.

[454] S. Paikaray, M.J. Hendry, J. Essilfie-Dughan, Controls on arsenate, molybdate, and selenate uptake by hydrotalcite-like layered double hydroxides, Chem. Geol. 345 (2013) 130–138. https://doi.org/10.1016/j.chemgeo.2013.02.015.

[455] K. Piekkari, K. Ohenoja, V. Isteri, P. Tanskanen, M. Illikainen, Immobilization of heavy metals, selenate, and sulfate from a hazardous industrial side stream by using calcium sulfoaluminate-belite cement, J. Clean. Prod. 258 (2020) 120560. https://doi.org/10.1016/j.jclepro.2020.120560.

[456] H.J.H. Brouwers, A hydration model of Portland Cement using the work of Powers and Brownyard, Eindhoven University of Technology, 2011.

[457] T. Zhang, P. Gao, R. Luo, Y. Guo, J. Wei, Q. Yu, Measurement of chemical shrinkage of cement paste: Comparison study of ASTM C 1608 and an improved method, Constr. Build. Mater. 48 (2013) 662–669. https://doi.org/10.1016/j.conbuildmat.2013.07.086.

[458] W. Chen, Hydration of slag cement. Theory, Modelling and Application, Ph.D Thesis, University of Twente, 2007.

[459] F. Avet, K. Scrivener, Effect of temperature on the water content of C-A-S-H in plain Portland and blended cements, Cem. Concr. Res. 136 (2020) 106124. https://doi.org/10.1016/j.cemconres.2020.106124.

[460] P. Juilland, E. Gallucci, R. Flatt, K. Scrivener, Dissolution theory applied to the induction period in alite

hydration, Cem. Concr. Res. 40 (2010) 831–844. https://doi.org/10.1016/j.cemconres.2010.01.012.

[461] M.P. Keradeh, S.A. Tabatabaei-Nezhad, A comprehensive evaluation of the effect of key parameters on the performance of DTPA chelating agent in modifying sandstone surface charge, Heliyon. 9 (2023) e21990. https://doi.org/10.1016/j.heliyon.2023.e21990.

[462] I. Novak, Geometrical description of chemical equilibrium and Le Châtelier's principle: Two-component systems, J. Chem. Educ. 95 (2018) 84–87. https://doi.org/10.1021/acs.jchemed.7b00665.

[463] W. Franco Santos, K. Schollbach, S. Melzer, S.R. van der Laan, H.J.H. Brouwers, Quantitative analysis and phase assemblage of basic oxygen furnace slag hydration, J. Hazard. Mater. 450 (2023) 131029. https://doi.org/10.1016/j.jhazmat.2023.131029.

[464] H. Majdoubi, R. Makhlouf, Y. Haddaji, M. Nadi, S. Mansouri, N. Semllal, M. Oumam, B. Manoun, J. Alami, H. Hannache, Y. Tamraoui, Valorization of phosphogypsum waste through acid geopolymer technology: synthesis, characterization, and environmental assessment, Constr. Build. Mater. 371 (2023) 130710. https://doi.org/10.1016/j.conbuildmat.2023.130710.

[465] W. Luo, B. Li, G. Yang, M. Xu, C. Pang, K.W. Kow, T. Wu, Utilisation of electrolytic manganese residue as a sulphate activator in producing concrete blocks with high-volume fly ash, J. Clean. Prod. 434 (2024). https://doi.org/10.1016/j.jclepro.2023.139813.

[466] L. Xia, S. Cao, Q. Li, X. Lu, Z. Liu, Co-treatment of copper smelting slag and gypsum residue for valuable metals and sulfur recovery, Resour. Conserv. Recycl. 183 (2022) 106360. https://doi.org/10.1016/j.resconrec.2022.106360.

[467] T. Zhang, J. Han, W. Liu, F. Jiao, W. Jia, W. Qin, Recovery of zinc and extraction of calcium and sulfur from zinc-rich gypsum residue by selective reduction roasting combined with hydrolysis, J. Environ. Manage. 331 (2023) 117256. https://doi.org/10.1016/j.jenvman.2023.117256.

Appendix A

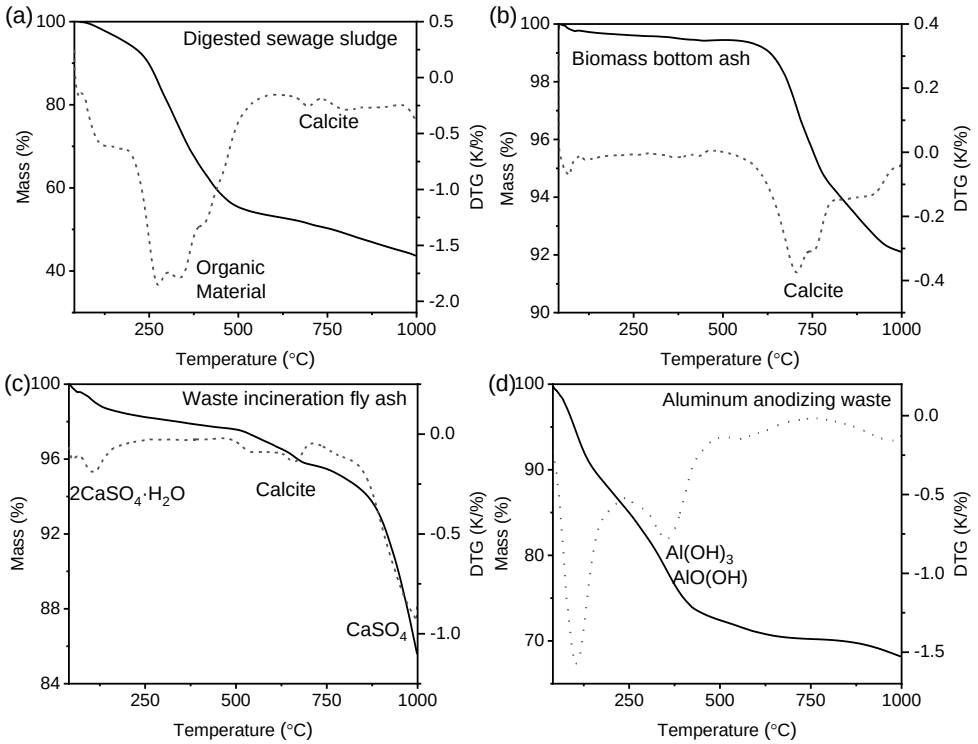

Fig. A.1: TG and DTG curves of the raw (a) digested sewage sludge, (b) biomass bottom ash, (c) waste incineration fly ash and (d) aluminum anodizing waste.

Table A.1: The leaching behavior of the raw materials.

Raw materials (mg/kg)	DSS	WIFA	BBA	AAW
Chloride	830	1920	1540	3490
Sulphate	2120	29320	12140	69910
Nitrate	7.90	103	8.6	-
As	2.65	0.16	0.07	0.04
Ni	3.85	0.50	-	-
Pb	4.25	0.34	10.46	0.12
Zn	1.75	2.94	16.28	0.02
Ba	0.15	0.55	3.22	0.05
Co	0.55	0.08	-	-
Cr	0.20	0.10	6.48	0.79
Cu	1.20	5.87	0.02	0.05
Mo	1.70	0.52	0.86	0.17
Sb	0.20	0.10	0.04	0.04
B	3.10	3.84	0.87	45250
Fe	38.4	0.62	-	-
Mg	486.8	287.2	0.17	13.28
Mn	0.70	5.41	-	0.04
Sr	1.95	50.81	32.1	0.73
NH_4^+	1500	-	-	-
Na^+	960	2870	1710	41280
K^+	540	280	3390	24
Ca^{2+}	460	12480	12760	133

Appendix B

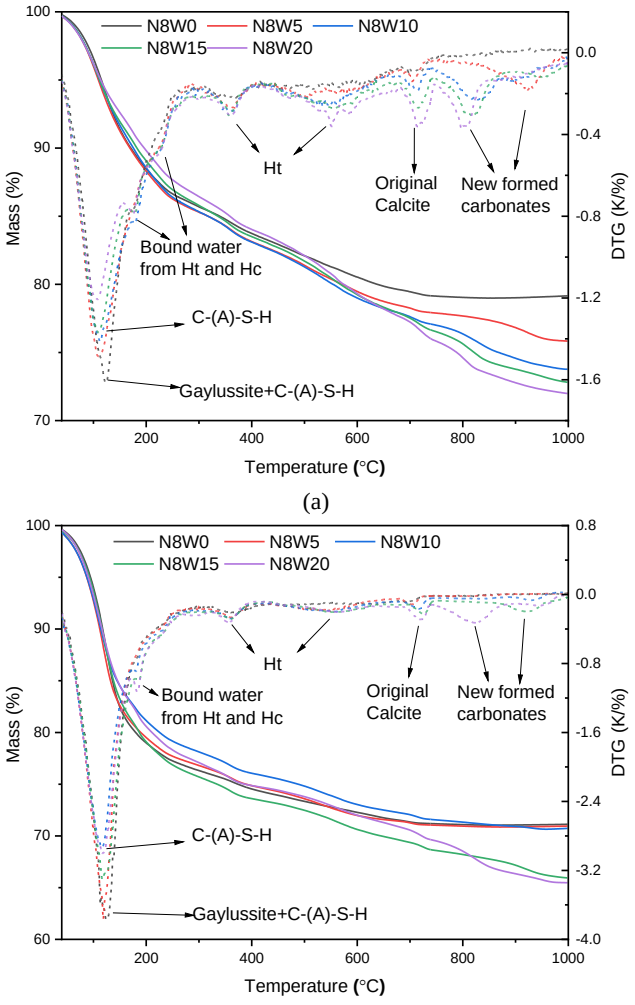

Fig. B.1: TG-DTG curves of reaction products with different WIFD replacement in N8W0-N8W20: (a) 28 d (b) 91 d (Ht-Hydrotalcite, Hc-Hemicarboaluminate).

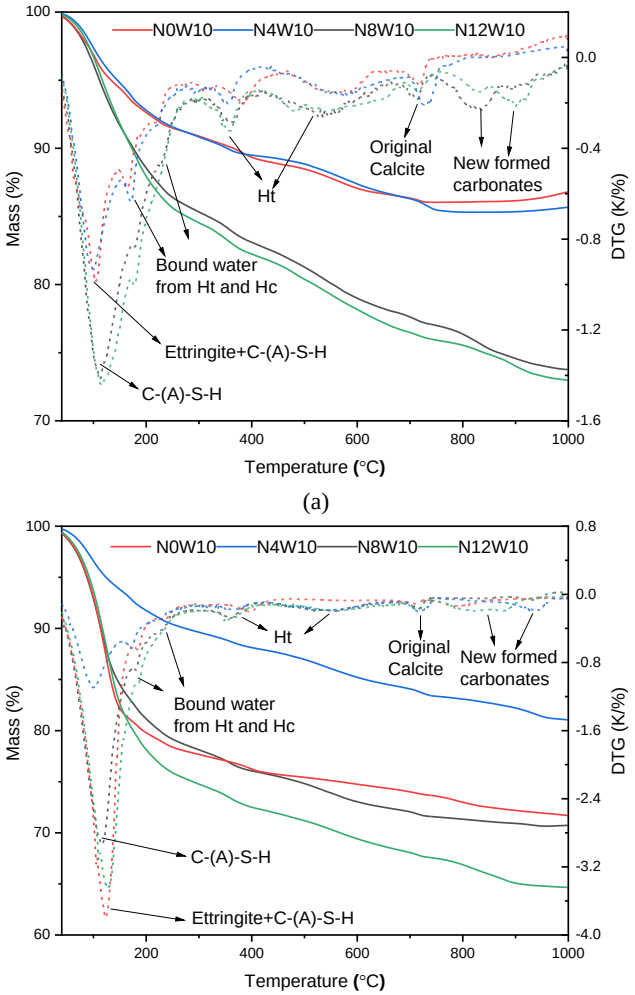

(a)

(b)

Fig. B.2: TG-DTG curves of reaction products with different amounts of additional Na_2CO_3 in N0W10-N12W10: (a) 28 d (b) 91 d (Ht-Hydrotalcite, Hc-Hemicarboaluminate).

Appendix C

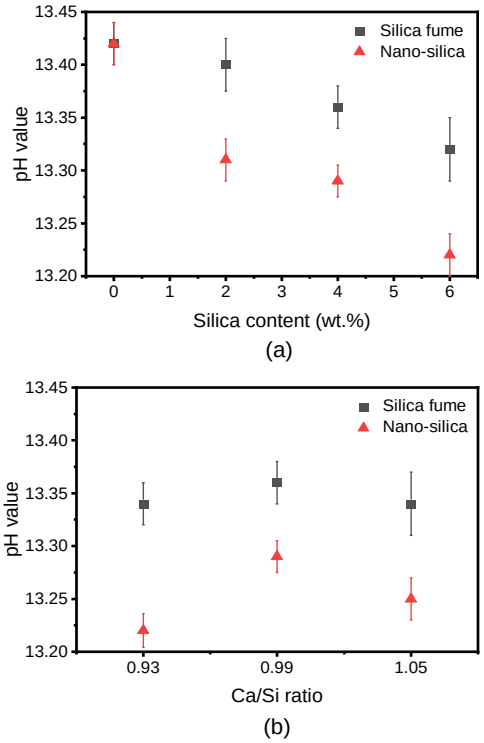

Fig. C.1: Initial pH values of the fresh paste with different (a) silica content and (b) starting Ca/Si ratio.

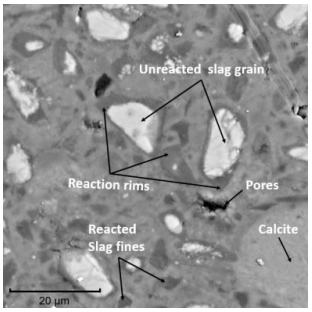

Fig. C.2: A typical BSE image of sodium carbonate-activated slag from the 28d sample Ref.

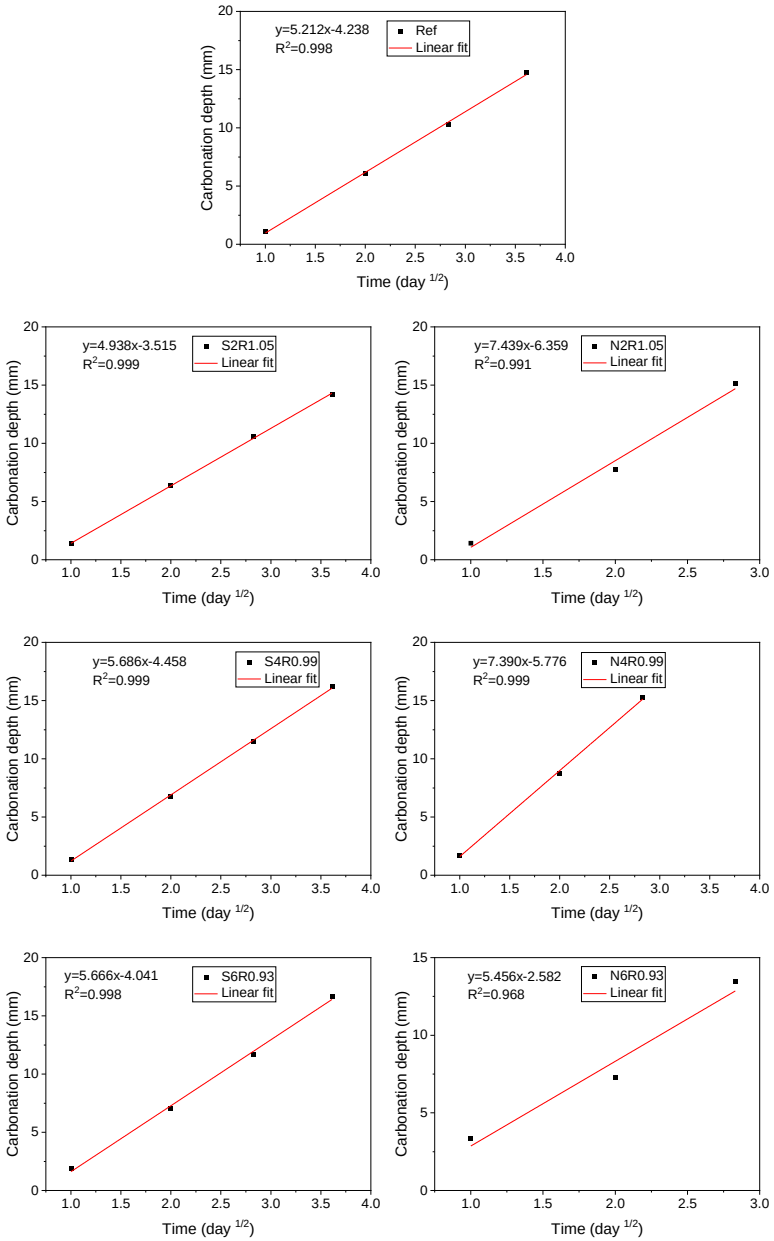

Fig. C.3: The fitting of accelerated carbonation rate in each mixture based on the carbonation depth (Figure continued on next page).

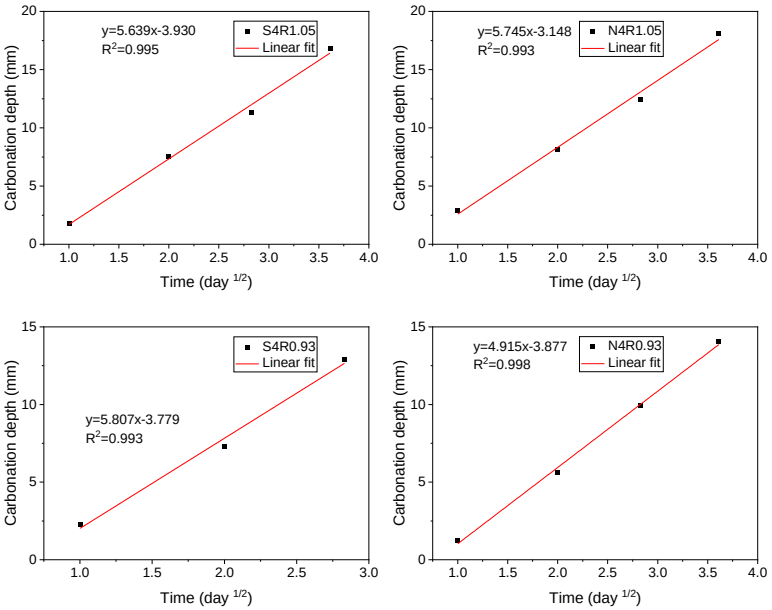

Fig. C.3: (continued).

Table C.1: The used CO_2 emission of raw ingredients and the formulation of different binders, including sodium silicate-activated GGBFS-CFA blended binder [134], sodium silicate and sodium hydroxide-activated CFA materials [278], Portland cement materials [279] and the sodium carbonate-WIFD activated GGBFS materials form this work (* an exchange rate 0.92 of $ to € was applied).

Raw materials		GGBFS	CFA	CEM I	SC	SH	SS	SF	NS	Water	FA	CA	WIFD
CO_2 emissions ($kg{\cdot}CO_2/t$)		143 [280]	27 [280]	820 [281]	110 [282]	1915 [134]	1514 [134]	14 [283]	461 [134]	0.2 [284]	13.9 [281]	45.9 [281]	
Market Price* (euro/t)		40 [285]	20 [285]	104 [284]	98 [59]	94 [284]	364 [284]	237 [283]	941 [286]	0.6 [284]	17 [284]	20 [284]	
Formulation of different binders from literature (kg/m^3)	[134]	315	135			21	28			160	800	1000	
	[134]	315	135			29			21.87	160	800	1000	
	[278]		408			41	103			26	647	1202	
	[279]			340						170	1878		
Formulation from this study (kg/m^3)	S4R0.99	389			27			18		270	800	1000	43
	N4R0.99	389			27				18	270	800	1000	43

Note: GGBFS – ground granulated blast furnace slag, CFA – coal fly ash, CEM I – Cement I 42.5 N, SC – sodium carbonate, SH – sodium hydroxide, SS – sodium silicate, SF – silica fume, NS – nano-silica, FA – fine aggregate, CA – coarser aggregate, WIFD – waste incineration filter dust.

Appendix D

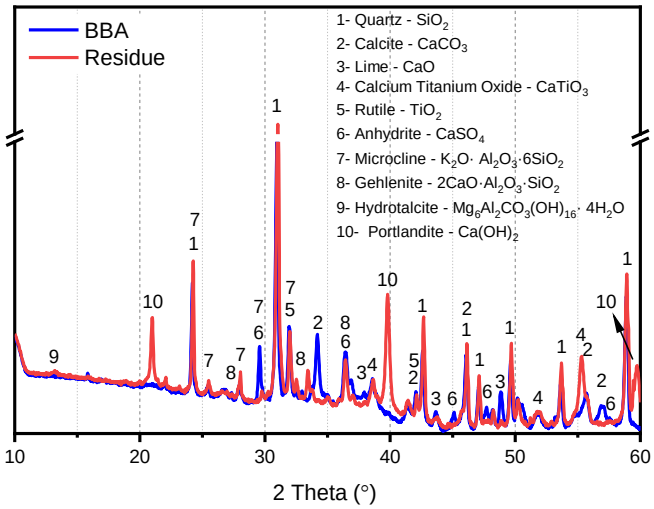

Fig. D.1: XRD pattern of the BBA and the residue BBA after 24 h reactive test in 8 M NaOH solution. (Legend: 1- Quartz, 2- Calcite, 3- Lime, 4- Calcium titanium oxide, 5- Rutile, 6- Anhydrite, 7- Microcline, 8- Gehlenite, 9- Hydrotalcite, 10- Portlandite).

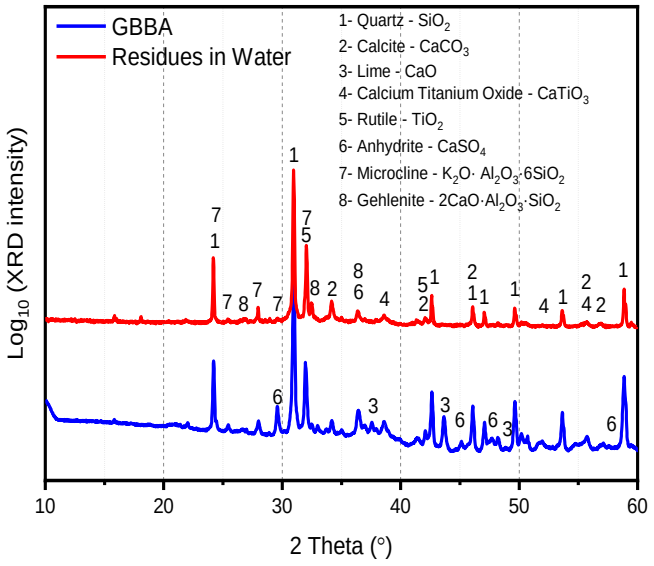

Fig. D.2: XRD pattern of the raw GBBA and the residue GBBA after the dissolution in distilled water. (Legend: 1- Quartz, 2- Calcite, 3- Lime, 4- Calcium titanium oxide, 5- Rutile, 6- Anhydrite, 7- Microcline, 8- Gehlenite).

Table D.1:Minerals data used in this work for the XRD analysis.

Mineral compound	#PDF-reference	ICSD
Calcite $CaCO_3$	01-072-1937	020179
Hydrotalcite $Mg_6Al_2CO_3(OH)_{16}$ $4H_2O$	01-089-0460	081963
Portlandite $Ca(OH)_2$	01-084-1271	202228
Quartz SiO_2	01-070-2517	041447
Gehlenite $Ca_2Al(AlSi)O_7$	01-089-5917	087144
Anhydrite $CaSO_4$	01-072-0916	016382
Microcline $K_2O{\cdot}Al_2O_3{\cdot}_6SiO_2$	01-087-1788	083532
Rutile TiO_2	01-077-0442	039168
Mullite $Al_{4.8}O_{9.6}Si_{1.2}$	01-079-1275	066263
Calcium titanium oxide $CaTiO_3$	01-076-2400	037263
Lime CaO	01-077-2010	060199
Sodium titanium silicate hydrate Na_4 $(TiO)_4$ $(SiO_4)_3{\cdot}6H_2O$	01-088-0703	085003
Hatrurite Ca_3SiO_5	01-086-0402	081100
Thenardite Na_2SO_4	01-070-1541	002895
Boehmite AlO(OH)	01-072-0359	015696
Bayerite $Al(OH)_3$	01-074-1119	026830

Table D.2: The chemical composition of the GBBA and residue GBBA after the dissolution in distilled water.

Oxide (%)	MgO	Al_2O_3	SiO_2	P_2O_5	SO_3	K_2O	CaO	TiO_2	Fe_2O_3	Others	Mass (g)
GBBA	2.5	7.5	49.6	1.2	2.6	2.1	17.1	3.2	2.6	4.3	20.0
Residue	2.3	7.6	49.9	1.2	0.6	1.6	14.2	3.3	2.7	4.4	18.9
Change	0.2	-0.1	-0.3	0.0	2.0	0.5	2.9	-0.1	-0.1	-0.1	

Note: all the chemical composition of the residue GBBA is normalized with the unreacted GBBA. The relatively low presence of negative numbers in changes can be attributed to sampling deviations.

Appendix E

Equation	y = a + b*x
Plot	RAr-7d
Weight	No Weighting
Intercept	-5.10462 ± 0.01906
Slope	1.09567 ± 0.00728
Residual Sum of Squares	0.00144
Pearson's r	0.99914
R-Square (COD)	0.99828
Adj. R-Square	0.99824

Equation	y = a + b*x
Plot	RA1.0-7d
Weight	No Weighting
Intercept	-5.25746 ± 0.02601
Slope	1.20623 ± 0.00994
Residual Sum of Squares	0.00268
Pearson's r	0.99868
R-Square (COD)	0.99736
Adj. R-Square	0.99729

Equation	y = a + b*x
Plot	RA1.2-7d
Weight	No Weighting
Intercept	-5.54712 ± 0.01717
Slope	1.18288 ± 0.00656
Residual Sum of Squares	0.00117
Pearson's r	0.9994
R-Square (COD)	0.9988
Adj. R-Square	0.99877

Equation	y = a + b*x
Plot	RHr-7d
Weight	No Weighting
Intercept	-4.83809 ± 0.01898
Slope	1.07946 ± 0.00725
Residual Sum of Squares	0.00143
Pearson's r	0.99912
R-Square (COD)	0.99824
Adj. R-Square	0.9982

Equation	y = a + b*x
Plot	RH1.0-7d
Weight	No Weighting
Intercept	-5.25961 ± 0.0262
Slope	1.16851 ± 0.01001
Residual Sum of Squares	0.00272
Pearson's r	0.99857
R-Square (COD)	0.99715
Adj. R-Square	0.99707

Equation	y = a + b*x
Plot	RH1.2-7d
Weight	No Weighting
Intercept	-5.39768 ± 0.01805
Slope	1.10078 ± 0.0069
Residual Sum of Squares	0.00129
Pearson's r	0.99924
R-Square (COD)	0.99847
Adj. R-Square	0.99843

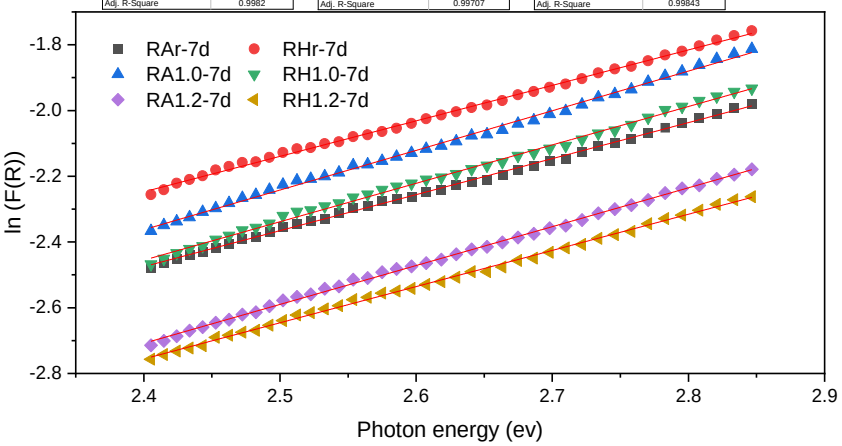

(a)

Equation	y = a + b*x
Plot	RAr-28d
Weight	No Weighting
Intercept	-4.99497 ± 0.06831
Slope	1.33126 ± 0.02612
Residual Sum of Squares	0.30733
Pearson's r	0.97022
R-Square (COD)	0.94132
Adj. R-Square	0.94096

Equation	y = a + b*x
Plot	RA1.0-28d
Weight	No Weighting
Intercept	-5.38724 ± 0.07384
Slope	1.29518 ± 0.02823
Residual Sum of Squares	0.35906
Pearson's r	0.96361
R-Square (COD)	0.92855
Adj. R-Square	0.92811

Equation	y = a + b*x
Plot	RA1.2-28d
Weight	No Weighting
Intercept	-5.97322 ± 0.09733
Slope	1.44605 ± 0.03721
Residual Sum of Squares	0.62389
Pearson's r	0.95033
R-Square (COD)	0.90313
Adj. R-Square	0.90253

Equation	y = a + b*x
Plot	RHr-28d
Weight	No Weighting
Intercept	-4.35522 ± 0.05772
Slope	1.17822 ± 0.02206
Residual Sum of Squares	0.2194
Pearson's r	0.97275
R-Square (COD)	0.94624
Adj. R-Square	0.94591

Equation	y = a + b*x
Plot	RH1.0-28d
Weight	No Weighting
Intercept	-5.38485 ± 0.07068
Slope	1.27507 ± 0.02702
Residual Sum of Squares	0.32898
Pearson's r	0.96892
R-Square (COD)	0.9388
Adj. R-Square	0.93842

Equation	y = a + b*x
Plot	RH1.2-28d
Weight	No Weighting
Intercept	-5.65758 ± 0.10097
Slope	1.35311 ± 0.0386
Residual Sum of Squares	0.67141
Pearson's r	0.93996
R-Square (COD)	0.88352
Adj. R-Square	0.88281

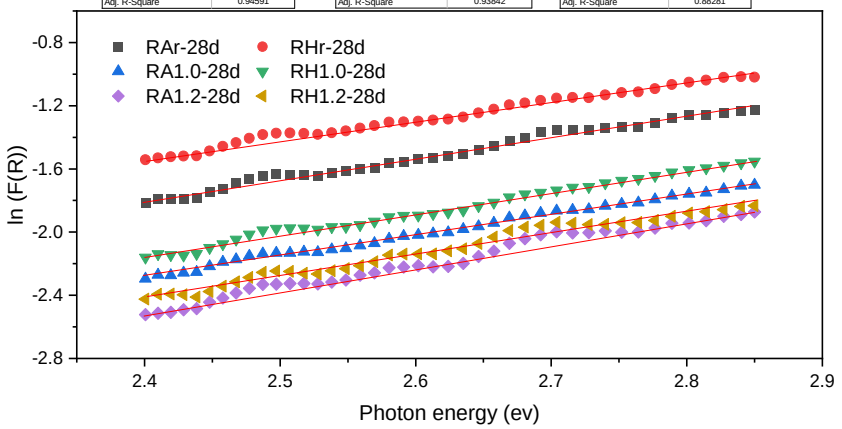

(b)

Fig. E.1: The determination of Urbach energy of the (a) 7d and (b) 28d RAr, RHr, RA1.0, RH1.0, RA1.2, and RH1.2 by linear fitting.

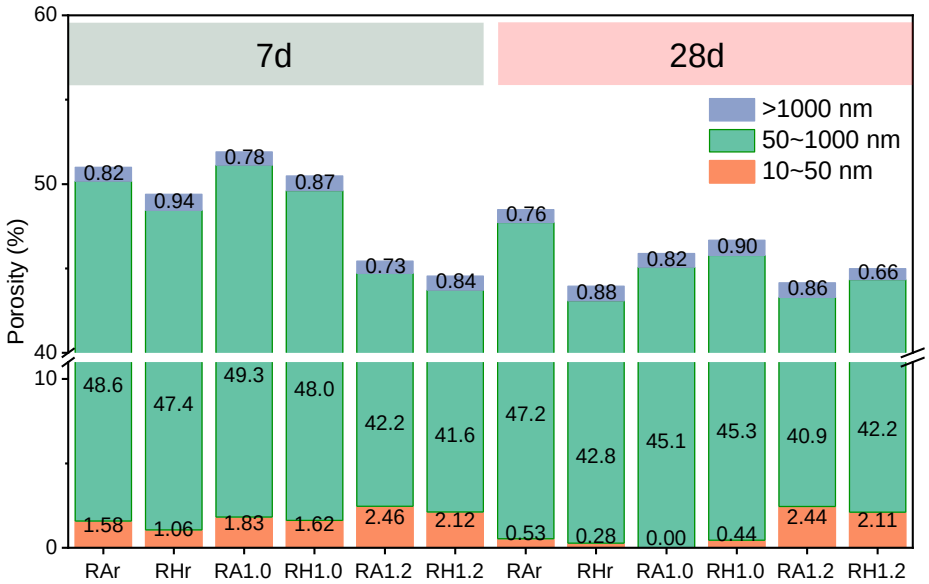

Fig. E.2: The porosity of each type of pores in the 7d and 28d geopolymers RAr, RHr, RA1.0, RH1.0, RA1.2 and RH1.2 (Note: no pores <10 nm are detected in all pastes according to MIP analysis).

List of abbreviations

AAMs	Alkali-activated materials
AFm	Alumina-ferric oxide-mono Phase
AFt	Alumina-ferric oxide-tri Phase
APC	Air pollution control
AAW	Aluminum anodizing waste
BA	Bottom ash
BBA	Biomass bottom ash
BET	Brunauer-Emmett-Teller
BFA	Biomass fly ash
BJH	Barrett – Joyner – Hallenda
BOF	Basic oxygen furnace
BSE	Backscattered electron
C-(A)-S-H	Calcium (aluminum) silicate hydrate
C_2S	Dicalcium silicate
Cc	Calcite
CFA	Class F fly ash
CH	Calcium hydroxide
d50	Particle size corresponding to the cumulative frequency of 50%
DS	Digestate sludge
DSS	Digested sewage sludge
DTG	Differential thermogravimetry
DTPA-5Na	Pentasodium diethylenetriamine pentaacetate
EDIPA	Ethanol-diisopropanolamine
EDTA	Ethylenediaminetetraacetic acid
EDX	Energy dispersive X-ray spectroscopy
EU	European Union
FA	Fly ash
FAU	Faujasite type zeolite X
FGD	Flue gas desulphurization
FT-IR	Fourier transform infrared spectroscopy
GBBA	Ground biomass bottom ash
GGBFS	Ground granulated blast furnace slag
GS	Geothermal silica
Hc	Hemicarbonaluminate
HDPE	High-density polyethylene
HS	Hydroxy-sodalite zeolite
Ht	Hydrotalcite
L/S	Liquid-to-Solid
LDHs	Layered double hydroxides
LOI	Loss on ignition
LTA	Linde type A Zeolite
M	Mole per liter

MIP	Mercury intrusion porosimetry
MK	Metakaolin
MKG	Metakaolin-based geopolymers
Ms	Silicate modulus
MS	Microsilica
M-S-H	Magnesium silicate hydrate
MSWI	Municipal solid waste incineration
MSWP	Municipal solid waste plant
N-(A)-S-H	Sodium (aluminum) silicate hydrate
NC	Sodium carbonate
NO_x	Nitrogen oxides
NS	Nano-silica
OPC	Ordinary Portland cement
PCO	Photocatalytic oxidation
PDSS	Pretreated digested sewage sludge
Q-XRD	Quantitative X-ray diffraction
RH	Relative humidity
RHA	Rice hull ash
RhB	Rhodamine B
SA	sodium aluminate
SEM	Scanning Electron Microscope
SF	Silica fume
SH	Sodium hydroxide
SQD	Soil Quality Decree
SS	Sodium silicate
TEM	Transmission electron microscope
TG	Thermogravimetry
TPH	Thermal Pressure Hydrolysis
UDL	Under detect limitation
UV	Ultraviolet
w/b	Water to binder ratio
WG	Waterglass
WIFA	Waste incineration fly ash
WIFD	Waste Incineration Filter Dust
WWTPs	Wastewater treatment plants
XRD	X-ray diffraction
XRF	X-ray fluorescence

Latin symbol		SI unit
a_0	Constant parameter in Eq. (7. 6)	-
a_0^*	Color value without UV irradiation	-
a_{t^*}	Color value of a* after t min of UV irradiation	-
C_{cl}	Cumulative leachable capacity of an element in each mix	mg/kg
C_i	Concentration of an element (i) in the leachate	mg/L
C_M	Amount of an element leached from the mix	mg/kg
C_R	Amount of an element leached from the raw materials	mg/kg
D	Diameter	mm
d	Day	d
E	Immobilization efficiency of the element in each mix	%
E_g	Band gap energy	eV
E_u	Urbach energy	eV
H	Height of cylinder mold	mm
h	Hour	h
hp	Planck constant	$J \cdot Hz^{-1}$
k	Permeability of sealing materials	m/s
M_c	Mass of carbonated samples	g
M_d	Mass of dry material	g
min	Minute	m
M_{mix}	Mass of mix	kg
M_r	Mass of dry residual	g
M_{raw}	Mass of raw materials	kg
M_t	Total mass change	g
M_{uc}	Mass of uncarbonated samples	g
R	Reflectance	%
R_x	Reactive content of element X	%
v	Vibration of the bond	cm^{-1}
V_i	Volume of the leachate	L
W_c	Moisture content from carbonated samples	%
W_R	Mass proportion of each ingredient in the mix	%
W_{uc}	Moisture content from uncarbonated samples	%
X_d	Mass content of element X in dry material	%
X_r	Mass content of element X in dry residual	%

Greek		SI unit
α	Kubelka-Munk optical absorption coefficient	%
ε	Total CO_2 and bound water adsorption	%
θ	Peak angle	°
υ	Photon's frequency	s^{-1}
φ	Color change efficiency	%

List of publications

Peer-reviewed journal papers

[1] **X. Ling**, K. Schollbach, G. Liu, G., H.J.H. Brouwers, The utilization of waste incineration filter dust (WIFD) in sodium carbonate activated slag mortars, ***Construction and Building Materials***, 313, 125494, 2021**.**

[2] **X. Ling**, W. Chen, K. Schollbach, H.J.H. Brouwers, Low permeability sealing materials based on sewage, digestate and incineration industrial by-products in the final landfill cover system, ***Construction and Building Materials***, 412, 134889, 2024.

[3] **X. Ling**, K. Schollbach, Y.X. Chen, H.J.H. Brouwers, The effect of nano-silica and silica fume on the sodium carbonate-activated slag system containing air pollution control residues, ***Waste Management***, 176, 52-63, 2024.

[4] **X. Ling**, W. Chen, K. Schollbach, H.J.H. Brouwers, Valorization of biomass bottom ash in alkali-activated GGBFS-fly ash: impact of biomass bottom ash characteristic, silicate modulus and aluminum-anodizing waste, ***Construction and Building Materials***, 428, 136408, 2024.

[5] **X. Ling**, D.R. Liu, K. Schollbach, W. Chen, Advancing self-cleaning performance in metakaolin-based geopolymers through in-situ zeolite formation and TiO_2 integration, ***Cement and Concrete Composites*** 150, 105567, 2024.

[6] **X. Ling**, Y.X. Chen, K. Schollbach, H.J.H. Brouwers, Carbonation of digested sewage sludge-based sealing material in a final landfill cover system: role of waterglass and additional industrial by-products (in preparation).

[7] **X. Ling**, Z.H. Jiang, K. Schollbach, W. Chen, H.J.H. Brouwers, Pentasodium diethylenetriamine pentaacetate (DTPA-5Na) activated basic oxygen furnace slag (in preparation).

[8] M.J. Ahmed, K. Lambrechts, **X. Ling**, K. Schollbach, H.J.H. Brouwers, Effect of hydroxide, carbonate, and sulfate anions on the β -dicalcium silicate hydration rate, ***Cement and Concrete Research***, 173, 107302, 2023.

[9] Z.H. Jiang, J. Zepper, **X. Ling**, K. Schollbach, H.J.H. Brouwers, Potassium citrate-activated pure BOF slag-based mortars utilizing carbonated and autoclaved BOF slag aggregates, ***Cement and Concrete Composites***,150, 105564, 2023. (Corresponding author)

[10] K.Z. Liu, Y. Long, L.Y. Chen, **X. Ling**, R. Yu, Z.H. Shui, S.X. Fei, W.Z. Yu, C. Li, K.Y. Ge, Mechanisms of autogenous shrinkage for Ultra-High Performance Concrete (UHPC) prepared with pre-wet porous fine aggregate (PFA), ***Journal of Building Engineering***, 54, 104622, 2022. (Corresponding author)

[11] J. Zepper, S. de Bruin, **X. Ling**, K. Schollbach, S. Laan, H.J.H. Brouwers, Improving the early reactivity of activated basic oxygen furnace slag – The influence of particle fineness and grinding aids, ***Journal of CO_2 Utilization***, 102821, 2024.

[12] T. Liu, Y.J. Tang, **X. Ling**, J.L. Stapper, W. Kunther, Q.L. Yu, $NaAlO_2$ activated slag and MSWI bottom ash: Phase assemblages and thermodynamic assessment of long-term leaching behavior, ***Cement and Concrete Composites***, 152, 105634, 2024.

[13] **X. Ling**, B. Li, M. Li, W. Hu, W. Chen, Thermal stability of Al-modified silica aerogels through epoxide-assisted sol–gel route followed by ambient pressure drying, ***Journal of Sol-Gel Science and Technology***, 87, 83-94, 2018.

[14] W. Chen, **X. Ling**, Q. Li, B. Yuan, B. Li, H.S. Ma, Experimental evidence on formation of ulexite in sulfoaluminate cement paste mixed with high concentration borate solution and its retarding effects, ***Construction and Building Materials***, 215, 777-785, 2019.

[15] B. Li, **X. Ling**, X. Liu, Q. Li, W. Chen, Hydration of Portland cements in solutions containing high concentration of borate ions: Effects of LiOH, ***Cement and Concrete Composites***, 102, 94-104, 2019.

Conferences

[1] **X. Ling**, K. Schollbach, H.J.H Brouwers. Green landfill liner for soil protection containing 100% industrial by-products. Materials Innovation Institute (M2i) Conference 2022, 4-5 April, Noordwijkerhout, the Netherlands, 2022.

[2] **X. Ling**, K. Schollbach, H.J.H Brouwers. The valorization of biomass incineration fly ash (BIFA) in the alkali-activated materials. The 4th International Conference on the Chemistry of Construction Materials (ICCCM 2023), 26-28 September, Karlsruhe, Germany, 2022.

[3] **X. Ling**, K. Schollbach, H.J.H Brouwers. The solidification of biomass bottom ash (BBA) in alkali-activated materials: role of BBA content, fineness and silica modulus (Ms) of activators. The 7th International Conference of Non-Traditional Cement & Concrete (NTCC2023), 25-28 June, Brno, Czech Republic, 2023.

[4] **X. Ling**, Z.H. Jiang, K. Schollbach, H.J.H Brouwers. New binder: stabilized gypsum and steel slag. Materials Innovation Institute (M2i) Conference 2023, 11-12 December, Arnhem, the Netherlands, 2023.

[5] **X. Ling**, K. Schollbach, H.J.H Brouwers. Recycle of contaminated gypsum in the BOF slag system. The 3rd International Conference of Sustainable Building Materials (ICSBM 2023), 25-27 September, Wuhan, China, 2023.

Curriculum vitae

Xuan Ling was born in Lanxi, Zhejiang Province, China on June 19, 1994. After finishing his primary, middle and high school educations in Lanxi and Jinhua, Zhejiang, he started to study at Wuhan University of Technology (WHUT) in September 2012 in Wuhan, China. In June 2016, he received his bachelor's degree majoring in Materials Science and Engineering. In September 2016, he continued his study at the School of Materials Science and Engineering (WHUT) as a master student supervised by Prof. Wei Chen, majoring in advanced cement-based materials and earning his master's degree in June 2019. His graduation project concerned the solidification of high concentration borate solutions in sulphoaluminate cement. In October 2019, he began his PhD study under the supervision of Prof. H.J.H. (Jos) Brouwers and Dr. K. (Katrin) Schollbach. The study was supported by China Scholarship Council and the department of Built Environment in Eindhoven University of Technology (TU/e), Eindhoven, the Netherlands. His PhD research includes the valorization of industrial solid wastes as ingredients for sustainable building materials, including landfill sealing materials, alkali-activated materials, and basic oxygen furnace (BOF) slag-based cement-free binder.

Bouwstenen is een publicatiereeks
van de Faculteit Bouwkunde,
Technische Universiteit Eindhoven.
Zij presenteert resultaten van
onderzoek en andere activiteiten op
het vakgebied der Bouwkunde,
uitgevoerd in het kader van deze
Faculteit.

Bouwstenen en andere proefschriften van de
TU/e zijn online beschikbaar via:
https://research.tue.nl/

Reeds verschenen in de serie
Bouwstenen

nr 1
Elan: A Computer Model for Building Energy Design: Theory and Validation
Martin H. de Wit
H.H. Driessen
R.M.M. van der Velden

nr 2
Kwaliteit, Keuzevrijheid en Kosten: Evaluatie van Experiment Klarendal, Arnhem
J. Smeets
C. le Nobel
M. Broos
J. Frenken
A. v.d. Sanden

nr 3
Crooswijk: Van 'Bijzonder' naar 'Gewoon'
Vincent Smit
Kees Noort

nr 4
Staal in de Woningbouw
Edwin J.F. Delsing

nr 5
Mathematical Theory of Stressed Skin Action in Profiled Sheeting with Various Edge Conditions
Andre W.A.M.J. van den Bogaard

nr 6
Hoe Berekenbaar en Betrouwbaar is de Coëfficiënt k in x-ksigma en x-ks?
K.B. Lub
A.J. Bosch

nr 7
Het Typologisch Gereedschap: Een Verkennende Studie Omtrent Typologie en Omtrent de Aanpak van Typologisch Onderzoek
J.H. Luiten

nr 8
Informatievoorziening en Beheerprocessen
A. Nauta
Jos Smeets (red.)
Helga Fassbinder (projectleider)
Adrie Proveniers
J. v.d. Moosdijk

nr 9
Strukturering en Verwerking van Tijdgegevens voor de Uitvoering van Bouwwerken
ir. W.F. Schaefer
P.A. Erkelens

nr 10
Stedebouw en de Vorming van een Speciale Wetenschap
K. Doevendans

nr 11
Informatica en Ondersteuning van Ruimtelijke Besluitvorming
G.G. van der Meulen

nr 12
Staal in de Woningbouw, Korrosie-Bescherming van de Begane Grondvloer
Edwin J.F. Delsing

nr 13
Een Thermisch Model voor de Berekening van Staalplaatbetonvloeren onder Brandomstandigheden
A.F. Hamerlinck

nr 14
De Wijkgedachte in Nederland: Gemeenschapsstreven in een Stedebouwkundige Context
K. Doevendans
R. Stolzenburg

nr 15
Diaphragm Effect of Trapezoidally Profiled Steel Sheets: Experimental Research into the Influence of Force Application
Andre W.A.M.J. van den Bogaard

nr 16
Versterken met Spuit-Ferrocement: Het Mechanische Gedrag van met Spuit-Ferrocement Versterkte Gewapend Betonbalken
K.B. Lubir
M.C.G. van Wanroy

nr 17
De Tractaten van Jean Nicolas Louis Durand
G. van Zeyl

nr 18
Wonen onder een Plat Dak: Drie Opstellen over Enkele Vooronderstellingen van de Stedebouw
K. Doevendans

nr 19
Supporting Decision Making Processes: A Graphical and Interactive Analysis of Multivariate Data
W. Adams

nr 20
Self-Help Building Productivity: A Method for Improving House Building by Low-Income Groups Applied to Kenya 1990-2000
P. A. Erkelens

nr 21
De Verdeling van Woningen: Een Kwestie van Onderhandelen
Vincent Smit

nr 22
Flexibiliteit en Kosten in het Ontwerpproces: Een Besluitvormingondersteunend Model
M. Prins

nr 23
Spontane Nederzettingen Begeleid: Voorwaarden en Criteria in Sri Lanka
Po Hin Thung

nr 24
Fundamentals of the Design of Bamboo Structures
Oscar Arce-Villalobos

nr 25
Concepten van de Bouwkunde
M.F.Th. Bax (red.)
H.M.G.J. Trum (red.)

nr 26
Meaning of the Site
Xiaodong Li

nr 27
Het Woonmilieu op Begrip Gebracht: Een Speurtocht naar de Betekenis van het Begrip 'Woonmilieu'
Jaap Ketelaar

nr 28
Urban Environment in Developing Countries
editors: Peter A. Erkelens
George G. van der Meulen (red.)

nr 29
Stategische Plannen voor de Stad: Onderzoek en Planning in Drie Steden
prof.dr. H. Fassbinder (red.)
H. Rikhof (red.)

nr 30
Stedebouwkunde en Stadsbestuur
Piet Beekman

nr 31
De Architectuur van Djenné: Een Onderzoek naar de Historische Stad
P.C.M. Maas

nr 32
Conjoint Experiments and Retail Planning
Harmen Oppewal

nr 33
Strukturformen Indonesischer Bautechnik: Entwicklung Methodischer Grundlagen für eine 'Konstruktive Pattern Language' in Indonesien
Heinz Frick arch. SIA

nr 34
Styles of Architectural Designing: Empirical Research on Working Styles and Personality Dispositions
Anton P.M. van Bakel

nr 35
Conjoint Choice Models for Urban Tourism Planning and Marketing
Benedict Dellaert

nr 36
Stedelijke Planvorming als Co-Produktie
Helga Fassbinder (red.)

nr 37
Design Research in the Netherlands
editors: R.M. Oxman
M.F.Th. Bax
H.H. Achten

nr 38
Communication in the Building Industry
Bauke de Vries

nr 39
Optimaal Dimensioneren van Gelaste Plaatliggers
J.B.W. Stark
F. van Pelt
L.F.M. van Gorp
B.W.E.M. van Hove

nr 40
Huisvesting en Overwinning van Armoede
P.H. Thung
P. Beekman (red.)

nr 41
Urban Habitat: The Environment of Tomorrow
George G. van der Meulen
Peter A. Erkelens

nr 42
A Typology of Joints
John C.M. Olie

nr 43
Modeling Constraints-Based Choices for Leisure Mobility Planning
Marcus P. Stemerding

nr 44
Activity-Based Travel Demand Modeling
Dick Ettema

nr 45
Wind-Induced Pressure Fluctuations on Building Facades
Chris Geurts

nr 46
Generic Representations
Henri Achten

nr 47
Johann Santini Aichel: Architectuur en Ambiguiteit
Dirk De Meyer

nr 48
Concrete Behaviour in Multiaxial Compression
Erik van Geel

nr 49
Modelling Site Selection
Frank Witlox

nr 50
Ecolemma Model
Ferdinand Beetstra

nr 51
Conjoint Approaches to Developing Activity-Based Models
Donggen Wang

nr 52
On the Effectiveness of Ventilation
Ad Roos

nr 53
Conjoint Modeling Approaches for Residential Group preferences
Eric Molin

nr 54
Modelling Architectural Design Information by Features
Jos van Leeuwen

nr 55
A Spatial Decision Support System for the Planning of Retail and Service Facilities
Theo Arentze

nr 56
Integrated Lighting System Assistant
Ellie de Groot

nr 57
Ontwerpend Leren, Leren Ontwerpen
J.T. Boekholt

nr 58
Temporal Aspects of Theme Park Choice Behavior
Astrid Kemperman

nr 59
Ontwerp van een Geïndustrialiseerde Funderingswijze
Faas Moonen

nr 60
Merlin: A Decision Support System for Outdoor Leisure Planning
Manon van Middelkoop

nr 61
The Aura of Modernity
Jos Bosman

nr 62
Urban Form and Activity-Travel Patterns
Daniëlle Snellen

nr 63
Design Research in the Netherlands 2000
Henri Achten

nr 64
Computer Aided Dimensional Control in Building Construction
Rui Wu

nr 65
Beyond Sustainable Building
editors: Peter A. Erkelens
Sander de Jonge
August A.M. van Vliet
co-editor: Ruth J.G. Verhagen

nr 66
Das Globalrecyclingfähige Haus
Hans Löfflad

nr 67
Cool Schools for Hot Suburbs
René J. Dierkx

nr 68
A Bamboo Building Design Decision Support Tool
Fitri Mardjono

nr 69
Driving Rain on Building Envelopes
Fabien van Mook

nr 70
Heating Monumental Churches
Henk Schellen

nr 71
Van Woningverhuurder naar Aanbieder van Woongenot
Patrick Dogge

nr 72
Moisture Transfer Properties of Coated Gypsum
Emile Goossens

nr 73
Plybamboo Wall-Panels for Housing
Guillermo E. González-Beltrán

nr 74
The Future Site-Proceedings
Ger Maas
Frans van Gassel

nr 75
Radon transport in Autoclaved Aerated Concrete
Michel van der Pal

nr 76
The Reliability and Validity of Interactive Virtual Reality Computer Experiments
Amy Tan

nr 77
Measuring Housing Preferences Using Virtual Reality and Belief Networks
Maciej A. Orzechowski

nr 78
Computational Representations of Words and Associations in Architectural Design
Nicole Segers

nr 79
Measuring and Predicting Adaptation in Multidimensional Activity-Travel Patterns
Chang-Hyeon Joh

nr 80
Strategic Briefing
Fayez Al Hassan

nr 81
Well Being in Hospitals
Simona Di Cicco

nr 82
Solares Bauen: Implementierungs- und Umsetzungs-Aspekte in der Hochschulausbildung in Österreich
Gerhard Schuster

nr 83
Supporting Strategic Design of Workplace Environments with Case-Based Reasoning
Shauna Mallory-Hill

nr 84
ACCEL: A Tool for Supporting Concept Generation in the Early Design Phase
Maxim Ivashkov

nr 85
Brick-Mortar Interaction in Masonry under Compression
Ad Vermeltfoort

nr 86
Zelfredzaam Wonen
Guus van Vliet

nr 87
Een Ensemble met Grootstedelijke Allure
Jos Bosman
Hans Schippers

nr 88
On the Computation of Well-Structured Graphic Representations in Architectural Design
Henri Achten

nr 89
De Evolutie van een West-Afrikaanse Vernaculaire Architectuur
Wolf Schijns

nr 90
ROMBO Tactiek
Christoph Maria Ravesloot

nr 91
External Coupling between Building Energy Simulation and Computational Fluid Dynamics
Ery Djunaedy

nr 92
Design Research in the Netherlands 2005
editors: Henri Achten
Kees Dorst
Pieter Jan Stappers
Bauke de Vries

nr 93
Ein Modell zur Baulichen Transformation
Jalil H. Saber Zaimian

nr 94
Human Lighting Demands: Healthy Lighting in an Office Environment
Myriam Aries

nr 95
A Spatial Decision Support System for the Provision and Monitoring of Urban Greenspace
Claudia Pelizaro

nr 96
Leren Creëren
Adri Proveniers

nr 97
Simlandscape
Rob de Waard

nr 98
Design Team Communication
Ad den Otter

nr 99
Humaan-Ecologisch Georiënteerde Woningbouw
Juri Czabanowski

nr 100
Hambase
Martin de Wit

nr 101
Sound Transmission through Pipe Systems and into Building Structures
Susanne Bron-van der Jagt

nr 102
Het Bouwkundig Contrapunt
Jan Francis Boelen

nr 103
A Framework for a Multi-Agent Planning Support System
Dick Saarloos

nr 104
Bracing Steel Frames with Calcium Silicate Element Walls
Bright Mweene Ng'andu

nr 105
Naar een Nieuwe Houtskeletbouw
F.N.G. De Medts

nr 106 and 107
Niet gepubliceerd

nr 108
Geborgenheid
T.E.L. van Pinxteren

nr 109
Modelling Strategic Behaviour in Anticipation of Congestion
Qi Han

nr 110
Reflecties op het Woondomein
Fred Sanders

nr 111
On Assessment of Wind Comfort by Sand Erosion
Gábor Dezsö

nr 112
Bench Heating in Monumental Churches
Dionne Limpens-Neilen

nr 113
RE. Architecture
Ana Pereira Roders

nr 114
Toward Applicable Green Architecture
Usama El Fiky

nr 115
Knowledge Representation under Inherent Uncertainty in a Multi-Agent System for Land Use Planning
Liying Ma

nr 116
Integrated Heat Air and Moisture Modeling and Simulation
Jos van Schijndel

nr 117
Concrete Behaviour in Multiaxial Compression
J.P.W. Bongers

nr 118
The Image of the Urban Landscape
Ana Moya Pellitero

nr 119
The Self-Organizing City in Vietnam
Stephanie Geertman

nr 120
A Multi-Agent Planning Support System for Assessing Externalities of Urban Form Scenarios
Rachel Katoshevski-Cavari

nr 121
Den Schulbau Neu Denken, Fühlen und Wollen
Urs Christian Maurer-Dietrich

nr 122
Peter Eisenman Theories and Practices
Bernhard Kormoss

nr 123
User Simulation of Space Utilisation
Vincent Tabak

nr 125
In Search of a Complex System Model
Oswald Devisch

nr 126
Lighting at Work: Environmental Study of Direct Effects of Lighting Level and Spectrum on Psycho-Physiological Variables
Grazyna Górnicka

nr 127
Flanking Sound Transmission through Lightweight Framed Double Leaf Walls
Stefan Schoenwald

nr 128
Bounded Rationality and Spatio-Temporal Pedestrian Shopping Behavior
Wei Zhu

nr 129
Travel Information: Impact on Activity Travel Pattern
Zhongwei Sun

nr 130
Co-Simulation for Performance Prediction of Innovative Integrated Mechanical Energy Systems in Buildings
Marija Trčka

nr 131
Niet gepubliceerd

nr 132
Architectural Cue Model in Evacuation Simulation for Underground Space Design
Chengyu Sun

nr 133
Uncertainty and Sensitivity Analysis in Building Performance Simulation for Decision Support and Design Optimization
Christina Hopfe

nr 134
Facilitating Distributed Collaboration in the AEC/FM Sector Using Semantic Web Technologies
Jacob Beetz

nr 135
Circumferentially Adhesive Bonded Glass Panes for Bracing Steel Frame in Façades
Edwin Huveners

nr 136
Influence of Temperature on Concrete Beams Strengthened in Flexure with CFRP
Ernst-Lucas Klamer

nr 137
Sturen op Klantwaarde
Jos Smeets

nr 139
Lateral Behavior of Steel Frames with Discretely Connected Precast Concrete Infill Panels
Paul Teewen

nr 140
Integral Design Method in the Context of Sustainable Building Design
Perica Savanović

nr 141
Household Activity-Travel Behavior: Implementation of Within-Household Interactions
Renni Anggraini

nr 142
Design Research in the Netherlands 2010
Henri Achten

nr 143
Modelling Life Trajectories and Transport Mode Choice Using Bayesian Belief Networks
Marloes Verhoeven

nr 144
Assessing Construction Project Performance in Ghana
William Gyadu-Asiedu

nr 145
Empowering Seniors through Domotic Homes
Masi Mohammadi

nr 146
An Integral Design Concept for Ecological Self-Compacting Concrete
Martin Hunger

nr 147
Governing Multi-Actor Decision Processes in Dutch Industrial Area Redevelopment
Erik Blokhuis

nr 148
A Multifunctional Design Approach for Sustainable Concrete
Götz Hüsken

nr 149
Quality Monitoring in Infrastructural Design-Build Projects
Ruben Favié

nr 150
Assessment Matrix for Conservation of Valuable Timber Structures
Michael Abels

nr 151
Co-simulation of Building Energy Simulation and Computational Fluid Dynamics for Whole-Building Heat, Air and Moisture Engineering
Mohammad Mirsadeghi

nr 152
External Coupling of Building Energy Simulation and Building Element Heat, Air and Moisture Simulation
Daniel Cóstola

nr 153
Adaptive Decision Making In Multi-Stakeholder Retail Planning
Ingrid Janssen

nr 154
Landscape Generator
Kymo Slager

nr 155
Constraint Specification in Architecture
Remco Niemeijer

nr 156
A Need-Based Approach to Dynamic Activity Generation
Linda Nijland

nr 157
Modeling Office Firm Dynamics in an Agent-Based Micro Simulation Framework
Gustavo Garcia Manzato

nr 158
Lightweight Floor System for Vibration Comfort
Sander Zegers

nr 159
Aanpasbaarheid van de Draagstructuur
Roel Gijsbers

nr 160
'Village in the City' in Guangzhou, China
Yanliu Lin

nr 161
Climate Risk Assessment in Museums
Marco Martens

nr 162
Social Activity-Travel Patterns
Pauline van den Berg

nr 163
Sound Concentration Caused by Curved Surfaces
Martijn Vercammen

nr 164
Design of Environmentally Friendly Calcium Sulfate-Based Building Materials: Towards an Improved Indoor Air Quality
Qingliang Yu

nr 165
Beyond Uniform Thermal Comfort on the Effects of Non-Uniformity and Individual Physiology
Lisje Schellen

nr 166
Sustainable Residential Districts
Gaby Abdalla

nr 167
Towards a Performance Assessment Methodology using Computational Simulation for Air Distribution System Designs in Operating Rooms
Mônica do Amaral Melhado

nr 168
Strategic Decision Modeling in Brownfield Redevelopment
Brano Glumac

nr 169
Pamela: A Parking Analysis Model for Predicting Effects in Local Areas
Peter van der Waerden

nr 170
A Vision Driven Wayfinding Simulation-System Based on the Architectural Features Perceived in the Office Environment
Qunli Chen

nr 171
Measuring Mental Representations Underlying Activity-Travel Choices
Oliver Horeni

nr 172
Modelling the Effects of Social Networks on Activity and Travel Behaviour
Nicole Ronald

nr 173
Uncertainty Propagation and Sensitivity Analysis Techniques in Building Performance Simulation to Support Conceptual Building and System Design
Christian Struck

nr 174
Numerical Modeling of Micro-Scale Wind-Induced Pollutant Dispersion in the Built Environment
Pierre Gousseau

nr 175
Modeling Recreation Choices over the Family Lifecycle
Anna Beatriz Grigolon

nr 176
Experimental and Numerical Analysis of Mixing Ventilation at Laminar, Transitional and Turbulent Slot Reynolds Numbers
Twan van Hooff

nr 177
Collaborative Design Support: Workshops to Stimulate Interaction and Knowledge Exchange Between Practitioners
Emile M.C.J. Quanjel

nr 178
Future-Proof Platforms for Aging-in-Place
Michiel Brink

nr 179
Motivate: A Context-Aware Mobile Application for Physical Activity Promotion
Yuzhong Lin

nr 180
Experience the City: Analysis of Space-Time Behaviour and Spatial Learning
Anastasia Moiseeva

nr 181
Unbonded Post-Tensioned Shear Walls of Calcium Silicate Element Masonry
Lex van der Meer

nr 182
Construction and Demolition Waste Recycling into Innovative Building Materials for Sustainable Construction in Tanzania
Mwita M. Sabai

nr 183
Durability of Concrete with Emphasis on Chloride Migration
Przemysław Spiesz

nr 184
Computational Modeling of Urban Wind Flow and Natural Ventilation Potential of Buildings
Rubina Ramponi

nr 185
A Distributed Dynamic Simulation Mechanism for Buildings Automation and Control Systems
Azzedine Yahiaoui

nr 186
Modeling Cognitive Learning of Urban Networks in Daily Activity-Travel Behavior
Şehnaz Cenani Durmazoğlu

nr 187
Functionality and Adaptability of Design Solutions for Public Apartment Buildings in Ghana
Stephen Agyefi-Mensah

nr 188
A Construction Waste Generation Model for Developing Countries
Lilliana Abarca-Guerrero

nr 189
Synchronizing Networks: The Modeling of Supernetworks for Activity-Travel Behavior
Feixiong Liao

nr 190
Time and Money Allocation Decisions in Out-of-Home Leisure Activity Choices
Gamze Zeynep Dane

nr 191
How to Measure Added Value of CRE and Building Design
Rianne Appel-Meulenbroek

nr 192
Secondary Materials in Cement-Based Products: Treatment, Modeling and Environmental Interaction
Miruna Florea

nr 193
Concepts for the Robustness Improvement of Self-Compacting Concrete: Effects of Admixtures and Mixture Components on the Rheology and Early Hydration at Varying Temperatures
Wolfram Schmidt

nr 194
Modelling and Simulation of Virtual Natural Lighting Solutions in Buildings
Rizki A. Mangkuto

nr 195
Nano-Silica Production at Low Temperatures from the Dissolution of Olivine - Synthesis, Tailoring and Modelling
Alberto Lazaro Garcia

nr 196
Building Energy Simulation Based Assessment of Industrial Halls for Design Support
Bruno Lee

nr 197
Computational Performance Prediction of the Potential of Hybrid Adaptable Thermal Storage Concepts for Lightweight Low-Energy Houses
Pieter-Jan Hoes

nr 198
Application of Nano-Silica in Concrete
George Quercia Bianchi

nr 199
Dynamics of Social Networks and Activity Travel Behaviour
Fariya Sharmeen

nr 200
Building Structural Design Generation and Optimisation including Spatial Modification
Juan Manuel Davila Delgado

nr 201
Hydration and Thermal Decomposition of Cement/Calcium-Sulphate Based Materials
Ariën de Korte

nr 202
Republiek van Beelden:
De Politieke Werkingen van het Ontwerp in Regionale Planvorming
Bart de Zwart

nr 203
Effects of Energy Price Increases on Individual Activity-Travel Repertoires and Energy Consumption
Dujuan Yang

nr 204
Geometry and Ventilation:
Evaluation of the Leeward Sawtooth Roof Potential in the Natural Ventilation of Buildings
Jorge Isaac Perén Montero

nr 205
Computational Modelling of Evaporative Cooling as a Climate Change Adaptation Measure at the Spatial Scale of Buildings and Streets
Hamid Montazeri

nr 206
Local Buckling of Aluminium Beams in Fire Conditions
Ronald van der Meulen

nr 207
Historic Urban Landscapes:
Framing the Integration of Urban and Heritage Planning in Multilevel Governance
Loes Veldpaus

nr 208
Sustainable Transformation of the Cities:
Urban Design Pragmatics to Achieve a Sustainable City
Ernesto Antonio Zumelzu Scheel

nr 209
Development of Sustainable Protective Ultra-High Performance Fibre Reinforced Concrete (UHPFRC):
Design, Assessment and Modeling
Rui Yu

nr 210
Uncertainty in Modeling Activity-Travel Demand in Complex Uban Systems
Soora Rasouli

nr 211
Simulation-based Performance Assessment of Climate Adaptive Greenhouse Shells
Chul-sung Lee

nr 212
Green Cities:
Modelling the Spatial Transformation of the Urban Environment using Renewable Energy Technologies
Saleh Mohammadi

nr 213
A Bounded Rationality Model of Short and Long-Term Dynamics of Activity-Travel Behavior
Ifigeneia Psarra

nr 214
Effects of Pricing Strategies on Dynamic Repertoires of Activity-Travel Behaviour
Elaheh Khademi

nr 215
Handstorm Principles for Creative and Collaborative Working
Frans van Gassel

nr 216
Light Conditions in Nursing Homes: Visual Comfort and Visual Functioning of Residents
Marianne M. Sinoo

nr 217
Woonsporen: De Sociale en Ruimtelijke Biografie van een Stedelijk Bouwblok in de Amsterdamse Transvaalbuurt
Hüseyin Hüsnü Yegenoglu

nr 218
Studies on User Control in Ambient Intelligent Systems
Berent Willem Meerbeek

nr 219
Daily Livings in a Smart Home: Users' Living Preference Modeling of Smart Homes
Erfaneh Allameh

nr 220
Smart Home Design: Spatial Preference Modeling of Smart Homes
Mohammadali Heidari Jozam

nr 221
Wonen: Discoursen, Praktijken, Perspectieven
Jos Smeets

nr 222
Personal Control over Indoor Climate in Offices: Impact on Comfort, Health and Productivity
Atze Christiaan Boerstra

nr 223
Personalized Route Finding in Multimodal Transportation Networks
Jianwe Zhang

nr 224
The Design of an Adaptive Healing Room for Stroke Patients
Elke Daemen

nr 225
Experimental and Numerical Analysis of Climate Change Induced Risks to Historic Buildings and Collections
Zara Huijbregts

nr 226
Wind Flow Modeling in Urban Areas Through Experimental and Numerical Techniques
Alessio Ricci

nr 227
Clever Climate Control for Culture: Energy Efficient Indoor Climate Control Strategies for Museums Respecting Collection Preservation and Thermal Comfort of Visitors
Rick Kramer

nr 228
Fatigue Life Estimation of Metal Structures Based on Damage Modeling
Sarmediran Silitonga

nr 229
A multi-agents and occupancy based strategy for energy management and process control on the room-level
Timilehin Moses Labeodan

nr 230
Environmental assessment of Building Integrated Photovoltaics: Numerical and Experimental Carrying Capacity Based Approach
Michiel Ritzen

nr 231
Performance of Admixture and Secondary Minerals in Alkali Activated Concrete: Sustaining a Concrete Future
Arno Keulen

nr 232
World Heritage Cities and Sustainable Urban Development:
Bridging Global and Local Levels in Monitoring the Sustainable Urban Development of World Heritage Cities
Paloma C. Guzman Molina

nr 233
Stage Acoustics and Sound Exposure in Performance and Rehearsal Spaces for Orchestras:
Methods for Physical Measurements
Remy Wenmaekers

nr 234
Municipal Solid Waste Incineration (MSWI) Bottom Ash:
From Waste to Value Characterization, Treatments and Application
Pei Tang

nr 235
Large Eddy Simulations Applied to Wind Loading and Pollutant Dispersion
Mattia Ricci

nr 236
Alkali Activated Slag-Fly Ash Binders: Design, Modeling and Application
Xu Gao

nr 237
Sodium Carbonate Activated Slag: Reaction Analysis, Microstructural Modification & Engineering Application
Bo Yuan

nr 238
Shopping Behavior in Malls
Widiyani

nr 239
Smart Grid-Building Energy Interactions: Demand Side Power Flexibility in Office Buildings
Kennedy Otieno Aduda

nr 240
Modeling Taxis Dynamic Behavior in Uncertain Urban Environments
Zheng Zhong

nr 241
Gap-Theoretical Analyses of Residential Satisfaction and Intention to Move
Wen Jiang

nr 242
Travel Satisfaction and Subjective Well-Being: A Behavioral Modeling Perspective
Yanan Gao

nr 243
Building Energy Modelling to Support the Commissioning of Holistic Data Centre Operation
Vojtech Zavrel

nr 244
Regret-Based Travel Behavior Modeling: An Extended Framework
Sunghoon Jang

nr 245
Towards Robust Low-Energy Houses: A Computational Approach for Performance Robustness Assessment using Scenario Analysis
Rajesh Reddy Kotireddy

nr 246
Development of sustainable and functionalized inorganic binder-biofiber composites
Guillaume Doudart de la Grée

nr 247
A Multiscale Analysis of the Urban Heat Island Effect: From City Averaged Temperatures to the Energy Demand of Individual Buildings
Yasin Toparlar

nr 248
Design Method for Adaptive Daylight Systems for buildings covered by large (span) roofs
Florian Heinzelmann

nr 249
Hardening, high-temperature resistance and acid resistance of one-part geopolymers
Patrick Sturm

nr 250
Effects of the built environment on dynamic repertoires of activity-travel behaviour
Aida Pontes de Aquino

nr 251
Modeling for auralization of urban environments: Incorporation of directivity in sound propagation and analysis of a framework for auralizing a car pass-by
Fotis Georgiou

nr 252
Wind Loads on Heliostats and Photovoltaic Trackers
Andreas Pfahl

nr 253
Approaches for computational performance optimization of innovative adaptive façade concepts
Roel Loonen

nr 254
Multi-scale FEM-DEM Model for Granular Materials: Micro-scale boundary conditions, Statics, and Dynamics
Jiadun Liu

nr 255
Bending Moment - Shear Force Interaction of Rolled I-Shaped Steel Sections
Rianne Willie Adriana Dekker

nr 256
Paralympic tandem cycling and handcycling: Computational and wind tunnel analysis of aerodynamic performance
Paul Fionn Mannion

nr 257
Experimental characterization and numerical modelling of 3D printed concrete: Controlling structural behaviour in the fresh and hardened state
Robert Johannes Maria Wolfs

nr 258
Requirement checking in the building industry: Enabling modularized and extensible requirement checking systems based on semantic web technologies
Chi Zhang

nr 259
A Sustainable Industrial Site Redevelopment Planning Support System
Tong Wang

nr 260
Efficient storage and retrieval of detailed building models: Multi-disciplinary and long-term use of geometric and semantic construction information
Thomas Ferdinand Krijnen

nr 261
The users' value of business center concepts for knowledge sharing and networking behavior within and between organizations
Minou Weijs-Perrée

nr 262
Characterization and improvement of aerodynamic performance of vertical axis wind turbines using computational fluid dynamics (CFD)
Abdolrahim Rezaeiha

nr 263
In-situ characterization of the acoustic impedance of vegetated roofs
Chang Liu

nr 264
Occupancy-based lighting control: Developing an energy saving strategy that ensures office workers' comfort
Christel de Bakker

nr 265
Stakeholders-Oriented Spatial Decision Support System
Cahyono Susetyo

nr 266
Climate-induced damage in oak museum objects
Rianne Aleida Luimes

nr 267
Towards individual thermal comfort: Model predictive personalized control of heating systems
Katarina Katic

nr 268
Modelling and Measuring Quality of Urban Life: Housing, Neighborhood, Transport and Job
Lida Aminian

nr 269
Optimization of an aquifer thermal energy storage system through integrated modelling of aquifer, HVAC systems and building
Basar Bozkaya

nr 270
Numerical modeling for urban sound propagation: developments in wave-based and energy-based methods
Raúl Pagán Muñoz

nr 271
Lighting in multi-user office environments: improving employee wellbeing through personal control
Sanae van der Vleuten-Chraibi

nr 272
A strategy for fit-for-purpose occupant behavior modelling in building energy and comfort performance simulation
Isabella I. Gaetani dell'Aquila d'Aragona

nr 273
Een architectuurhistorische waardestelling van naoorlogse woonwijken in Nederland: Het voorbeeld van de Westelijke Tuinsteden in Amsterdam
Eleonore Henriette Marie Mens

nr 274
Job-Housing Co-Dependent Mobility Decisions in Life Trajectories
Jia Guo

nr 275
A user-oriented focus to create healthcare facilities: decision making on strategic values
Emilia Rosalia Catharina Maria Huisman

nr 276
Dynamics of plane impinging jets at moderate Reynolds numbers – with applications to air curtains
Adelya Khayrullina

nr 277
Valorization of Municipal Solid Waste Incineration Bottom Ash - Chemical Nature, Leachability and Treatments of Hazardous Elements
Qadeer Alam

nr 278
Treatments and valorization of MSWI bottom ash - application in cement-based materials
Veronica Caprai

nr 279
Personal lighting conditions of office workers - input for intelligent systems to optimize subjective alertness
Juliëtte van Duijnhoven

nr 280
Social influence effects in tourism travel: air trip itinerary and destination choices
Xiaofeng Pan

nr 281
Advancing Post-War Housing: Integrating Heritage Impact, Environmental Impact, Hygrothermal Risk and Costs in Renovation Design Decisions
Lisanne Claartje Havinga

nr 282
Impact resistant ultra-high performance fibre reinforced concrete: materials, components and properties
Peipeng Li

nr 283
Demand-driven Science Parks: The Perceived Benefits and Trade-offs of Tenant Firms with regard to Science Park Attributes
Wei Keat Benny Ng

nr 284
Raise the lantern; how light can help to maintain a healthy and safe hospital environment focusing on nurses
Maria Petronella Johanna Aarts

nr 285
Modelling Learning and Dynamic Route and Parking Choice Behaviour under Uncertainty
Elaine Cristina Schneider de Carvalho

nr 286
Identifying indoor local microclimates for safekeeping of cultural heritage
Karin Kompatscher

nr 287
Probabilistic modeling of fatigue resistance for welded and riveted bridge details. Resistance models and estimation of uncertainty.
Davide Leonetti

nr 288
Performance of Layered UHPFRC under Static and Dynamic Loads: Effects of steel fibers, coarse aggregates and layered structures
Yangyueye Cao

nr 289
Photocatalytic abatement of the nitrogen oxide pollution: synthesis, application and long-term evaluation of titania-silica composites
Yuri Hendrix

nr 290
Assessing knowledge adoption in post-disaster reconstruction: Understanding the impact of hazard-resistant construction knowledge on reconstruction processes of self-recovering communities in Nepal and the Philippines
Eefje Hendriks

nr 291
Locating electric vehicle charging stations: A multi-agent based dynamic simulation
Seheon Kim

nr 292
De invloed van Lean Management op de beheersing van het bouwproces
Wim van den Bouwhuijsen

nr 293
Neighborhood Environment and Physical Activity of Older Adults
Zhengying Liu

nr 294
Practical and continuous luminance distribution measurements for lighting quality
Thijs Willem Kruisselbrink

nr 295
Auditory Distraction in Open-Plan Study Environments in Higher Education
Pieternella Elizabeth Braat-Eggen

nr 296
Exploring the effect of the sound environment on nurses' task performance: an applied approach focusing on prospective memory
Jikke Reinten

nr 297
Design and performance of water resistant cementitious materials– Mechanisms, evaluation and applications
Zhengyao Qu

nr 298
Design Optimization of Seasonal Thermal Energy Storage Integrated District Heating and Cooling System: A Modeling and Simulation Approach
Luyi Xu

nr 299
Land use and transport: Integrated approaches for planning and management
Zhongqi Wang

nr 300
Multi-disciplinary optimization of building spatial designs: co-evolutionary design process simulations, evolutionary algorithms, hybrid approaches
Sjonnie Boonstra

nr 301
Modeling the spatial and temporal relation between urban land use, temperature, and energy demand
Hung-Chu Chen

nr 302
Seismic retrofitting of masonry walls with flexible deep mounted CFRP strips
Ömer Serhat Türkmen

nr 303
Coupled Aerostructural Shape and Topology Optimization of Horizontal-Axis Wind Turbine Rotor Blades
Zhijun Wang

nr 304
Valorization of Recycled Waste Glass and Converter Steel Slag as Ingredients for Building Materials: Hydration and Carbonation Studies
Gang Liu

nr 305
Low-Carbon City Development based on Land Use Planning
Gengzhe Wang

nr 306
Sustainable energy transition scenario analysis for buildings and neighborhoods - Data driven optimization
Shalika Saubhagya Wickramarachchi Walker

nr 307
In-between living and manufactured: an exploratory study on biobuilding components for building design
Berrak Kirbas Akyurek

nr 308
Development of alternative cementitious binders and functionalized materials: design, performance and durability
Anna Monika Kaja

nr 309
Development a morphological approach for interactive kinetic façade design: Improving multiple occupants' visual comfort
Seyed Morteza Hosseini

nr 310
PV in urban context: modeling and simulation strategies for analyzing the performance of shaded PV systems
Ádám Bognár

nr 311
Life Trajectory, Household Car Ownership Dynamics and Home Renewable Energy Equipment Adoption
Gaofeng Gu

nr 312
Impact of Street-Scale Built Environment on Walking/Cycling around Metro Stations
Yanan Liu

nr 313
Advances in Urban Traffic Network Equilibrium Models and Algorithms
Dong Wang

nr 314
Development of an uncertainty analysis framework for model-based consequential life cycle assessment: application to activity-based modelling and life cycle assessment of multimodal mobility
Paul Martin Baustert

nr 315
Variable stiffness and damping structural joints for semi-active vibration control
Qinyu Wang

nr 316
Understanding Carsharing-Facilitating Neighborhood Preferences
Juan Wang

nr 317
Dynamic alignment of Corporate Real Estate to business strategies: An empirical analysis using historical data and in-depth modelling of decision making
Howard Cooke

nr 318
Local People Matter: Towards participatory governance of cultural heritage in China
Ji Li

nr 319
Walkability and Walkable Healthy Neighborhoods
Bojing Liao

nr 320
Light directionality in design of healthy offices: exploration of two methods
Parisa Khademagha

nr 321
Room acoustic modeling with the time-domain discontinuous Galerkin method
Huiqing Wang

nr 322
Sustainable insulating lightweight materials for enhancing indoor building performance: miscanthus, aerogel and nano-silica
Yuxuan Chen

nr 323
Computational analysis of the impact of façade geometrical details on wind flow and pollutant dispersion
Xing Zheng

nr 324
Analysis of urban wind energy potential around high-rise buildings in close proximity using computational fluid dynamics
Yu-Hsuan Jang

nr 325
A new approach to automated energy performance and fault detection and diagnosis of HVAC systems: Development of the 4S3F method
Arie Taal

nr 326
Innovative Admixtures for Modifying Viscosity and Volume Change of Cement Composites
Hossein Karimi

nr 327
Towards houses with low grid dependency: A simulation-based design optimization approach
Zahra Mohammadi

nr 328
Activation of demand flexibility for heating systems in buildings: Real-life demonstration of optimal control for power-to-heat and thermal energy storage
Christian Finck

nr 329
A computational framework for analysis and optimisation of automated solar shading systems
Samuel B. de Vries

nr 330
Challenges and potential solutions for cultural heritage adaptive reuse: a comparative study employing the Historic Urban Landscape approach
Nadia Pintossi

nr 331
Shared control in office lighting systems
Tatiana Aleksandrovna Lashina

nr 332
Comfort in Urban Public Spaces
You Peng

nr 333
Numerical modelling of metal soap formation in historical oil paintings
Gerardus Johannes Anna Maria Eumelen

nr 334
A transdisciplinary decision-making approach to food-water-energy nexus: A guide towards sustainable development
Maryam Ghodsvali

nr 335
Numerical modelling of transient low-frequency sound propagation and vibration in buildings
Indra Sihar

nr 336
Characterization of impact sound from lightweight joist floors
Yi Qin

nr 337
Cities for Children: Supporting Children and Caregivers in Participatory Urban Planning
Özlemnur Ataol

nr 338
Engaging the unengaged: Exploring citizen participation in nature-based solutions in China
Li Dai

nr 339
Municipal Solid Waste Incineration Residues: analysis, treatments, and applications
Ekaterina Loginova

nr 340
Enhancing the Uptake of Nature-Based Solutions in Urban Settings: An Information Systems Approach
Shahryar Ershad Sarabi

nr 341
Work Schedule Arrangements in Two-Adult Households with Children
Bilin Han

nr 342
Increasing awareness of urban cultural heritage using digital technologies: empirical design and analysis of a new multi-media web platform
Benshuo Wang

nr 343
Mechanical and physical properties of fibre-cement composites using alternative natural fibres
Katerina Kochova

nr 344
Numerical and experimental investigation of urban microclimate in a real compact heterogeneous urban area
Nestoras Antoniou

nr 345
Examining in-class activities to facilitate academic achievement in higher education: A framework for optimal indoor environmental conditions
Henk W. Brink

nr 346
High-temperature resistant geopolymers: composition, microstructure and performance
Kinga Malgorzata Klima

nr 347
Individual and household decision-making in shared parking
Qianqian Yan

nr 348
In-situ formation of LDHs in Alkali activated binders
Tao Liu

nr 349
Condition assessment of concrete sewer pipes through an integrated experimental-numerical approach
Irene C. Scheperboer

nr 350
In situ PU-based characterization of sound absorbing materials for room acoustic modeling purposes
Baltazar Briere de La Hosseraye

nr 351
Uncertainty analysis and management in building energy data mining: A bottom-up approach considering the temporal and spatial aspect of data
Waqas Khan

nr 352
Personalized Heating Control Systems to improve thermal comfort and reduce energy consumption
Michal Veselý

nr 353
Restorative value of the urban greenscape: Urban residential streets as restorative environments
Robert P. van Dongen

nr 354
Urban ventilation and the compact Mediterranean city: numerical investigations of the dynamic relationships between density, morphology and wind flow
Olga Palusci

nr 355
Data science for buildings: a multi-scale approach bridging occupants to smart-city energy planning
Julien Leprince

nr 356
Class Association Rule Models for Predicting Transportation Mode Choice
Jiajia Zhang

nr 357
Acceptance and use of autonomous vehicles
Zhihui Tian

nr 358
Consumer Acceptance of Crowdshipping Services
Chenyu Wang

nr 359
Determinants of habitual participation in leisure-time physical activity and active travel in life trajectories
Xiaoyue Chen

nr 360
Analysis of Citizens' Motivation and Intention Using Modern Information Technology in Urban Planning Public Participation
Wenshu Li

nr 361
Linking smart and physical port cities. Port-city interface areas: from obsolete/isolated to smart environments.
Mercè de Miguel Capdevila

nr 362
Assessment and improvement of indoor thermal comfort and energy demand of Chinese heritage apartment buildings under climate change
Muxi Lei

nr 363
Indoor airflow and heat transfer in a cross-ventilated generic building: wind tunnel experiments and computational fluid dynamics analyses
Katarina Kosutova

nr 364
A Robotic Construction Simulation Platform for Light-weight Prefabricated Structures.
Aiyu Zhu

nr 365
Lifetime prediction of vertical-axis wind turbines based on CFD simulations and high-cycle fatigue modeling
Feiyu Geng

nr 366
Computational modeling of convective heat transfer at building surfaces
Samy Iousef

nr 367
Numerical simulation of the atmospheric boundary layer with application to natural ventilation
Raffaele Vasaturo

nr 368
Bouwen zonder scrupules. De Nederlandse bouwnijverheid tijdens de bezetting en de eerste jaren van wederopbouw (1940-1950)
Geert-Jan Mellink

nr 369
Factors Promoting a Positive Experienced Neighborhood Public Space--A Virtual Environment-based analysis.
Yuwen Zhao

nr 370
Place quality making in high-speed railway station areas: Devising place quality indicators for urban design, beyond the transport-land use divide
Jinglun Du

nr 371
Sustainable Bio-based Adsorptive Concrete for Phosphorus Removal
Fan Wu

nr 372
The physical workplace as a resource for mental health: A salutogenic approach to a mentally healthy workplace design at home and at the office
Lisanne Bergefurt

nr 373
High-end application of basic oxygen furnace steel slag as sustainable building materials
Muhammad Jawad Ahmed

nr 374
Energy-Efficient Urban Rail Transit Operations: Models, Algorithms, and Applications
Kang Huang

nr 375
Household Energy Efficiency Adoption: Influencing Factors and Diffusion Interventions
Hua Du

nr 376
High-temperature resistant geopolymer-based materials out of industrial residuals.
Yan Luo

nr 377
A Simulation Approach Exploring the Impacts of Land Use Variables on Travel Behavior.
Xiaoming Lyu

nr 378
Understanding and modelling individual preferences for Mobility as a Service
Valeria Caiati

nr 379
Linking the physical and digital built environment - Enabling occupant-centric decision-making using cross-domain semantic digital twins
Alex Donkers

nr 380
Indoor Air Quality in Daycare Centers: Assessing and Mitigating Indoor Exposure on Young Children
Hailin Zheng

nr 381
A Data-Driven Approach to Understanding Visitors' Behavior to Reduce the Negative Effects of Tourism in Historical Cities
Sezi Karayazi

nr 382
Wind effects on internal depressurization for asbestos abatement
Anjali Radhakrishnan Jayakumari

nr 383
Spatiotemporal Graph Convolutional Neural Network for Robust and Accurate Traffic Flow Prediction
Yutian Liu

nr 384
Photo-responsive functional aluminosilicate cementitious materials - Design, Performance and Durability
Daoru Liu

nr 385
High-end applications of basic oxygen furnace slag as a cementitious binder. Phase Assemblage, Mechanical & Chemical Activation, Composites Application
Winnie Franco Santos

nr 386
Towards improved performance modelling of distributed PV systems in the built environment
Bin Meng

nr 387
Development of sustainable insulation materials. Design, performance and applications
Alex Koh Chuen Hon

nr 388
Simulations of Sandwich Panel Systems under Fire: Two-Scale Methods for Connections, Pyrolysis for Insulation, Experimental Validations
Qingfeng Xu

nr 389
Long-term Mechanical Performance of the Flax Fiber Reinforced Polymer Composites Considering the Environmental Effects
Bowen Xu

nr 390
Quality engineering and control for digital fabrication with concrete
Derk Bos

nr 391
Structural Engineering of 3D Printed Strain Hardening Cementitious Composites. From micro-scale analysis to application
Karsten Nefs

nr 392
Children's Outdoor Play in the Digital Age; The Role of Digital Interventions in Stimulating Children's Outdoor Play Behavior
Avin Khalilollahi

nr 393
Biophilic design and integrating nature in architecture: Guidelines for three-dimensional green spaces to innovate architectural typologies and create impact for sustainability
Weijie Zhong

nr 394
Crafting Smart Homes: Innovative Design Strategies to Enhance Housing Quality for Ageing Well
Chuan Ma

nr 395
Valorization of Natural Fibers and Municipal Solid Waste Incineration (MSWI) Bottom Ash in Building Composite
Helong Song

nr 396
Digital Placemaking and Healthy Ageing. A user-centric approach for empowering senior citizens in inclusive decision-making of future healthy ageing neighbourhoods
Peyman Najafi

nr 397
Optimizing aerodynamic performance in cycling. - Analyses of drafting strategies and skinsuit design through computational simulations and wind tunnel experiments
Thijs Druenen

nr 398
A simulation-based analytical framework for heat battery in residential use cases.
Shuwei Wang

nr 399
Design and performance of alternative cementitious materials using industrial solid wastes - carbonation and chemical activation
Yanjie Tang

This thesis addresses global challenges like climate change and resource depletion by exploring the recycling and reuse of industrial solid waste in building materials. It investigates various wastes, including sludge from wastewater treatment, fly ash from incineration, gas purification residues, and steel slag. High-efficiency applications tailored to these materials' properties are developed for construction purposes. Results show that these wastes can be used effectively as landfill cover and cementitious systems, reducing carbon emissions and reliance on natural resources while promoting circular economy principles. Key innovations include sludge-based landfill cover materials, which demonstrate low permeability and minimal heavy metal leaching, making them safe and durable with a lifespan of over 50 years. Durability tests confirmed that even after carbonation, permeability remained within regulatory limits. Additionally, cement-free binders are developed using residues from incineration plants and biomass incineration. These alkali-activated materials provide a sustainable alternative to Portland cement, significantly reducing CO2 emissions. Finally, the study explores self-cleaning materials based on metakaolin and promising slag-based binders from steel production, which exhibit good mechanical properties and hydration behavior. Overall, the research presents innovative solutions for recycling industrial solid waste in construction, contributing to sustainable building practices and a reduction in environmental impact.

DEPARTMENT OF THE BUILT ENVIRONMENT

TU/e EINDHOVEN UNIVERSITY OF TECHNOLOGY